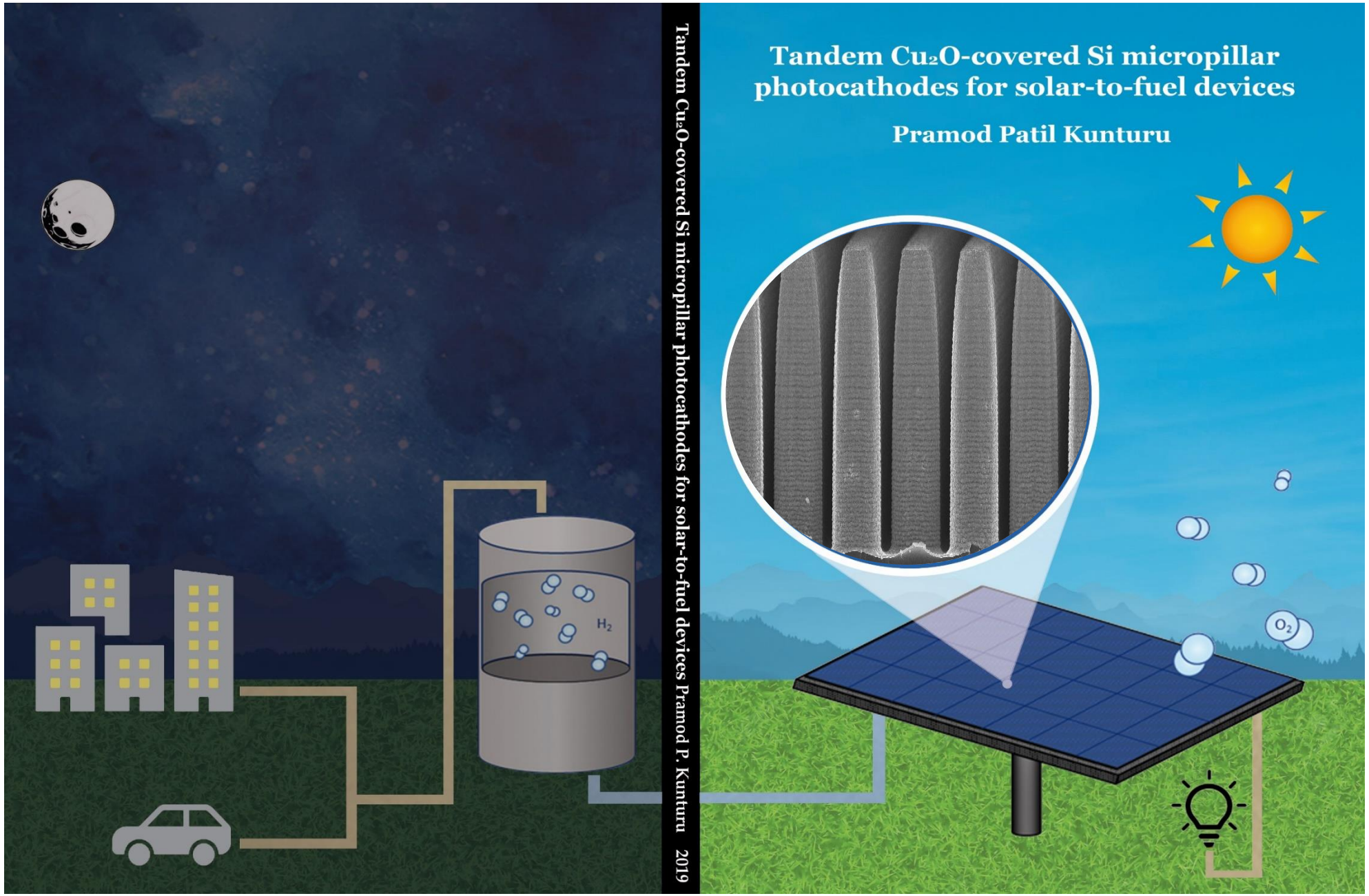
Tandem Cu_2O-covered Si micropillar photocathodes for solar-to-fuel devices
Pramod Patil Kunturu
H_2
O_2
Tandem Cu_2O-covered Si micropillar photocathodes for solar-to-fuel devices Pramod P. Kunturu 2019

TANDEM Cu_2O-COVERED SILICON MICROPILLAR PHOTOCATHODES FOR SOLAR-TO-FUEL DEVICES

Pramod Patil Kunturu

Members of the committee:

Chairman:	Prof.dr. J.L. Herek	University of Twente
Promotor:	Prof.dr.ir. J. Huskens	University of Twente
Members:	Prof.dr. N.H. Katsonis	University of Twente
	Prof.dr. G. Mul	University of Twente
	Prof.dr.ir. J.E. ten Elshof	University of Twente
	Prof.dr. J.N.H. Reek	University of Amsterdam
	Dr. W.A. Smith	Delft University of Technology

The research described in this thesis was performed within the laboratories of the Molecular NanoFabrication (MnF) group, the MESA+ Institute for Nanotechnology, and the Department of Science and Technology (TNW) of the University of Twente (UT). This research was supported by the Karnataka state government under the D Devraj Urs Videshi Vyasanga Vetana scheme.

UNIVERSITY OF TWENTE. MESA+ INSTITUTE FOR NANOTECHNOLOGY MnF

Tandem Cu_2O-covered silicon micropillar photocathodes for solar-to-fuel devices

ISBN: 978-90-365-4780-2

DOI: 10.3990/1.9789036547802

Cover art: Isadora Silva and Luca Ricciardi

Printed by: Gildeprint – The Netherlands

TANDEM Cu_2O-COVERED SILICON MICROPILLAR PHOTOCATHODES FOR SOLAR-TO-FUEL DEVICES

DISSERTATION

to obtain
the degree of doctor at the University of Twente,
on the authority of the rector magnificus,
prof. dr. T.T.M. Palstra,
on account of the decision of the doctorate board,
to be publicly defended
on Friday, July 5, 2019, at 16:45 h

by

Pramod Patil Kunturu

born August 6, 1989
in Huvina Hadagali, India

This dissertation has been approved by the promotor:

Prof. dr. ir. J. Huskens University of Twente

This thesis is dedicated to my family and friends

Table of Contents

Chapter 1

General Introduction

1.1 Introduction

Human beings have taken advantage of non-renewable fossil fuel as the main energy source for more than a century. The increase of the energy demand is due to the growing world's population with the migration of people towards urban areas owing to industrial development and worldwide integration.[1] A major amount of the existing energy stream is created from combusting fossil fuels like oil, coal and natural gas, stored in the earth crust. As a consequence, we encounter two main disadvantages which are threatening our living world. Firstly, an energy crisis may occur in the near future due to limited reserves of fossil fuels in the Earth, and sources will disappear soon.[2] Secondly, the burning of fossil fuels (particularly oil and coal) leads to the emission of greenhouse and polluting gases such as carbon dioxide (CO_2), sulfur dioxide (SO_2) and nitrogen oxides ($NO_{(x)}$). These gases contaminate the air and contribute to global warming and climate change.[3]

For these aforementioned reasons, we as researchers focus on solving this problem based on practically achievable solutions. Figure 1.1 shows schematically the estimation of total fossil fuel reserves and the yearly potential for renewable energy resources.[4] An attainable solution to this issue is the use of renewable energy resources like solar, wind, biomass, hydro, etc. These energy sources do not vanish like fossil fuels but are available in a regular manner.[5, 6] Furthermore, renewable energy sources can meet our energy demand as well as conditions like being secure, nature-friendly and a longstanding primary energy source on a global scale. From all these energy resources which are depicted in Figure 1.1, solar energy is the largest one with the potential to meet all our energy needs. At the Earth surface, a striking amount of energy, in the form of solar radiation, of approximately 120,000 TW is received, out of which the combined land

areas receive ~25,000 TW continuously. The amount of solar energy is larger than all remaining renewable resources together.[5, 7]

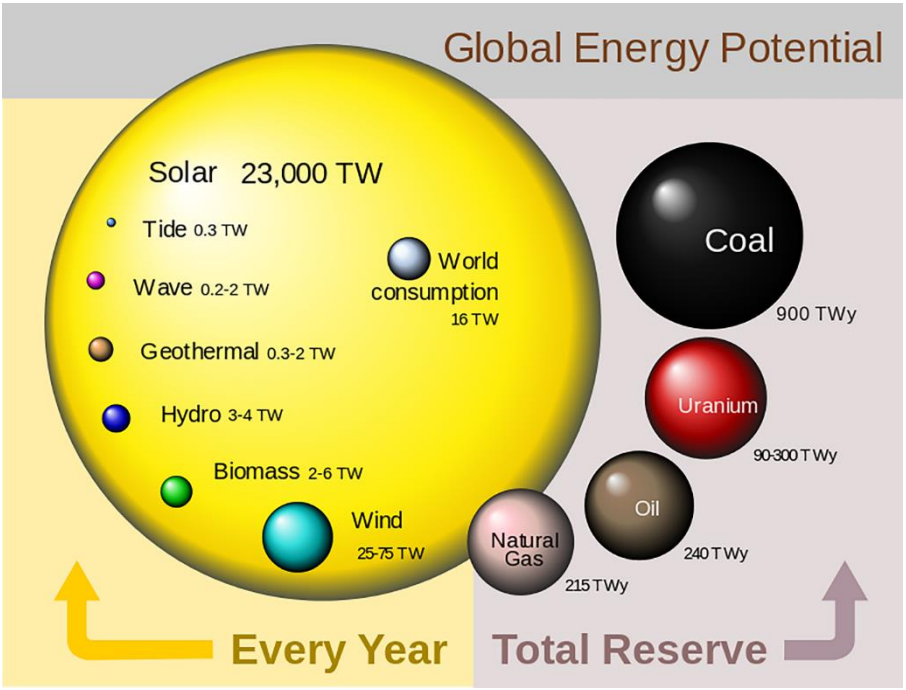

Figure 1.1 Schematic diagram of comparison between non-renewable and renewable total energy reserves with world energy consumption (in TWy). The volume of each sphere represents the total amount of energy recoverable from the finite reserves and the energy recoverable per year from renewable sources.[4]

At present, the conversion of sunlight into usable electricity is already well-established on the global scale by using photovoltaic (PV) cells. Solar PV modules are already an economical renewable energy technology to use for domestic and personal transport purposes. In the Netherlands, the combined installed PV capacity has surpassed 1.5 GW in 2018 and is expected to reach 6 GW by 2020, and 20 GW by 2035.[8] Unfortunately, the main drawback of this energy source is the intermittency of the sun (Figure 1.2). The availability of solar energy is highly fluctuating with respect to

geographic locations, and it is subjected to seasonal and day-night cycles and is dependent on the presence of clear sky conditions.[9]

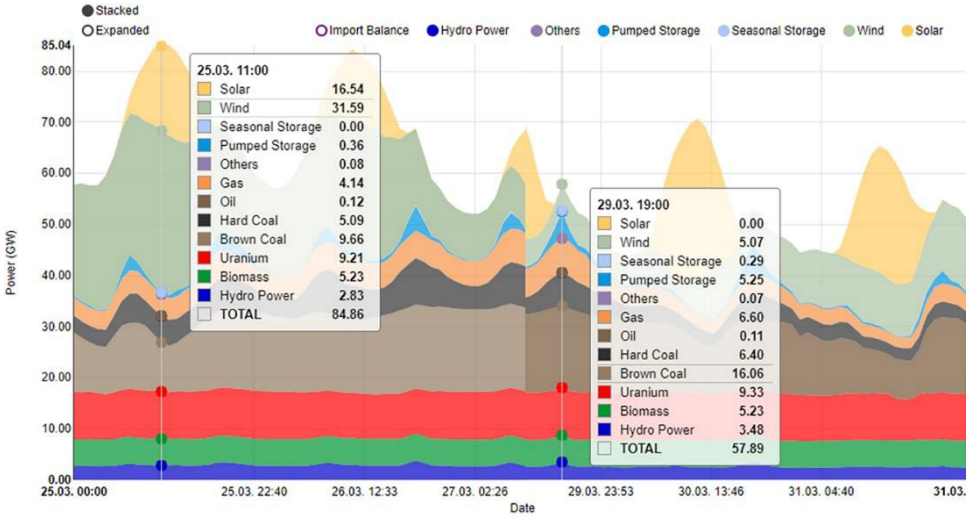

Figure 1.2 Electricity production in Germany in week 13 2019.[10]

Therefore, it is essential to develop new ways on a global scale to use solar energy to produce fuels (like hydrogen, methane, methanol, etc.) in order to store energy in chemical bonds of molecules. The concept is known as solar-to-fuel (S2F) or photoelectrochemical (PEC) water splitting, in which sunlight and water produce hydrogen gas, which has been demonstrated to be working at small scales, but is on its way towards commercialization.[11]

A PEC water splitting device consists of few important components, i.e. semiconductor materials, catalysts, an electrolyte solution, and an ion exchange membrane. Semiconductors with a suitable bandgap are the main materials to absorb photons of sufficient energy to generate electron-hole pairs. These photogenerated charge carriers are transferred towards the (photo)electrocatalyst-liquid junction to split water into hydrogen (H_2) and oxygen (O_2). To drive this reaction, a minimum photovoltage of 1.23 V is needed. In practice, an extra voltage (~0.6 V) is required due to cell resistances and the overpotential of the oxygen evolution reaction. In order to drive the water splitting reaction efficiently by sunlight, photo-absorbing materials must meet the following requirements:

I. The material should be earth-abundant, inexpensive and non-toxic.
II. It must have a sufficient band gap to absorb a large amount of sunlight and generate sufficient photovoltage to drive the reaction.
III. High performance with good stability in contact with acidic/basic electrolyte under illumination.

Figure 1.3 shows the many possible semiconductors and their band edge positions with respect to the hydrogen evolution reaction (HER) and oxygen evolution reaction (OER) potentials. Most of them are not appropriate to fulfill the above-mentioned requirements.

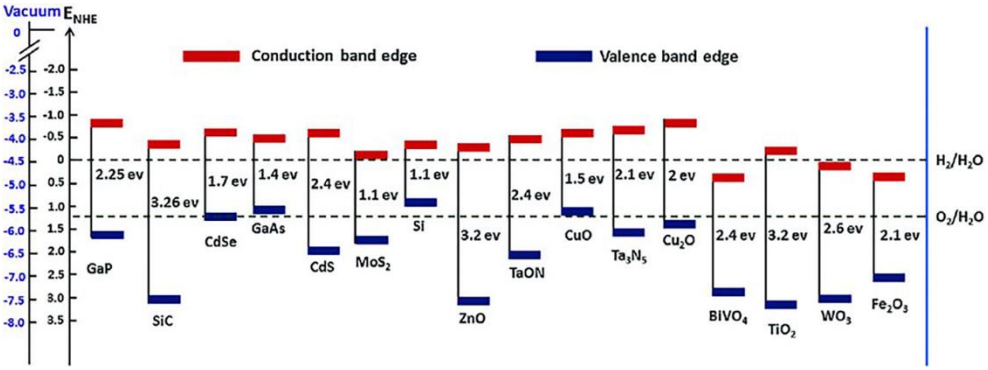

Figure 1.3 Band edge positions of semiconductors in contact with the aqueous electrolyte at pH = 0 relative to NHE and the vacuum level. For comparison, the HER and OER redox potentials are also presented.[12] This figure was reproduced with permission from ref. 12, Copyright 2016 The Royal Society of Chemistry

Cuprous oxide (Cu_2O), with a band gap of 2.0 eV, makes a very interesting candidate for the hydrogen evolution reaction (HER) in a S2F device. Cu_2O is non-toxic, is available in large quantities and is available by facile synthesis methods. Cu_2O can be used as a photocathode for water splitting and as a solar cell to power conversion and theoretically provide 18% solar-to-hydrogen conversion efficiency and 20% power conversion efficiency.[13] However, due to the self-photocorrosion phenomenon of Cu_2O in the electrolyte under illumination and an insufficient photovoltage to drive

unassisted water splitting, its application as an effective photocathode for HER is problematic. The former issue can be improved by surface passivation through overlayers formed by, e.g., atomic layer deposition (ALD). The latter one can be addressed by making a tandem PEC configuration with a second semiconductor to achieve extra voltage.
Silicon, is another promising material due to its high abundance and a band gap of 1.1 eV, absorbing a large fraction of solar light. In addition, numerous studies have been investigated on the nano/micro-fabrication structuring to enhance optical properties, the creation of junctions by doping (phosphorus and boron) to increase photoelectrical efficiency. Therefore, a tandem PEC system of Cu_2O and Si constitutes a good way to make an efficient photocathode for an S2F device.

1.2 Aim and scope of the thesis

The main focus of the work described in this thesis is on cuprous oxide (Cu_2O) as a photocathode in a S2F device for photoelectrochemical solar water splitting. In particular, we considered two main reasons to select this material. Firstly, previous studies have reported PEC performance with satisfactory photocurrent density and stability using protection overlayers. Yet, there is a need to understand aspects such as band energy alignment between the p-type photocathode and n-type protection layers. Furthermore, we also attempt to improve the stability by using easily processible carbon-based protection layers (carbon film, g-C_3N_4) over Cu_2O films. Secondly, the Cu_2O photocathode is introduced in the tandem PEC concept, by combining Cu_2O as a top absorber with microstructured Si with a pn-junction, to investigate the possibility of such S2F devices to obtain a sufficiently high photovoltage to drive unassisted solar water splitting reaction.

Chapter 2 provides a literature overview on implementing a variety of device configurations and effective protection strategies for enhancing the photostability of photoelectrodes. In addition, we pay attention to the

fundamental aspects of protection strategies that address issues of stability and catalytic performance. We then analyze the fundamental aspects of the charge transfer mechanism between the semiconductor-protection layer to achieve stable solid-liquid interfaces.

In Chapter 3, a thin carbon film coating is applied on electrodeposited Cu_2O films and on Cu_2O/CuO heterostructure films grown by thermal oxidation. A simple solution-based method is used that employs a carbon precursor (glucose) to suppress the normally occurring Cu_2O photocorrosion when the materials is in contact with the electrolyte. The coverage and thickness of the carbon films are controlled by the concentration of the glucose solution and the number of deposition cycles. Furthermore, the roles of the carbon coating in enhancing the photostability and charge recombination is analyzed, as well as the mechanism of charge carrier transport under illumination.

In Chapter 4, a layered graphitic carbon nitride (g-C_3N_4) material is used as a suitable protection layer for Cu_2O to show the possibility to enhance the charge carrier separation by forming a type-II or z-scheme heterojunction photocathode. Two different deposition techniques are used to passivate Cu_2O with g-C_3N_4 nanosheets and nanowires, with the goal of constructing highly stable Cu_2O/g-C_3N_4 heterojunction photocathodes. Optical photoluminescence (PL) studies have been performed to investigate the separation efficiency of charge carriers, migration and recombination behavior.

In Chapter 5, a tandem PEC concept is introduced by combining Cu_2O and Si photoabsorbers to fabricate highly efficient and stable photocathodes from abundant materials. This study exhibits the impact of high-quality protection layers (ZnO and TiO_2) on Si-Cu_2O micropillar arrays created by pulsed laser deposition (PLD), with the goal to overcome photodegradation and achieve long-term PEC operation. The Si microwire array height and pitch are varied as well as the thickness of Cu_2O and Cu_2O/CuO layers, and limiting factors

are evaluated. Both the photoelectrical and photoelectrochemical performance are assessed and compared with planar devices.

In Chapter 6, based on the promising effect of Si/Cu_2O tandem photocathodes, we made a S2F device that is based on tapered Si microwire arrays, to enhance optical and PEC performance (*i.e.*, to provide high light absorption and photovoltage of Cu_2O). As a result, a benchmark tandem Si/Cu_2O/Ga_2O_3/TiO_2/RuO_x microwire photocathode is developed, and its current density, photovoltage and long-term performance under continuous illumination are assessed.

1.3 References

1. A. Lewandowska-Bernat and U. Desideri, *Appl. Energ.*, 2018, **228**, 57-67.
2. T. Covert, M. Greenstone and C. R. Knittel, *J. Econ. Perspect.*, 2016, **30**, 117-138.
3. J. A. Poole, C. S. Barnes, J. G. Demain, J. A. Bernstein, M. A. Padukudru, W. J. Sheehan, G. G. Fogelbach, J. Wedner, R. Codina, E. Levetin, J. R. Cohn, S. Kagen, J. M. Portnoy and A. E. Nel, *J. Allergy Clin. Immunol*, 2019, DOI: https://doi.org/10.1016/j.jaci.2019.02.018.
4. R. Perez and M. Perez, *A fundamental look at energy reserves for the planet*, The International Energy Agency SHCP Solar Update, 2009.
5. A. Hussain, S. M. Arif and M. Aslam, *Renew. Sust. Energ. Rev.,* 2017, **71**, 12-28.
6. T. W. John Twidell, *Renewable Energy Resources*, london, 3 edn., 2015.
7. N. S. Lewis, *Science*, 2016, **351**, aad1920.
8. E. Bellini, Netherlands a gigawatt solar market, pv-magazine, 2019, https://www.pv-magazine.com/2019/01/09/netherlands-a-gigawatt-solar-market/, (accessed April/01/ 2019).

9. B. Sivaneasan, N. K. Kandasamy, M. L. Lim and K. P. Goh, *Appl. Energ,* 2018, **218**, 36-45.
10. Fraunhofer Institute for solar energy systems (ISE) Energy charts, https://www.energy-charts.de/power.htm, (accessed April/01/2019).
11. S. D. Tilley, *Adv. Energy Mater.*, 2019, **9**, 1802877.
12. A. G. Tamirat, J. Rick, A. A. Dubale, W.-N. Su and B.-J. Hwang, *Nanoscale Horiz.*, 2016, **1**, 243-267.
13. J. Luo, L. Steier, M.-K. Son, M. Schreier, M. T. Mayer and M. Grätzel, *Nano Lett.*, 2016, **16**, 1848-1857.

Chapter 2

Boosting solar water splitting performance of photoelectrodes by surface protection strategies

Photoelectrochemical (PEC) water splitting for hydrogen generation from sunlight has been extensively studied as a promising method to solve the energy crisis and ecological problems triggered by the extensive use of fossil fuels. Among the several issues connected with photoelectrode materials, like light absorption, charge separation and transport, and charge transfer, a key challenge is to achieve long-lived PEC performance without deterioration of the semiconductor materials involved. Numerous efforts have been focused on implementing a variety of configurations and effective protection strategies in enhancing the photostability of photoelectrodes. In this review we pay attention to the fundamental aspects of protection strategies suggested to address the stability and catalytic performance issues. The charge transfer mechanism that occurs at interfaces between the protection layer and the photoelectrode is analyzed. The roles of the protection layer in enhancing stability and in band bending strategies to obtain higher PEC activity are discussed as well. All discussions are presented within the context of hydrogen (HER) and oxygen evolution reactions (OER).

2.1 Introduction

The implementation of solar light harvesting by photovoltaic (PV) solar cell technology is proceeding quickly. PV directly converts sunlight into electricity but, due to the periodic, territorial and discontinuous nature of sunlight, we need methods to efficiently store part of the resulting energy.[1, 2] The biggest challenge is to accomplish storage in a cost-effective way on the terawatt scale.[3] Sunlight-driven photoelectrochemical water splitting has developed into one of the most encouraging ways for the ecologically and economic production of hydrogen as a clean fuel and energy storage medium. All-in-one photosynthetic assembly (APA)[4] is a set of integrated devices to achieve photoelectrochemical (PEC, *i.e.*, combined PV+electrolysis-based) water splitting using an integrated structure.[5-7]

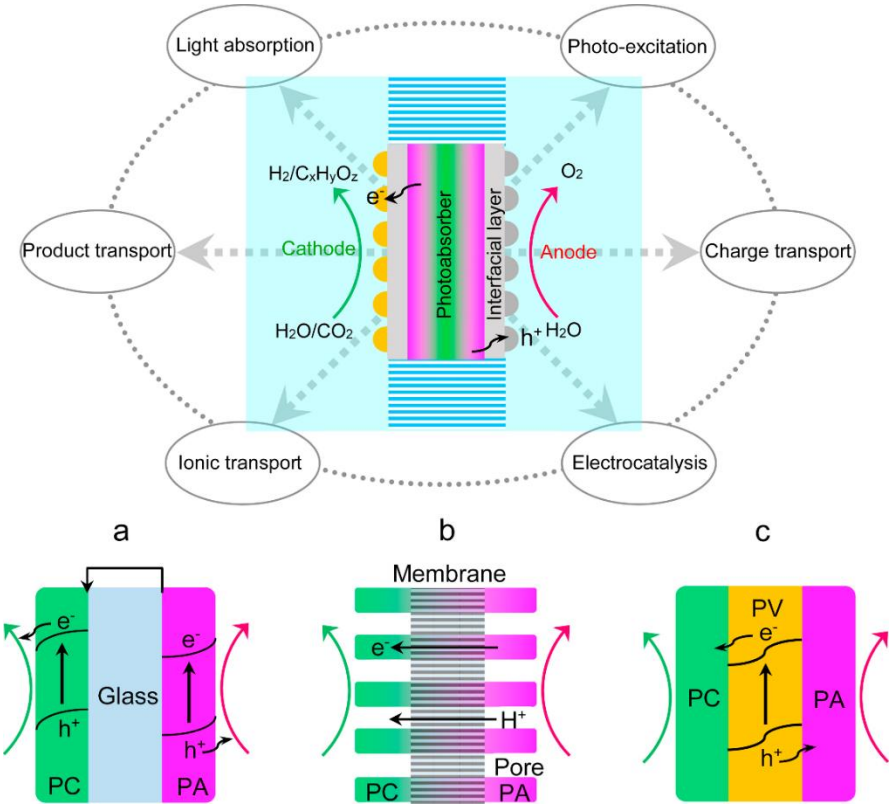

Figure 2.1 Photochemical processes in an all-in-one photosynthetic device and its classification: (a) photoelectrochemical diode and (b) all-in-one membrane, (c) monolithic PV/PEC device. PA-photoanode and PC-photocathode. Reprinted from[4] Copyright (2018), with permission from Elsevier.

A complete PEC device for solar water splitting includes various vital components. In particular, a PEC water splitting device having semiconductor materials to create photocathodes and photoanodes is one of the promising approaches for a sustainable and efficient way to generate hydrogen from an economic point of view.[8] The overall solar water splitting reaction in a PEC device (see Figure 2.1) consists of three parts: (i) absorption of sunlight by semiconductors into generated electron-hole pairs, (ii) the separation and transportation of charge carriers towards the electrode interfaces, possibly

decorated with an additional co-catalyst, and (iii) these charges are transported across the semiconductor-electrolyte or catalyst-electrolyte interface in order to drive the reduction and oxidation of the water.[9-12] The oxidative half-reaction leads to production of oxygen from H_2O or OH^-, *i.e.,* the oxygen evolution reaction (OER), whereas the reductive half-reaction produces H_2 from H^+ or H_2O, *i.e.,* the hydrogen evolution reaction (HER).[13, 14] The gas products of the overall PEC water splitting reaction can be formed in a single compartment and then collected separately to avoid the back reaction. Alternatively, using a wired or monolithic device, both reactions can be carried out in different compartments, such as oxidation (at the photoanode) and reduction (at photocathode) reactions,[15] which excludes the requirement for an extra gas separation step.[16] However, to decrease associated resistance or ohmic losses and confined pH ramp overpotentials (η), this technique not only needs high ionic strength but also strong acid or strong base electrolytic environment.[17]

Until now, there has been significant research work put into establishing numerous configurations to construct an efficient PEC device. One above-mentioned configuration is to join two semiconductor photoabsorbers in series to build a PEC tandem cell. The recombination of photogenerated charge carriers at the interface occurs between photocathode/anode, whereas photogenerated minority charge carriers in the dual photoabsorbers are transported in the direction of the interface between semiconductor/electrolyte solution to carry out the specific half-reactions (Figure 2.1a). Recent works are focused in the direction of more innovative 3D-architectures based on micro/nanowire, and micro/nano-rod assembly (Figure 2.1b). A fascinating design is the silicon-based micro/nanowire array idea proposed by the Joint Center for Artificial Photosynthesis (JCAP) in USA (Caltech, Berkeley).[18] In this configuration, a proton-conducting membrane is one of the essential components in which the 3D micro/nanowire arrays have to be implanted and decorated with appropriate electrocatalysts, both for oxygen-evolution and hydrogen-evolution reactions. Another possibility is a fully integrated system where the photovoltaics (PV) is combined with a photoabsorber on top to create

a PV/PEC device (Figure 2.1c). The introduced PV cell provides additional bias generated from the junction. However, PVs are sensitive to an electrolyte solution, and it thus has to be passivated against corrosion from the electrolyte by covering with a protection layers. The PV cell may be single or multiple junction, which can be replaced by dye-sensitized solar cells (DSCs) or perovskite solar cells.

The rational design of a PEC device requires consideration of the interplay among different components:

1) Tandem photoabsorber materials are used to absorb a larger range of the solar spectrum for maximizing the photocurrent densities while providing sufficient photovoltage by well-matched alignment of their bandgaps. Despite constant efforts, the solar-to-hydrogen (STH) conversion efficiency is limited for PEC devices. The losses during charge carrier separation and transportation processes at the solid-liquid interfaces are related to slow kinetics and the necessity of an overpotential to drive the water splitting reactions.

2) Co-catalysts are decorated on both photoelectrodes for an efficient use of the redox potential to promote the HER and OER. Incorporation of an electrocatalyst onto the surface of a photoabsorber increases the performance of the device. The roles of these catalysts include a) to passivate the recombination sites; b) to tune the band structure energetics. A protecting layer can serve as a charge transfer layer between the photoabsorber and the catalytic sites or could be composed of a conformal coating of stable electrocatalyst.

3) An ion-selective separation membrane used to avoiding explosive gas mixtures and enable fast transport of protons. The membrane should be tailored to provide a minimum transfer resistance to protons to achieve a minimum thickness and also to hamper gas permeation. The membrane must be in good contact with the electrodes, and thus minimize the resistances at the interface.

4) Systematic architecture design to maximize charge transport, productivity, cost efficiency and minimization of ion transport losses. The ionic resistance in a monolithic device tends to be higher than in a wired-electrode device. The long

pathways for proton migration results in current density asymmetries in the electrode surfaces, ultimately resulting in large ohmic losses. To overcome the limitations, photoelectrodes can be designed on the microscale.

This review presents the key aspects of protection strategies for solar water splitting devices, targeting on stable inorganic thin film materials. First, we examine recent progress on PEC device configurations that include the PEC tandem cell, PV/PEC tandem cell and PV-electrolyzer hybrid system. We begin with a discussion of physical aspects, and then attempt to distinguish the advantages and limitations of each device configuration. Secondly, we focus on analyzing fundamental understanding on charge transfer mechanisms at the interfaces between dual semiconductors (solid-solid) and semiconductor/ electrolyte (solid-liquid), which is important to predict innovative, superior performing materials, and ultimately for efficient solar–to–hydrogen (STH) efficiency. Thirdly, we review recent advances in facile passivating techniques (conventional and emerging) and less expensive routes to protecting unstable photoelectrodes for STH application. Finally, technical remarks on practical PEC tandem device systems are addressed along with main concluding key points.

2.2 PEC water splitting device configuration

Although the best way to produce H_2 from solar energy is still a subject of debate, so-called unassisted water splitting, aided only by solar light, is moving toward maturity and becoming one of the most rapidly developing scientific fields.[19, 20] Based on the concept of PEC water splitting, the simplest configuration includes one-sided light-absorption components (semiconductors) as either the anode or cathode to perform water oxidation or reduction. To date, numerous semiconductors have been studied as photoelectrode materials for PEC water splitting, including TiO_2,[21] WO_3,[22] α-Fe_2O_3,[23] ZnO,[24] $SrTiO_3$,[25] Si,[26] InP,[27] Cu_2O,[28] $BiVO_4$,[29] and TaON.[30]

However, for direct water splitting to occur, the half-cell must meet several key criteria simultaneously: (i) the semiconductors must generate a sufficient bandgap (E_g > 2.0 eV) upon irradiation to split water; (ii) the bulk bandgap must efficiently utilize the solar spectrum (λ > 460 nm); (iii) the band edge potentials at the surfaces must straddle the H_2 and O_2 redox potentials; and (iv) the photo-induced charge carriers must be highly selective for water splitting. Otherwise, any unfulfilled aspects must be rendered by external electric energy. However, no cost-effective material satisfies all these technical requirements to date. Efforts are ongoing to design integrated energy conversion devices to meet these criteria, mainly focusing on three devices: PEC tandem cells, integrated photovoltaic cell (PV)/PEC devices and PV/electrolyser hybrid devices.

2.2.1 PEC tandem cells

In PEC tandem cells, the integration of the photoanode and photocathode is responsible for the two separate water redox half-reactions. In the PEC dual band gap system, there are two configurations of the device, based on whether the large bandgap material is a n-type photoanode or p-type photocathode. In both configurations, the higher wavelength photons, transmitted through the top large-bandgap photoabsorber, are absorbed and harvested by the bottom small-bandgap photoabsorber (Figure 2.2). Due to band bending, the photogenerated holes in n-type photoanode and electrons in p-type photocathode are transferred toward the semiconductor-electrolyte interface to oxidize and reduce water into O_2 and H_2, respectively. At the ohmic contact recombination occurs of electrons of the photoanode and holes of the photocathode that connects both photoelectrodes. In this tandem device system each material is responsible for the appropriate half reaction of water splitting.

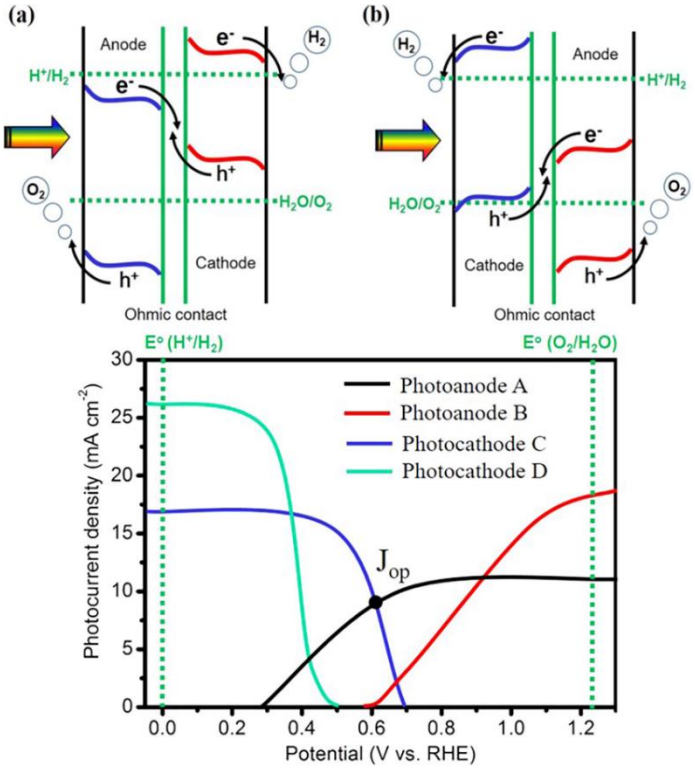

Figure 2.2 Schematic of tandem PEC water splitting device with (a) a large bandgap photoanode and a small bandgap photocathode. (b) a large bandgap photocathode and a small bandgap photoanode. (c) A comparison of J–V curves of four hypothetical photoelectrodes, including two photoanodes and two photocathodes, to construct a PEC tandem device. The combination of photoanode A and photocathode C gives the most efficient tandem device in terms of maximum operating current density (J_{OP}). Reproduced with permission of IOP Publishing Ltd.[31]

Overall water splitting efficiencies can be calculated from *J-V* data for each material in a tandem configuration. The intersection of the two linear sweep voltammetry (LSV) graphs or overlapped two individual *J–V* curves for each photocathode and photoanode indicates the maximum operating current density (J_{OP}) for the overall water splitting system. The performance of single

photoelectrodes for each half reaction, particularly in the low bias voltage region, is responsible for the overall water splitting activity. Figure 2.2c shows a pathway to construct a PEC tandem device by comparing *J-V* data of two hypothetical photoanodes and photocathodes. Although at the high bias voltage region photoanode B and photocathode D give higher photocurrent densities, photoanode A and photocathode C allow to construct a more efficient tandem device because of the higher operating current density (J_{OP}). The theoretical value of J_{OP} is calculated without considering optical losses due to the top light absorber and ohmic losses between the photoelectrodes. This focuses attention on the importance of reaching a high photocurrent density at the low voltage bias region for each photoelectrode in constructing an efficient tandem device. Aforementioned straightforward configuration provides promising advantages over PV-biased PEC tandem devices in terms of low price, simplicity and high performance.

The important outcomes of a study of Fountaine *et al.*, as above mentioned model, with more realistic values, shows an efficiency of 28.3% with bandgaps of E_g = 1.59 and 0.92 eV (Figure 2.3a). Deutsch *et al.*[32]and Atwater *et al.*,[33] reported benchmarking STH efficiencies by tuning the bandgap combination of 1.8 eV and 1.2 eV achieving 16% and 19% in a monolithic GaInP/GaInAs tandem devices, respectively. It is possible to improve the STH efficiency towards >20% by using 1.7 eV and 1.1 eV bandgap photoabsorber materials. For instance, Si, which has a bandgap of 1.1 eV and is earth abundant, is almost ideal for a bottom photoabsorber in a tandem device. In addition, Si can be fabricated into an n-type photoanode and p-type photocathode by controlled doping with boron and phosphorus, respectively. The state-of-art Si-based PV cell pair with $BiVO_4$ photoanode material has shown an only modest operating current density or STH efficiency (~ 5%) in the PEC performance due to the poor photocurrent output from $BiVO_4$.[34] Recent studies showed that gentle nitrogen treatment of $BiVO_4$ effectively reduced the bandgap by 0.2 eV compared to as-

synthesized pure $BiVO_4$, which enhances the prospects for its practical application to PEC water splitting.[35] Yet, it still has a wide band gap (~2.27 eV), which means that the efficiency will never surpass 10 mA cm^{-2} under 1 sun illumination condition (Figure 2.3b), indicating that a photoabsorber with a smaller E_g should be considered.

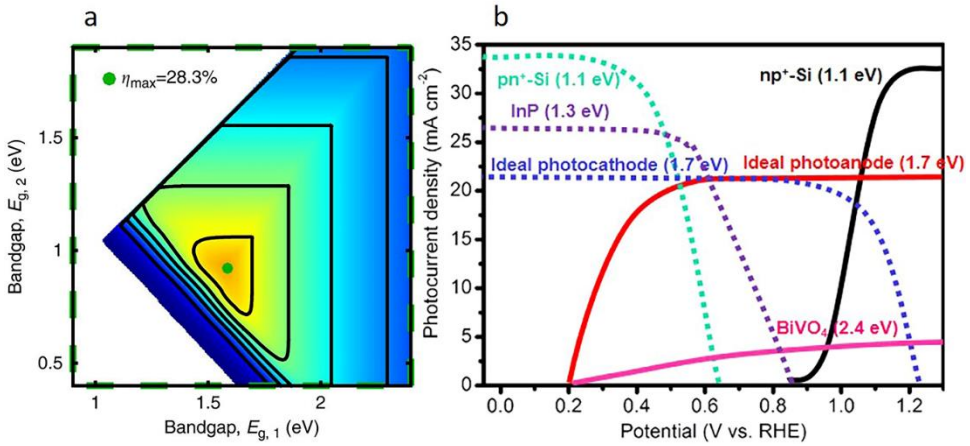

Figure 2.3 (a) High-performance realistic case for a tandem PEC cell (η_{max} = 28.3%, E_g = 1.59 and 0.92 eV), where contour lines mark every 5% and maximum efficiency points are indicated. Reproduced with permission.[36] Copyright 2016, Nature Publishing Group. and (b) J–V curves of state-of-the-art p–n+ Si-based photocathode,[37] n–p+ Si-based photoanode,[38] InP-based photocathode[27] and $BiVO_4$-based photoanode[35] to construct a PEC tandem device based on Si bottom cell. The J–V curves of the ideal photocathode and photoanode are also projected. Note that the parasitic light absorption from the top light absorber and current matching condition between the top and bottom light absorbers should be taken into account in the real tandem device. Reproduced with permission of IOP Publishing Ltd.[31]

Consequently, the photoanode and photocathode should be n -type and p -type semiconductors, respectively, with good ohmic contact to eliminate the electrical resistance.[39] The wire configuration is convenient for assembling the components, whereas the wireless configuration is more suitable for

industrial manufacture. Two main configurations for the photoanode and photocathode have been developed, as shown in Figure 2.4; one is side-by-side, named parallel illumination mode (Mode P), and the other is in series, named tandem illumination mode (Mode T).[40] Mode P exposes each photoelectrode to the full solar spectrum without requiring a transparent substrate, whereas Mode T more efficiently utilizes the solar energy, with the photoanode positioned in front of the photocathode. In summary, the Mode T with the wireless configuration could be a promising candidate for commercial applications because of the convenient assembly and more efficient solar light utilization.[41]

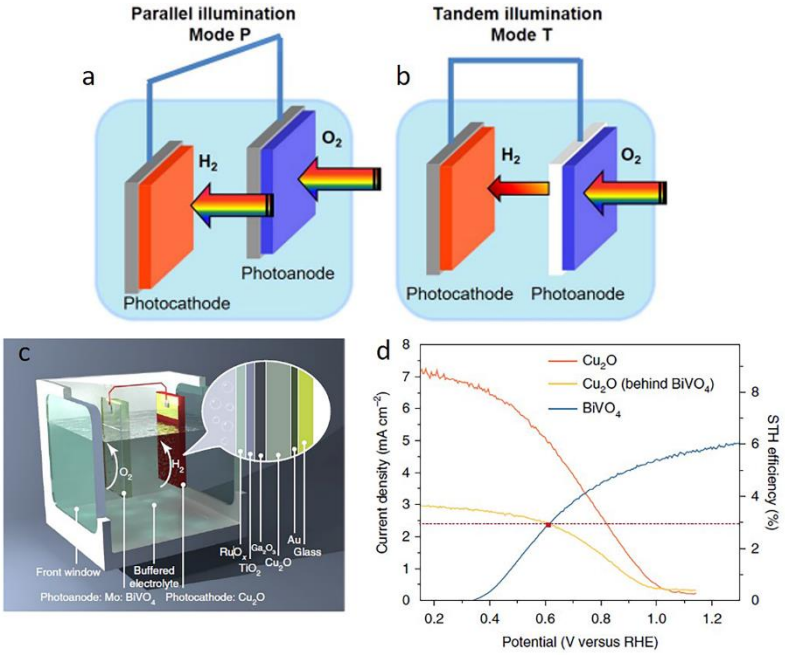

Figure 2.4 Schematic of PEC tandem cell under (a) tandem (Mode T) or (b) parallel (Mode P) illumination.[31] (c) Illustration of the all-oxide tandem solar water splitting device, consisting of Cu_2O as the photocathode and molybdenum-doped $BiVO_4$ (Mo: $BiVO_4$) as the photoanode without bias. (d) *J–E* response under simulated air mass 1.5 G chopped illumination for the

Cu_2O photocathode, $BiVO_4$ photoanode and Cu_2O photocathode behind the $BiVO_4$ photoanode.[28]

Whereas n-type materials have been studied thoroughly for PEC water splitting, relatively few p-type materials have been reported.[42-44] Currently, with increasing availability of p-type materials, some well-designed and modified PEC tandem cells are achieving cost-effectiveness and good stability. p-Type metal oxide semiconductors, which have been developed in the past few decades, are promising candidates to replace the aforementioned p -type cathodes because of their better stability, better cost-efficiency, greater earth abundance and facile fabrication process.[45-47] To demonstrate the remarkable performance of the new Cu_2O photocathode, Michael Grätzel *et al.*[28] constructed an unassisted overall solar water splitting tandem device by pairing it with the state-of-the-art $BiVO_4$ photoanode (Figure 2.4c). The light passes first through the front $BiVO_4$ absorber before reaching the Cu_2O absorber, and with this Cu_2O photoelectrode, a record STH conversion efficiency of ~3% was achieved for this all-oxide based device as shown in Figure 2.4d.

Recent studies showed that pairing with p-Si in a tandem PEC cell can provide a substantially higher photovoltage and operating photocurrent.[48] However, major challenges still face PEC tandem cells, although this type of device can theoretically achieve a maximum η_{STH} of 29.7%.[49] The real η_{STH} of a PEC tandem cell suffers from the lack of materials with the appropriate bandgap energy, suitable band edge positions, and sufficient photon harvesting in both the front and rear electrodes.[50] A favorable configuration of a PEC tandem device having a photoanode and photocathode are to achieve efficient and economical un-biased solar water splitting. Theoretical modeling studies showed the highest achievable efficiencies for dual high-quality photoabsorber materials PEC tandem device reach as high as 41%.[36]

2.2.2 PV/PEC Tandem cells

Compared with PEC tandem cells that require well-designed bandgap energies and band edge positions of p-type photocathodes and n-type photoanodes, the PEC/PV tandem cells are attractive for alleviating this aspect of the requirements. In this configuration, the maximum J_{op} can be obtained by balancing solar-light harvesting between the front PEC cells and the rear PV cells. Compared with PV cells with relatively low bandgap energy, photocurrent generation from PEC cells is a bottleneck for realizing high STH efficiency of PEC/PV tandem cells because of the limited candidates for photoelectrode materials. Furthermore, balancing solar light absorption between the PEC and PV cells should also be considered in the optimization of PEC/PV tandem cells. The band diagram regarding the charge transfer process in PEC/PV tandem cells is schematically shown in Figure 2.5.

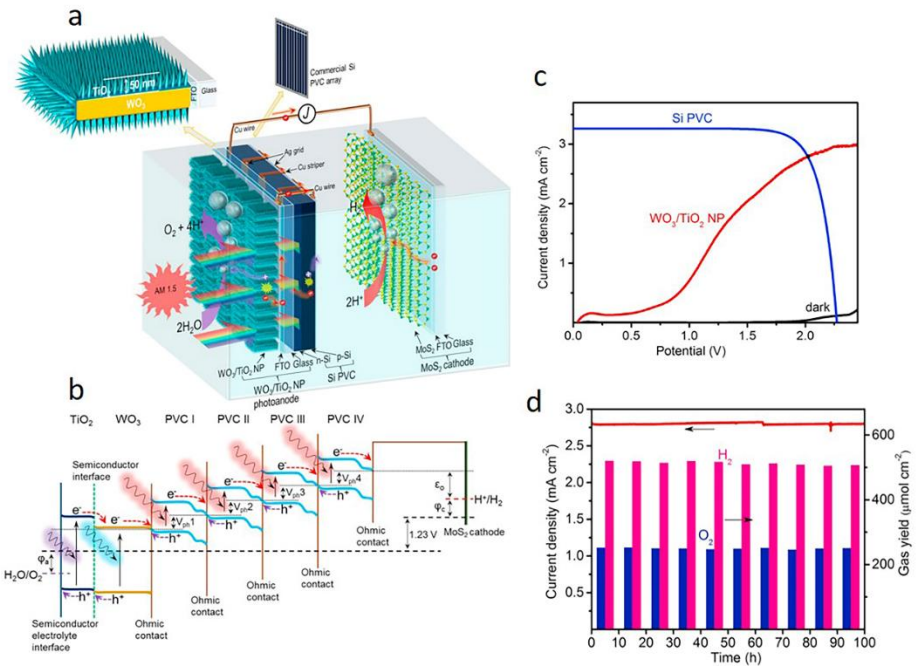

Figure 2.5 (a) Schematic representation of a PEC tandem cell. The front WO_3/TiO_2 nanoprickles photoanode is formed from an assembly of vertically aligned WO_3 nanoplates epitaxially coated with an anatase TiO_2 nanoprickle morphology overlayer, which prevents WO_3 NPs from being oxidized/etched and improves the O_2 evolution kinetics. The rear Si PVC is composed of four single-junction monocrystal Si solar cells in series, which harvest the transmitting longer-wavelength light to produce bias potential. (b) Schematic illustration of energy level diagram of the PEC tandem cell. This integrated system offers an utmost exploitation of sunlight and the matching band structures of different components enables the self-sustaining water splitting solely with solar energy. (c) *J-V* characteristics of the WO_3/TiO_2 NP photoanode tested in a two-electrode system with a MoS_2 cathode as counter cathode, and Si PVC under the AM 1.5 illumination filtered by the WO_3/TiO_2 NP photoanode. (d) J-t curves and gas yield of the PEC tandem cell for 100 h operation tested in 1 M $HClO_4$ under the AM 1.5 illumination.[51]

Y Sun *et al.*[51] reported a stable, long-life, and low-cost PEC tandem cell, which consists of a front WO_3/TiO_2 NP photoanode, a rear Si PVC and a counter MoS_2 cathode, for self-sustained solar water splitting (Figure 2.5a). The PEC tandem cells exhibits a close-to-unity Coulomb efficiency and a reasonable STH efficiency of 3.4%, in which the photocurrent of the WO_3/ TiO_2 photoanode is improved by 80% without any obvious decay after 100 h of continuous testing (Figure 2.5d). Although the efficiency is not the highest value compared to the reported PEC tandem cells, it does represent the highest value for tandem cells without using expensive PVC cells. Luo *et al.* inverted the PEC/PV tandem cell configuration to a PV/PEC configuration using a semitransparent perovskite $CH_3NH_3PbBr_3$ (E_g = 2.3 eV) PV cell in front and a $CuIn_xGa_{1-x}Se_2$(E_g = 1.1 eV) as the photocathode.[52] The well-matched bandgaps enabled efficient panchromatic harvesting of the solar spectrum, resulting in an η_{STH} of approximately 6.3%. However, when the perovskite $CH_3NH_3PbBr_3$ PV cell was replaced with a perovskite $CH_3NH_3PbI_3$ PV cell, the high absorptivity of the $CH_3NH_3PbI_3$ dramatically reduced the η_{STH} to 2.6%.[53] The bandgap tunability of the halide perovskite family (1.1–2.3 eV) probably enables the design of a PEC/PV tandem device in which a large-bandgap perovskite solar cell could be used to drive smaller-bandgap photoelectrodes.[54] With the development of sufficient electrode stabilization strategies, tandem systems that employ perovskite materials with Si photoelectrodes may yield η_{STH} >20% in the near future.

2.2.3 PV/Electrolyzer Hybrid System

The design of an unassisted water splitting device with a power conversion device and catalytic device separated by a conducting contact can significantly increase η_{STH} because it allows the charge to directly reach catalytic locations. Early attempts at developing devices based on multi-junctions of a Si PV device wired with a Co–Mo cathode and Fe–Ni–O anode were lasting for more than 18 h and achieved η_{STH} of approximately 2.5%.[55, 56] In this Co–Mo cathode/Fe–Ni–O anode–Si PV cell, the Co–Mo cathode/Fe–

Ni–O anode was a typical electrolyser, and the PV cell was regarded as the electrical supply, forming a so-called PV/electrolyser hybrid device.[57]

The PV/electrolyser devices allow to separate the photoabsorber from the electrolyte, and thus water-sensitive materials such as gallium and indium phosphides could be used for unassisted water splitting. May *et al.* reported a PV/ electrolyser device consisting of GaInP/GaInAs as photovoltaics, Rh as the H_2 catalyst and RuO_2 as the O_2 catalyst.[58] The η_{STH} achieved with this device was ~14%. Rau *et al.* replaced the Rh/RhO_2 electrolyser with a proton exchange membrane (PEM) electrolyser and used GaInP/GaInAs as the photovoltaics, which resulted in an η_{STH} as high as 16.8% under outdoor irradiation.[59] Jaramillo *et al.*[60] reported, a system consisting of two polymer electrolyte membrane electrolysers in series with one InGaP/GaAs/GaInNAsSb triple-junction solar cell (Figure 2.6a), which produced a large enough voltage to drive both electrolysers with no additional energy input. The cross-point of a dual-electrolyser *I*–*V* curve and a solar cell *I*–*V* curve is the system-coupling point and indicates the operating voltage (V_{OP}) and current (I_{OP}) for the system (Figure 2.6b). This system produced H_2 with a 48 h average STH efficiency of 30%, the highest efficiency reported to date for any solar H_2 production system (Figure 2.6c). The solar cell and dual-electrolyser were well matched near the maximum power point of the solar cell, ensuring PV-electrolysis performance near the optimum. This work demonstrates the potential for building extremely high-efficiency solar H_2 production systems using current state-of-the-art commercially available solar cells and laboratory PEM electrolysers. However, it is unclear whether this approach is viable for practical water photolysis modules, because the fabrication cost is currently very expensive for large scale integration.

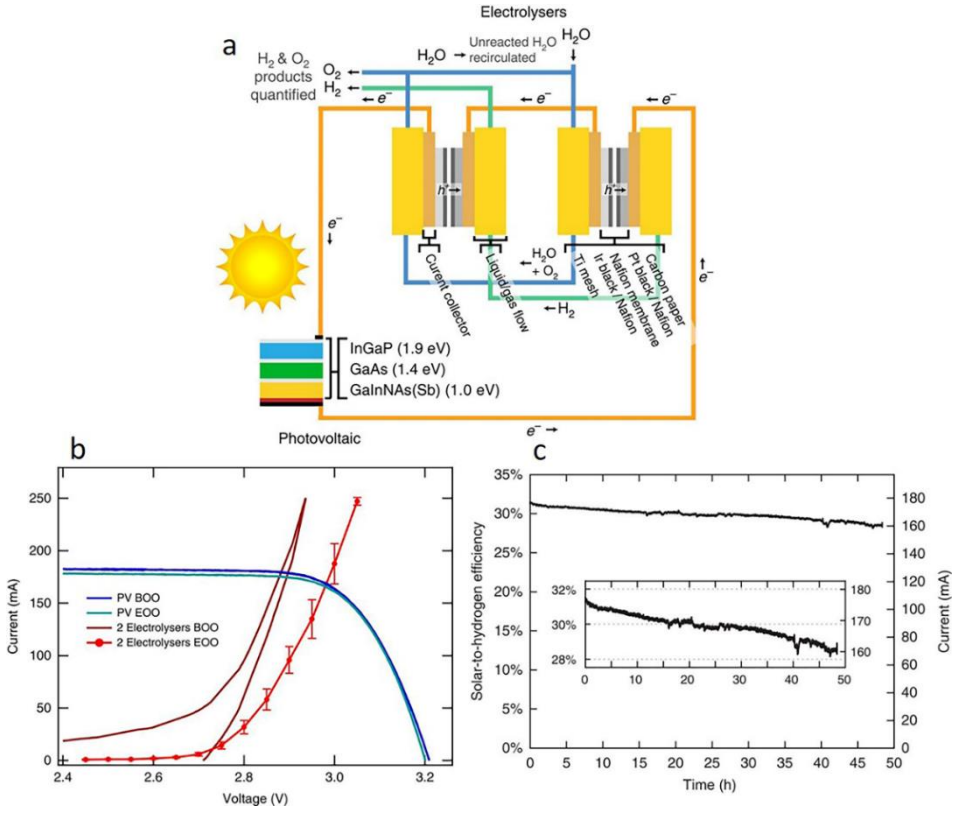

Figure 2.6 (a) Schematic representation of a PV-electrolysis system consisting of a triple-junction solar cell and two PEM electrolysers connected in series. (b) The I–V characteristics of the triple-junction solar cell and the dual-electrolyser at both beginning-of-operation (BOO) and end-of-operation (EOO). The blue and cyan curves are the solar cell I–V curves under 42 suns at BOO and EOO, respectively. The dark and light red curves are the I–V curves of the dual-electrolysers at BOO and EOO, respectively. (c) The STH efficiency of the PV-electrolysis system was measured over a 48 h continuous operation. The right vertical axis shows the current passing through the dual electrolyser and the left vertical axis shows the corresponding STH efficiency. The inset highlights a smaller *y* axis range for improved clarity.[60]

2.3 Semiconductor interface junctions

2.3.1 Photoelectrochemistry of semiconductors

To design an efficient PEC water splitting device, it is necessary to study the semiconductor photochemistry mechanism, the thermodynamic and kinetic parameters of semiconductor-liquid junctions and the electrocatalyst surfaces.[12] Many studies showed that it is important to address the semiconductor device physics and PV performance of semiconductors in contact with rapid, reversible redox species.[61, 62] A concise view of PEC semiconductor/liquid junctions is presented in this section, employing the well-developed approaches presented in earlier books and reviews.[63-68]

Prior to contact (Figure 2.7a) with a redox species in an electrolyte, the Fermi level of a semiconductor is not at the same level as the electrochemical potential – qE^0 *(A/A-)* where the E^0 is the Nernst potential of the redox pair *(A/ A-)*, acceptor *A*, and the donor *A*-.[12] Once semiconductor and electrolyte are brought into contact, electrons will flow between the semiconductor and the solution until equilibrium is established (Figure 2.7b). The formation of the junction indicates that charge transfer results in an interfacial electric field and both of the energy levels move to equilibrium.[69] As the charge density of the liquid is typically several orders of magnitude larger than that of the semiconductor, the semiconductor electrochemical potential level is moved to align with the Fermi level of the electrolyte. After equilibrium, the electrochemical potential (Fermi level) is similar at every point of the structure.[31, 65] As seen in Figure 2.7c, a Schottky-type diode can effectively separate photogenerated electron-hole pairs in a semiconductor-liquid junction with band bending under illumination. This junction phenomenon is an important aspect of photoelectrochemistry.

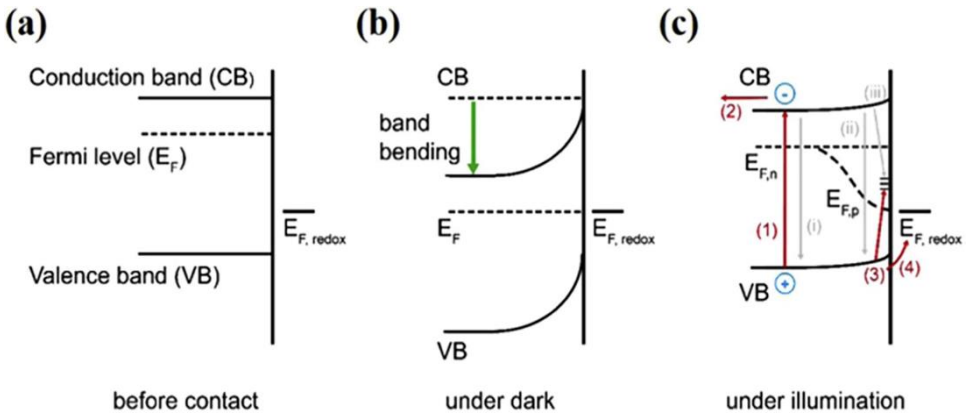

Figure 2.7 Schematic of the band diagrams under different conditions. (a) Prior to contact between the semiconductor and the electrolyte. (b) Upon contact under equilibrium conditions in the dark. (c) Quasi-equilibrium with illumination. The various processes are labeled as follows. (1) Charge excitation by light; (2) electron extraction through back contact; (3) hole transfer to surface states; (4) hole transfer to the electrolyte; (i) bulk recombination; (ii) surface recombination; (iii) electron trap by surface states. Reproduced with permission of IOP Publishing Ltd.[31]

Upon illumination ($h\nu > E_g$), electron–hole pairs are generated within the semiconductor as a result of electron excitation from the valance band to the conduction band (process 1 in Figure 2.7 c). [70-72] A quasi-Fermi level can then be derived by simply interpreting the steady-state carrier concentration of holes as representing a quasi-equilibrium situation ($E_{F,p}$ in Figure 2.7 c). Similarly, a quasi-Fermi level of electrons is also obtained ($E_{F,n}$ in Figure 2.7 c). But since the electron concentration is expected to be similar to the equilibrium value, $E_{F,n}$ is typically close to that under equilibrium. Under the likely assumption that one can probe the $E_{F,n}$ through back contact under equilibrium conditions(e.g., through the measurement of the open circuit voltage, Voc), the difference between the EF (under dark, Figure 2.7 b) and the $E_{F,n}$ (under illumination, Figure 2.7 c) represents the V_{ph} (maximum photovoltage).[70, 71] The recombination of photogenerated electron–hole pairs can take place either in bulk (process i in Figure 2.7 c) or

near surface (processes ii and iii in Figure 2.7 c), which may involve processes such as Shockley– Read–Hall recombination (through levels associated with defects or impurities), radiation (band to band) recombination.[72-74]

Photoelectrochemistry of semiconductor is an important tool to figure out the processes that oversee the operation of a photocatalytic system. In PEC water splitting device, the H^+/H_2 redox species are interesting for a p-type semiconductor photocathodes, and O_2/H_2O species for an n-type semiconductor photoanodes. It is important to achieve high efficiencies in PEC system, this depending on all three major processes: light absorbing, separating photogenerated charges, and inducing hydrogen and oxygen evolution reactions (HER and OER). Lastly, the photogenerated electrons and holes pathways and their influence on the achievable open circuit voltage (V_{OC}) of an illuminated semiconductor is presented in (Figure 2.7c).

2.3.2 Stability of photoelectrode-electrolyte junctions

One of the largest barriers to overcome is to achieve a stable PEC reaction in either strongly basic or acidic electrolytes without degradation of the semiconductor photoelectrodes. This requires the semiconductors to have proper band alignment relative to the water redox potentials, *e.g.*, the conduction band minimum (CBM) of the p-type photocathode should be higher (more negative in potential) than the water reduction potential H^+/H_2, and the valence band maximum (VBM) of the n-type photoanode, lower (more positive in potential) than the water oxidation potential O_2/H_2O.

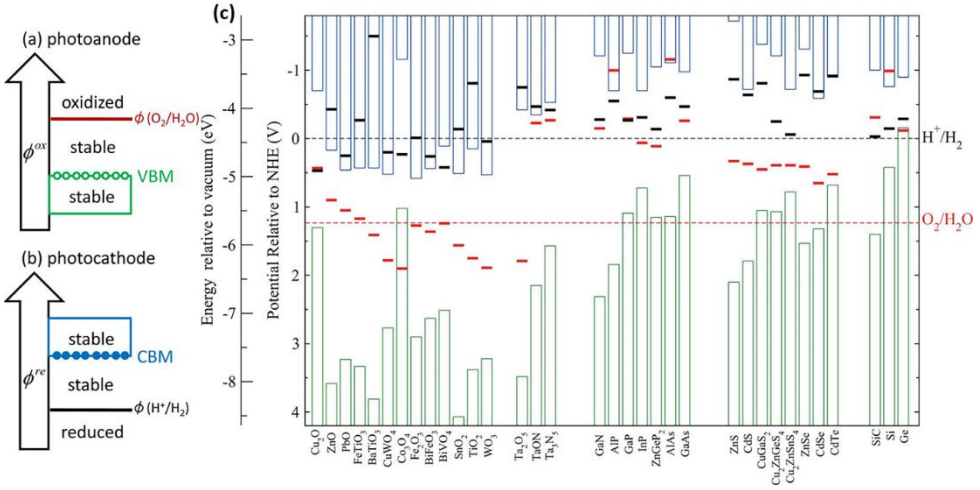

Figure 2.8 Stability change of (a) the photoanode, as its oxidation potential ϕ_{ox} shifts up from below the VBM to above $\phi(O_2/H_2O)$ and of (b) the photocathode, as its reduction potential ϕ_{re} shifts down from above the CBM to below $\phi(H^+/H_2)$. (c) Calculated oxidation potential ϕ_{ox} (red bars) and reduction potential ϕ_{re} (black bars) relative to the NHE and vacuum levels for a series of semiconductors in solution at pH = 0, at ambient temperature 298.15 K and pressure 1 bar. The water redox potentials $\phi(O_2/H_2O)$ and $\phi(H^+/H_2)$ (dashed lines) and the valence (green columns) and conduction (blue columns) band edge positions at pH = 0.[75] Reprinted with permission. Copyright (2012) American Chemical Society.

When the photoanode or photocathode is in contact with the electrolytic solution, the photogenerated holes in the valence band and electrons in the conduction band can oxidize and reduce either water or the semiconductor material itself. Whether the semiconductor is resistant to this photocorrosion depends on the alignment of the thermodynamic oxidation potential (ϕ_{ox}) relative to $\phi(O_2/H_2O)$ for the photoanode, and the thermodynamic reduction potential (ϕ_{re}) relative to $\phi(H^+/H_2)$ for the photocathode. Figure 2.8a shows the stability change of the photoanode as its oxidation potential (ϕ_{ox}) shifts up from

below VBM to above $\phi(O_2/H_2O)$, and Figure 2.8b shows the stability change of the photocathode as its reduction potential (ϕ_{re}) shifts down from above the conduction band minimum (CBM) to below $\phi(H^+/H_2)$. For a semiconductor the VBM of which is higher than $\phi(O_2/H_2O)$ and CBM lower than $\phi(H^+/H_2)$, it is not a suitable photoanode or photocathode material, and its stability depends only on the alignment of oxidation potential (ϕ_{ox}) relative to VBM and reduction potential (ϕ_{re}) relative to CBM. In general, a semiconductor is stable with respect to the hole oxidation if its oxidation potential (ϕ_{ox}) is lower than either $\phi(O_2/H_2O)$ or its VBM and is stable with respect to the electron reduction if its reduction potential (ϕ_{re}) is higher than either $\phi(H^+/H_2)$ or its CBM.[76-78]

Most photoelectrodes with relatively high photocurrents, such as Si, III–V and chalcopyrite semiconductors, *etc*., are prone to be corroded quickly leading to a larger voltage penalty due to the increased pH gradients at the surface of the electrode at high ionic fluxes, and therefore , in general, these materials have a very narrow window of stability as based on Pourbaix diagrams.[75, 79, 80] The photocorrosion of the material can be reduced by the use of relevant catalysts which improves charge transfer kinetics (i.e., k_{HER} or k_{OER}) at the solid/liquid interface, and consequently reduces the surface oxidation.[80, 81] However, this strategy cannot prevent photoelectrodes from degradation during the night time, where the materials do not have the benefit of a photovoltage to provide a stabilizing anodic or cathodic bias.[82]

Kinetic enhancement via morphology modifications can also be an approach for improving the stability of photoelectrodes. For instance, nonplanar geometries, such as a rod or pillar array can reduce the distance that minority carriers must travel, and thus the charge transfer kinetics can be significantly improved as shown in previous studies.[12, 83] However, this approach also has the fundamental issue that it does not resolve the problem of degradation in the dark.

In the case of Si – one of the most frequently used photoelectrode materials, a Si surface exposed to an acidic electrolyte deactivates by forming oxide or silicic acid, *i.e.* SiO_2 and H_2SiO_3, *etc*., whereas it decomposes into $H_2SiO_4^{2-}$

under strong alkaline conditions.[81] III–V semiconductors (GaAs, $GaInP_2$ and others), which give photo-absorber materials with the most efficient solar-to-hydrogen conversion efficiencies (STH) reported so far (14%), are also prone to chemical decomposition in strong acid, but this process takes place much more slowly.[58] Using metal oxides with high intrinsic chemical stability is also a widely used strategy, however, as described earlier, the relatively low PEC performance of those metal oxides restricts their application in practical water splitting systems. Since Bockris *et al.* demonstrated a meaningful stability report using a crystalline n-Si photoanode protected by a Pt thin film under strongly acidic (pH 0) conditions for water oxidation (i.e., OER) in 1984,[84] several protected Si devices with metallic protective catalyst films, including Ni (for OER)[85] and Ti (for HER)[86] have been demonstrated.

In the aforementioned approaches, using a protection layer with a high chemical stability for efficient photoactive semiconductors may provide an appropriate strategy to secure a stable water splitting reaction at PEC electrodes. When the protection layer material has a reduction potential (ϕ_{re}) which is more negative than the CB of the photocathode, the system is thermodynamically stable under HER conditions. Similarly, a protective material with a more positive oxidation potential (ϕ_{ox}) than the VB of the photoanode can be applied for the OER. For instance, TiO_2 has a very negative ϕ_{re} (relative to RHE) compared to the HER potential[75] indicating that TiO_2 can be an effective protection material for photocathodes, as shown in Figure 2.8c.

Grätzel *et al.*[28] and Buonassisi *et al.*[87] demonstrated successfully that atomic layer deposited Ga_2O_3 can provide a buffer layer between Cu_2O and TiO_2 , thus functioning as a protection layer. The idea was to maximize band bending within Cu_2O by introducing Ga_2O_3. PEC and IPCE (incident photon conversion efficiency) measurements are presented in Figure 2.9(a, b). In comparison to an electrode with an AZO (Al-doped zinc oxide) layer, the electrode with Ga_2O_3 showed a 0.5 V anodic shift of the onset potential. A detailed comparison was made between Ga_2O_3 and AZO, which also served

the purpose of increasing band bending when integrated with Cu_2O. But AZO features a significant mismatch with Cu_2O in terms of the potential of the conduction band minimum (ECB), which impedes electron transfer from Cu_2O to AZO. As such, AZO is much less desired for the same purpose (Figure 2.9 c, d).

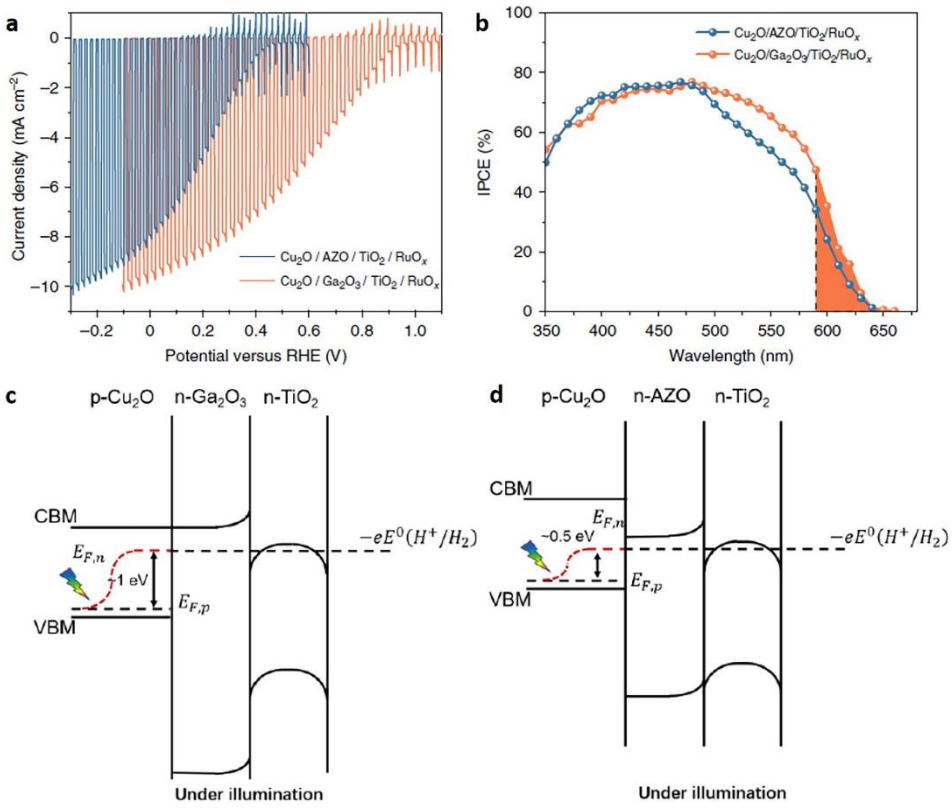

Figure 2.9 (a) *J–E* response under simulated one-sun air mass 1.5 G chopped illumination for Cu_2O nanowire photocathodes with AZO/TiO_2/RuO_x and Ga_2O_3/TiO_2/RuO_x. (b) Corresponding wavelength-dependent IPCE measurements. The shaded area represents the contribution of the excitonic effect to the total quantum yield. (c and d) Band diagrams of Cu_2O/Ga_2O_3/TiO_2 and Cu_2O/AZO/TiO_2 in equilibrium under illumination, respectively. Reprinted by permission from Nature[28] Copyright 2019.

2.3.3 Surface passivation and charge separation mechanism

The stability of the overall material can be improved by adding a protective layer that acts as a physical barrier between the harsh external environment and the semiconductor. Ideally, the protection layer would consist of a conformal surface coating by a robust material, which is sufficiently thick to prevent a direct contact of the semiconductor with the electrolyte but also sufficiently transparent and conductive to avoid limiting of the light harvesting efficiency or the charge transfer (see Figure 2.10a). Given a sufficiently thick encapsulation layer, the semiconductor does not electronically equilibrate with the electrolyte, but rather with the overlayer. In this scenario, the energetics of the semiconductor is dictated by the so-called ''buried'' junction created at the interface with the overlayer, instead of by the classical semiconductor-liquid junction described above. Alternatively, in the case where the protection layer is sufficiently thin to allow the direct tunneling of electrons (i.e. a few nanometers), the electronic influence of the overlayer is minimized. As depicted in Figure 2.10b, the surface states appear within the bandgap of the semiconductor, instead of contributing to the conduction and valence bands. One can further distinguish between deep states, near the center of the bandgap, and shallow states, closer to the VB or the CB.[88] By acting over the surface with reagents that strongly bind the dangling bonds, it is possible to suppress these surface states. Indeed, the resulting bonding and antibonding orbitals move away from the band gap, alleviating the deleterious effect of these states.[89]

D. Bae *et al.*[82] demonstrated a thin TiO_2 layer (100 nm), grown by high power impulse magnetron sputtering (HiPIMS), as a protection layer for a p-type silicon photocathode for HER (Figure 2.10 c). The HiPIMS-grown TiO_2 film along with Pt as co-catalyst produced a V_{OC} of ~0.5 V vs. RHE in 1 M KOH and showed a 4% decay over 24 h in KOH. In contrast, the sample with the TiO_2 of similar thickness deposited using conventional DC sputtering, showed 20% loss in photocurrent for the same time interval. This approach resulted in an

apparent enhanced stability owing to the higher degree of ionization for the HiPIMS plasma during sputtering process, and consequently to the minimization of unprotected Si surface.

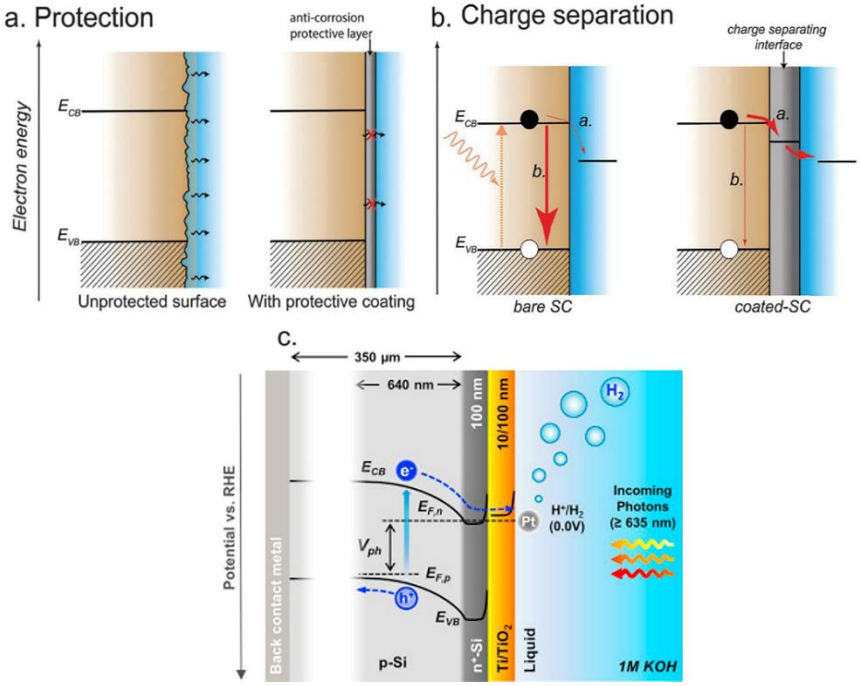

Figure 2.10 (a) Main effects of surface treatments on semiconductor materials. The protection of the semiconductor against (photo)corrosion by encapsulating with a robust material. (b) Enhancement of the charge separation by depositing an additional semiconducting layer that selectively accepts one of the carriers. a, b processes in the Figure (b) are showing the electron extraction and recombination processes, respectively. Reproduced with permission.[90] Copyright 2015, The Royal Society of Chemistry. (c) Schematic cross section of the sample used for photocatalytic activity (HER) experiments. The sample is illuminated at the Ti/TiO_2 side (TiO_2 on top). Schematic energy diagram of the illuminated sample in equilibrium with H^+/H_2 reaction is also shown. Reproduced with permission from Elsevier,[82] Copyright (2016).

Studies have shown that multiple properties of the protection layer should be optimized for efficient charge transport under PEC conditions, including, but not limited to, the conductivity type, and band bending across the layer thickness. In general, metal oxide layers with n-type conductivity have been investigated as cathodic protection layers for the HER.[91-94] It has been widely accepted that electrons separated by a buried junction migrate to the solid/liquid interface through the CB of n-type protection materials[95-98] as shown in Figure 2.10c. Inversely, metal oxide layers with p-type conductivity coupled with photoanodes can transport holes via the VB of the protection layer to the solid/liquid interface for the OER. In the case of very thin oxide insulators, such as SiO_2 and Al_2O_3, direct tunneling of charge carriers across the protection layers has also been reported.[99-101] Interestingly, Hu *et al.*[102] reported that a thick amorphous TiO_2 protection layer is applicable for the protection of photoanodes for the OER due to hole transport through the bulk and a surface barrier of a leaky TiO_2 owing to defects in the bulk of the protection layer, which is also known as a state-mediated transport as introduced by Campet *et al.*[103] In the case of a highly-doped n-type protection layer for photoanodes, electrons created by the OER are injected into the CB of the protection layer and transported inwards toward the underlying photoabsorber. The electrons in the protection layer's CB then recombine with holes at the interface between the photoanode and the protection layer. The holes to recombine with electrons from the CB of the protection layer are the photogenerated holes transported through the VB of the photoabsorber, as shown by Mei *et al.* using c-Si and TiO_2.[104]

2.4 Passivation techniques against corrosion

Stabilization of photoelectrodes and the long-standing strength of catalysts are thus significant and a necessity for the progress of scalable and industrial based solar fuel technologies. The most common technique to protect unstable photoelectrodes is passivating them with thin films that are more stable towards photocorrosion both thermodynamically and kinetically. Conventional methods have generally about applying chemically stable

coatings. Unfamiliar methods targeting at elongating the lifetime of photoelectrodes and electrocatalysts, referred to here as emerging, have been reported in the literature in the past few years. These techniques are based on protection mechanisms different from surface passivation (Figure 2.11) and provide an alternative to the conventional thin film approach. Emerging techniques provide, in principle, easier preparation and better scalability, and in some cases have already shown stabilities comparable with thin film technologies.

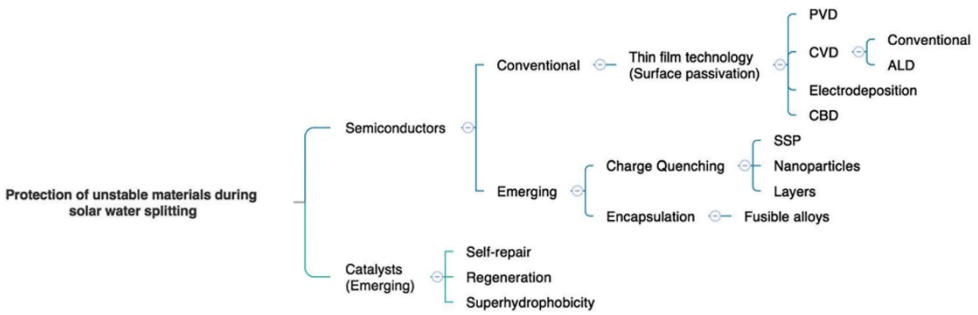

Figure 2.11 Conventional and emerging protection approaches used to protect photocorrodible materials for solar fuel application. Reproduced with permission[105] Copyright 2017, The Royal Society of Chemistry

2.4.1 Conventional protection mechanisms for photoelectrodes

Unstable semiconductors are being coated with nanometer scale thin films of materials including metals or metal silicides,[106-109] wide band gap semiconductors,[110] transparent conducting oxides,[111, 112] transition metals and their oxides,[113, 114] and organic polymers.[115] Most recent studies deal with the fabrication of these using ALD,[116] which allows for ultra-thin films with limited charge transfer resistance. Physical vapor deposition (PVD) also allows for conformal and thickness-controlled deposition of protecting materials. Other classical techniques such as electrodeposition, sol–gel, chemical bath, and spray deposition have a low cost of implementation but

often result in porous films.[117] The porosity diminishes the efficacy of anti-corrosion coatings since it can allow the electrolyte to reach the surface of the underlying layer. These methods have been studied extensively and have been the focus of several reviews.[118-121] Conventional methods have been summarized in Figure 2.11. We cover here briefly the various approaches in the conventional categories and their reported use and results.

It is worth noting that the reported stabilities of most of the examples gathered in Table 2.1 do not make reference to the lifetime of the materials. Indeed, stability tests are often performed for an arbitrary amount of time, after which the performance of the photoelectrodes is still significantly high. Therefore, their actual lifetime (or even half-life) is potentially higher than the values reported in Table 2.1. Figure 2.11, on the other hand, separates the approaches in terms of the governing principle of the protection mechanism.

Table 2.1 Summary of conventional and emerging protection mechanisms for unstable semiconductor photoelectrodes. Reproduced with permission[105] Copyright 2017, The Royal Society of Chemistry

Protection mechanism							
Type	Method	Technology	Advantages	Disadvantages	Coatings	Electrolyte (pH)	Reported stability after protection
Conventional	Thin film technology	PVD	• Precise overall composition control.	• Line-of-sight deposition[a] • May damage the substrate due to high-energy impacts. • Lack of chemical control at the interface.	TiO_2[53,55,90] $NiRuO_x$[62]	TiO_2: 1 M $HClO_4$[53] 1 M KOH[55] 1 M KOH[90] $NiRuO_x$: 0.25 M $NaSO_4$ (7.2)[62]	TiO_2: 75 h[53] 8 h[55] 60 h[90] 1.5 h[62,b]
		CVD	• Precise composition and thickness control. • Conformal coating.	• Limited to materials with suitable precursor volatility, stability and deposition chemistry.	TiO_2[45] TiO_2[91] C (diamond)[92]	0.5 M H_2SO_4[45] N/A N/A	N/A N/A N/A
		CVD (ALD)	• Conformal and uniform deposition on porous materials. • High degree of thickness control.	• Often lengthy procedures and with high operational costs.	TiO_2[49,51,53,90,93–97] SnO_2[98] Ga_2O_3[99]	TiO_2: 1 M H_2SO_4[96] 1 M NaOH[96] 0.5 M $C_8H_5KO_4$ (4)[97] 1 M Phosphate (7)[96] 1 M KOH[90] 1 M $HClO_4$[53] SnO_2:0.5 M $NaSO_4$ (5)[98] Ga_2O_3:0.5 M $NaSO_4$ (4)[99]	TiO_2: 8 h[96] 8 h[96] 12 h[97] 18 h[96] 60 h[90] 72 h[53] SnO_2: 57 h[98] Ga_2O_3: 20 min[99]
		Electrodeposition	• Coating of porous materials. • Thickness control. • Low. implementation cost.	• Limited by deposition conditions. • Requires conductive substrate/path. • Often leads to porous coatings.	CuO[100] MoS_{2+x}[51] C (sp^2, sp^3)[101,c]	0.05 M $NaSO_4$ (7)[100] 0.5 M $NaSO_4$ (4)[51] 0.5 M H_2SO_4[101]	20 min[100] 10 h[51] 24 h[101]
		CBD[d]	• Low implementation cost.	• Often leads to porous coatings.	FeOOH[102] ZnS[103] NiO_x[64]	0.5 M $NaSO_4$ (7) 0.25 M K_2SO_3, 0.35 M Na_2S (13.3)[103] 0.1 M $NaSO_4$ (6)	2 h[102] 5 h[103] 20 min[64]
Emerging	Nanoparticles	Pre-synthesized	• Leaching. • Non-optimal protection.	• Simple preparation.	$ZnFe_2O_4$[75] CuS[104] Ni[74]	0.5 M Na_2S[75] 1 M $NaSO_4$ (5)[104] 1 M $NaSO_4$ (5)[74]	1 h[75] 1 h[104] 30 min[74]
		SSP	• Low. implementation cost. • Simple procedure. • Multifunctional coatings. • Scalable.	• Lack of film quality control. • Lack of conformal coating.	$[(CoI)Ti_{11}O_{14}(O^iPr)_{17}]$[68] $[Ti_2(OEt)_8(NiCl)]_2$[65–67,699] $[Ti_4(OEt)_{15}(CoCl)]$[65]	0.1 M K_2SO_4 (9.2)[65] 1 M KCl (9.2)[67]	24 h[65] 4 h[67]
	Fusible alloys		• Recyclability. • Simple procedure. • Double light path.[e]	• Limited to back illumination.	Field's metal[37]	0.1 M borate (8.5)[37]	1 h[37]
	Self-healing and regenerating materials		• Prolonged lifetimes.	• Specific to certain materials.	CoO_x[20] $CuRhO_2$[79] Fe-FeO_x[78] CdS, CdSe[105]	0.1 M phosphate (7)[20] 1 M NaOH[79] 0.1 M KOH (13)[78] 1.25 M NaOH, 0.2 M Na_2S[105]	50 h[20] 8 h[79] 72 h[78] 10 h[105]
	Superhydrophobic materials		• Reaction-protection feedback.	• Catalyst contact with electrolyte diminished.	Fe[106] ZnO/Si[107] TiO_2/ZnO[85] SiC/Si[87]	Water[106,f] 0.4 M $NaSO_4$[107] N/A[85] 0.4 M $NaSO_4$[87]	168 h[106,f] 700 h[107] N/A[85] 2000 h[87]

Early results on the surface protection of photocorrodible semiconductors were based on relatively thick layers of TiO_2 prepared by sol–gel,[122] or chemical vapor deposition (CVD)[123] techniques. As a result, the protected semiconductor photoelectrodes had often poor PEC performance due to a substantial voltage drop across the resistive films.[58, 124] It is worth noting that a conformal overlayer protects a photoactive material and can form a buried junction,[125] which has the advantage that the absolute band edge position is decoupled from the thermodynamic water splitting potentials.[126]

The widely used TiO_2 ALD protection layers, while allowing for conformal and thickness control, are also challenging to scale up for commercialization of solar fuels technology. Furthermore, catalytically active layers must still be deposited on top of the protection layer. An illustrative example is Cu_2O as photocathode for H_2 evolution. Cu_2O is an attractive material for tandem water splitting systems since it is a p-type semiconductor with a direct band gap of 2 eV, which corresponds to a maximum theoretical photocurrent of 14.7 mA cm^{-2}.[127] Cu_2O displayed modest activities until the demonstration of protection by a conformal coating deposited by ALD (20 nm Ga_2O_3/ 100 nm TiO_2) with RuO_x as a catalyst, showing stable operation exceeding 100 h with high PEC photocurrent for oxide materials under light illumination (Figure 2.12 c).[28] To show the practical impact of this photocathode, Cu_2O was paired with $BiVO_4$ as the photoanode to construct an all-oxide unassisted solar water splitting tandem device, achieving ~3% solar-to-hydrogen conversion efficiency.

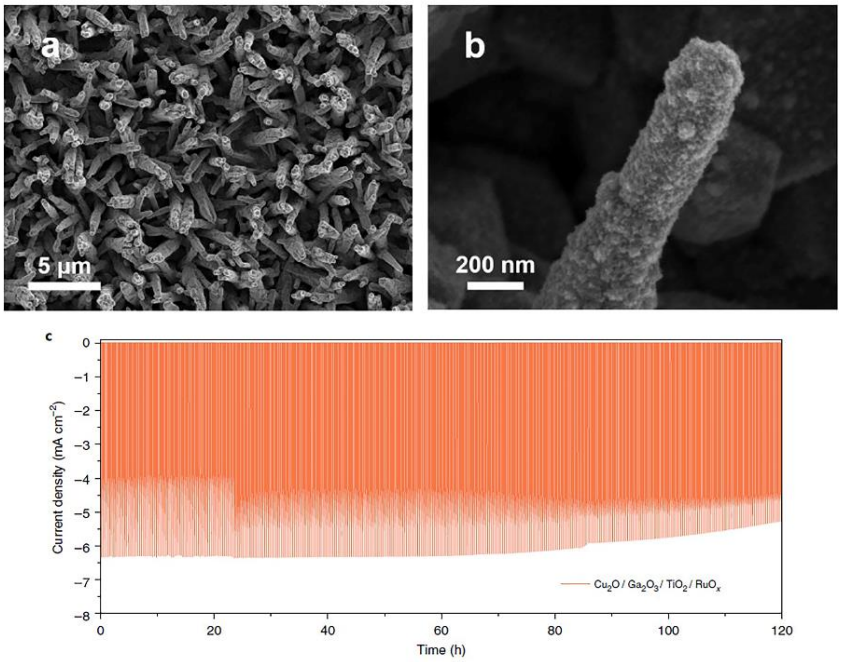

Figure 2.12 SEM images of Cu_2O nanowire photocathodes modified with Ga_2O_3/TiO_2/RuOx: (a) top view image and (b) high resolution image of a single wire. (c) Stability test at a fixed bias of 0.5 V versus RHE with chopped illumination and continuous stirring. Reprinted by permission from Nature[28] Copyright 2019.

In addition, some carbon-based materials, such as amorphous carbon, graphitic carbon nitride[128], and graphene oxide,[129, 130] have also been used to protect photoelectrodes.[131] Zhang *et al.* reported carbon-protected Cu_2O nanowire arrays that showed improved stability with a carbon layer compared with the bare nanowires.[132] The thin, uniform layer of carbon (20 nm) was deposited by the decomposition of a glucose solution on Cu_2O at 550 °C in an N_2 atmosphere. The thickness-controllable carbon film served as the electron transport and protective layer with favorable optical properties. The carbon-protected Cu_2O also showed photocurrent enhancement from -2.28 mA cm^{-2} to -3.95 mA cm^{-2} at 0 V, and the

photocurrent decay was inhibited from 87.4% to 19.3% over a 20 min stability test.

2.4.2 Emerging protection mechanisms for photoelectrodes

Several innovative and more scalable approaches have been recently explored to tackle the instability of narrow band-gap semiconductors and catalysts under water-splitting conditions. We have grouped here the approaches by the governing principle of the protecting mechanism, namely charge quenching (which includes single source precursor chemistry, nanoparticles and other layers) and encapsulation. The charge quenching process helps in effectively improving crystallinity, reducing strain and suppressing charge–carrier recombination, resulting in enhanced overall photocurrent density and stability during the PEC water splitting.[133] In addition, these techniques provide straightforward and inexpensive fabrication processes to stabilize and activate photoelectrodes for application to PEC water splitting systems.[134]

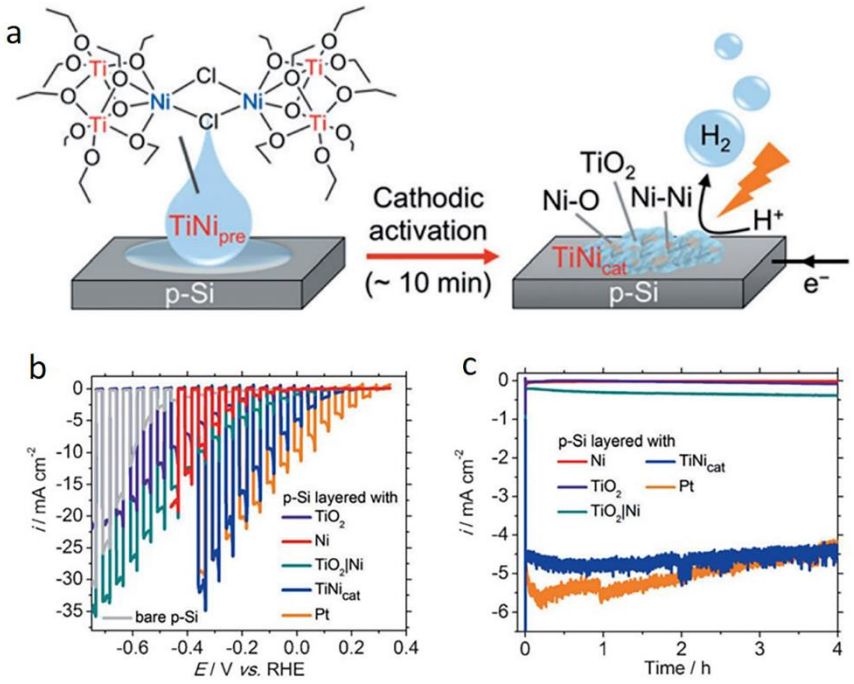

Figure 2.13 (a) Schematic representation of the preparation of a TiNi-modified p-Si electrode by a dual process: drop casting of a precursor form, $TiNi_{pre}$, followed by in situ cathodic activation to form $TiNi_{cat}$ for protection and catalytic activation of the p-Si photocathode (b) LSV scans measured in an aqueous pH 9.2 electrolyte solution (0.1 M borate and 1 M KCl) under chopped solar light irradiation (AM 1.5G) with a scan rate of 5 mV s^{-1} . (c) Chronoamperometry of photocathodes recorded at 0 V vs. RHE under solar light irradiation (AM 1.5G) for 4 h.[135] Reproduced with permission of John Wiley & Sons. Copyright 2015.

Solution-processed SSP (Single source precursor) chemistry is an attractive approach for preparing multifunctional materials on a large scale, as it bypasses the need for expensive equipment and processing. A SSP contains all of the required elements for a desired composite material, allowing for its synthesis in a simple, one-step procedure. The selection of a suitable SSP allows for the production of mono-, bi- and multifunctional coatings. In

recent years, highly versatile and scalable SSP approaches for preparing multifunctional films on photoelectrodes have been developed.[134, 136, 137] Hydrolytic decomposition of titanium or polyoxotitanate compounds resulted in amorphous TiO_2 films in a single-step.[138] Using SSPs such as those depicted in Figure 2.13, p-Si/$TiNi_{cat}$ was selected because a film is prepared by the simple drop casting of the molecular single-source precursor onto the p-Si surface at room temperature, followed by cathodic *in-situ* activation to form the catalytically active $TiNi_{cat}$ film. The p-Si/$TiNi_{cat}$ photocathode exhibited a photocurrent density of 5 mA cm^{-2} in an aqueous pH 9.2 solution at 0 V vs. RHE with a quantitative faradaic efficiency for 4 hours prolonged hydrogen generation with a stable photocurrent, which are among the best-known noble metal-free H_2 evolution catalysts (HEC) and O_2 evolution catalysts (OEC).[135] Although SSP chemistry is not yet able to generate fully conformal protection layers, its charge quenching capabilities have already shown increased stabilities and activities thus making it a viable alternative to conventional methods, with extremely facile preparation, multifunctional character, and good stabilities.

Deposition of nanoparticles directly on top of a photocorrodible semiconductor can significantly suppress the corrosion reaction by charge quenching as was demonstrated by spin-coating Ni nanoparticles onto the surface of a Cu_2O/CuO photocathode.[139] After 20 min of simulated solar illumination, the nickel-decorated Cu_2O/CuO heterojunction retained 1.5 times more of the initial photocurrent than bare Cu_2O/CuO.[140] Since the rate of both anodic and cathodic corrosion depends on the concentration of holes and electrons,[141] respectively, a decrease in the latter would slow photodegradation. An alternative charge quenching approach that does not share the disadvantage of the non-conformal nature of nanoparticles, used ferrihydrite as a hole-storage layer that was able to protect unstable Ta_3N_5, TaON and $BiVO_4$ photoanodes against photocorrosion.[142]

Lead-halide perovskites have achieved efficiencies of over 20% and are the fastest-developing technology in the history of photovoltaics.[143] However,

their infamous fragility in the presence of traces of water, even low amounts of moisture, makes them unsuitable for direct use as light harvesters in aqueous solution for the production of H_2 through water splitting.[144-146] However, perovskites can be protected by a simple metal encapsulating technique that is scalable and potentially also applicable to a wide range of photocorrodible materials. Fan *et al.*[147] reported perovskite films with large grain sizes up to 5 µm grown directly from liquid phase metal by using Pb–Sn eutectic alloying technique. This unique growth mechanism, a less-toxic and efficient perovskite solar cell with a power conversion efficiency (PCE) of 14.04% was demonstrated, while pure Sn and Pb perovskite solar cells prepared in this manner yielded PCEs of 4.62% and 14.21%, respectively (Figure 2.14). This alloying technique can open up a new direction to further explore different alloy systems.

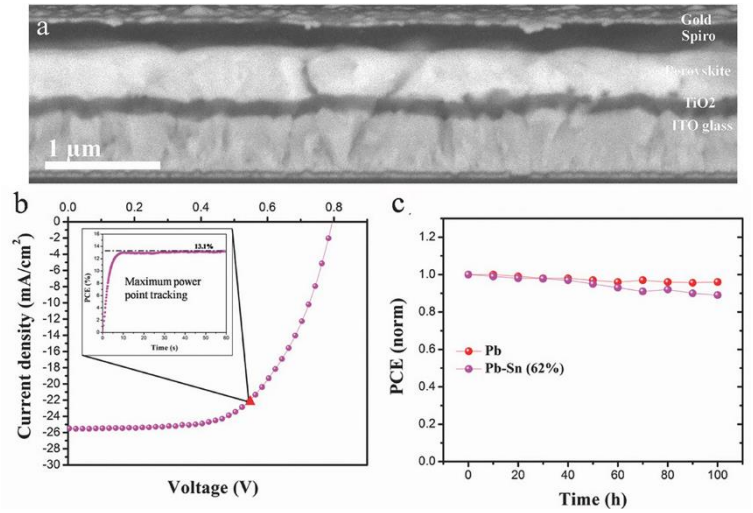

Figure 2.14 (a) Cross-sectional SEM image of perovskite solar cell fabricated from eutectic alloy. (b) *J–V* curve of champion cell based on eutectic alloy with a PCE of 14.04%. The inset shows the scan-rate-independent maximum power point tracking for 60 s, resulting in a stabilized PCE of 13.1%. (c) Stability test of solar cell devices based on pure Pb and eutectic alloy for 100 h at room temperature.[147] Reproduced with permission of John Wiley & Sons. Copyright 2019.

The main drawback of this approach is that the photoelectrodes cannot be illuminated from the front, and must therefore be able to be prepared on a transparent substrate.[107, 148] On the other hand, this is also an advantage, as light will be reflected at the metal coating back into the electrode, thus increasing the photons absorbed and charges generated.[149]

2.5 Conclusions and perspectives

Artificial photosynthesis allows storing solar energy as a chemical fuel and complements photovoltaic technology as it directly addresses the intermittence problem of electricity generation. Combinations of narrow band gap semiconductors with suitable catalysts could yield high STH efficiencies for this application, but such materials are often unstable under water splitting conditions.

We reviewed PEC stability and protection techniques for photoelectrodes of integrated photoelectrochemical (PEC) devices and developed a case study to illustrate their impact on evolutions in performance. Firstly, In this review we have presented the fundamental aspects of PEC water splitting and different device configurations with detailed working principles and scientific challenges of solar-driven water splitting. In essence, to achieve unassisted water splitting with higher STH efficiency, in PEC configurations, PV/PEC and PV–electrolyser tandem devices are a viable option toward achieving highly efficient unassisted solar water splitting in the near future. However, as these systems require more than two PV cells in tandem, they are unlikely to be economically viable unless the cost of materials substantially decreases.

Secondly, the semiconductor-liquid electrolyte junction is the most challenging interface for short-term stability, while catalyst and electrolyte degradation is more relevant and challenging for reliability and long term durability. Additionally, technological development occurs in the

demonstration of many scientific studies to understand the fundamentals of charge carrier transport, and to make more efficient PEC systems. In this review we introduced representative charge carrier transport mechanisms: electron transport via the conduction band (for photocathodes) and hole transport – via valence band (for photoanodes), tunneling via very thin insulating oxide, via defect states (for photoanodes), and via hole–electron recombination at the photoanode/metal-oxide interface. In particular, exposing the photoabsorber directly to the electrolyte, or protecting it (using protecting films or separation through wires), significantly affects the degradation of photoabsorber components. Similarly, exposing electrocatalysts directly to irradiation or hiding them in the dark significantly affects degradation of the catalysts. For PEC device designs utilizing wires and separating charge generation (i.e. photoabsorbers) and electrochemical reaction (i.e. catalysts), the risk of self-oxidization of the semiconductor instead of the reactant (i.e. water) is eliminated, and long-term durability is more plausible.

Conventionally, the issue of photoelectrode instability has been tackled with thin film technology. The vast majority of literature on this subject deals with thin films of wide band gap semiconductor materials (such as Ga_2O_3, TiO_2 and AZO) deposited through operationally costly techniques, such as ALD or sputtering. While these techniques allow the formation of conformal and thin protection layers, the preparation is technically demanding and challenging to be scalable for global demand. However, even in the cases where photoelectrode instability was successfully hindered with ALD coatings, the problem of catalyst degradation in such systems often persists.

Finally, we introduced emerging methods for protecting and activating unstable light-harvesting materials. Firstly, charge quenching techniques were summarized. Single source precursor chemistry was shown as a special case to generate multifunctional layers able to both protect and drive the HER and OER in one simple preparation procedure. Secondly, we showed the use of fusible alloys to protect highly unstable materials, such as lead

halide PVKs. This approach, where a protecting and electrically conducting layer of a fusible alloy was placed on top of a highly unstable perovskite layer showing a record stability for this material in aqueous solution, is potentially applicable to other photocorrodible materials. Despite the promise of these approaches, there are still many challenges in designing stable and active photoelectrodes for water splitting. Ultimately, the method of choice should be simple, cost-effective and scalable.

The biggest challenge for photoabsorber materials is still materials discovery. We are in need of new materials with suitable bandgaps and band edges. New materials characterization tools and techniques offer insights that are critically important to future developments of this field.[150-152] The ultimate target of the entire solar fuel research field is to design and produce a cost-effective, highly efficient and stable photoanode and/or photocathode for oxygen and/or hydrogen production, either by employing a particulate system or a PEC device. The past decade has witnessed many innovations in combinations of materials, nanoarchitecture design and co-catalyst optimization which address the main issues existing in the reported efficient photoelectrodes.

2.6 References

1. K. Engeland, M. Borga, J.-D. Creutin, B. François, M.-H. Ramos and J.-P. Vidal, *Renew. Sust. Energ. Rev.*, 2017, **79**, 600-617.
2. P. Denholm and R. M. Margolis, *Energy Policy*, 2007, **35**, 2852-2861.
3. N. S. Lewis, *Science*, 2007, **315**, 798.
4. G. Liu, J. Xu and K. Wang, *Mater. Today Energy.*, 2018, **10**, 368-379.
5. J. Marshall, *Nature*, 2014, **510**, 22-24.
6. D. G. Nocera, *Acc. Chem. Res.*, 2012, **45**, 767-776.
7. K. S. Joya, Y. F. Joya, K. Ocakoglu and R. van de Krol, *Angew. Chem.*, 2013, **52**, 10426-10437.

8. A. T. Garcia-Esparza and K. Takanabe, *J. Mater. Chem. A*, 2016, **4**, 2894-2908.
9. D. Bae, T. Pedersen, B. Seger, M. Malizia, A. Kuznetsov, O. Hansen, I. Chorkendorff and P. C. K. Vesborg, *Energy Environ. Sci.*, 2015, **8**, 650-660.
10. A. Kudo and Y. Miseki, *Chem. Soc. Rev.*, 2009, **38**, 253-278.
11. J. Schneider, M. Matsuoka, M. Takeuchi, J. Zhang, Y. Horiuchi, M. Anpo and D. W. Bahnemann, *Chem. Rev.*, 2014, **114**, 9919-9986.
12. M. G. Walter, E. L. Warren, J. R. McKone, S. W. Boettcher, Q. Mi, E. A. Santori and N. S. Lewis, *Chem. Rev.*, 2010, **110**, 6446-6473.
13. E. Fabbri and T. J. Schmidt, *ACS Catal.*, 2018, **8**, 9765-9774.
14. C. C. L. McCrory, S. Jung, I. M. Ferrer, S. M. Chatman, J. C. Peters and T. F. Jaramillo, *J. Am. Chem. Soc.*, 2015, **137**, 4347-4357.
15. S. Y. Reece, J. A. Hamel, K. Sung, T. D. Jarvi, A. J. Esswein, J. J. H. Pijpers and D. G. Nocera, *Science*, 2011, **334**, 645.
16. B. Seger, I. E. Castelli, P. C. K. Vesborg, K. W. Jacobsen, O. Hansen and I. Chorkendorff, *Energy Environ. Sci.*, 2014, **7**, 2397-2413.
17. J. Jin, K. Walczak, M. R. Singh, C. Karp, N. S. Lewis and C. Xiang, *Energy Environ. Sci.*, 2014, **7**, 3371-3380.
18. J. M. Spurgeon, M. G. Walter, J. Zhou, P. A. Kohl and N. S. Lewis, *Energy Environ. Sci.*, 2011, **4**, 1772-1780.
19. M. Grätzel, *Nature*, 2001, **414**, 338.
20. W. S. Yang, J. H. Noh, N. J. Jeon, Y. C. Kim, S. Ryu, J. Seo and S. I. Seok, *Science*, 2015, **348**, 1234.
21. S. Kment, F. Riboni, S. Pausova, L. Wang, L. Wang, H. Han, Z. Hubicka, J. Krysa, P. Schmuki and R. Zboril, *Chem. Soc. Rev.*, 2017, **46**, 3716-3769.
22. A. Jelinska, K. Bienkowski, M. Jadwiszczak, M. Pisarek, M. Strawski, D. Kurzydlowski, R. Solarska and J. Augustynski, *ACS Catal.*, 2018, **8**, 10573-10580.
23. T. Vincent, M. Gross, H. Dotan and A. Rothschild, *Int. J. Hydrog. Energy*, 2012, **37**, 8102-8109.

24. J. Kegel, I. M. Povey and M. E. Pemble, *Nano Energy.*, 2018, **54**, 409-428.
25. B. Modak and S. K. Ghosh, *J. Phys. Chem. C*, 2015, **119**, 23503-23514.
26. W. Vijselaar, R. M. Tiggelaar, H. Gardeniers and J. Huskens, *ACS Energy Lett.*, 2018, **3**, 1086-1092.
27. L. Gao, Y. Cui, R. H. J. Vervuurt, D. van Dam, R. P. J. van Veldhoven, J. P. Hofmann, A. A. Bol, J. E. M. Haverkort, P. H. L. Notten, E. P. A. M. Bakkers and E. J. M. Hensen, *Adv.Funct. Mater.*, 2016, **26**, 679-686.
28. L. Pan, J. H. Kim, M. T. Mayer, M.-K. Son, A. Ummadisingu, J. S. Lee, A. Hagfeldt, J. Luo and M. Grätzel, *Nat. Catal.*, 2018, **1**, 412-420.
29. W. S. dos Santos, M. Rodriguez, J. M. O. Khoury, L. A. Nascimento, R. J. P. Ribeiro, J. P. Mesquita, A. C. Silva, F. G. E. Nogueira and M. C. Pereira, *ChemSusChem*, 2018, **11**, 589-597.
30. H. Ullah, A. A. Tahir, S. Bibi, T. K. Mallick and S. Z. Karazhanov, *Appl Catal B.*, 2018, **229**, 24-31.
31. S. Chu, W. Li, Y. Yan, T. Hamann, I. Shih, D. Wang and Z. Mi, *Nano Futures*, 2017, **1**, 022001.
32. J. L. Young, M. A. Steiner, H. Döscher, R. M. France, J. A. Turner and Todd G. Deutsch, *Nat. Energy*, 2017, **2**, 17028.
33. W.-H. Cheng, M. H. Richter, M. M. May, J. Ohlmann, D. Lackner, F. Dimroth, T. Hannappel, H. A. Atwater and H.-J. Lewerenz, *ACS Energy Lett.*, 2018, **3**, 1795-1800.
34. F. F. Abdi, L. Han, A. H. M. Smets, M. Zeman, B. Dam and R. van de Krol, *Nat. Commun.*, 2013, **4**, 2195.
35. T. W. Kim, Y. Ping, G. A. Galli and K.-S. Choi, *Nat. Commun.*, 2015, **6**, 8769.
36. K. T. Fountaine, H. J. Lewerenz and H. A. Atwater, *Nat. Commun.*, 2016, **7**, 13706.
37. H.-P. Wang, K. Sun, S. Y. Noh, A. Kargar, M.-L. Tsai, M.-Y. Huang, D. Wang and J.-H. He, *Nano Lett.*, 2015, **15**, 2817-2824.
38. X. Yu, P. Yang, S. Chen, M. Zhang and G. Shi, *Adv. Energy Mater.*, 2017, **7**, 1601805.

39. S. Wang, P. Chen, Y. Bai, J.-H. Yun, G. Liu and L. Wang, *Adv. Mater.*, 2018, **30**, 1800486.
40. C. Ding, W. Qin, N. Wang, G. Liu, Z. Wang, P. Yan, J. Shi and C. Li, *Phys. Chem. Chem. Phys.*, 2014, **16**, 15608-15614.
41. J. H. Kim, Y. Jo, J. H. Kim, J. W. Jang, H. J. Kang, Y. H. Lee, D. S. Kim, Y. Jun and J. S. Lee, *ACS Nano*, 2015, **9**, 11820-11829.
42. B. J. Trześniewski and W. A. Smith, *J. Mater. Chem. A*, 2016, **4**, 2919-2926.
43. J. Zhao, T. M. Gill and X. Zheng, *Nano Res.*, 2018, **11**, 3499-3508.
44. B. J. Trześniewski, I. A. Digdaya, T. Nagaki, S. Ravishankar, I. Herraiz-Cardona, D. A. Vermaas, A. Longo, S. Gimenez and W. A. Smith, *Energy Environ. Sci.*, 2017, **10**, 1517-1529.
45. C. X. Kronawitter, L. Vayssieres, S. Shen, L. Guo, D. A. Wheeler, J. Z. Zhang, B. R. Antoun and S. S. Mao, *Energy Environ. Sci.*, 2011, **4**, 3889-3899.
46. A. Kudo, *MRS Bull.*, 2011, **36**, 32-38.
47. B. D. Alexander, P. J. Kulesza, I. Rutkowska, R. Solarska and J. Augustynski, *J. Mater. Chem.*, 2008, **18**, 2298-2303.
48. A. Vilanova, T. Lopes, C. Spenke, M. Wullenkord and A. Mendes, *Energy Storage Materials*, 2018, **13**, 175-188.
49. S. Hu, C. Xiang, S. Haussener, A. D. Berger and N. S. Lewis, *Energy Environ. Sci.*, 2013, **6**, 2984-2993.
50. S. Haussener, C. Xiang, J. M. Spurgeon, S. Ardo, N. S. Lewis and A. Z. Weber, *Energy Environ. Sci.*, 2012, **5**, 9922-9935.
51. Q. Zeng, J. Bai, J. Li, B. Zhou and Y. Sun, *Nano Energy.*, 2017, **41**, 225-232.
52. J. Luo, Z. Li, S. Nishiwaki, M. Schreier, M. T. Mayer, P. Cendula, Y. H. Lee, K. Fu, A. Cao, M. K. Nazeeruddin, Y. E. Romanyuk, S. Buecheler, S. D. Tilley, L. H. Wong, A. N. Tiwari and M. Grätzel, *Adv. Energy Mater.*, 2015, **5**, 1501520.
53. Gurudayal, D. Sabba, M. H. Kumar, L. H. Wong, J. Barber, M. Grätzel and N. Mathews, *Nano Lett.*, 2015, **15**, 3833-3839.

54. Y.-S. Chen, J. S. Manser and P. V. Kamat, *J. Am. Chem. Soc.*, 2015, **137**, 974-981.
55. Z. Li, W. Luo, M. Zhang, J. Feng and Z. Zou, *Energy Environ. Sci.*, 2013, **6**, 347-370.
56. Y. Yamada, N. Matsuki, T. Ohmori, H. Mametsuka, M. Kondo, A. Matsuda and E. Suzuki, *Int. J. Hydrog. Energy*, 2003, **28**, 1167-1169.
57. N. A. Kelly, T. L. Gibson and D. B. Ouwerkerk, *Int. J. Hydrog. Energy*, 2008, **33**, 2747-2764.
58. M. M. May, H.-J. Lewerenz, D. Lackner, F. Dimroth and T. Hannappel, *Nat. Commun.*, 2015, **6**, 8286.
59. S. Rau, S. Vierrath, J. Ohlmann, A. Fallisch, D. Lackner, F. Dimroth and T. Smolinka, *Energy Technol.*, 2014, **2**, 43-53.
60. J. Jia, L. C. Seitz, J. D. Benck, Y. Huo, Y. Chen, J. W. D. Ng, T. Bilir, J. S. Harris and T. F. Jaramillo, *Nat. Commun.*, 2016, **7**, 13237.
61. R. F. Pierret, *Advanced Semiconductor Fundamentals*, Pearson Education, Inc, 2 edn., 2003.
62. K. K. N. S. M. Sze *Physics of Semiconductor Devices* A John Wiley & sons, inc, 3 edn., 2007.
63. D. Bae, B. Seger, P. C. K. Vesborg, O. Hansen and I. Chorkendorff, *Chem. Soc. Rev.*, 2017, **46**, 1933-1954.
64. Y. He, T. Hamann and D. Wang, *Chem. Soc. Rev.*, 2019, DOI: 10.1039/C8CS00868J.
65. C. Jiang, S. J. A. Moniz, A. Wang, T. Zhang and J. Tang, *Chem. Soc. Rev.*, 2017, **46**, 4645-4660.
66. M. F. Lichterman, S. Hu, M. H. Richter, E. J. Crumlin, S. Axnanda, M. Favaro, W. Drisdell, Z. Hussain, T. Mayer, B. S. Brunschwig, N. S. Lewis, Z. Liu and H.-J. Lewerenz, *Energy Environ. Sci.*, 2015, **8**, 2409-2416.
67. D. G. Boucher, J. R. Speller, R. Han, F. E. Osterloh and M. J. Rose, *ACS Appl. Energy Mater.*, 2019, **2**, 66-79.
68. D. Zhang, J. Shi, W. Zi, P. Wang and S. Liu, *ChemSusChem*, 2017, **10**, 4324-4341.

69. Z. Zhang and J. T. Yates, *Chem. Rev.*, 2012, **112**, 5520-5551.
70. M. X. Tan, C. N. Kenyon, O. Krüger and N. S. Lewis, *J. Phys. Chem. B*, 1997, **101**, 2830-2839.
71. O. Krüger, C. N. Kenyon, M. X. Tan and N. S. Lewis, *J. Phys. Chem. B*, 1997, **101**, 2840-2849.
72. C. N. Kenyon, M. X. Tan, O. Krüger and N. S. Lewis, *J. Phys. Chem. B*, 1997, **101**, 2850-2860.
73. W. Shockley, *Van Nostrand: New York*, 1950, **7**.
74. Y. G. a. N. B. G. A. Many, *Semiconductor Surfaces*, North-Holland : New York, 1965.
75. S. Chen and L.-W. Wang, *Chem. Mater.*, 2012, **24**, 3659-3666.
76. S.-M. Park and M. E. Barber, *J. Electroanal. Chem.*, 1979, **99**, 67-75.
77. M. Pourbaix, *Atlas of electrochemical equilibria in aqueous solutions*, National Association of Corrosion Engineers: Houston, TX, 2 edn., 1974.
78. X. Li, Z. Li and J. Yang, *Phys. Rev. Lett.*, 2014, **112**, 018301.
79. K. Walczak, Y. Chen, C. Karp, J. W. Beeman, M. Shaner, J. Spurgeon, I. D. Sharp, X. Amashukeli, W. West, J. Jin, N. S. Lewis and C. Xiang, *ChemSusChem*, 2015, **8**, 544-551.
80. O. Savadogo, *Sol. Energy Mater. Sol. Cells*, 1998, **52**, 361-388.
81. N. Takeno, *Atlas of Eh-pH diagrams Intercomparison of thermodynamic databases*, National Institute of Advanced Industrial Science and Technology, Tokyo, 2005.
82. D. Bae, S. Shayestehaminzadeh, E. B. Thorsteinsson, T. Pedersen, O. Hansen, B. Seger, P. C. K. Vesborg, S. Ólafsson and I. Chorkendorff, *Sol. Energy Mater. Sol. Cells*, 2016, **144**, 758-765.
83. A. Standing, S. Assali, L. Gao, M. A. Verheijen, D. van Dam, Y. Cui, P. H. L. Notten, J. E. M. Haverkort and E. P. A. M. Bakkers, *Nat. Commun.*, 2015, **6**, 7824.
84. A. Q. Contractor and J. O. M. Bockris, *Electrochim. Acta*, 1984, **29**, 1427-1434.
85. G. Li and S. Wang, *J. Electroanal. Chem.*, 1987, **227**, 213-221.

86. B. Seger, A. B. Laursen, P. C. K. Vesborg, T. Pedersen, O. Hansen, S. Dahl and I. Chorkendorff, *Angew. Chem.*, 2012, **51**, 9128-9131.
87. Y. S. Lee, D. Chua, R. E. Brandt, S. C. Siah, J. V. Li, J. P. Mailoa, S. W. Lee, R. G. Gordon and T. Buonassisi, *Adv. Mater.*, 2014, **26**, 4704-4710.
88. A. Heller, *Acc. Chem. Res.*, 1981, **14**, 154-162.
89. R. Cohen, L. Kronik, A. Shanzer, D. Cahen, A. Liu, Y. Rosenwaks, J. K. Lorenz and A. B. Ellis, *J. Am. Chem. Soc.*, 1999, **121**, 10545-10553.
90. N. Guijarro, M. S. Prévot and K. Sivula, *Phys. Chem. Chem. Phys.*, 2015, **17**, 15655-15674.
91. C. G. Morales-Guio, S. D. Tilley, H. Vrubel, M. Grätzel and X. Hu, *Nat. Commun.*, 2014, **5**, 3059.
92. A. Paracchino, V. Laporte, K. Sivula, M. Grätzel and E. Thimsen, *Nat. Mater.*, 2011, **10**, 456.
93. B. Seger, T. Pedersen, A. B. Laursen, P. C. K. Vesborg, O. Hansen and I. Chorkendorff, *J. Am. Chem. Soc.*, 2013, **135**, 1057-1064.
94. M. R. Shaner, S. Hu, K. Sun and N. S. Lewis, *Energy Environ. Sci.*, 2015, **8**, 203-207.
95. Y. Bu and J.-P. Ao, *Green Energy Environ.*, 2017, **2**, 331-362.
96. S. D. Tilley, M. Schreier, J. Azevedo, M. Stefik and M. Graetzel, *Adv.Funct. Mater.*, 2014, **24**, 303-311.
97. A. J. Nozik and R. Memming, *J. Phys. Chem.*, 1996, **100**, 13061-13078.
98. K. Wedege, D. Bae, E. Dražević, A. Mendes, P. C. K. Vesborg and A. Bentien, *RSC Adv.*, 2018, **8**, 6331-6340.
99. I. A. Digdaya, B. J. Trześniewski, G. W. P. Adhyaksa, E. C. Garnett and W. A. Smith, *J. Phys. Chem. C*, 2018, **122**, 5462-5471.
100. E. Lee, J. Lee, J.-H. Kim, K.-H. Lim, J. Seok Byun, J. Ko, Y. Dong Kim, Y. Park and Y. S. Kim, *Nat. Commun.*, 2015, **6**, 6785.
101. A. G. Scheuermann, K. W. Kemp, K. Tang, D. Q. Lu, P. F. Satterthwaite, T. Ito, C. E. D. Chidsey and P. C. McIntyre, *Energy Environ. Sci.*, 2016, **9**, 504-516.

102. S. Hu, M. R. Shaner, J. A. Beardslee, M. Lichterman, B. S. Brunschwig and N. S. Lewis, *Science*, 2014, **344**, 1005.
103. G. Campet, C. Puprichitkun and Z. W. Sun, *J. Electroanal. Chem.*, 1989, **269**, 435-445.
104. B. Mei, T. Pedersen, P. Malacrida, D. Bae, R. Frydendal, O. Hansen, P. C. K. Vesborg, B. Seger and I. Chorkendorff, *J. Phys. Chem. C*, 2015, **119**, 15019-15027.
105. M. Crespo-Quesada and E. Reisner, *Energy Environ. Sci.*, 2017, **10**, 1116-1127.
106. F. A. L. Laskowski, M. R. Nellist, R. Venkatkarthick and S. W. Boettcher, *Energy Environ. Sci.*, 2017, **10**, 570-579.
107. M. Crespo-Quesada, L. M. Pazos-Outón, J. Warnan, M. F. Kuehnel, R. H. Friend and E. Reisner, *Nat. Commun.*, 2016, **7**, 12555.
108. P. Da, M. Cha, L. Sun, Y. Wu, Z.-S. Wang and G. Zheng, *Nano Lett.*, 2015, **15**, 3452-3457.
109. L.-F. Gao, W.-J. Luo, Y.-F. Yao and Z.-G. Zou, *ChemComm*, 2018, **54**, 11459-11462.
110. M. F. Lichterman, K. Sun, S. Hu, X. Zhou, M. T. McDowell, M. R. Shaner, M. H. Richter, E. J. Crumlin, A. I. Carim, F. H. Saadi, B. S. Brunschwig and N. S. Lewis, *Catal. Today*, 2016, **262**, 11-23.
111. K. Sun, S. Shen, J. S. Cheung, X. Pang, N. Park, J. Zhou, Y. Hu, Z. Sun, S. Y. Noh, C. T. Riley, P. K. L. Yu, S. Jin and D. Wang, *Phys. Chem. Chem. Phys.*, 2014, **16**, 4612-4625.
112. R. Liu, Z. Zheng, J. Spurgeon and X. Yang, *Energy Environ. Sci.*, 2014, **7**, 2504-2517.
113. T. Singh, T. Lehnen, T. Leuning and S. Mathur, *J. Vac. Sci. Technol.*, 2015, **33**, 010801.
114. F. Rodríguez-Hernández, D. C. Tranca, A. Martínez-Mesa, L. Uranga-Piña and G. Seifert, *J. Phys. Chem. C*, 2016, **120**, 25851-25860.
115. S. Mubeen, J. Lee, N. Singh, M. Moskovits and E. W. McFarland, *Energy Environ. Sci.*, 2013, **6**, 1633-1639.

116. A. G. Scheuermann and P. C. McIntyre, *J. Phys. Chem. Lett.*, 2016, **7**, 2867-2878.
117. S. Hu, N. S. Lewis, J. W. Ager, J. Yang, J. R. McKone and N. C. Strandwitz, *J. Phys. Chem. C*, 2015, **119**, 24201-24228.
118. B. Mei, B. Seger, T. Pedersen, M. Malizia, O. Hansen, I. Chorkendorff and P. C. K. Vesborg, *J. Phys. Chem. Lett.*, 2014, **5**, 1948-1952.
119. K. Benyahia, A. Benhaya and M. S. Aida, *J. Semicond.*, 2015, **36**, 103001.
120. N. Memarian, S. M. Rozati, I. Concina and A. Vomiero, *Materials*, 2017, **10**, 773.
121. R. Tang-Kong, R. Winter, R. Brock, J. Tracy, M. Eizenberg, R. H. Dauskardt and P. C. McIntyre, *ACS Appl. Mater. Interfaces*, 2018, **10**, 37103-37109.
122. X. Wang, F. Shi, X. Gao, C. Fan, W. Huang and X. Feng, *Thin Solid Films*, 2013, **548**, 34-39.
123. T. Maruyama and S. Arai, *Sol. Energy Mater. Sol. Cells*, 1992, **26**, 323-329.
124. P. Perez-Rodriguez, W. Vijselaar, J. Huskens, M. Stam, M. Falkenberg, M. Zeman, W. Smith and A. H. M. Smets, *Prog. Photovoltaics*, 2018, **27**, 245-254.
125. A. C. Nielander, M. R. Shaner, K. M. Papadantonakis, S. A. Francis and N. S. Lewis, *Energy Environ. Sci.*, 2015, **8**, 16-25.
126. R. Wick and S. D. Tilley, *J. Phys. Chem. C*, 2015, **119**, 26243-26257.
127. J. Luo, L. Steier, M.-K. Son, M. Schreier, M. T. Mayer and M. Grätzel, *Nano Lett.*, 2016, **16**, 1848-1857.
128. X. Ma, J. Zhang, B. Wang, Q. Li and S. Chu, *Appl Surf Sci.*, 2018, **427**, 907-916.
129. C. Yu and X. Zhang, *ChemElectroChem*, 2019, **6**, 2004-2012.
130. J. Young Kim, J.-W. Jang, D. Hyun Youn, J. Yul Kim, E. Sun Kim and J. Sung Lee, *RSC Adv.*, 2012, **2**, 9415-9422.

131. T.-F. Hou, A. Shanmugasundaram, M. A. Hassan, M. A. Johar, S.-W. Ryu and D.-W. Lee, *Int. J. Hydrog. Energy*, 2018, DOI: https://doi.org/10.1016/j.ijhydene.2018.05.105.
132. Z. Zhang, R. Dua, L. Zhang, H. Zhu, H. Zhang and P. Wang, *ACS Nano*, 2013, **7**, 1709-1717.
133. J. W. Park, M. A. Mahadik, G. W. An, S. Y. Lee, G. Piao, S. H. Choi, W.-S. Chae, H.-S. Chung, H. Park and J. S. Jang, *Sol. Energy Mater. Sol. Cells*, 2018, **187**, 207-218.
134. Y.-H. Lai, D. W. Palm and E. Reisner, *Adv. Energy Mater.*, 2015, **5**, 1501668.
135. H. S. P. Yi-Hsuan Lai, Jenny Z. Zhang, Peter D. Matthews, Dominic S. Wright, and Erwin Reisner, *Chem. Eur. J*, 2015, **21**, 3919 – 3923.
136. Y.-H. Lai, T. C. King, D. S. Wright and E. Reisner, *Chem. Eur. J*, 2013, **19**, 12943-12947.
137. Y.-H. Lai, C.-Y. Lin, Y. Lv, T. C. King, A. Steiner, N. M. Muresan, L. Gan, D. S. Wright and E. Reisner, *ChemComm*, 2013, **49**, 4331-4333.
138. N. Li, P. D. Matthews, H.-K. Luo and D. S. Wright, *ChemComm*, 2016, **52**, 11180-11190.
139. A. A. Dubale, C.-J. Pan, A. G. Tamirat, H.-M. Chen, W.-N. Su, C.-H. Chen, J. Rick, D. W. Ayele, B. A. Aragaw, J.-F. Lee, Y.-W. Yang and B.-J. Hwang, *J. Mater. Chem. A*, 2015, **3**, 12482-12499.
140. S. Cao, X. Yan, Z. Kang, Q. Liang, X. Liao and Y. Zhang, *Nano Energy.*, 2016, **24**, 25-31.
141. H. Gerischer and W. Mindt, *Electrochim. Acta*, 1968, **13**, 1329-1341.
142. G. Liu, J. Shi, F. Zhang, Z. Chen, J. Han, C. Ding, S. Chen, Z. Wang, H. Han and C. Li, *Angew. Chem.*, 2014, **53**, 7295-7299.
143. B.-w. Park, N. Kedem, M. Kulbak, D. Y. Lee, W. S. Yang, N. J. Jeon, J. Seo, G. Kim, K. J. Kim, T. J. Shin, G. Hodes, D. Cahen and S. I. Seok, *Nat. Commun.*, 2018, **9**, 3301.
144. B. Philippe, B.-W. Park, R. Lindblad, J. Oscarsson, S. Ahmadi, E. M. J. Johansson and H. Rensmo, *Chem. Mater.*, 2015, **27**, 1720-1731.

145. S. N. Habisreutinger, T. Leijtens, G. E. Eperon, S. D. Stranks, R. J. Nicholas and H. J. Snaith, *Nano Lett.*, 2014, **14**, 5561-5568.
146. T. Jiang and W. Fu, *RSC Adv.*, 2018, **8**, 5897-5901.
147. M. M. Tavakoli, S. M. Zakeeruddin, M. Grätzel and Z. Fan, *Adv. Mater.*, 2018, **30**, 1705998.
148. Y. Wu, P. Wang, X. Zhu, Q. Zhang, Z. Wang, Y. Liu, G. Zou, Y. Dai, M.-H. Whangbo and B. Huang, *Adv. Mater.*, 2018, **30**, 1704342.
149. S. Nam, C. T. K. Mai and I. Oh, *ACS Appl. Mater. Interfaces*, 2018, **10**, 14659-14664.
150. T. Okino, Y. Furukawa, Y. Nabekawa, S. Miyabe, A. Amani Eilanlou, E. J. Takahashi, K. Yamanouchi and K. Midorikawa, *Sci. Adv.*, 2015, **1**, e1500356.
151. J. Miao, P. Ercius and S. J. L. Billinge, *Science*, 2016, **353**, aaf2157.
152. A. Johannes, D. Salomon, G. Martinez-Criado, M. Glaser, A. Lugstein and C. Ronning, *Sci. Adv.*, 2017, **3**, eaao4044.

Chapter 3

Efficient solar water splitting photocathodes comprising a copper oxide heterostructure protected by a thin carbon layer

Photoelectrochemical (PEC) solar water splitting has received extensive attention because it promises to provide an alternative and sustainable source of energy. A key challenge is to achieve a stable PEC system in either acidic or basic electrolyte without degradation of the (photo)electrodes. We have used a cubic Cu_2O film and porous granular bilayer Cu_2O/CuO composite with a carbon protection layer as photocathode materials. The films were deposited under different conditions, such as variation of the electrodeposition time, thermal oxidation of the Cu_2O films in air vs. nitrogen atmosphere and deposition of the carbon materials, and were investigated structurally and regarding their PEC performance. The optimized electrodes showed photocurrents up to 6.5 mA/cm^{-2} and 7.5 mA/cm^{-2} at potentials of 0 V and -0.1 V vs RHE at pH 5.5, respectively. The stabilities of the Cu_2O/C and Cu_2O/CuO/C photocathodes, at a low bias of 0.3 V vs RHE, were retained after 50 h. The strongly improved photostability of the photocathodes in comparison to electrodes in the absence of a carbon overlayer, is attributed to a more effective charge transfer and a protective role of carbon against photocorrosion.

3.1 Introduction

The process of utilizing solar energy to produce hydrogen from water has gained increased attention to find ecologically benign alternative energy sources.[1] Hydrogen is considered a next-generation fuel,[2-6] however presently it is produced primarily from burning fossil fuels.[7, 8] To make the process sustainable, hydrogen will need to be produced using renewable energy sources such as sunlight.[9-11]

In developing economical, large-scale solar-to-hydrogen technologies, photoelectrochemical (PEC) cells that use earth-abundant materials have received increased attention.[12, 13] However, long-term stability of these materials under PEC process conditions is an important issue.[14-19] Among the photocathode materials used in PEC water splitting devices, cuprous and cupric oxides (Cu_2O and CuO) fulfill many requirements. These involve proper band gaps, low cost and ease of fabrication. Cu_2O has a direct band gap of 2.0 eV which could theoretically deliver a photocurrent of 14.7 mA/cm^2 and a power conversion efficiency of 20% as a solar cell.[20-24] Minami *et al.*[25] and Wong *et al.*[26] have achieved efficiencies of 8% and 6% using devices with $Zn_{1-x}Ge_x$-O and $Al_xGa_{1-x}O$ multi-component oxide thin films with Cu_2O-based heterojunction solar cells, respectively. These multi-component oxides act as n-type oxide thin-film window layers, having smaller conduction band offsets (ΔE_c because of a difference in electron affinity between the p-Cu_2O and the n-semiconductor. This smaller ΔE_c leads to a higher device efficiency.

Cu_2O and CuO have favorable and direct band gaps of approximately 2.0 – 2.6 eV and 1.3 – 1.6 eV, respectively, depending on the synthetic methods and morphology of the nanomaterials.[23, 27-33] Although copper oxides absorb a vast portion of the solar spectrum, some key challenges prohibit the formation of highly efficient and robust photocathodes.[34, 35] One of the main issues in using copper oxides as a photocathode is a relatively strong electron–hole pair recombination, leading to a short minority carrier diffusion length. The minority charge carrier diffusion length is limited to

about 20-200 nm depending on the synthesis process, while the film must typically be at least 1 µm thick to absorb most of the sunlight. It is therefore clear that efficient separation of the photoexcited electron-hole pairs is crucial. Thus, layer-by-layer fabrication and band bending strategies are used with suitable composite materials to achieve efficient copper oxide photocathodes.[31, 32, 36] Another issue is the photostability in aqueous electrolytes, as the redox potentials for the reduction and oxidation of copper oxides lie within the water splitting potentials, this causes photocorrosion of the material.[37-39] Although numerous research efforts have been made to enhance the charge carrier collection in photocathodes by doping, decorating with cocatalysts and nanostructure engineering, the photostability remains an issue for this material.[30, 31, 40-42]

Cu_2O/CuO heterojunction structures, which can be created in an easy manner exhibiting high surface area, fast electron transport and sufficient conductivity, are particularly appealing as materials for photocathodes. Recently, the studies by P. Diao *et al.*[32] and Bing-Joe Hwang *et al.*[31] found that Cu_2O/CuO heterojunctions facilitate the photogenerated electron-hole separation and improve the charge transfer efficiency. At the same time, these studies showed a limited stability caused by photocorrosion in the electrolyte solution. To address these drawbacks, in their pioneering studies, Grätzel and co-workers[43, 44] proposed a Cu_2O/Ga_2O_3-buried p–n junction with multiple protective layers using atomic layer deposition (ALD); the highest photocurrent reached up to 10 mA cm^{-2} at a potential of 0 V vs RHE. After coupling a noble metal electrocatalyst with a RuO_2 cocatalyst, enabled stable operation exceeding 100 h. However, the complicated fabrication process and the expensive apparatus required for the ALD method, along with the scarcity of Ru and Pt, limit large-scale PEC applications of this approach.

Thus, it is of high importance to develop alternative methods and improve strategies to provide a scalable, facile, low-cost, and environmentally friendly method to manufacture a coating-layer-protected and thus highly

stable photocathode for extended operation of Cu_2O/CuO in aqueous electrolytes. Postcoating Cu_2O/CuO heterostructures with thin protection layers of highly capacitive materials allows improving the chemical stability of the photocathodes. Deposition of ultrathin amorphous and porous carbon,[45, 46] graphene,[29, 47] reduced graphene oxide,[48] and graphitic carbon nitride nanosheets[49] on Cu_2O films have been reported recently to provide good electronic properties and improved chemical stability. In particular, coating Cu_2O/CuO heterostructures with a thin layer of carbon provides specific advantages because of its high surface area as well as the electrical double-layer charge storage behavior and its non-toxic nature. Yet, utilization of expensive techniques, like CVD and high temperature pyrolysis, might limit its widespread applicability.[50-52]

In this work, we focus on the synthesis of cubic Cu_2O films and porous granular bilayer composite Cu_2O/CuO heterostructure photocathodes, prepared by electrodeposition on FTO followed by thermal oxidation. The roles of electrodeposition time and atmosphere during thermal oxidation were investigated. To promote charge carrier collection and address the limited stability and photocorrosion, we prepared Cu_2O/CuO/C heterostructure photocathodes, in which the carbon thin layer is deposited in a “green”, surfactant–free, deposition process using an aqueous glucose solution as a carbon precursor. Next to thorough PEC performance measurements, a systematic pre- and post-characterization of the heterostructured photocathode is provided with respect to the stability of the photocathodes.

3.2 Results and Discussion

The fabrication of thin carbon layer-protected Cu_2O/CuO heterojunction photocathodes is shown in Scheme 3.1. The deposition of Cu_2O on fluorine-doped tin oxide (FTO)-covered glass substrates was achieved by electrodeposition using a lactate-stabilized copper sulfate solution, as reported previously.[53] During the electrodeposition of Cu_2O, performed at a constant cathodic potential of -1.25 V at varying deposition times, an even

and uniform yellowish-orange layer formed on the FTO substrate. The samples were subsequently subjected to heat treatment at 400 °C for 1 h in O_2 atmosphere, upon which the formation of Cu_2O/CuO heterostructures was observed (analysis discussed below). Subsequently, a solution-based glucose coating of the bare Cu_2O films and of the Cu_2O/CuO heterostructures was applied, followed by annealing of the samples under N_2 environment to form the carbon film as a protective layer (Scheme 3.1b and d).

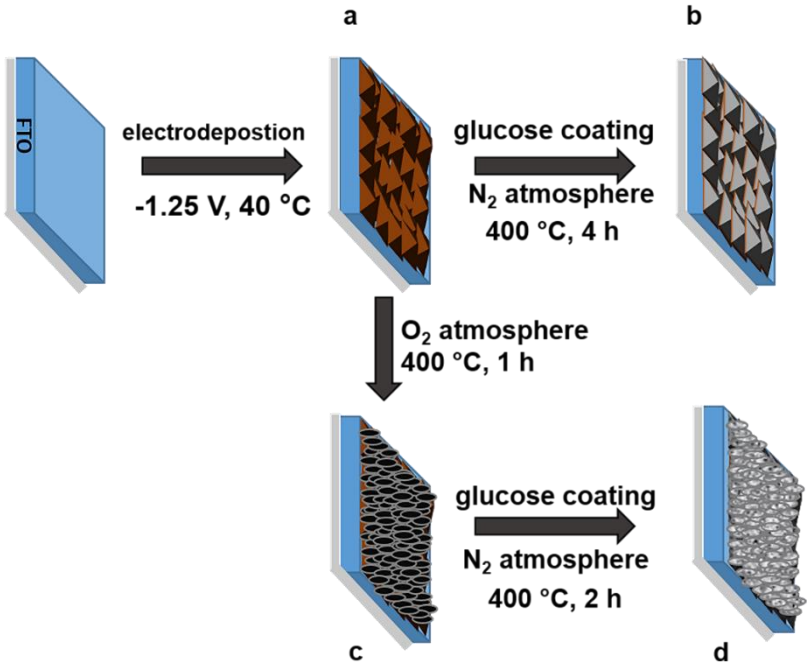

Scheme 3.1. Photocathode fabrication process of glass/FTO/Cu_xO/carbon: (a) electrodeposition of a Cu_2O film on an FTO-covered glass substrate, (b) carbon deposition by aqueous solution coating of glucose followed by thermal annealing in N_2 atmosphere, (c) heterostructure formation by thermal annealing of Cu_2O film in O_2 atmosphere, (d) carbon deposition by solution coating of glucose followed by thermal annealing in N_2 atmosphere.

3.2.1 Electrodeposition and optimization of Cu_2O film thickness

The morphology of Cu_2O films were synthesized by variation of the electrodeposition time (1000 s to 6000 s) at constant cathodic potential. Clearly, a time of 1000 s was insufficient to achieve full coverage, but uniform and compact films with film thicknesses of 1.8 µm and 3.2 µm were obtained at deposition times of 3000 s and 6000 s, respectively. At the applied deposition potential (-1.25 V), the Cu^{2+} ions present in the electrodeposition solution usually precipitate into Cu_2O while Cu co-deposition is suppressed.[20, 54] In the beginning, Cu_2O nuclei are formed on the bare FTO substrate at a relatively high cathodic current density. Once a certain surface density of nuclei is reached, further growth of the layer is facilitated and the current density decreased to reach a plateau after approx. 1000 s.[55]

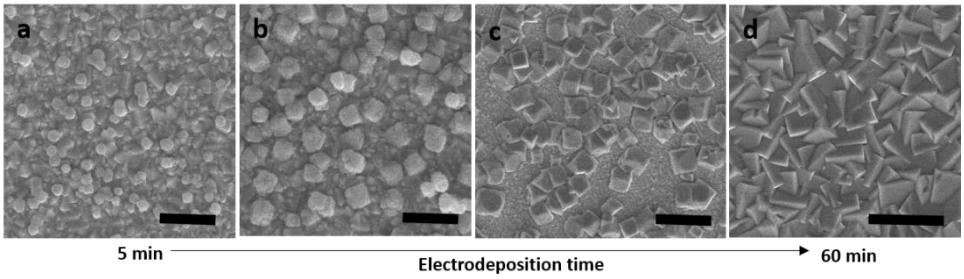

Figure 3.1 SEM morphological images shows growth mechanism of cubic Cu_2O nanofilm with different electrodeposition time.

The initial decrease of cathodic current density with the deposition time is due to the depletion of the metal ion concentration near the electrode surface. The following plateau current is attributed to the formation of cuprous oxide on the surface.[56] First, small grains nucleated on the substrate surface to form cubic islands as shown in Figure 3.1. As the deposition time increased, a specific preferred orientation developed to present a texture first with isolated (Figure 3.1 b-d) and later with interconnected cubes

(Figure 3.2 a-d). The specific preferred orientation was observed by Askimoto and co-workers,[57] who showed that the crystallographic orientation is important to reduce the optical reflection resulting in improved performance in electrical rectification and photosensitivity.[58]

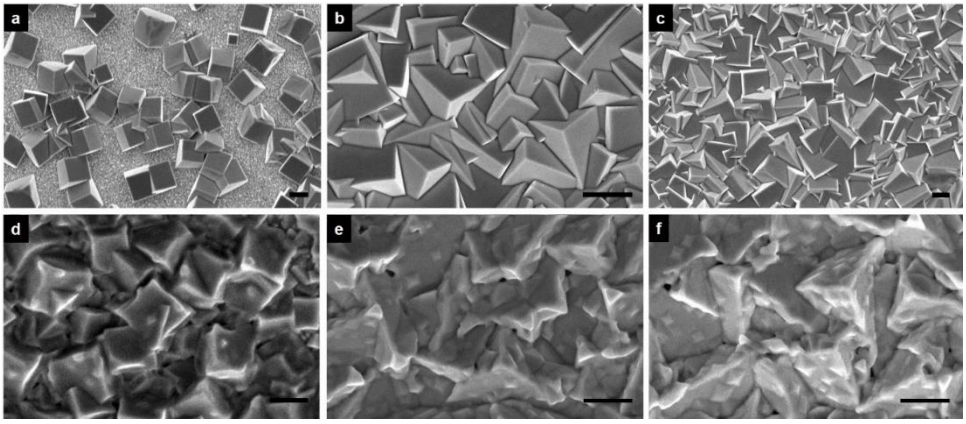

Figure 3.2 SEM images of electrodeposited Cu_2O films on FTO substrates with various electrodeposition times: (a) 1000 s (b) 3000 s (c) 6000 s, and (d, e, f) the corresponding carbon-coated Cu_2O films prepared by subsequent glucose deposition (3 mg/ml in water) and annealing. Scale bars: 1 µm.

3.2.2 Fabrication of Cu_2O/CuO heterostructure

The as-electrodeposited Cu_2O films were subsequently exposed to heat treatment at 400 °C in O_2 atmosphere for 1 h, thus leading to the formation of a CuO layer on top of the Cu_2O film to form a Cu_2O/CuO heterojunction. As shown in Figure 3.3 (a-c) the top-view morphology of the original Cu_2O film was changed after the thermal oxidation step, resulting in a more granular and porous morphology. This observation indicates that the outer layer of the Cu_2O film was transformed into CuO, and a Cu_2O/CuO heterojunction was formed during thermal oxidation. In oxygen-rich atmosphere, the main resulting phase is cupric oxide, CuO.[43, 59] The thickness of the Cu_2O and the CuO layers in Cu_2O/CuO composite varied with the

thermal oxidation time. When the temperature was set at 400 °C for 1 h, the sample consisted of two layers, where the top layer is CuO that lies on top of the remaining Cu_2O. When the thermal oxidation time was increased to 3 h, the film of Cu_2O was oxidized completely, and the material was turned fully into porous CuO. These results confirm that the layer thickness ratio of CuO and Cu_2O can be tuned by variation of the thermal oxidation time.

3.2.3 Carbon layer coating

The electrodeposited Cu_2O thin films and Cu_2O/CuO heterostructures were immersed in a glucose solution (3 mg/ml). and dried at ambient conditions to remove the solvent. Then the samples were annealed at 400 °C in N_2 environment for 2 h to form carbon-coated copper oxide heterostructures. During the initial phase of the annealing, the glucose dehydrates and cross-links, and as the reaction continues, aromatization and carbonization take place,[37, 45] resulting in a firm carbonized shell covering the surface. Figure 3.2 (d-f) and 3.3 (d-f) show the carbon-coated Cu_2O thin films and Cu_2O/CuO heterostructures, respectively, after deposition and annealing of the carbon layer.

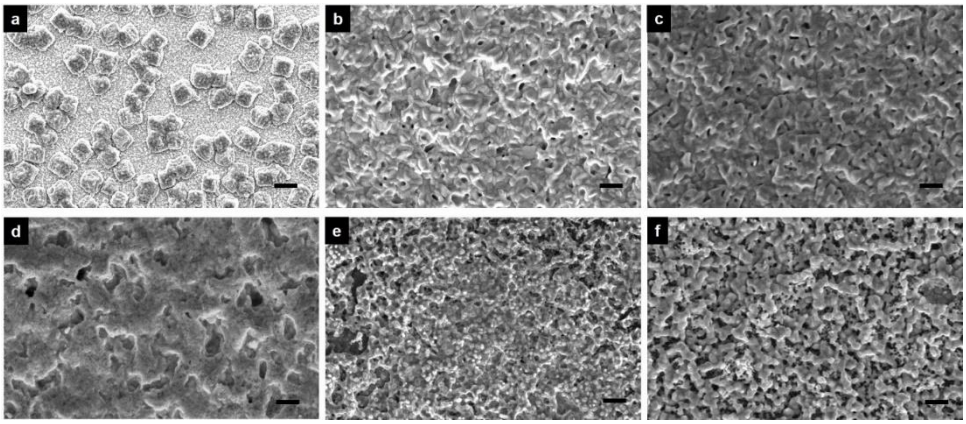

Figure 3.3 SEM images of Cu_2O/CuO heterostructure films on FTO substrate, made by electrodeposition, at various electrodeposition times of (a) 1000 s (b) 3000 s (c) 6000 s, and followed by annealing in O_2 atmosphere, and (d, e, f) the corresponding carbon-coated Cu_2O/CuO films prepared by subsequent glucose deposition (3 mg/ml in water) and annealing. Scale bars: 1 µm.

Figure 3.4 depicts high-resolution transmission electron microscopy (HR-TEM) coupled with energy-dispersive X-ray spectroscopy (EDX) analysis on a single Cu_2O crystal covered with a thin carbon layer. The HR-TEM images (Figure 3.4a, c) of carbon-protected Cu_2O and Cu_2O/CuO show clearly the 15 nm thick carbon layer covering the surface of the Cu_2O and Cu_2O/CuO heterostructures. EDX (Figure 3.4b, d) and high-angle annular dark field (HAADF) images (insets) with Cu and C elemental mapping illustrate the Cu_2O and Cu_2O/CuO heterostructures covered with a high quality amorphous carbon layer.

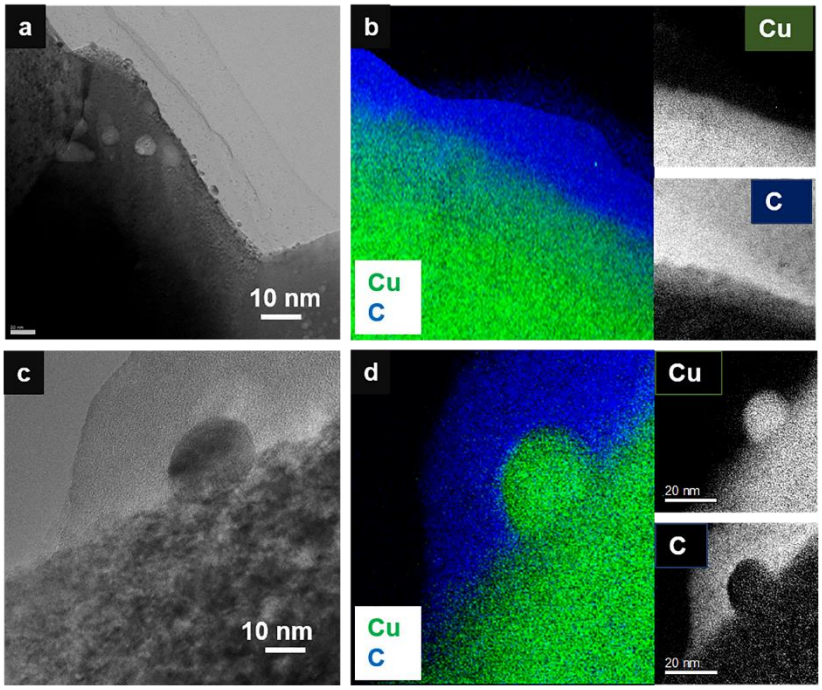

Figure 3.4 TEM and EDX characterization of the Cu_2O/C (a, b) and Cu_2O/CuO/C (c, d) heterostructures (electrodeposition time 3000 s and concentration of glucose solution is 3 mg/ml). (a, c) TEM cross section view, (b, d) combined elemental mapping with element mapping of Cu and C.

The XRD spectra of deposited carbon-coated Cu_2O, CuO (made by full thermal oxidation of pre-grown Cu_2O), and Cu_2O/CuO photocathode thin films on FTO with 3000 s electrodeposition time are presented in Figure 3.5a. The Cu_2O sample exhibited strong diffraction peaks of (110), (111) and (200), corresponding to single-phase cubic Cu_2O. The film after annealing in oxygen flow at 400 °C for 3 h exhibited a crystalline structure in which the Cu_2O has transformed into single-phase monoclinic CuO with distinct peaks for the $(\bar{1}11)$, (200) and (020) crystal planes, while peaks for Cu_2O were completely absent. When annealing in oxygen at 400 °C for 15 min to 1 h, the XRD results confirmed the presence of both Cu_2O and CuO (Figure 3.6).

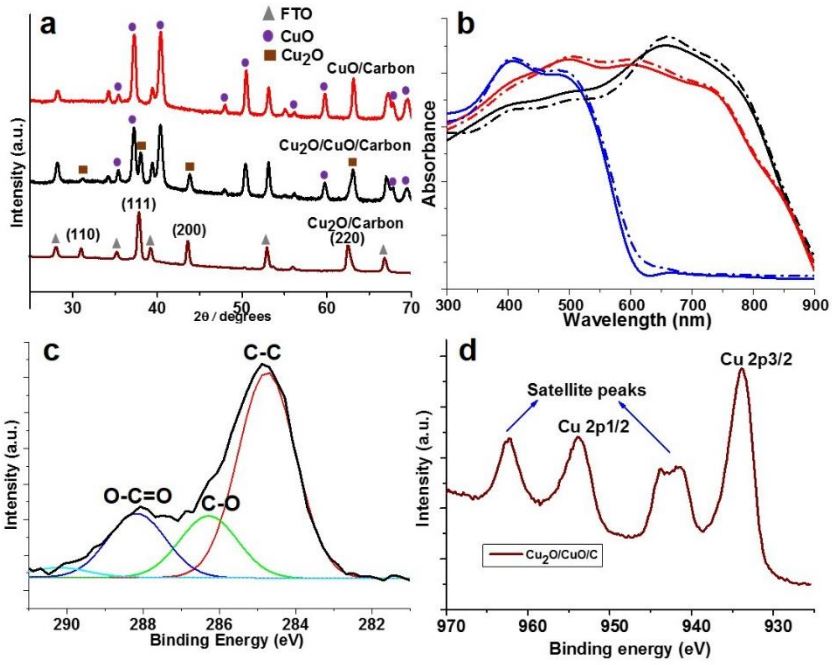

Figure 3.5 Characterization of copper oxide samples (3000 s electrodeposition time) of different phases. (a) X-ray diffraction patterns of samples Cu_2O/C (brown line), Cu_2O/CuO/C (black line) and CuO/C (red line). (b) UV-Vis absorbance spectra of Cu_2O (blue line), CuO (black line) and Cu_2O/CuO (red line) with (dotted line) and without (solid line) a carbon layer, derived from diffuse reflectance spectra. XPS core level spectra of the (c) C 1s and (d) Cu 2p regions of the Cu_2O/CuO/C sample.

To evaluate the optical absorption properties of the photocathode films, UV-Vis diffuse reflectance spectra were measured (Figure 3.5b). The light absorption properties of the carbon-coated Cu_2O and the Cu_2O/CuO heterostructured films are important to evaluate their use as photocatalysts for HER. The color of the as-deposited Cu_2O films ranged from bright yellow to dark red depending on the thickness. After thermal oxidation, the front side of the film changed to black, indicating the formation of CuO. The

yellowish-orange color can still be distinguished from the backside of the film, implying that the inner layer of Cu_2O survived the thermal oxidation, while this was absent in pure CuO. The pure Cu_2O has an absorption edge at about 600 nm (Figure 3.5b), while the Cu_2O/CuO heterostructure extends the absorption edge to approx. 900 nm due to the low band gap energy of CuO. Tauc plots, which were obtained from UV-Vis spectra, are commonly used to determine the band gap energy of a semiconductor based on the Kubelka-Munk theory.[60-62] We confirmed the different band gaps of Cu_2O, Cu_2O/CuO and CuO of 2.15 eV, 1.72 eV and 1.54 eV, respectively. A minor shift in band gap energies occurred upon carbon layer deposition on the Cu_2O/CuO heterostructures (Figure 3.6d). Minor variation of the band gap energy may lead to a slightly improved absorptivity of the material.

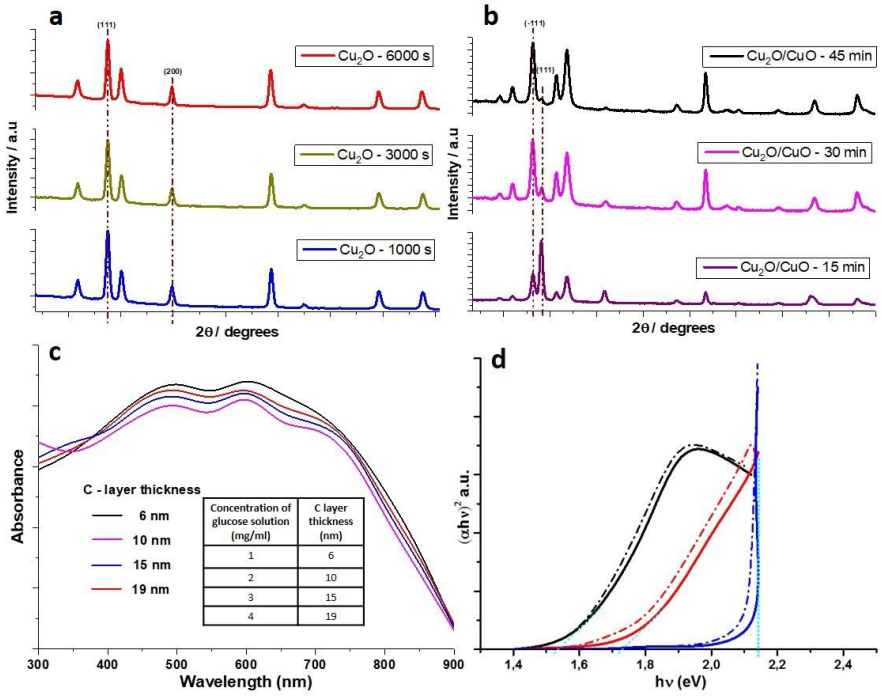

Figure 3.6 XRD patterns of (a) Cu_2O thin films deposited on FTO with different deposition time and (b) Cu_2O/CuO heterostructures at different annealing time. (c) The UV-vis absorption spectra of increasing thickness carbon-coated Cu_2O/CuO heterostructures prepared at different concentrations of glucose. (d) Band gap estimation via Kubelka–Munk theory for with (solid line) and without (dashed line) carbon-coated Cu_2O (blue line), CuO (black line) and Cu_2O-CuO (red line) heterostructures.

To gain insight into the chemical composition of the photoelectrode, we carried out XPS measurements on the Cu_2O/CuO/C heterostructures. High-resolution XPS spectra for C 1s and Cu 2p core levels are presented in Figure 3.5c-d. The C spectrum show a strong peak at 284.8 eV, corresponding to C–C, implying the formation of a carbon layer on the Cu_2O/CuO surface (Figure 3.5c). The other two peaks with lower intensity at 286.5 and 288.4,

belonging to C−O and O−C=O, respectively, indicate some retaining oxygen content. The Cu 2p region of the XPS spectrum of Cu_2O/CuO/C is shown in Figure 3.5d, where the two sharp and symmetrical peaks centered at 932.5 and 953.3 eV are assigned to Cu 2p 3/2 and Cu 2p1/2 of CuO, respectively. The presence of two other (satellite) peaks at relatively higher binding energies, 943.1 and 962.8 eV, also indicate the existence of CuO on the surface of the substrate. Due to the comparatively high thickness of the CuO, the underlying Cu_2O is invisible in this analysis.

The concentration of the aqueous glucose solution plays an important role in controlling the thickness of the final carbon layer on the copper oxide surface. Due to increase of the carbon layer thickness, light absorption in the visible light region was compromised (Figure 3.6c). More importantly, the SEM and TEM images of the 15 nm thin carbon-coated Cu_2O and Cu_2O/CuO heterostructures clearly show that the surfaces were smooth with no noticeable fractures. Apparently, the carbon layer helps to maintain the integrity of the heterostructures compared with the remaining heterostructures, which showed the presence of isolated fractures, which would be unattractive for PEC application of such a photocathode due to an enhanced tendency toward photocorrosion. From a combined perspective of layer conformability and light absorption, the thickness of the carbon layer needs optimization to obtain a higher active performance and better stability for copper oxides as photocatalysts in water reduction.

3.2.4 Photoelectrochemical characterization

To investigate the PEC performance of Cu_2O, CuO, and Cu_2O/CuO films, without and with a protecting carbon layer at various thickness on the photocathodes, linear sweep voltammetry measurements were performed in a 1 M Na_2SO_4 electrolyte (pH 5.5) under chopped AM 1.5G (100 mW cm^{-2}) illumination using a conventional three-electrode system, with the photocathode on FTO, Ag/AgCl electrode and Pt mesh as a working electrode, reference electrode, and counter electrode, respectively. As shown in Figure 3.7, all photocathodes showed a reductive photocurrent,

which was predominantly attributed to the PEC water reduction. The photocurrent densities of the Cu_2O and CuO films were not high (Figure 3.7 a and b), with values of −2.5mA cm^{-2} and –2 mA cm^{-2} at 0.0 V vs. RHE respectively. These values are consistent with an earlier study.[63] The low photocurrent density is attributed to the sluggish reaction kinetics and to self-reduction of the copper oxide film.[64, 65] After thermal oxidation at 400 °C for 1 h, the resulting Cu_2O/CuO heterostructured film exhibited enhanced photoactivity compared to the pure Cu_2O and CuO films. As can be seen in the Figure 3.7c, the photocurrent density at 0 V vs. RHE reached −5.1 mA cm^{-2}, which more than double compared to those obtained on Cu_2O and CuO films. In the Cu_2O/CuO thin film, downward band bending occurs at the interface with the electrolyte, thus promoting the flow of electrons toward the electrolyte solution. The carbon-protected thin films gave enhanced current densities (Figure 3.7d-f), of which the copper oxide heterostructured photocathode showed a current density of -6.5 mA/cm^2 at 0 V vs RHE under simulated 1 sun irradiation, which was the highest photocurrent among all samples tested here. When protecting the Cu_2O and Cu_2O/CuO films with a 15 nm carbon layer, the enhanced performance is attributed to further facilitating quick electron transfer to the surface and suppressing photocorrosion of the photocathode film.

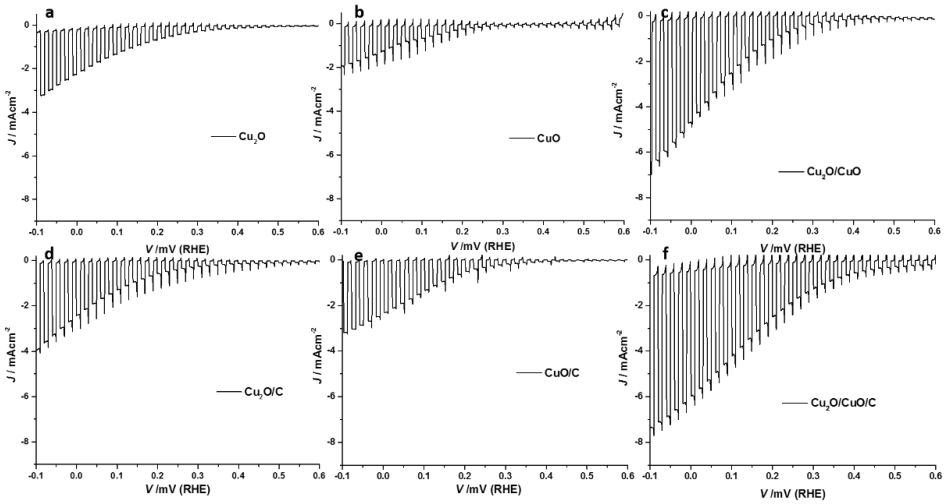

Figure 3.7. PEC performance of non-coated (a-c) and coated (d-f) copper oxide photocathodes (deposition time: 3000 sec, carbon layer: 15 nm) under simulated AM 1.5G chopped illumination.

The performance of catalytic HER of the photocathodes under AC response was studied with electrochemical impedance spectroscopy (EIS), both in dark and under light illumination. This investigation was performed in order to evaluate the charge-transfer resistance (R_{ct}) at the photocathode/ solution interface. As observed in Figure 3.8a, the Nyquist plots are strongly affected by the illumination applied onto the PEC cell indicating a significantly reduced charge transfer resistance compared to dark conditions. Both in dark and under illumination, the charge transfer resistance decreased in the order Cu_2O, Cu_2O/CuO, and Cu_2O/CuO/C, indicating that illumination accelerates the charge transfer reaction due to the photoinduced increase of carrier density. This trend with photocathode structure and composition agrees well with the trend of photocurrent density described above, signifying that the Cu_2O/CuO/C heterostructure provides facilitated charge transfer across the photocathode material to the solution interface, indicating stronger electronic coupling between the

layers. This explains why the heterostructure and carbon-coated photocathodes exhibited the best PEC performance for HER. Figure 3.8b shows the correlation between electrodeposition time to deposit the cuprous oxide layer on the FTO substrate and the thickness of the Cu_2O/CuO heterostructure after annealing the samples in O_2 atmosphere. The layer thickness ratio between Cu_2O and CuO in the mixed oxide layer is depending on the initial Cu_2O layer thickness. Thus the effect of the Cu_2O electrodeposition time on the PEC activity of the Cu_2O/CuO heterostructure is also visible here. First, the formation of the Cu_2O/CuO heterostructure provides a large space-charge region potential, which boosts the electron-hole separation efficiency and decreases the electron-hole recombination rate. Second, the CuO layer formed on the surface of Cu_2O noticeably increases the light absorption due to its narrower band gap, and tuning the layer thickness resulting in a much more efficient utilization of light by the underlying Cu_2O film.

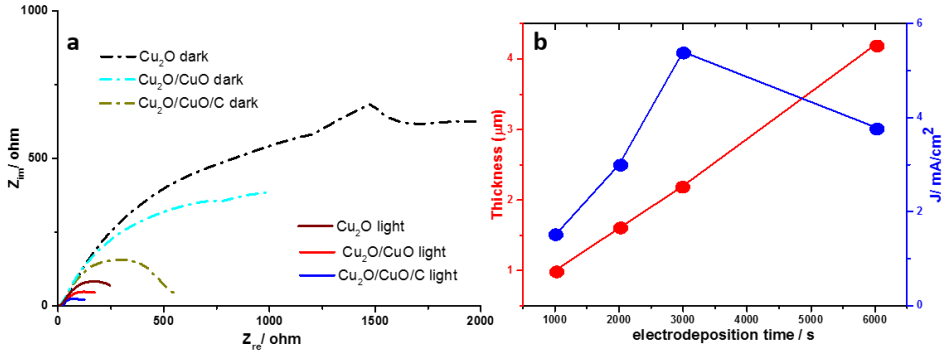

Figure 3.8. (a) Nyquist plots of Cu oxide-based photocathodes (carbon-coated and non-coated) both in the dark and under illumination in 1.0 M Na_2SO_4 electrolyte at pH 5.5. (b) Relationship between electrodeposition time with thickness of sample non-coated bare Cu_2O/CuO on FTO and photocurrent density.

The photostability of the photocathodes under illumination was evaluated by chronoamperometric measurements at 0 V vs RHE in 1 M Na_2SO_4 electrolyte (Figure 3.9). The bare Cu_2O and CuO photocathodes showed (Figure 3.9a-c) a low photostability, and after 4000 s the current density approached zero. However, in case of Cu_2O/CuO the heterostructure both the activity and stability were improved during the 4000 s measurement. The average photocurrent density remained at about 55%, indicating a decay of less than 45%. In fact, this is a rather small decay compare to single copper oxide photocathodes without a protecting layer. As shown in Figure 3.9d-f, all carbon-protected Cu_2O, CuO and Cu_2O/CuO thin films exhibited significantly enhanced photocurrents and photostabilities compared with the non-protected photocathodes (Figure 3.9a-c). As presented in Figure 3.9, all photocathodes showed currents even when the light was off, i.e. a dark current, and particularly the non-protected photocathodes showed higher dark currents compare to carbon-protected photocathodes. Probably, direct contact of the photocathode surface with the electrolyte results in surface degradation and photocorrosion by constant surface charging. Upon applying an optimum 15 nm thickness of carbon on the photocathodes, the photocorrosion of the surface was inhibited. The most optimal case was observed again for the Cu_2O/CuO/C heterostructure film, which showed maintained performance for over 1 h.

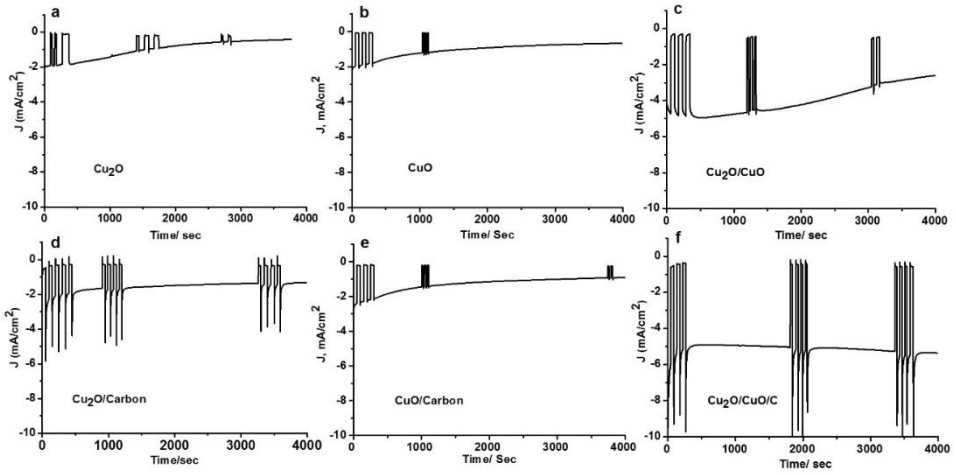

Figure 3.9. PEC stability of copper oxide carbon coated and non-coated photocathode samples.

To examine the cause for the decrease in PEC stability of the photocathodes, XRD and XPS spectra were taken for the Cu_2O/C and Cu_2O/CuO/C samples after performing the PEC measurements (Figure S8). The XRD spectrum shows the appearance of new peaks at 44.2^0 and 51.3^0, which indicates the formation of Cu particles on the surface. The significant morphological surface changes were observed clearly in SEM images after PEC testing (Figure 3.10). In agreement with the elemental compositions obtained from the XPS spectra, these data confirmed photocorrosion and concomitant morphological changes. The PEC performance of Cu_2O/CuO heterostructured samples with carbon coatings of various thicknesses investigated. The photocurrents increased with increasing carbon layer thickness from 5 - 15 nm, while for a thickness of 20 nm it slightly decreased. These results confirm that a 15 nm carbon coating is the most optimal layer thickness regarding PEC performance and stability.

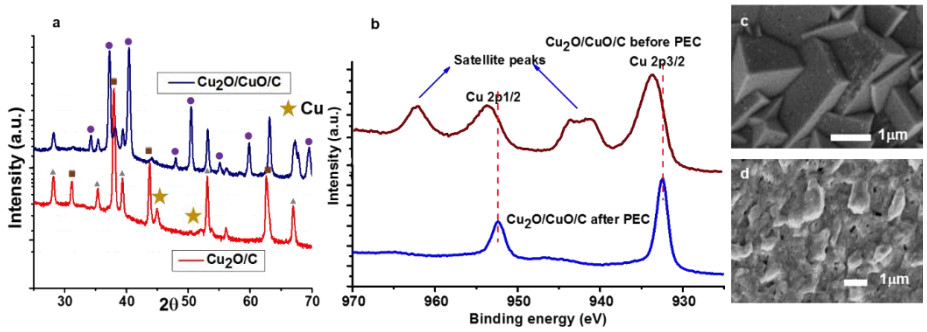

Figure 3.10 (a) XRD patterns of Cu_2O/C and Cu_2O/CuO/C after PEC measurements (b) The Cu 2p region of the XPS spectra of Cu_2O/CuO/C photocathode before and after 4000 s PEC testing. The SEM images of (c) Cu_2O/C and (d) Cu_2O/CuO/C after PEC measurements.

Furthermore, here we showed long-run stability at 0.3 V vs RHE (i.e. - 0.2 V vs Ag/AgCl) under simulated AM 1.5G illumination. The heterostructure photocathode showed excellent stability over 50 h (Figure 3.11a) with a continuous hydrogen generation and the amount of hydrogen evolved is also measured with time (Figure 3.11b). Its confirmed that the measured photocurrent of the Cu_2O/CuO/C photocathode arises from hydrogen evolution reaction by water splitting rather than any other unwanted side reactions. The amounts of H_2 evolved in initial 5 h from the Cu_2O/CuO/C heterostructure photocathode at 0.3 V vs RHE was 48 µmol. The obtained initial faradaic efficiencies is 92% and there is no major decline in the performance during the test. While, the purpose of this photostability study at 0.3 V vs RHE to show its stable condition according to pourbaix diagram for copper. The IPCE measurements indicate for the carbon coated–Cu_2O/CuO photoelectrode enhanced in the long wavelength region and strong absorption due to the red shifts in the bandgap transition from the introduction of CuO and the conformal coating of carbon layer(Figure 3.11c). This improvement of the IPCEs is in agreement with the UV-Vis diffuse reflectance spectra. It is worth noticing that a maximum IPCE of 70% was

achieved at a wavelength of 580 nm, the results demonstrate that the recombination of charge carriers is efficiently inhibited and improve the charge transfer processes by incorporating CuO and carbon coating.

To the addition, study the efficiency of photogenerated charge carriers separation and transfer in the photoelectrode samples, the photoluminescence (PL) emission spectra of Cu_2O, Cu_2O/CuO and Cu_2O/CuO/C heterostructure are measured with an excitation wavelength of 432 nm (Figure 3.11d). It is known that a higher PL emission intensity peak corresponds to a higher carrier recombination rate, that is, a shorter lifetime of the electron−hole pairs[66, 67]. It can be clearly seen that strikingly different PL intensity of bare Cu_2O which exhibits strong intense peak at 650 nm, whereas both the signals of other heterojunction with and without carbon layer are evidently quenched, indicating that both CuO and carbon can participate in separation and transportation of charge carriers effectively from Cu_2O.

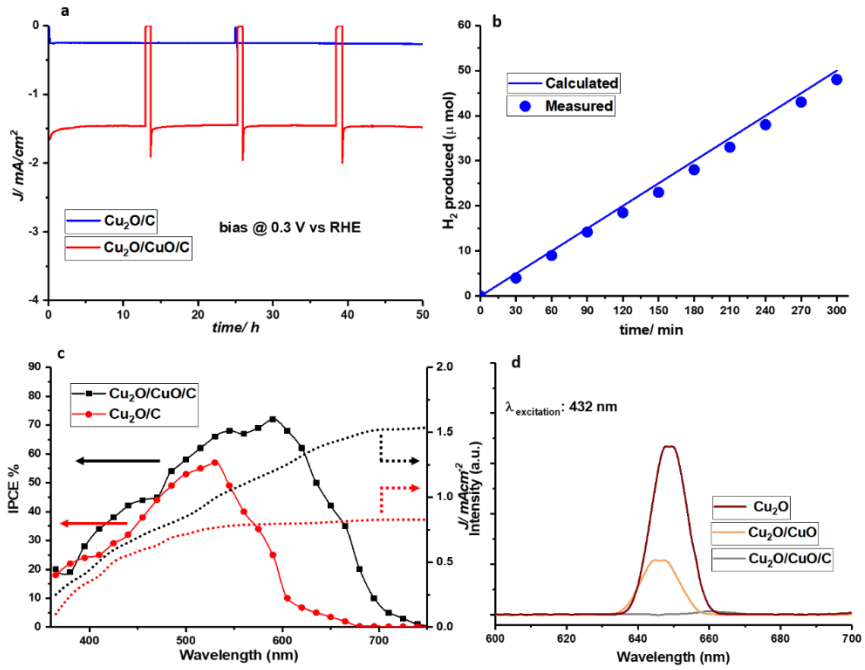

Figure 3.11 (a) Long-run photostability of Cu_2O/C and Cu_2O/CuO/C heterostructure under light illumination at applied bias 0.3 V vs RHE. (b) The amount of hydrogen evolved from the Cu_2O/CuO/C heterostructure as determined by gas chromatography. (c) IPCE spectra with integrated photocurrent density of Cu_2O and Cu_2O/CuO/C heterostructure photocathodes under monochromatic illumination (d) Photoluminescence spectra of the as-prepared Cu_2O, Cu_2O/CuO and Cu_2O/CuO/C heterostructures under 432 nm excitation.

An interesting observation made by analysing on the roles of the carbon coating in enhancing the photocurrent and photostability. This fact arises by incorporating with CuO and certain thickness of carbon film on Cu_2O photocathode (Scheme 2). This is most likely because the deposition of a carbon layer influences a suitable energy level position with respect to the electrolyte redox levels so that electrons are effectively transported in the

direction of the surface to reduce water into hydrogen[68-70]. This is supported by the charge-transfer resistance (R_{ct}) in Impedance spectroscopy (Figure 3.8a) and PL peak intensity (Figure 3.11d).

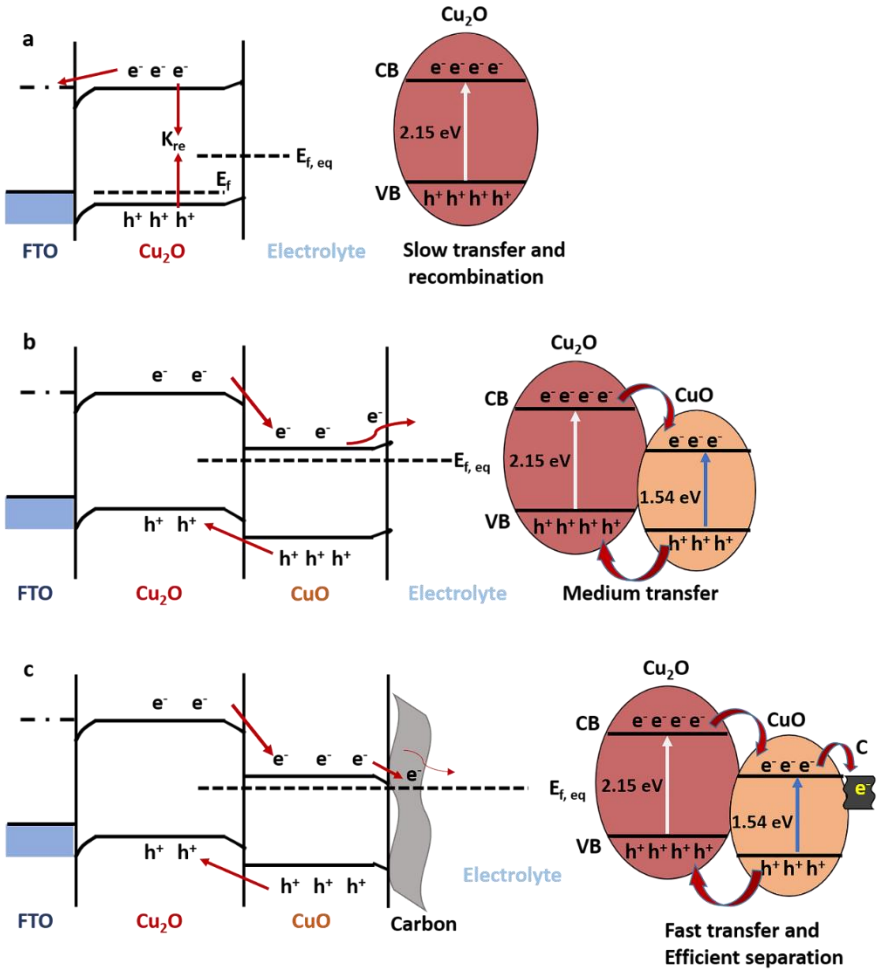

Scheme 2. Schematics of charge recombination (K_{re}) and charge transport processes upon visible light illumination, and the role of the carbon layer in (a) bare Cu_2O (b) Cu_2O/CuO and (c) Cu_2O/CuO/C photocathodes, as well as charge transfer taking place in the corresponding band diagrams.

3.3 Conclusions

In the work presented here, we have demonstrated tuning of the electrodeposition time and application of a carbon protecting layer by solution processing, which combined resulted in Cu_2O/CuO heterostructure photocathodes with improved current density and stability. The Cu_2O film morphology and coverage on FTO substrates showed dependence on deposition time. With increasing deposition time at constant potential the crystal grain size increased, and many truncated cubes exposed the triangular faces parallel to the substrate. The PEC performance, as characterized by photocurrent density and photostability, was enhanced significantly by incorporating an optimum thickness of the carbon protection layer. The best performing devices showed photocurrents up to 6.5 mA/cm^{-2} and 7.5 mA/cm^{-2} at a potential of 0 V and - 0.1 V vs RHE at pH 5.5 respectively. Conformal coating of a carbon protection layer allows stable operation at low-bias for 50 h. To the best of our knowledge this is the highest performance yet reported for a cocatalyst-free Cu_2O/CuO heterostructure photocathode. The carbon protection strategy prohibits surface degradation and photocorrosion efficiently. The results presented here suggest that the key factors to an efficient and stable performance are: (i) electrodeposition time, (ii) thermal oxidation to create a heterostructure copper oxide layer, and (iii) the combination of a high quality surface p-n junction with a carbon protection layer. The carbon coating suppresses a dark current that results from surface degradation, and assists in improved electron transfer. Overall, the photocathodes made from earth-abundant copper oxide materials and stabilized with an easily applied and cost-effective solution deposition process, may become promising candidates for practical solar fuel production.

3.4 Acknowledgements

Dr. Wouter Vijselaar is thanked for helpful discussions and for his assistance with the PEC measurements. Gerard Kip is acknowledged for XPS measurements. Rico Keim is thanked for the TEM and EDX characterization. We thank Dr. Alexander Milbrat and Prof. Guido Mul for use of the solar simulator.

3.5 Materials and methods

3.5.1 Electrodeposition of Cu_2O

The Cu_2O films were prepared by a time based amperometric (I-t curve) deposition method. In brief, the electrodeposition of Cu_2O was performed using a VersaSTAT 4 potentiostat using a two-electrode configuration, in which the FTO substrate (Sigma-Aldrich, TEC 7, 7 Ω/sq) serves as the working electrode and a platinum mesh as the counter electrode. The deposition was conducted at -1.25 V, in an electrolyte solution consisting of 0.2 M $CuSO_4$ (Copper sulfate pentahydrate , Sigma-Aldrich, 99%), 3 M lactic acid ($C_3H_6O_3$, Sigma-Aldrich, 85%), and 0.5 M K_2HPO_4 buffer (di-potassium hydrogen phosphate, Merck, 99%). The pH of the electrolyte solution was adjusted to 12 by the addition of 3 M KOH (potassium hydroxide pellets, Acros organics, 85%) solution. The thickness of the Cu_2O films was controlled by varying the deposition time (1000 s, 3000 s and 6000 s), while the temperature was kept at 40 °C using a hot water bath with an in situ temperature probe.

3.5.2 Fabrication of Cu_2O/CuO and CuO heterostructures

The Cu_2O/CuO heterostructures were fabricated by thermal oxidation of as deposited Cu_2O films (deposition time 3000 s) in the presence of air at 400 °C for 1 h, and the pure CuO film was prepared by thermal oxidation of the Cu_2O film in air at 400 °C for 3 h.

3.5.3 Carbon coating on Cu_2O, CuO and Cu_2O/CuO heterostructure photocathodes

Carbon coating layers on Cu_2O and CuO, Cu_2O/CuO photocathodes were achieved by hydrothermal treatment of glucose followed by annealing at high temperature in air and N_2 atmosphere respectively. Prepared copper oxide photocathodes were immersed in 20 ml of an aqueous glucose (3 mg/ml) solution for 8 h and dried at ambient condition. The glucose-coated photocathodes were kept in a furnace for 4 h at 400 °C, resulting in melting and carbonization of glucose to form an activated carbon layer.

3.5.4 Material characterization

XRD measurements were performed on a Bruker D2 (Cu Kα source) diffractometer. UV/Vis diffuse reflectance spectra (DRS) were recorded with a UV/Vis spectrophotometer (Thermo Scientific, Evolution 600), the reflectance data were converted to Kulbelka–Munk plots and the corresponding Tauc plots. A Sirion HR-SEM (FEI instruments) was used for SEM experiments. TEM imaging of the deposited photocathodes was performed using a Philips CM300ST-FEG microscope equipped with a Kevex EDX detector. The X-ray Photoelectron spectroscopy (XPS) measurements were performed on a Quantera SXM (Physical Electronics) instrument, equipped with an Al Kα X-ray source (1486.6 eV). Photoluminescence (PL) spectra were recorded by perkin elmer ls 55 fluorescence spectrometer.

3.5.5 PEC Measurements

To measure the photoelectrical characteristics (IPCE and PEC) of the Cu_2O/CuO/C heterostructure photocathode, samples were positioned perpendicular to a 300 W xenon arc light source, which is filtered to modify its output to AM 1.5G spectrally. Upon installation of the lamp, the lamp was calibrated by VLSI Standards Inc. Before every measurement the lamp was checked by a calibrated Si solar cell, supplied by VLSI Standards Inc., for spectral mismatch. PEC measurements were recorded on a VersaSTAT 4 potentiostat using a linear voltage sweep from −0.1 to 0.6 V at a rate of 0.2

mV s−1. The three-electrode configuration using an aqueous solution of 1 M Na_2SO_4 (Sigma-Aldrich, 99%) at pH 5.5 with formic acid, consists of Ag/ AgCl in saturated KCl as a reference electrode, a Pt mesh as a counter electrode and the prepared copper oxide photocathode as a working electrode. Electrochemical impedance spectroscopy (EIS) was performed using an AC amplitude of 10 mV and a frequency range between 100 KHz to 0.1 Hz. The measured EIS data were obtained at an applied bias of 0 V vs. RHE at room temperature. The potential was converted to the RHE reference electrode by the Nernst equation:

$E = E_{Ag/AgCl} + 0.059\ pH + E^{o}_{Ag/AgCl}$

Where $E^{o}_{Ag/AgCl} = 0.197$ V at 25°C

3.5.6 Hydrogen production

The hydrogen evolution was measured using a teflon-cell connected to a highly sensitive gas chromatograph (CompactGC Interscience). The GC was equipped with a Pulsed Discharge Detector to determine the amount H_2 in the argon carrier gas. Argon was flowed with 5 ml/min through the 1 M Na_2SO_4 electrolyte consists of Ag/ AgCl in saturated KCl as a reference electrode, a Pt mesh as a counter electrode and the prepared copper oxide photocathode as a working electrode.

3.6 References

1. P. V. Kamat, *J. Phys. Chem. C*, 2007, **111**, 2834-2860.
2. S. Ardo, D. Fernandez Rivas, M. A. Modestino, V. Schulze Greiving, F. F. Abdi, E. Alarcon Llado, V. Artero, K. Ayers, C. Battaglia, J.-P. Becker, D. Bederak, A. Berger, F. Buda, E. Chinello, B. Dam, V. Di Palma, T. Edvinsson, K. Fujii, H. Gardeniers, H. Geerlings, S. M. H. Hashemi, S. Haussener, F. Houle, J. Huskens, B. D. James, K. Konrad, A. Kudo, P. P. Kunturu, D. Lohse, B. Mei, E. L. Miller, G. F. Moore, J. Muller, K. L.

Orchard, T. E. Rosser, F. H. Saadi, J.-W. Schüttauf, B. Seger, S. W. Sheehan, W. A. Smith, J. Spurgeon, M. H. Tang, R. van de Krol, P. C. K. Vesborg and P. Westerik, *Energy Environ Sci.*, 2018, **11**, 2768-2783.

3. R. J. Detz, J. N. H. Reek and B. C. C. van der Zwaan, *Energy Environ Sci.*, 2018, **11**, 1653-1669.
4. L. Yu, H. Zhou, J. Sun, F. Qin, F. Yu, J. Bao, Y. Yu, S. Chen and Z. Ren, *Energy Environ Sci.*, 2017, **10**, 1820-1827.
5. J. Azevedo, L. Steier, P. Dias, M. Stefik, C. T. Sousa, J. P. Araújo, A. Mendes, M. Graetzel and S. D. Tilley, *Energy Environ Sci.*, 2014, **7**, 4044-4052.
6. B. A. Pinaud, J. D. Benck, L. C. Seitz, A. J. Forman, Z. Chen, T. G. Deutsch, B. D. James, K. N. Baum, G. N. Baum, S. Ardo, H. Wang, E. Miller and T. F. Jaramillo, *Energy Environ Sci.*, 2013, **6**, 1983-2002.
7. J. M. Bergthorson, *Prog. Energy Combust. Sci.*, 2018, **68**, 169-196.
8. A. Kudo and Y. Miseki, *Chem. Soc. Rev.*, 2009, **38**, 253-278.
9. X. Chen, S. Shen, L. Guo and S. S. Mao, *Chem. Rev.*, 2010, **110**, 6503-6570.
10. Z. Chen, T. F. Jaramillo, T. G. Deutsch, A. Kleiman-Shwarsctein, A. J. Forman, N. Gaillard, R. Garland, K. Takanabe, C. Heske, M. Sunkara, E. W. McFarland, K. Domen, E. L. Miller, J. A. Turner and H. N. Dinh, *J. Mat. Res.*, 2011, **25**, 3-16.
11. F. E. Osterloh, *Chem. Soc. Rev.*, 2013, **42**, 2294-2320.
12. M. G. Walter, E. L. Warren, J. R. McKone, S. W. Boettcher, Q. Mi, E. A. Santori and N. S. Lewis, *Chem. Rev.*, 2010, **110**, 6446-6473.
13. J. Luo, J.-H. Im, M. T. Mayer, M. Schreier, M. K. Nazeeruddin, N.-G. Park, S. D. Tilley, H. J. Fan and M. Grätzel, *Science*, 2014, **345**, 1593.
14. B. D. Alexander, P. J. Kulesza, I. Rutkowska, R. Solarska and J. Augustynski, *J. Mat. Chem.*, 2008, **18**, 2298-2303.
15. R. Saito, Y. Miseki, W. Nini and K. Sayama, *ACS Comb. Sci.*, 2015, **17**, 592-599.
16. A. G. Scheuermann, J. P. Lawrence, K. W. Kemp, T. Ito, A. Walsh, C. E. D. Chidsey, P. K. Hurley and P. C. McIntyre, *Nat. Mater.*, 2015, **15**, 99.

17. J. H. Montoya, L. C. Seitz, P. Chakthranont, A. Vojvodic, T. F. Jaramillo and J. K. Nørskov, *Nat. Mater.*, 2016, **16**, 70.
18. C. Jiang, S. J. A. Moniz, A. Wang, T. Zhang and J. Tang, *Chem. Soc. Rev.*, 2017, **46**, 4645-4660.
19. Q. Yan, J. Yu, S. K. Suram, L. Zhou, A. Shinde, P. F. Newhouse, W. Chen, G. Li, K. A. Persson, J. M. Gregoire and J. B. Neaton, *Proc. Natl. Acad. Sci. U.S.A.*, 2017, **114**, 3040.
20. Y. C. Zhou and J. A. Switzer, *Mater Res. Innov.*, 1998, **2**, 22-27.
21. A. Paracchino, V. Laporte, K. Sivula, M. Grätzel and E. Thimsen, *Nat. Mater.*, 2011, **10**, 456.
22. B. K. Meyer, A. Polity, D. Reppin, M. Becker, P. Hering, P. J. Klar, T. Sander, C. Reindl, J. Benz, M. Eickhoff, C. Heiliger, M. Heinemann, J. Bläsing, A. Krost, S. Shokovets, C. Müller and C. Ronning, *physica status solidi (b)*, 2012, **249**, 1487-1509.
23. A. Paracchino, J. C. Brauer, J.-E. Moser, E. Thimsen and M. Graetzel, *J. Phys. Chem. C*, 2012, **116**, 7341-7350.
24. C. G. Morales-Guio, S. D. Tilley, H. Vrubel, M. Grätzel and X. Hu, *Nat. Commun.*, 2014, **5**, 3059.
25. M. Tadatsugu, N. Yuki and M. Toshihiro, *Appl. Phys. Express*, 2016, **9**, 052301.
26. K. T. Wong, S. Zhuk, S. Masudy-Panah and K. G. Dalapati, *Materials*, 2016, **9**.
27. A. Radi, D. Pradhan, Y. Sohn and K. T. Leung, *ACS Nano*, 2010, **4**, 1553-1560.
28. A. Bhaumik, A. M. Shearin, R. Patel and K. Ghosh, *Phys. Chem. Chem. Phys.*, 2014, **16**, 11054-11066.
29. A. A. Dubale, W.-N. Su, A. G. Tamirat, C.-J. Pan, B. A. Aragaw, H.-M. Chen, C.-H. Chen and B.-J. Hwang, *J. Mater. Chem. A*, 2014, **2**, 18383-18397.
30. A. A. Dubale, C.-J. Pan, A. G. Tamirat, H.-M. Chen, W.-N. Su, C.-H. Chen, J. Rick, D. W. Ayele, B. A. Aragaw, J.-F. Lee, Y.-W. Yang and B.-J. Hwang, *J. Mater. Chem. A*, 2015, **3**, 12482-12499.

31. A. A. Dubale, A. G. Tamirat, H.-M. Chen, T. A. Berhe, C.-J. Pan, W.-N. Su and B.-J. Hwang, *J. Mater. Chem. A*, 2016, **4**, 2205-2216.
32. Y. Yang, D. Xu, Q. Wu and P. Diao, *Sci. Rep.*, 2016, **6**, 35158.
33. W. Septina, R. R. Prabhakar, R. Wick, T. Moehl and S. D. Tilley, *Chem. Mater.*, 2017, **29**, 1735-1743.
34. L. Zhang, D. Jing, L. Guo and X. Yao, *ACS Sustain. Chem. Eng.*, 2014, **2**, 1446-1452.
35. W. Zhang, X. Yang, Q. Zhu, K. Wang, J. Lu, M. Chen and Z. Yang, *Ind. Eng. Chem. Res.*, 2014, **53**, 16316-16323.
36. Z. Li and Z. Zhang, *Nano Res.*, 2018, **11**, 1530-1540.
37. Z. Zhang, R. Dua, L. Zhang, H. Zhu, H. Zhang and P. Wang, *ACS Nano*, 2013, **7**, 1709-1717.
38. S. Emin, F. F. Abdi, M. Fanetti, W. Peng, W. Smith, K. Sivula, B. Dam and M. Valant, *J. Electroanal. Chem.*, 2014, **717-718**, 243-249.
39. Y. J. Jang, J.-W. Jang, S. H. Choi, J. Y. Kim, J. H. Kim, D. H. Youn, W. Y. Kim, S. Han and J. Sung Lee, *Nanoscale*, 2015, **7**, 7624-7631.
40. S. D. Tilley, M. Schreier, J. Azevedo, M. Stefik and M. Graetzel, *Adv. Funct. Mater.*, 2013, **24**, 303-311.
41. P. Bornoz, F. F. Abdi, S. D. Tilley, B. Dam, R. van de Krol, M. Graetzel and K. Sivula, *J. Phys. Chem. C*, 2014, **118**, 16959-16966.
42. C. G. Morales-Guio, L. Liardet, M. T. Mayer, S. D. Tilley, M. Grätzel and X. Hu, *Angew. Chem.*, 2014, **54**, 664-667.
43. J. Luo, L. Steier, M.-K. Son, M. Schreier, M. T. Mayer and M. Grätzel, *Nano Lett.*, 2016, **16**, 1848-1857.
44. L. Pan, J. H. Kim, M. T. Mayer, M.-K. Son, A. Ummadisingu, J. S. Lee, A. Hagfeldt, J. Luo and M. Grätzel, *Nat Catal.*, 2018, **1**, 412-420.
45. J. Hou, C. Yang, H. Cheng, S. Jiao, O. Takeda and H. Zhu, *Energy Environ Sci.*, 2014, **7**, 3758-3768.
46. W. Shi, X. Zhang, S. Li, B. Zhang, M. Wang and Y. Shen, *Appl Surf Sci.*, 2015, **358**, 404-411.
47. E. Kecsenovity, B. Endrődi, P. S. Tóth, Y. Zou, R. A. W. Dryfe, K. Rajeshwar and C. Janáky, *J. Am. Chem. Soc.*, 2017, **139**, 6682-6692.

48. P. D. Tran, S. K. Batabyal, S. S. Pramana, J. Barber, L. H. Wong and S. C. J. Loo, *Nanoscale*, 2012, **4**, 3875-3878.
49. X. Xu, Y. Liu, Y. Zhu, X. Fan, Y. Li, F. Zhang, G. Zhang and W. Peng, *ChemElectroChem*, 2017, **4**, 1498-1502.
50. E. Frackowiak and F. Béguin, *Carbon*, 2001, **39**, 937-950.
51. R. R. Devarapalli, S. Szunerits, Y. Coffinier, M. V. Shelke and R. Boukherroub, *ACS Appl. Mater. Interfaces*, 2016, **8**, 4298-4302.
52. L. Yu, G. Li, X. Zhang, X. Ba, G. Shi, Y. Li, P. K. Wong, J. C. Yu and Y. Yu, *ACS Catal.*, 2016, **6**, 6444-6454.
53. A. Paracchino, N. Mathews, T. Hisatomi, M. Stefik, S. D. Tilley and M. Grätzel, *Energy Environ Sci.*, 2012, **5**, 8673-8681.
54. T. D. Golden, M. G. Shumsky, Y. Zhou, R. A. VanderWerf, R. A. Van Leeuwen and J. A. Switzer, *Chem. Mater.*, 1996, **8**, 2499-2504.
55. P. E. de Jongh, D. Vanmaekelbergh and J. J. Kelly, *Chem. Mater.*, 1999, **11**, 3512-3517.
56. H. Rahal, R. Kihal, A. M. Affoune and S. Rahal, *Chinese J. Chem. Eng.*, 2018, **26**, 421-427.
57. K. Akimoto, S. Ishizuka, M. Yanagita, Y. Nawa, G. K. Paul and T. Sakurai, *Sol. Energy*, 2006, **80**, 715-722.
58. T. Mahalingam, J. S. P. Chitra, S. Rajendran and P. J. Sebastian, *Semicond. Sci. Technol.*, 2002, **17**, 565.
59. R. D. Schmidt-Whitley, M. Martinez-Clemente and A. Revcolevschi, *J Cryst Growth.*, 1974, **23**, 113-120.
60. L. Li, G. Li, J. Xu, J. Zheng, W. Tong and W. Hu, *Phys. Chem. Chem. Phys.*, 2010, **12**, 10857-10864.
61. Y. Zhang, N. Zhang, Z.-R. Tang and Y.-J. Xu, *ACS Nano*, 2012, **6**, 9777-9789.
62. J. Fang and Y. Xuan, *RSC Adv.*, 2017, **7**, 56023-56033.
63. H. Qi, J. Wolfe, D. Fichou and Z. Chen, *Sci. Rep.*, 2016, **6**, 30882.
64. C. Y. Toe, Z. Zheng, H. Wu, J. Scott, R. Amal and Y. H. Ng, *Angew. Chem.*, 2018, **57**, 13613-13617.

65. C. Y. Toe, J. Scott, R. Amal and Y. H. Ng, *J. Photochem. Photobiol*, 2018, DOI: https://doi.org/10.1016/j.jphotochemrev.2018.10.001.
66. H. Shi, G. Chen, C. Zhang and Z. Zou, *ACS Catal.*, 2014, **4**, 3637-3643.
67. X. Han, D. Xu, L. An, C. Hou, Y. Li, Q. Zhang and H. Wang, *Appl Catal B.*, 2019, **243**, 136-144.
68. T. J. Bandosz and C. O. Ania, *Adv. Sci.*, 2018, **5**, 1800293.
69. D. M. Murphy, R. J. Cullen, D. R. Jayasundara, R. L. Doyle, M. E. G. Lyons and P. E. Colavita, *J. Phys. Chem. C*, 2013, **117**, 22768-22777.
70. Y. Miyajima, Y. Tison, C. E. Giusca, V. Stolojan, H. Watanabe, H. Habuchi, S. J. Henley, J. M. Shannon and S. R. P. Silva, *Carbon*, 2011, **49**, 5229-5238.

Chapter 4

Improving charge separation in Cu_2O/g-C_3N_4/CoS photocathodes by a Z-scheme heterojunction to achieve enhanced performance and photostability

Fabricating efficient hetrojunction photocathodes to accelerate charge transport and long-term stability are important to enhance visible light-driven hydrogen evolution. With the strategic combination of type-II band edge heterojunctions and passivation layers of graphitic carbon nitride (g-C_3N_4), Cu_2O/g-C_3N_4/CoS photocathodes have been fabricated which achieve high photostability. We used spin coating and electrospinning techniques to synthesize g-C_3N_4 nanosheets and nanowires, respectively, which were deposited on Cu_2O on FTO substrates. In case of Cu_2O/g-C_3N_4 nanosheets, the loading of g-C_3N_4 was varied from 1 to 7 wt% and the highest photocatalytic activity (5.8 mA/cm^2 at 0 V RHE) was obtained for the heterojunction prepared from the 5 wt% solution. On the other hand, the loading of g-C_3N_4 nanowires was varied by varying the electrospinning time from 0.5 to 12 min, and the heterojunction with 8 min spinning time displayed the highest photocurrent density of 6.6 mA cm^{-2} at 0 V vs RHE under visible light irradiation. The higher photocatalytic activity and better stability of the Cu_2O/g-C_3N_4 nanowires (8 min)/CoS heterojunction arises from the effective separation and transport of photogenerated charge carriers, which was confirmed by photoluminescence and photocurrent measurements, and from proper protection of the underlying Cu_2O photocathode. Importantly, the Cu_2O/g-C_3N_4 heterojunction decorated by CoS proved to be effective for enhancing the stabilization of the Cu_2O photocathode. About 90-95% of the photocurrent density was retained after 5 h of illumination and the faradaic efficiency for hydrogen evolution reached 80%.

4.1 Introduction

Using photocatalysts to produce hydrogen by solar water splitting is important to reduce CO_2 emission from burning fossil fuels, and to contribute to solving the energy crisis and avoiding environmental pollution.[1-3] Currently, metal oxide semiconductor photocatalysts have been widely investigated.[4-7] But, due to their wide band gap, metal oxides, such as TiO_2 (3 eV)[8] and ZnO (3.2 eV),[9] are photoactive in the UV region, which prevents their use in practical applications.[10, 11]

The visible-light-driven photocatalytic activity of copper oxide photocathodes has been extensively studied for the hydrogen evolution from water, CO_2 reduction and degradation of organic pollutants.[12-18] Cu_2O is a p-type photocathode with a direct and suitable narrow bandgap of approximately 2.0 – 2.2 eV,[19-23] is nontoxic, has a large natural abundance, and is cheap to synthesize.[24-28] However, it is challenging to gain a high quantum efficiency and long-term stability. Because of a mismatch between the material's absorptivity and its minority charge carrier diffusion length (20-200 nm), recombination of photogenerated electron-hole pairs occurs, which restricts its applications in photocatalysis.[13, 25, 28-31]

Recently, researchers have investigated thin films of a semiconductor on top of a photoabsorber to improve the photocatalytic activity and photostability by forming a phase interface and a protection layer between the photoabsorber and charge carrier-extraction layers.[28, 32-34] However, the low stability of these passivating materials in acidic and alkaline media limits their practical operation. Using synthesized Cu_2O in combination with other semiconductors in multilayer-structured hybrids may improve the separation efficiency and protect the Cu_2O underneath from photo-corrosion. The interaction between the metal oxide semiconductor photocatalyst and the protective layer facilitates the suitable band bending to provide separation of the photogenerated charge carriers and to enhance the photostability of Cu_2O.[35] Yet, the conformal coating of such materials

commonly needs a complex fabrication process and expensive equipment like atomic layer deposition (ALD).

Photostability is an important materials property for application in solar energy devices, and it is determined by how fast the photogenerated electrons can be separated to prevent recombination and promote the photocatalytic efficiency.[36-42] The use of a semiconductor Z-scheme heterojunction system can efficiently overcome shortcomings of a single photocatalyst, and enhance the light absorption range.[40, 43] In addition, by selecting two suitable semiconductors to construct a Z-scheme heterojunction the charge carrier transport to the interface can be improved and recombination of electron-hole pairs be suppressed.[44] Graphitic carbon nitride, g-C_3N_4, has been widely studied for use in such heterojunctions because of its stability under acidic conditions and its eco-friendly properties.[45] More recently, Wang *et al.* developed a visible-light polymeric photocathode of g-C_3N_4 for hydrogen production, gas sensing, LEDs and oxidation.[46-50] Since then, g-C_3N_4 is widely investigated for use in photocatalysis.[50-52] g-C_3N_4 is a type of metal-free photocatalyst with a narrow band gap (~2.5-2.7 eV).[39, 53-55] In addition, g-C_3N_4 is inexpensive, easily synthesized, and chemically stable, and it exhibits a graphite-like structure.[56-58] These polymeric photocatalysts have been considered for the ability to increase the charge separation efficiency because of their π–conjugated structure.[59, 60] In contrast, bulk g-C_3N_4 limits the catalytic activity because of the greater number of recombination boundaries and few active sites, whereby photogenerated charge carriers recombine rapidly.[61] In contrast, polymeric g-C_3N_4 with different morphologies (nanowires and nanosheets) improve the charge separation efficiency, and have demonstrated to be one of the favorable protection layers to enhance the photocatalytic performance.[37, 62-65]

Here we show the development of a multi-layered Cu_2O/g-C_3N_4/CoS photocathode for visible light-driven hydrogen evolution. In this stack, g-C_3N_4 is used as passivation layer for the Cu_2O photocathode. The Cu_2O film

is directly deposited on a conductive FTO (Fluorine-doped tin oxide) glass substrate by electrodeposition. Spin coating and electrospinning methods were used to deposit g-C_3N_4 to construct the type-II heterojunction. A possible photocatalytic mechanism of the Cu_2O/g-C_3N_4 layer structure is investigated by photoluminescence measurements. Additionally, we compared as synthesized photocathodes with different morphology, coverage and loading amount of g-C_3N_4, and their effect on the separation of electron-hole pairs, charge carrier transport properties and long-term photostability is assessed. In this work, electrodeposited cobalt sulfide (CoS) nanoparticles are used to provide hydrogen evolution reaction (HER) activity with low overpotentials and high photocurrents.

4.2 Results and Discussion

The fabrication of the Cu_2O/g-C_3N_4/CoS heterojunction photocathode is shown in Scheme 4.1. Firstly, a p-type Cu_2O photocathode film was deposited on a conductive FTO substrate. Next, the g-C_3N_4 passivating layer is deposited using two different methods, spin-coating of nanosheets or electrospinning of nanofibers, to investigate the effect on electron-hole separation and stability. Lastly, cobalt sulfide (CoS) is introduced as a co-catalyst on the Cu_2O/g-C_3N_4 heterojunction to assess the influence on the photocurrent density and the H_2 evolution reaction.

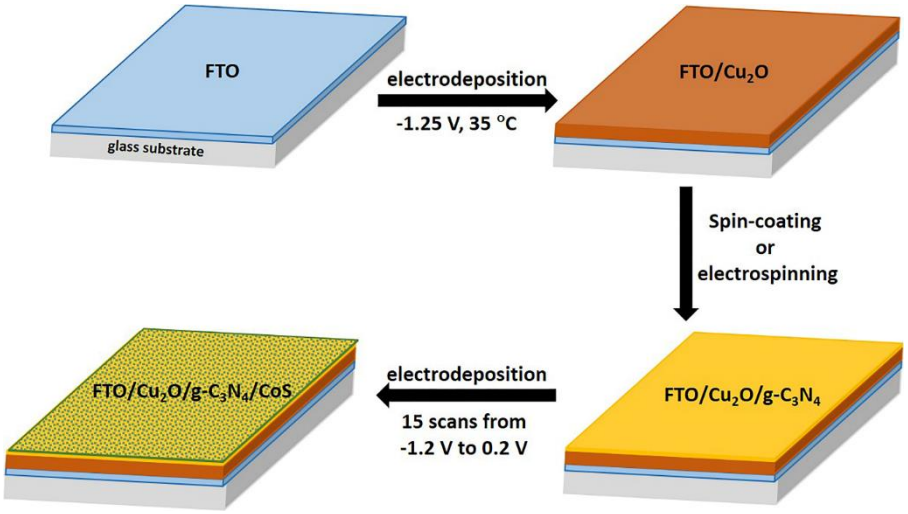

Scheme 4.1 Schematic drawing of the Cu_2O/g-C_3N_4/CoS photocathode. A Cu_2O film is electrodeposited on an FTO substrate, a protection layer of graphitic carbon nitride in bulk, nanosheet or nanowire forms is deposited by spin-coating (bulk, nanosheets) or electrospinning (nanowires), and cobalt sulfide (CoS) is deposited as a co-catalyst by electrodeposition.

In general, the performance of metal oxide photoelectrodes to drive solar-to-hydrogen conversion is limited by charge carrier transport to the semiconductor-liquid interface and recombination within the film.[22, 66] We need to control the materials properties, such as crystallographic orientation, carrier charge lifetime, and semiconductor film thickness, to enhance the photocurrent generation. Cu_2O films were deposited keeping the cathodic potential constant over the course of deposition while changing the deposition time. The effect of the deposition rate on film coverage over the FTO substrate is discussed in the next section and correlated to photocurrent generation in the aqueous electrolyte under illumination. The deposition parameters are optimized to provide a Cu_2O film that produces the highest photocurrent, and these films are chosen for more detailed

fabrication of the Cu_2O/g-C_3N_4 heterojunction and their PEC study presented subsequently.

4.2.1 Preparation of Cu_2O films

Cu_2O films were deposited on fluorine-doped tin oxide (FTO) glass substrates by electrodeposition using a lactate-stabilized copper sulfate solution, as reported previously.[66] During the electrodeposition of Cu_2O, a constant cathodic potential of -1.25 V was applied for various deposition times. Figure 4.1 shows the surface morphologies of the Cu_2O films electrodeposited on FTO substrates, observed at top-view, for various deposition times ranging from 3 to 45 min. As the deposition time was increased, the Cu_2O film coverage on the exposed surface area of the FTO substrate increased. An even and uniform yellowish-orange layer of Cu_2O with different thickness formed on the FTO substrate. Complete coverage of the exposed FTO substrate by Cu_2O was achieved at around 30 min. At short deposition times, the crystal grains were small and showed a cubic structure, whereas with increasing deposition time 3-faced pyramid structures were observed.[67] Because of the high pH (12) of the bath, the grain size of Cu_2O was rather large due to the low nucleation density, resulting in Cu_2O films with columnar grains along the direction to the FTO substrate.[68]

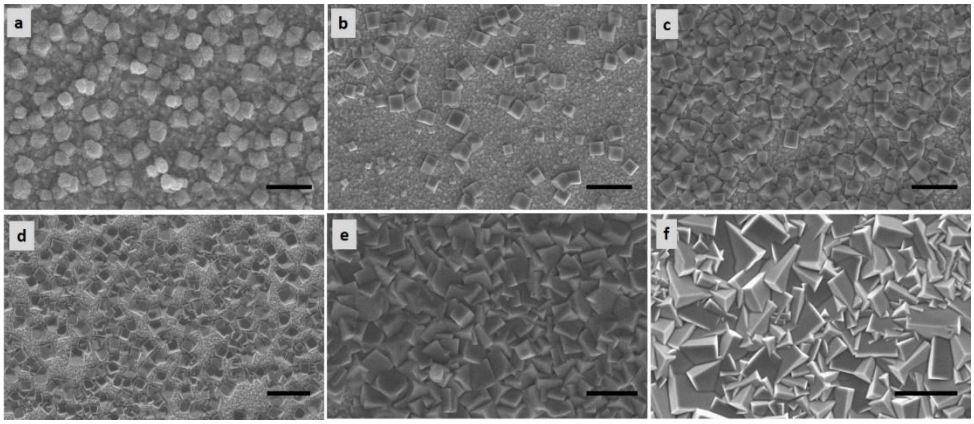

Figure 4.1 SEM images of Cu_2O films on FTO substrates electrodeposited at a constant potential of -1.25 V with varying deposition time: (a) 3 min, (b) 8 min, (c) 15 min, (d) 20 min, (e) 35 min, and (f) 45 min. Scale bars 2 µm.

4.2.2 Synthesis of bulk, nanosheets, and nanowires of $g\text{-}C_3N_4$

Graphitic carbon nitride ($g\text{-}C_3N_4$) is commonly prepared by the thermal polycondensation of various inexpensive nitrogen-rich precursors such as urea,[69] thiourea,[70] melamine,[50] cyanamide,[71] dicyandiamide,[72] or mixtures thereof.[73-75] In this work, $g\text{-}C_3N_4$ was synthesized from thermal polycondensation of melamine. Bulk, nanosheets and nanowire-like $g\text{-}C_3N_4$ structures were synthesized as shown in Scheme 4.2. The bulk structure of $g\text{-}C_3N_4$ obtained from the calcination can be clearly seen from the SEM image (Figure 4.2a). The as-prepared $g\text{-}C_3N_4$ bulk shows irregular shape with wrinkles.

Scheme 4.2 Schematic illustration of the main routes of preparing bulk g-C_3N_4 from melamine and, in subsequent steps, the nanosheet and nanowire forms. Ultrasonication is used for exfoliation of the bulk structure into a few-layer g-C_3N_4 nanosheets. Nanowire-like g-C_3N_4 is synthesized by electrospinning of a nanosheets-containing ethanol solution with PVP as a supporting polymer.

As illustrated in Scheme 4.2, bulk g-C_3N_4 was suspended in ethanol to create a yellow dispersion, and then sonicated to achieve exfoliation resulting in nanosheets (Figure 4.2b). This exfoliation process is similar to that reported for other layered materials, and has been shown to be influenced significantly by the surface energy of used solvent.[76] After sonication, the dispersion was centrifuged at 4000 rpm to remove aggregates, giving rise to a highly stable and homogeneous light-yellow dispersion of g-C_3N_4 nanosheets. The as-prepared g-C_3N_4 nanosheets showed a distinctly different structure compared to that of bulk g-C_3N_4, and exhibited thin layers with clean surfaces. The length and width of the g-C_3N_4 nanosheets lie in the range of 2 μm to 8 μm.

Hereafter, g-C_3N_4 nanowires were obtained from electrospinning the nanosheets solution with PVP as a supporting polymer, followed by annealing in N_2 atmosphere at 400 °C to obtain pure one-dimensional elongated g-C_3N_4 nanowires (Figure 4.2c). The prepared nanowires were relatively uniform with a diameter of ~100 nm.

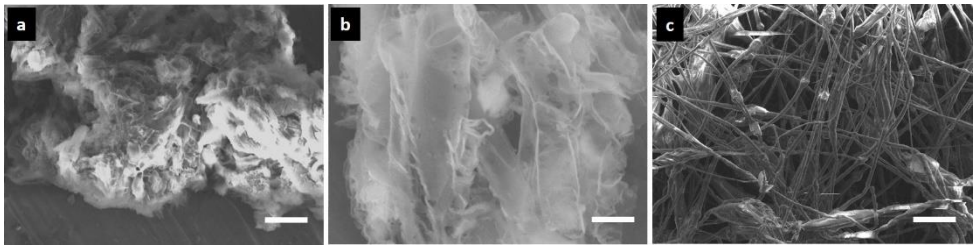

Figure 4.2 SEM images of the different morphologies of g-C_3N_4 structures: (a) bulk, (b) nanosheets, and (c) nanowires, as prepared by the procedures depicted in Scheme 4.2. All three samples were dispersed in ethanol and drop-casted on Al foil before SEM characterization. Scale bars 2 µm.

4.2.3 $Cu_2O/g\text{-}C_3N_4$ type-II heterojunction films

The nano-morphologies (nanosheets and nanowires) obtained from bulk g-C_3N_4, are advantageous for the use as passivation layer on top of Cu_2O to create a type–II, Z-scheme heterojunction photocathode with improved charge separation for PEC hydrogen production.[77] The $Cu_2O/g\text{-}C_3N_4$ bulk heterojunction was prepared by spin-coating of bulk g-C_3N_4 in ethanol solution without applying ultra-sonication (Figure 4.3). A bulky and dense two-dimensional structure consisting of small thick sheets with wrinkles and an irregular shape was formed. With increasing loading amount of the bulk g-C_3N_4 on Cu_2O film, growing of the layer thickness was observed (Figure 4.3b,d). The $Cu_2O/g\text{-}C_3N_4$ nanosheets heterojunction photocathodes were synthesized by suspending a specific amount of exfoliated g-C_3N_4 powder into ethanol, followed by spin-coating of the dispersion on an electrodeposited Cu_2O film and drying at 60 °C in air. Correspondingly, the coverage of g-C_3N_4 in the $Cu_2O/g\text{-}C_3N_4$ structure can be controlled by varying the wt% of exfoliated g-C_3N_4 during spin-coating.

SEM images of a bare Cu_2O film on an FTO substrate and of $Cu_2O/g\text{-}C_3N_4$ heterojunction films prepared with different wt% of nanosheets are shown in Figure 4.4. The heterojunction photocathodes are indicated as Cu_2O/(x-wt %)g-C_3N_4, with x the employed wt% used during spin-coating. The top-view SEM images reveal that the coverage of the nanosheet layer is directly

proportional to the amount of g-C_3N_4 in the ethanol solution used for spin-coating. Furthermore, the intimate surface contact between Cu_2O and g-C_3N_4 nanosheets layer is shown in the SEM cross-section in Figure 4.4f.

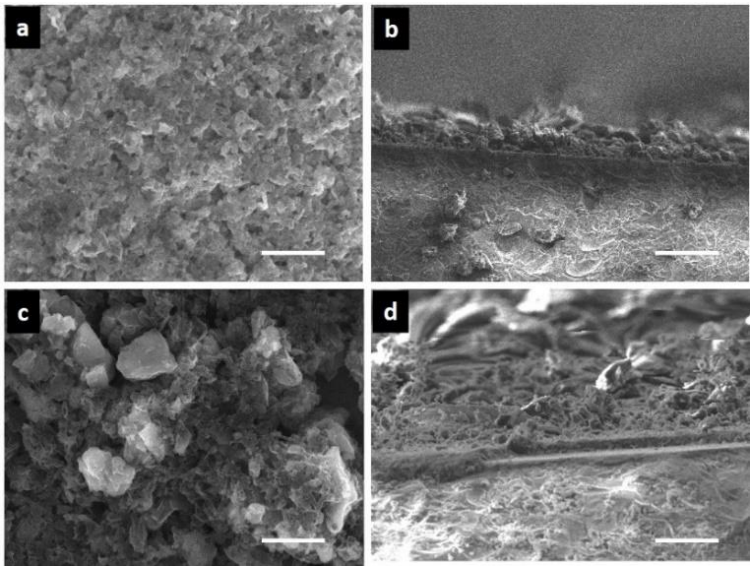

Figure 4.3 SEM (top view and cross section) images of Cu_2O/ bulk g-C_3N_4 heterojunction photocathodes after spin-coating with an ethanolic suspension with various wt% (a, b) 5 wt% and (c, d) 7 wt%. Scale bars in (a, c) 2 µm; in (b, d) 10 µm.

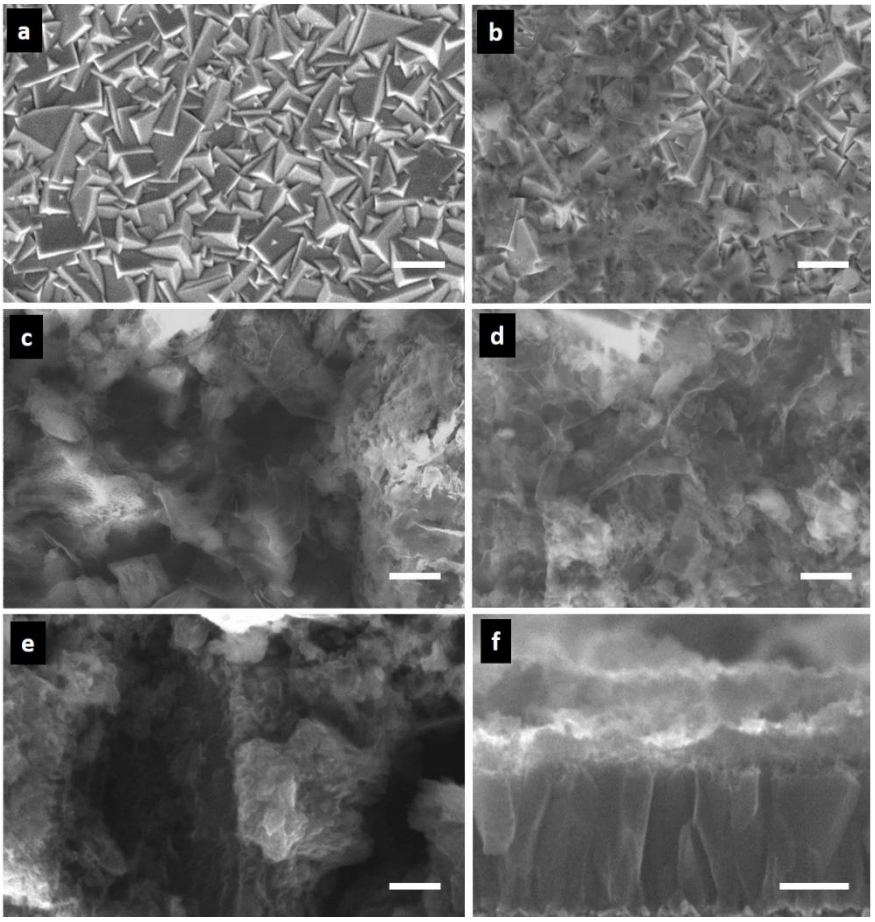

Figure 4.4 SEM images of (a) electrodeposited Cu_2O film on an FTO substrate and of $Cu_2O/g\text{-}C_3N_4$ heterojunction photocathodes after spin-coating with an ethanolic suspension with various wt% of $g\text{-}C_3N_4$ nanosheets: (b) 1 wt%, (c) 3 wt%, (d) 5 wt%, and (e, f) 7 wt%. Scale bars in (a-e) 2 µm; in (f) 500 nm.

The $Cu_2O/g\text{-}C_3N_4$ nanowire heterojunction photocathodes were synthesized by electrospinning of $g\text{-}C_3N_4$ nanowires followed by post-annealing. In this process, a mixture of an exfoliated $g\text{-}C_3N_4$ powder (500 mg) and PVP (1 g, 10 wt.%) was dissolved in ethanol and magnetically stirred for overnight to obtain a homogeneous solution. Finally, this solution was used for

electrospinning and a Cu_2O film on FTO was used as a collector. In the post-annealing process (400 °C for 4 h), the exfoliated g-C_3N_4 nanosheets aggregate, which reduces the defect density.[78] Figure 4.5 shows the top-view SEM images of the Cu_2O/g-C_3N_4 nanowire heterostructures fabricated by electrospinning. The surface morphology of the g-C_3N_4 nanowires on Cu_2O films is observed to be smooth and elongated with a relatively uniform diameter of ~200 nm. The SEM images also show the presence of some agglomerated g-C_3N_4 lumps. At a short electrospinning time (30 to 60 s), the deposition of the g-C_3N_4 nanowires did not result in a homogeneous coverage of the Cu_2O surface. However, with increasing electrospinning time the coverage and thickness of the g-C_3N_4 nanowire layer increased. These samples are represented as Cu_2O/(x min) g-C_3N_4 heterojunction, where 'x' is the electrospinning time.

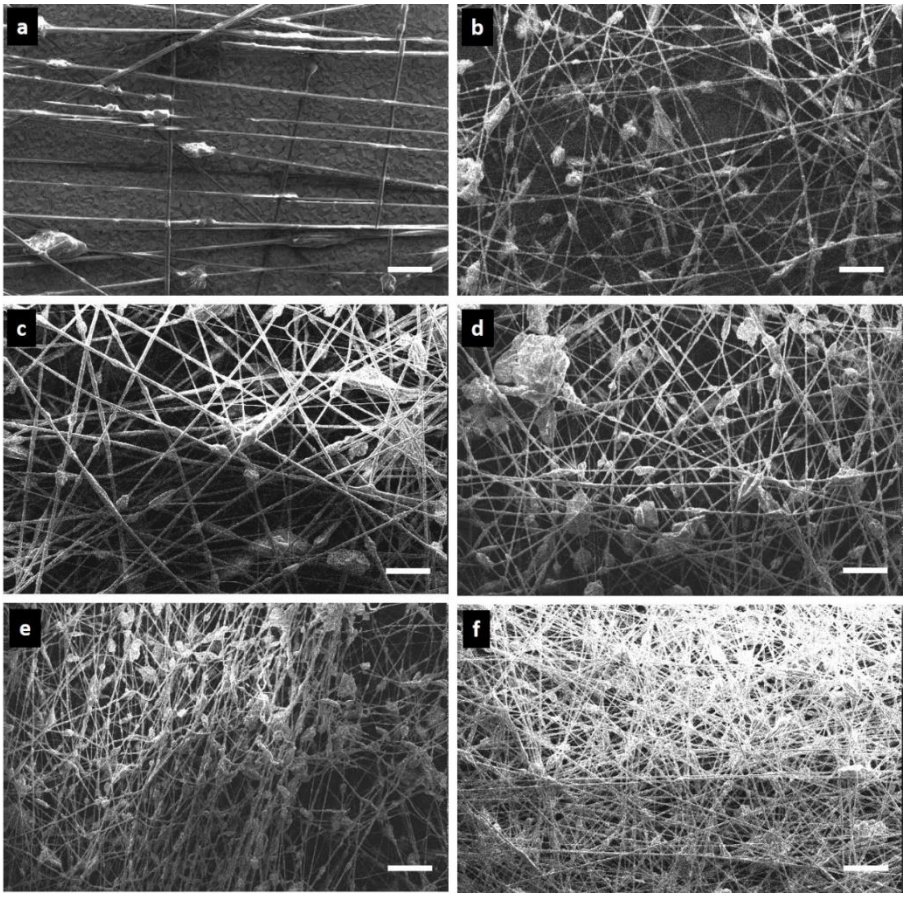

Figure 4.5 SEM images of Cu_2O/g-C_3N_4 heterojunction photocathodes with g-C_3N_4 nanowires deposited at varying electrospinning times: (a) 30 s, (b) 1 min, (c) 3 min, (d) 5 min, (e) 8 min, and (f) 12 min. Scale bars 2 µm.

4.2.4 Deposition of the CoS co-catalyst on Cu_2O/g-C_3N_4 heterojunctions

The CoS co-catalyst was deposited on the Cu_2O/g-C_3N_4 heterojunctions via electrochemical deposition similar to a procedure reported earlier.[79] Characteristic SEM and TEM images of complete multi-layered Cu_2O/g-C_3N_4/CoS heterojunction photocathodes are depicted in Figures 4.6 and 4.7 respectively. As seen in the SEM images (Figure 4.6), the CoS nanoparticles

were uniformly distributed over the whole surface of the g-C_3N_4 nanosheets and nanowires. Furthermore, the as-deposited CoS nanoparticles on the g-C_3N_4 nanowires appear less agglomerated compared to the deposition on the g-C_3N_4 nanosheets, possibly because of the wrinkled structure of the nanosheets. The fine distribution of the CoS nanoparticles over the surface may be beneficial for the catalytic performance of the HER.

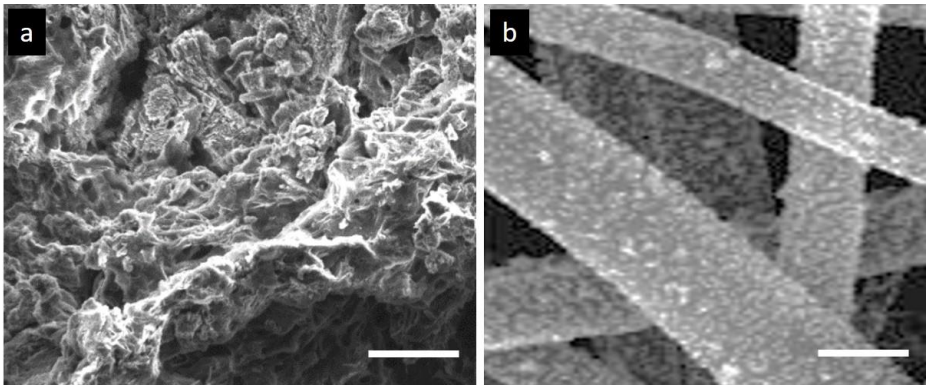

Figure 4.6 SEM images of (a) Cu_2O/5wt% g-C_3N_4 nanosheets, and (b) Cu_2O/(8 min) g-C_3N_4 nanowires decorated with CoS by electrodeposition, using 5 mM cobalt(II) chloride hexahydrate and 0.5 M thiourea by consecutive linear scans (for 15 times) from −1.2 V to 0.2 V vs Ag/AgCl, 25 mV/s. Scale bars 500 nm.

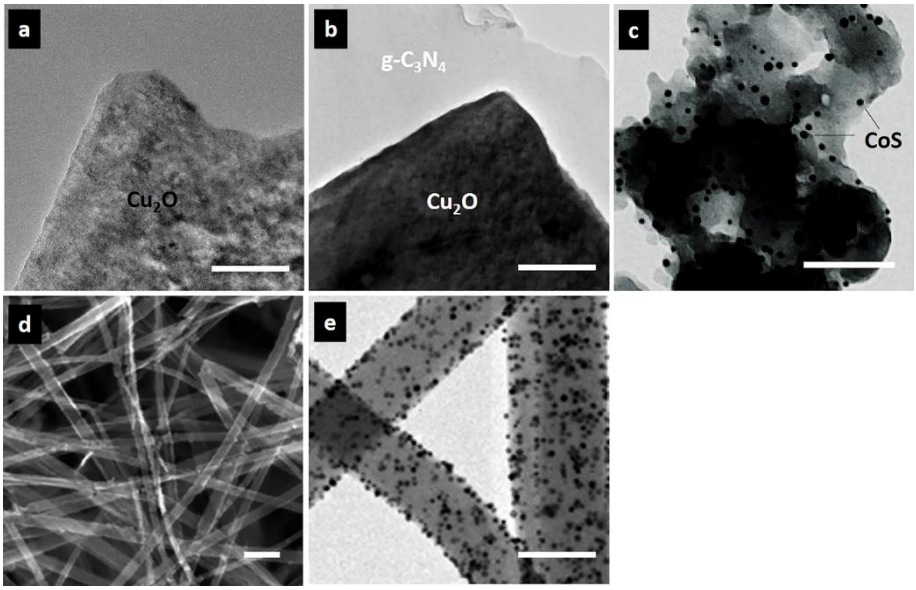

Figure 4.7 TEM images of (a) electrodeposited bare Cu_2O film, (b) Cu_2O/5 wt% C_3N_4 nanosheets, (c) Cu_2O/5 wt% C_3N_4 nanosheets decorated with CoS nanoparticles, (d) Cu_2O/(8 min) g-C_3N_4 nanowires , and (e) Cu_2O/(8 min) g-C_3N_4 nanowires decorated with CoS nanoparticles. Scale bars in a, b and c is 500 nm; in c and e 250 nm.

4.2.5. Surface characterization

Figure 4.8 shows X-ray diffraction (XRD) patterns of all three morphologies, *i.e.*, bulk, nanosheets and nanowires of g-C_3N_4. Bulk g-C_3N_4 shows a characteristic dominant interlayer-stacking diffraction peak indexed to the (002) plane at 27.7°, which corresponds to an interlayer distance of d = 0.324 nm, attributed to the stacking of the conjugated aromatic system. The diffraction intensity of the (002) peak in the exfoliated g-C_3N_4 nanosheets and nanowires is weakened and exhibits only one peak at 27.5°, which indicates that the layered structure was largely lost. From recent literature data, the results indicated a good agreement of the XRD patterns of the g-C_3N_4 bulk, nanosheets and nanowires.[80-84]

In Figure 4.8b, typical XRD patterns for Cu_2O, Cu_2O/g-C_3N_4 NSs/CoS and Cu_2O/g-C_3N_4 NWs/CoS are presented, and major diffraction peaks with 2θ values of 31.5°, 37.6°, 44°, and 63° are observed, corresponding to the (110), (111), (200), and (220) reflections for the as-deposited Cu_2O on FTO. Additionally, the main characteristic peak of the g-C_3N_4 nanosheets and nanowires at 27.5° was observed. The additional signals at 36°, 38.7°, 53.5°, and 67.4° can be assigned to the (210), (211), (311), and (201) planes of the CoS nanoparticles, in accordance with published data.[79] XRD peaks of the bare Cu_2O film on FTO substrate (Figure 4.8b) overlap with the CoS diffraction peaks at 36°, 39.6°, and 54°, which arise from the FTO substrate as reported in previous studies.[85-87] In addition, Roger *et al.*[88] showed the XRD pattern of a blank FTO substrate given for comparison showing that the majority of the FTO reflections are overlapping with the cobalt sulfide peaks.

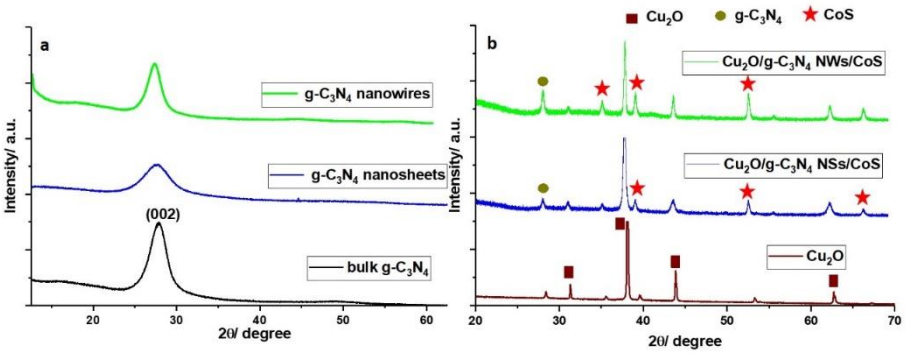

Figure 4.8 XRD patterns of as prepared (a) bulk (black line), nanosheets (blue line) and nanowires (green line) g-C_3N_4, and (b) electrodeposited bare Cu_2O film on FTO (brown), Cu_2O/5 wt% g-C_3N_4 nanosheets/CoS (blue) and Cu_2O/(8 min) g-C_3N_4 nanowires/CoS (green).

Furthermore, we have carried out X-ray photoelectron spectroscopy (XPS) experiments on a Cu_2O/g-C_3N_4 nanowires/CoS multilayer sample (Figure 4.9). The survey scan XPS spectrum of the stack reveals the expected elements, indicating the presence of C, N, Cu, Co and S (Figure 4.9a). As

shown in the high-resolution XPS spectrum of the C 1s region in Figure 4.9b, the characteristic peaks at the binding energies of 288.7 eV, 286.0 eV, and 284.8 eV are attributed to sp^2-carbon of g-C_3N_4 originating from the triazine rings (N-C=N and C-$(N)_3$) and C=C functional groups, respectively. The high-resolution XPS spectrum of the N 1s region shown in Figure 4.9c can be deconvoluted into three main peaks corresponding to the nitrogen atoms in the aromatic rings (C-N=C), tertiary nitrogen (C-$(N)_3$) and amino groups (N-H) centered at 398.7 eV, 400.2 eV, and 401.6 eV, respectively. The XPS spectrum of the Cu 2p core region is shown in Figure 4.9d. The major peaks for Cu $2p_{3/2}$ and Cu $2p_{1/2}$ for Cu(I) are located at binding energies of 932.6 eV and 952.5 eV, respectively, which are similar to the values reported for Cu_2O.[27, 89] In Figure 4.9e, two Co 2p peaks are observed at ca. 781 eV and 796.2 eV, which are attributed to Co $2p_{3/2}$ and Co $2p_{1/2}$, respectively. Similarly, in Figure 4.9f the S 2p peak at 162−163.5 eV shows the presence of sulfur in a S^{2-} oxidation state. Particularly the oxidation states of both Co and S, as evidenced by their XPS spectra, provide evidence of the composition as CoS.[79]

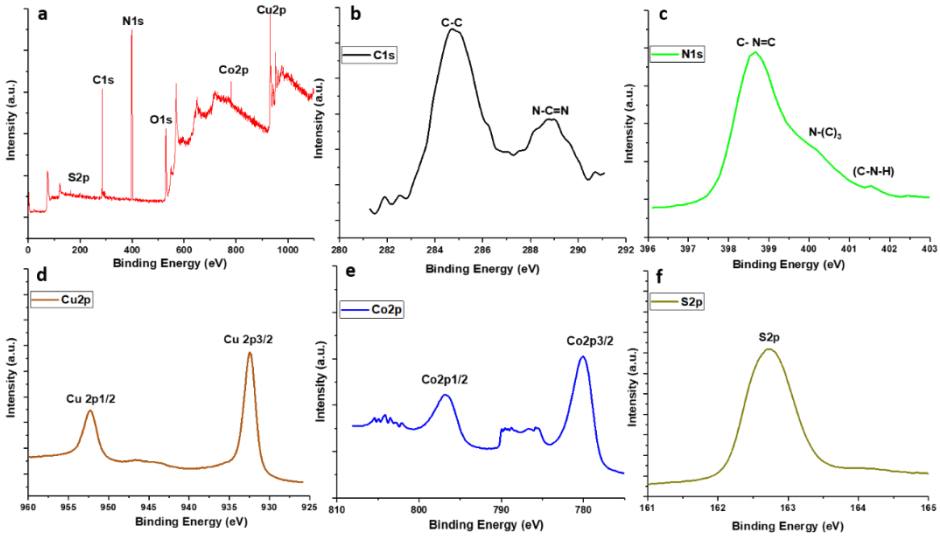

Figure 4.9 (a) XPS survey spectrum for Cu_2O/(8 min g-C_3N_4 nanowires/CoS heterojunction photocathode and (b–f) the corresponding high-resolution C1s, N1s, Cu2p, Co2p, and S2p XPS spectra.

4.2.6 Optical characterization

The UV–visible diffuse reflectance spectroscopy (UV-DRS) spectra of electrodeposited Cu_2O, as prepared g-C_3N_4 bulk (5 wt%), nanosheets (5 wt%) and nanowires (8 min) deposited on FTO substrates by spin coating and electrospinning techniques, respectively, were recorded and analyzed. The optical properties of the as-prepared photocathodes are shown in Figure 4.9a. The corresponding Kubelka-Munk plots of $(\alpha hv)^2$ *vs.* photon energy (hv) in Figure 4.9b/c were derived to estimate the band gap. The band gaps can be estimated from the intercepts of the tangents to the $(\alpha hv)^2$ vs. photon energy (hv) plots as shown in Figure 4.10b/c.

For comparison, the UV-vis diffuse reflectance spectra (DRS) of bulk g-C_3N_4, g-C_3N_4 nanowires, and g-C_3N_4 nanosheets are displayed in Figure 4.10a. The estimated band gap energies of these samples are approximately 2.62, 2.49 and 2.4 eV, respectively. The absorption edge of g-C_3N_4 occurs at around 480 nm, which is consistent with previous reports.[36-39] The band gaps of the

multilayered Cu_2O photocathodes with all different morphologies of $g\text{-}C_3N_4$, $Cu_2O/g\text{-}C_3N_4$ bulk, $Cu_2O/g\text{-}C_3N_4$ nanowires and $Cu_2O/g\text{-}C_3N_4$ nanosheets, were estimated to be 2.23, 2.35 and 2.3 eV, respectively (Figure 4.10c). The Cu_2O film as deposited shows an absorption edge at about 630 nm related to the intrinsic absorption of the Cu_2O semiconductor. Thus, all three multilayer heterostructures of $Cu_2O/g\text{-}C_3N_4$ showed a red-shift of the band edge absorption, which is attributed to the improved interaction between the individual components promoting the separation of charge carriers and electron transfer across the phase interface.

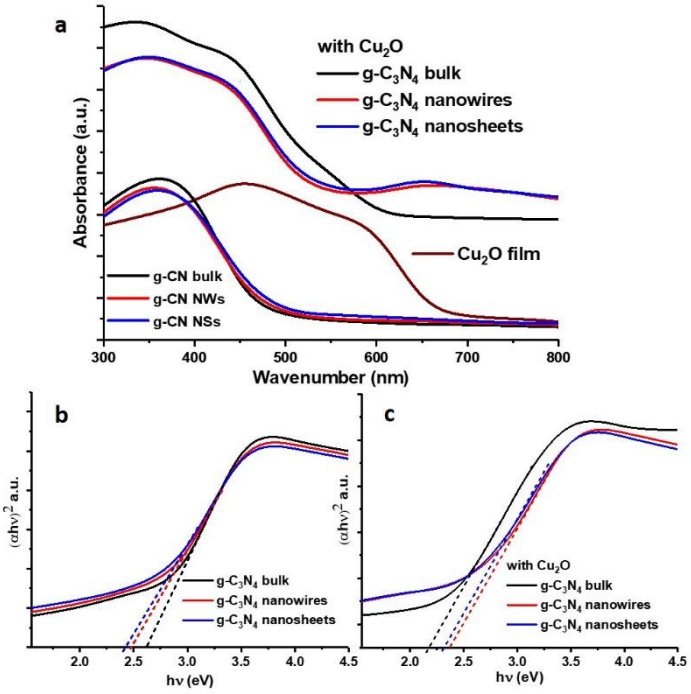

Figure 4.9 (a) UV–vis diffuse reflectance absorption spectra of bulk $g\text{-}C_3N_4$, $g\text{-}C_3N_4$ nanowires and $g\text{-}C_3N_4$ nanosheets without and with underlying Cu_2O film (in these measurements, materials were deposited on FTO substrates) and (b, c) the corresponding Kubelka-Munk plots of $(\alpha h\nu)^2$ vs. photon energy ($h\nu$).

Optical photoluminescence (PL) measurements were performed to study the separation efficiency, migration and recombination of charge carriers. The photoluminescence (PL) emission spectra of bulk g-C_3N_4, Cu_2O/bulk g-C_3N_4, Cu_2O/g-C_3N_4 nanosheets/CoS, and Cu_2O/g-C_3N_4 nanowires/CoS were assessed using an excitation wavelength of 432 nm (Figure 4.10a). A lower PL emission intensity corresponds to a lower carrier recombination rate, that is, a longer lifetime of the photogenerated charge carriers (electron-hole pairs).[90, 91] In Figure 4.11a, it can be clearly seen that the bulk g-C_3N_4 exhibits a strong PL intensity band at 468 nm and shows broad emission in the range of 451-485 nm originating from recombination sites present in the material. The PL intensity dramatically decreased upon combination with Cu_2O, as compared to bulk g-C_3N_4, indicating a higher electron transfer and lower recombination.[92] The Cu_2O/g-C_3N_4 nanosheets/CoS and Cu_2O/g-C_3N_4 nanowires/CoS displayed a further reduction of the PL peak intensity, suggesting the highest separation efficiency of electron-hole pairs. This may be attributed to a more efficient transfer of the photogenerated electrons in the conduction bands of Cu_2O and g-C_3N_4 to the CoS nanoparticles. Also, these results indicate that both the CoS nanoparticles and the g-C_3N_4 nanowires and nanosheets can promote the transport of photogenerated electrons from Cu_2O.

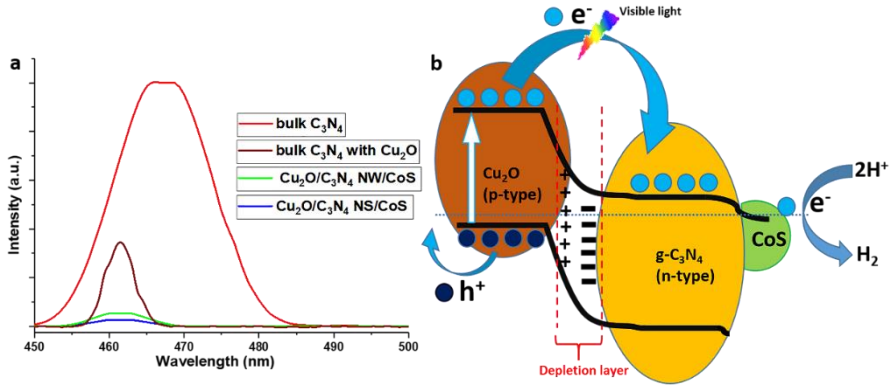

Figure 4.11 (a) Photoluminescence (PL) spectra of bulk $g\text{-}C_3N_4$, Cu_2O/bulk $g\text{-}C_3N_4$, Cu_2O/(5wt%)$g\text{-}C_3N_4$ nanosheets/CoS, and Cu_2O/(8 min)$g\text{-}C_3N_4$ nanowires/CoS multilayer photocathodes at an excitation wavelength of 325 nm. (b) Schematic of the proposed photocatalysis mechanism for HER and the transfer and separation of photo-induced charges in the fabricated CoS-decorated $Cu_2O/g\text{-}C_3N_4$ multilayered heterojunction photocathode.

Based on the above measurements, the projected photocatalysis mechanism is shown in Figure 4.11b. After the electrodeposition of CoS nanoparticles onto $Cu_2O/g\text{-}C_3N_4$, a type-II heterojunction–semiconductor stack is formed. Once the heterojunction is illuminated, photogenerated charge carriers in the conduction band of Cu_2O and can rapidly transfer onto the surface decorated with CoS nanoparticles via $g\text{-}C_3N_4$ nanosheets or nanowires. CoS nanoparticles act as electron sinks, suppress the recombination of photoinduced electrons and holes due to the Schottky barrier formation at the interface, and promote the lifetime and separation efficiency of the charge carrier pairs.[91]

4.2.7 Photoelectrical and photoelectrochemical measurements

Solar cell (photocurrent-voltage) measurements were carried out for FTO/Cu_2O photocathodes with a Cu_2O film with a thickness varying from

250-1300 nm (Figure 4.12a). As shown in Table 4.1, an electrodeposited 1000 nm thick Cu_2O film on FTO showed the highest open-circuit potential (V_{oc}) and highest short-circuit current density (J_{sc}) compared to the other Cu_2O samples with different film thicknesses. Therefore, this thickness was used for all other experiments carried out with g-C_3N_4 and CoS. The *JV* measurements were also performed for multi-layered heterojunction Cu_2O/g-C_3N_4/CoS photocathodes having 5 wt% g-C_3N_4 nanosheets and 8 min nanowires as a protection layer for Cu_2O, and the measurements are shown in Figure 4.12b. The corresponding photovoltaic parameters are summarized in Table 4.1.

From the values of the photovoltaic (PV) parameters it is evident that the addition of g-C_3N_4 overlayer to the Cu_2O boosts both the J_{SC} and V_{OC} significantly; also the *FF* values are increased. Particularly, in the case of g-C_3N_4 nanosheets, a J_{SC} of 5.4 mA/cm^2 and a V_{OC} of 0.48 V were obtained, which surpassed those of g-C_3N_4 nanowires (J_{SC}: 5 mA/cm^2, V_{OC}: 0.45 V). Likely, the effect is due to the more transparent nature of the g-C_3N_4 nanosheets compared to the nanowires. The overall significant improvement in the PV performance is attributed to the synergetic effect of the Cu_2O and g-C_3N_4 in the Cu_2O/g-C_3N_4 heterojunction. The electrons from the conduction band of Cu_2O are quickly transferred to the surface via the g-C_3N_4. The presence of both materials with intimate surface contact between them successfully promoted Z-scheme band bending, extended the charge carrier transport, and consequently suppressed the recombination process.

Additionally, electrodeposition of CoS onto the Cu_2O/g-C_3N_4 (nanosheets and nanowires) heterojunction was carried out, and PV measurements were performed on these substrates (Figure 4.12b). Although the incorporation of CoS caused a slight decrease in the V_{OC} (from 0.48 to 0.43 V for nanosheets, and from 0.45 to 0.43 V for nanowires), the J_{SC} was increased (from 5.4 to 6.0 mA/cm^2 for nanosheets and from 5.0 to 5.6 mA/cm^2 for nanowires). In this way, the Cu_2O PV performance was

significantly improved by the incorporation of a heterojunction with a co-catalyst on it.

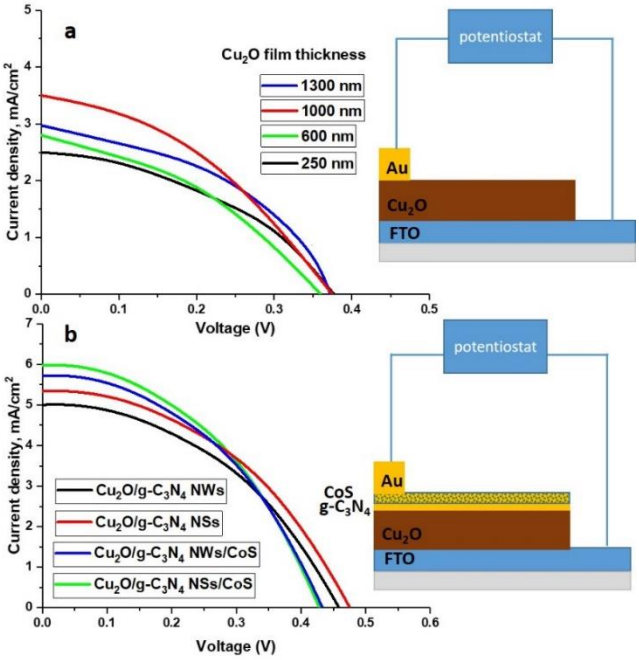

Figure 4.12 Photocurrent density-voltage (*J*–*V*) curves of the dry solar cells composed of (a) Cu_2O films with various film thicknesses and (b) $Cu_2O/g\text{-}C_3N_4$ heterojunction films, with $g\text{-}C_3N_4$ nanosheets (NSs) or nanowires (NWs), with and without CoS nanoparticles.

Table 4.1 Overview of characteristics of different Cu_2O photocathodes with various film thicknesses and Cu_2O/g-C_3N_4 heterojunction films with g-C_3N_4 nanosheets (NSs) or nanowires (NWs), with and without CoS nanoparticles.

	J_{SC} mA/cm²	V_{OC} (V)	FF (%)
Cu_2O films with different thickness (nm)			
250	2.5	0.37	28
600	2.8	0.36	26
1000	3.5	0.38	32
1300	3.0	0.37	25
Cu_2O/g-C_3N_4 heterojunction			
Cu_2O/g-C_3N_4 NSs	5.4	0.48	33
Cu_2O/g-C_3N_4 NSs/CoS	6.0	0.43	31
Cu_2O/g-C_3N_4 NWs	5.0	0.45	30
Cu_2O/g-C_3N_4 NWs/CoS	5.6	0.43	32

The spin-coating and electrospinning methods allowed us to control the loading of g-C_3N_4 nanosheets and nanowires on the Cu_2O films . In the former case, the coverage is controlled by simply varying the weight fraction of dispersed g-C_3N_4 powder in an ethanol solution used for spin-coating, in the latter case by changing the electrospinning time. The setup for assessing the photoelectrochemical (PEC) performance of the multi-layer heterojunction photocathodes is shown in Figure 4.13. Linear sweep voltammetry (LSV) was performed under simulated solar light for photocathode samples of Cu_2O/g-C_3N_4/CoS with 5wt% g-C_3N_4 nanosheets or 8 min electrospun g-C_3N_4 nanowires. During the photocurrent density-voltage (*J-E*) measurement, bubbles were found to evolve from the photocathode which is direct evidence of the HER.

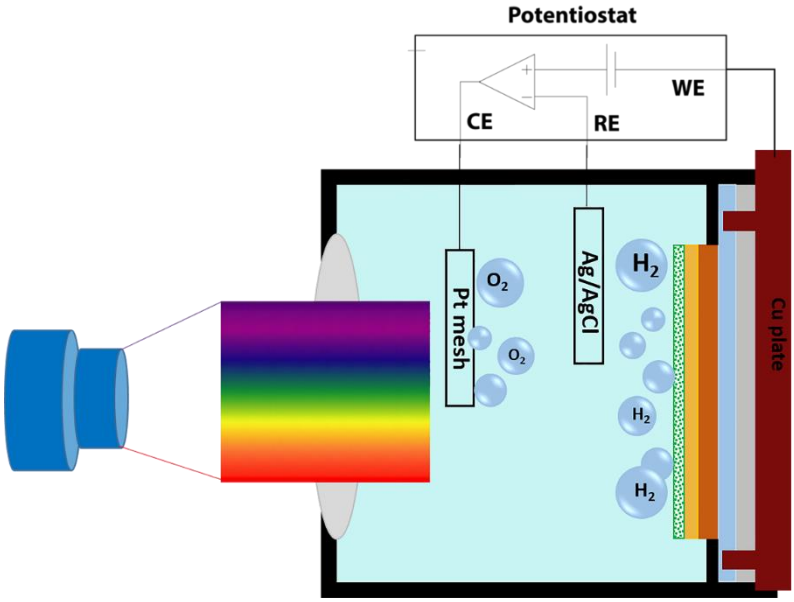

Figure 4.13 Schematic representation of the PEC measurement setup for the water splitting reaction.

At a potential of 0 V vs RHE, the $Cu_2O/g\text{-}C_3N_4/CoS$ photocathode samples showed significantly higher photocurrent densities than the bare Cu_2O films and the heterostructures without CoS co-catalyst (Figure 4.14). For lower loadings, the $g\text{-}C_3N_4$ nanosheets and nanowires layers did not sufficiently cover the Cu_2O film underneath. On the contrary, the photocatalytic activity is limited by structure defects generated during higher loadings of $g\text{-}C_3N_4$ on Cu_2O film (7 wt% in case of nanosheets and 12 min electrospun nanowires), which may serve as recombination centers for photo-generated charge-carriers.[93] The highest photocurrent density was obtained for the Cu_2O/8-min $g\text{-}C_3N_4$ nanowires/CoS photocathode (Figure 4.14).

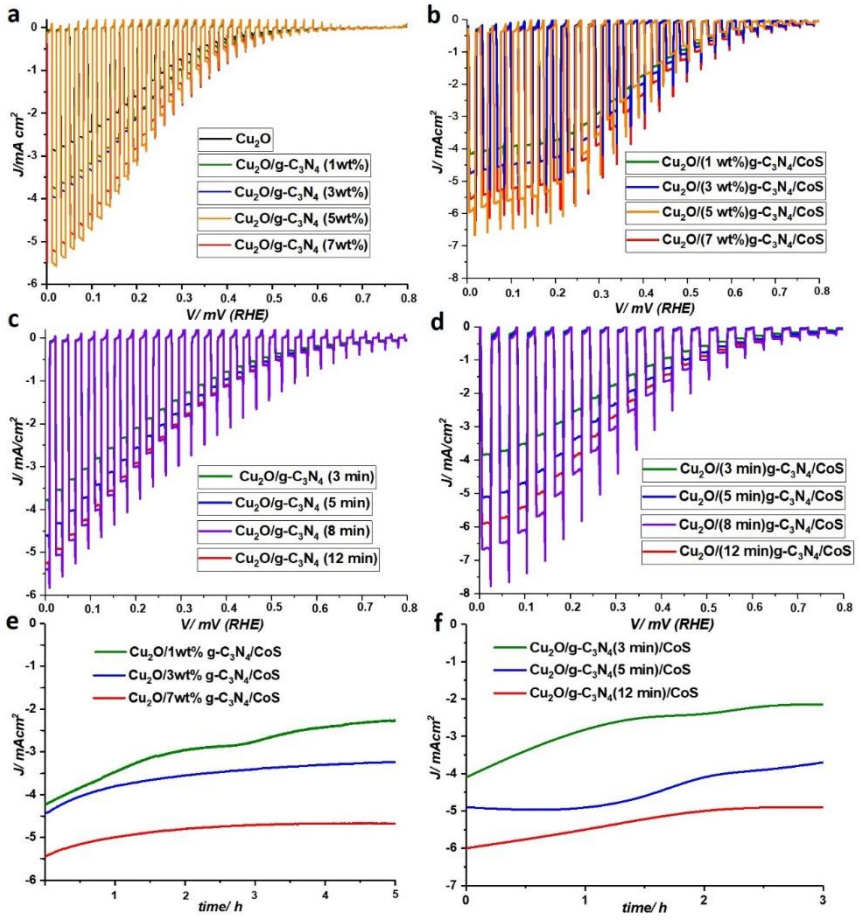

Figure 4.14 PEC (a-d) activity towards HER and (e-f) photostability performance at 0 V vs. RHE of Cu_2O/g-C_3N_4/CoS photocathodes with different loadings of nanosheets and nanowires on Cu_2O films under simulated AM 1.5G chopped illumination.

The photocurrent densities of the films which contain CoS NPs were much higher than without co-catalyst, indicating that the co-catalyst indeed enhanced the photocatalytic H_2 evolution. The heterojunction photocathodes showed excellent stability over 5 h (Figure 4.15) with a

continuous hydrogen generation. The amount of hydrogen evolved was measured over time (Figure 4.15b). The measured photocurrents for all photocathodes were used for the hydrogen evolution reaction by water splitting rather than any other unwanted side reactions. The amounts of H_2 evolved in the initial 3 h from the Cu_2O/5wt% $g\text{-}C_3N_4$ nanosheets/CoS and Cu_2O/(8 min) $g\text{-}C_3N_4$ nanowires/CoS photocathodes at 0 V vs RHE was 80 µ mol and 60 µ mol respectively. The obtained average faradaic efficiencies were nearly 80% for both photocathodes over the whole course of the reaction.

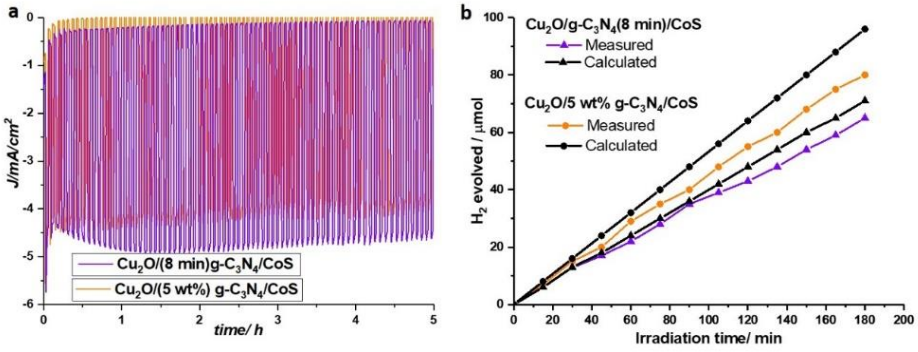

Figure 4.15 (a) PEC stability performance at 0 V vs. RHE of $Cu_2O/g\text{-}C_3N_4/CoS$ photocathode with 5wt% $g\text{-}C_3N_4$ nanosheets and 8 min electrospun nanowires on Cu_2O films and (b) corresponding theoretically calculated (black lines) and experimentally measured (orange, violet lines) H_2 evolution vs. time curves under simulated AM 1.5G chopped illumination.

The PEC performance (Figure 4.14 & 4.15) of the heterojunction photocathodes clearly exhibits the role of $g\text{-}C_3N_4$ as an effective protection layer for Cu_2O photocathodes. In addition, the enhancement of the photostability is attributed to the effect of $g\text{-}C_3N_4$ morphology, surface coverage, and loading. $g\text{-}C_3N_4$ nanosheets and nanowires passivate the Cu_2O film, encouraging the solar water reduction with efficient separation of photogenerated charge carriers. In summary, we find that the deposition

methods and morphology of g-C_3N_4 play important roles in passivation as well as obtaining higher photocurrent densities for the photocathodes.

4.3 Conclusions

In summary, the main progress in this work is the fabrication and testing of a multi-layered Cu_2O/g-C_3N_4/CoS heterojunction photocathode with improved charge transport and stability, thus achieving efficient and stable PEC hydrogen generation. The Cu_2O/(8 min)g-C_3N_4/CoS nanowire and 5 wt% nanosheets based heterojunction photocathodes reached photocurrent densities of 6.6 mA cm^2 and 5.5 mA/cm^2 at 0 V vs. RHE, respectively. Moreover, as fabricated photocathodes showed remarkably improved photostability for 5 h with faradaic efficiencies of nearly 80 % under 1 sun illumination. A photoluminescence study showed that the high PEC performance originates from enhanced charge separation and better protection. The type II or Z-scheme band structure in Cu_2O/g-C_3N_4 offers a great driving force for charge transport from the Cu_2O to g-C_3N_4. Importantly, this work provides an efficient, cost-effective and simple strategy to prepare the copper-based photocathode heterostructures used in solar water splitting devices, which is also appropriate to synthesis further photoelectrode heterostructures.

4.4 Acknowledgments

We thank Cavit Eyövge, Karin Nieuwenhuijzen and Prof. Han Gardeniers for helping with the electrospinning technique. Gerard Kip is acknowledged for XPS measurements. Rico Keim is thanked for the HR-TEM characterization. Mark Smithers is thanked for the HR-SEM images. We thank Dr. Alexander Milbrat and Prof. Guido Mul for use of the solar simulator.

4.5 Materials and methods

4.5.1 Electrodeposition of Cu_2O film

The Cu_2O films were prepared electrochemically by a time-based amperometric (i-t curve) technique.[22] In brief, the electrodeposition of Cu_2O was performed using a CHI760D electrochemical workstation using a two-electrode configuration, the FTO substrate (fluorine-doped tin oxide, Sigma-Aldrich, TEC 7, 7 Ω/sq), and a platinum mesh as a working electrode and counter electrode respectively. The deposition was conducted at -1.25 V, in a lactate-based copper electrolytic bath solution consisting of 0.2 M $CuSO_4$ (copper sulfate, Sigma-Aldrich, 99%), 3 M lactic acid ($C_3H_6O_3$, Sigma-Aldrich, 85%), and 0.5 M K_2HPO_4 buffer (dipotassium hydrogen phosphate, Merck, 99%). The pH of the electrolyte solution was adjusted to 12 by the addition of 3 M KOH solution. The thickness of the Cu_2O films was controlled by varying the deposition time (500 - 2500 s), while the temperature was kept at 35 °C using a hot water bath with an in situ temperature probe.

4.5.2 Synthesis and deposition of graphitic-C_3N_4 bulk, nanosheets and nanowires

Bulk graphitic carbon nitride (g-C_3N_4) was prepared as follows: 5 g melamine powder was placed in an alumina crucible with lid, which was put into a calcination furnace and heated to 550 °C for 4 h with a ramp of 3 °C/min under air. After natural cooling, a dark-yellow powder consisting of bulk g-C_3N_4 was obtained.

To prepare g-C_3N_4 nanosheets, the bulk g-C_3N_4 was ground into a fine powder in a mortar for further use. The bulk g-C_3N_4 was exfoliated by ultra-sonication for 6 h in an ethanol solvent.[76] After carefully collecting the top light-yellow solution to remove the un-exfoliated g-C_3N_4, the dried material was placed into an oven at 90 °C to remove excess ethanol, providing g-C_3N_4 nanosheets as a light-yellow solid material.

g-C_3N_4 nanowires were prepared by an electrospinning method.[80] g-C_3N_4 nanosheets were mixed with polyvinylpyrrolidone (PVP, avg. mol wt 40 kDa, Sigma-Aldrich) in an ethanol solvent. PVP was used as the supporting polymer to enable electrospinning of g-carbon nitride. The mixture was mixed homogeneously by sonication. Electrospinning of the suspension was carried out using an infusion syringe pump with a flat tip needle as the spinning head and a 50 kV dual polarity high-voltage power supply. The syringe pump was used to control the flow rate, whereas the high voltage supply was used to charge the needle and the collector. A 2 cm x 2 cm FTO substrate was placed on the aluminum foil which was connected to the high voltage supply for the collection of the g-C_3N_4 nanowires. Then calcination was performed at 400 °C for 4 h in Ar atmosphere.

When using Cu_2O films electrodeposited on FTO coated glass substrates, bulk g-C_3N_4 and nanosheets were deposited by spin coating of a dark-yellow bulk-g-C_3N_4 solution and ultrasonicated exfoliated g-C_3N_4-solution, respectively. The nominal weight ratios of g-C_3N_4 to Cu_2O used were 1, 3, 5 and 7 wt %. Cu_2O/g-C_3N_4 nanowires samples were fabricated by electrospinning the exfoliated g-C_3N_4-solution onto a Cu_2O film while varying the electrospinning time from 0.5 – 12 min.

4.5.3 Cobalt sulfide (CoS) co-catalyst electrodeposition

When using a Cu_2O/g-C_3N_4 heterojunction as a working electrode, CoS was deposited by electrodeposition, using a saturated Ag/AgCl reference electrode and platinum mesh as a counter electrode. The electrolyte solution contained 5 mM cobalt(II) chloride hexahydrate and 0.5 M thiourea, and was applied by consecutive (15 times) linear scans from −1.2 V to 0.2 V vs Ag/AgCl conducted at a scan rate of 5 mV/s. Thereafter, the substrate was rinsed with DI water several times and dried at 60 °C for 2 h.[79]

4.5.4 Material characterization

XRD measurements were performed on a Bruker D2 (Cu Kα source) diffractometer. UV/Vis diffuse reflectance spectra (DRS) were recorded with

a UV/Vis spectrophotometer (Thermo Scientific, Evolution 600), the reflectance data were converted to Kulbelka–Munk plots. Photoluminescence spectroscopy measurements of each samples was performed on a fluorescence spectrophotometer (Perkin Elmer) using an excitation wavelength of 325 nm. Sirion HR-SEM (FEI instruments) was used for SEM experiments. TEM imaging of the deposited photocathodes was performed using a Philips CM300ST-FEG microscope equipped with a Kevex EDX detector. The X-ray Photoelectron spectroscopy (XPS) measurements were performed on a Quantera SXM (Physical Electronics) instrument, equipped with an Al Kα X-ray source (1486.6 eV).

4.5.5 Photoelectrical (*J-V*) measurements

To measure the photoelectrical characteristics of the multilayered Cu_2O/g-C_3N_4/CoS heterostructure photocathodes, samples were positioned perpendicular to a 300 W xenon arc light source, which was filtered to modify its spectral output to AM 1.5G. Upon installation of the lamp, the lamp was calibrated by VLSI Standards Inc. Before every measurement, the lamp was checked by a calibrated Si solar cell, supplied by VLSI Standards Inc., for the spectral mismatch. *JV* measurements were performed on a VersaSTAT 4 potentiostat using a linear voltage sweep from −0.1 to 0.6 V at a scan rate of 0.1 V s^{-1}.

4.5.6 Photoelectrochemical (*J-E*) measurements

PEC measurements were recorded on a VersaSTAT 4 potentiostat using a linear voltage sweep from −0.1 to 0.6 V vs RHE at a rate of 0.2 mV s^{-1}. A three-electrode configuration was used, employing an electrolyte of an aqueous solution of 1 M Na_2SO_4 set at pH 5.5 with formic acid, a Ag/AgCl in saturated KCl as a reference electrode, a Pt mesh as a counter electrode and the prepared copper oxide photocathode as a working electrode. The potential was converted to the RHE reference electrode by the Nernst equation:

$E = E_{Ag/AgCl} + 0.059\ pH + E^{o}_{Ag/AgCl}$

Where $E^{o}_{Ag/AgCl} = 0.197$ V at 25 ^{o}C

4.5.7 Hydrogen production

The hydrogen evolution was measured using a Teflon-cell connected to a highly sensitive gas chromatograph (CompactGC Interscience). The GC was equipped with a Pulsed Discharge Detector to determine the amount H_2 in the argon carrier gas. Argon flowed with 5 ml/min through the 1 M Na_2SO_4 electrolyte consists of Ag/ AgCl in saturated KCl as a reference electrode, a Pt mesh as a counter electrode and the prepared Cu_2O/g-C_3N_4/CoS heterojunction photocathode as a working electrode.

4.6 References

1. K. Sivula and R. van de Krol, *Nat. Rev. Mater.*, 2016, **1**, 15010.
2. M. G. Walter, E. L. Warren, J. R. McKone, S. W. Boettcher, Q. Mi, E. A. Santori and N. S. Lewis, *Chem. Rev.*, 2010, **110**, 6446-6473.
3. Q. Xi, G. Gao, M. Jin, Y. Zhang, H. Zhou, C. Wu, Y. Zhao, L. Wang, P. Guo and J. Xu, *Appl Surf Sci*, 2019, **471**, 714-725.
4. Y. Yang, S. Niu, D. Han, T. Liu, G. Wang and Y. Li, *Adv. Energy Mater.*, 2017, **7**, 1700555.
5. K. Sivula, *J. Phys. Chem. Lett.*, 2013, **4**, 1624-1633.
6. K. Sivula, F. Le Formal and M. Grätzel, *ChemSusChem*, 2011, **4**, 432-449.
7. N. Wu, J. Wang, D. N. Tafen, H. Wang, J.-G. Zheng, J. P. Lewis, X. Liu, S. S. Leonard and A. Manivannan, *J. Am. Chem. Soc.*, 2010, **132**, 6679-6685.
8. A. Walsh, Y. Yan, M. N. Huda, M. M. Al-Jassim and S.-H. Wei, *Chem. Mater.*, 2009, **21**, 547-551.
9. S. Anandan, N. Ohashi and M. Miyauchi, *Appl. Catal. B Environ.*, 2010, **100**, 502-509.

10. A. Kudo and Y. Miseki, *Chem. Soc. Rev.*, 2009, **38**, 253-278.
11. J. C. Colmenares, M. A. Aramendía, A. Marinas, J. M. Marinas and F. J. Urbano, *Appl. Catal., A.*, 2006, **306**, 120-127.
12. C. G. Morales-Guio, S. D. Tilley, H. Vrubel, M. Grätzel and X. Hu, *Nat. Commun.*, 2014, **5**, 3059.
13. J. Luo, L. Steier, M.-K. Son, M. Schreier, M. T. Mayer and M. Grätzel, *Nano Lett.*, 2016, **16**, 1848-1857.
14. S. Sun, X. Zhang, Q. Yang, S. Liang, X. Zhang and Z. Yang, *Prog. Mater. Sci.*, 2018, **96**, 111-173.
15. C. Zhou, J. Cheng, K. Hou, Z. Zhu and Y. Zheng, *Chem. Eng. Sci.*, 2017, **307**, 803-811.
16. R. K. Goud, A. K. V., T. R. Reddy, B. Vinod and S. Shravani, *AIP Conf. Proc.*, 2018, **1966**, 020003.
17. X. Gou, G. Wang, J. Yang, J. Park and D. Wexler, *J. Mat. Chem.*, 2008, **18**, 965-969.
18. M. Schreier, J. Luo, P. Gao, T. Moehl, M. T. Mayer and M. Grätzel, *J. Am. Chem. Soc.*, 2016, **138**, 1938-1946.
19. A. Paracchino, V. Laporte, K. Sivula, M. Grätzel and E. Thimsen, *Nat. Mater.*, 2011, **10**, 456.
20. T. Minami, T. Miyata and Y. Nishi, *Solar Energy*, 2014, **105**, 206-217.
21. A. A. Dubale, A. G. Tamirat, H.-M. Chen, T. A. Berhe, C.-J. Pan, W.-N. Su and B.-J. Hwang, *J. Mater. Chem. A*, 2016, **4**, 2205-2216.
22. A. Paracchino, J. C. Brauer, J.-E. Moser, E. Thimsen and M. Graetzel, *J. Phys. Chem. C*, 2012, **116**, 7341-7350.
23. Z. Zhang, R. Dua, L. Zhang, H. Zhu, H. Zhang and P. Wang, *ACS Nano*, 2013, **7**, 1709-1717.
24. Y.-F. Zhao, Z.-Y. Yang, Y.-X. Zhang, L. Jing, X. Guo, Z. Ke, P. Hu, G. Wang, Y.-M. Yan and K.-N. Sun, *J. Phys. Chem. C*, 2014, **118**, 14238-14245.
25. L. Pan, J. H. Kim, M. T. Mayer, M.-K. Son, A. Ummadisingu, J. S. Lee, A. Hagfeldt, J. Luo and M. Grätzel, *Nat. Catal.*, 2018, **1**, 412-420.

26. M. Abdelfatah, J. Ledig, A. El-Shaer, A. Wagner, V. Marin-Borras, A. Sharafeev, P. Lemmens, M. M. Mosaad, A. Waag and A. Bakin, *Sol. Energy Mater. Sol. Cells*, 2016, **145**, 454-461.
27. A. A. Dubale, C.-J. Pan, A. G. Tamirat, H.-M. Chen, W.-N. Su, C.-H. Chen, J. Rick, D. W. Ayele, B. A. Aragaw, J.-F. Lee, Y.-W. Yang and B.-J. Hwang, *J. Mater. Chem. A*, 2015, **3**, 12482-12499.
28. Y. Yang, D. Xu, Q. Wu and P. Diao, *Sci. Rep.*, 2016, **6**, 35158.
29. K. P. Musselman, A. Marin, L. Schmidt-Mende and J. L. MacManus-Driscoll, *Adv. Funct. Mater.*, 2012, **22**, 2202-2208.
30. A. Martínez-García, V. K. Vendra, S. Sunkara, P. Haldankar, J. Jasinski and M. K. Sunkara, *J. Mater. Chem. A*, 2013, **1**, 15235-15241.
31. Y. J. Jang, J.-W. Jang, S. H. Choi, J. Y. Kim, J. H. Kim, D. H. Youn, W. Y. Kim, S. Han and J. Sung Lee, *Nanoscale*, 2015, **7**, 7624-7631.
32. S. D. Tilley, M. Schreier, J. Azevedo, M. Stefik and M. Graetzel, *Adv. Funct. Mater.*, 2014, **24**, 303-311.
33. W. Septina, R. R. Prabhakar, R. Wick, T. Moehl and S. D. Tilley, *Chem. Mater.*, 2017, **29**, 1735-1743.
34. J. Azevedo, L. Steier, P. Dias, M. Stefik, C. T. Sousa, J. P. Araújo, A. Mendes, M. Graetzel and S. D. Tilley, *Energy Environ. Sci.*, 2014, **7**, 4044-4052.
35. J. S. Daubert, G. T. Hill, H. N. Gotsch, A. P. Gremaud, J. S. Ovental, P. S. Williams, C. J. Oldham and G. N. Parsons, *ACS Appl. Mater. Interfaces*, 2017, **9**, 4192-4201.
36. P. Zhang, T. Wang and H. Zeng, *Appl. Surf. Sci.*, 2017, **391**, 404-414.
37. S. Liang, Y. Zhou, Z. Cai and C. She, *Appl Organomet Chem.*, 2016, **30**, 932-938.
38. S. Zuo, H. Xu, W. Liao, L. Sun, D. Han, J. Zan, B. Zhang, D. Li and D. Xia, *Appl Organomet Chem.*, 2018, **32**, e4448.
39. Y. Tian, B. Chang, J. Fu, B. Zhou, J. Liu, F. Xi and X. Dong, *J. Solid State Chem.*, 2014, **212**, 1-6.
40. X. Ma, J. Zhang, B. Wang, Q. Li and S. Chu, *Appl. Surf. Sci.*, 2018, **427**, 907-916.

41. K. Jayaramulu, T. Toyao, V. Ranc, C. Rösler, M. Petr, R. Zboril, Y. Horiuchi, M. Matsuoka and R. A. Fischer, *J. Mater. Chem. A*, 2016, **4**, 18037-18042.
42. T. Aditya, J. Jana, A. Pal and T. Pal, *ACS Omega*, 2018, **3**, 9318-9332.
43. Z. Lan-Rong, H. Gui-Fang, L. Dong-Feng, T. Qing-Nan, Y. Ke, S. Yuan, C. Shengli, Z. Xue-Ao and H. Wei-Qing, *J. Phys. D*, 2017, **50**, 355501.
44. U. Shaislamov and H.-J. Lee, *J. Korean Phys. Soc.*, 2016, **69**, 1242-1246.
45. G. Dong, Y. Zhang, Q. Pan and J. Qiu, *J. Photochem. Photobiol*, 2014, **20**, 33-50.
46. A. Wang, C. Wang, L. Fu, W. Wong-Ng and Y. Lan, *Nano-micro lett.*, 2017, **9**, 47.
47. F. Goettmann, A. Fischer, M. Antonietti and A. Thomas, *Angew. Chem.*, 2006, **45**, 4467-4471.
48. Y. Hou, Z. Wen, S. Cui, X. Feng and J. Chen, *Nano Lett.*, 2016, **16**, 2268-2277.
49. G. Wu, Y. Hu, Y. Liu, J. Zhao, X. Chen, V. Whoehling, C. Plesse, G. T. M. Nguyen, F. Vidal and W. Chen, *Nat. Commun.*, 2015, **6**, 7258.
50. X. Wang, K. Maeda, A. Thomas, K. Takanabe, G. Xin, J. M. Carlsson, K. Domen and M. Antonietti, *Nat. Mater.*, 2008, **8**, 76.
51. Y. Zheng, Y. Jiao, Y. Zhu, L. H. Li, Y. Han, Y. Chen, A. Du, M. Jaroniec and S. Z. Qiao, *Nat. Commun.*, 2014, **5**, 3783.
52. J. Bian, Q. Li, C. Huang, J. Li, Y. Guo, M. Zaw and R.-Q. Zhang, *Nano Energy*, 2015, **15**, 353-361.
53. K. Bhunia, M. Chandra, S. Khilari and D. Pradhan, *ACS Appl. Mater. Interfaces*, 2018, DOI: 10.1021/acsami.8b12183.
54. P. Niu, L.-C. Yin, Y.-Q. Yang, G. Liu and H.-M. Cheng, *Adv. Mater.*, 2014, **26**, 8046-8052.
55. Y. Huo, J. Zhang, K. Dai, Q. Li, J. Lv, G. Zhu and C. Liang, *Appl. Catal. B Environ.*, 2019, **241**, 528-538.
56. W.-J. Ong, L.-L. Tan, Y. H. Ng, S.-T. Yong and S.-P. Chai, *Chem. Rev.*, 2016, **116**, 7159-7329.

57. M. Gao, J. Feng, Z. Zhang, M. Gu, J. Wang, W. Zeng, Y. Lv, Y. Ren, T. Wei and Z. Fan, *ACS Appl. Nano Mater*, 2018, **1**, 6733-6741.
58. L. Lu, Z. Lv, Y. Si, M. Liu and S. Zhang, *Appl. Surf. Sci.*, 2018, **462**, 693-712.
59. P.-K. Chuang, K.-H. Wu, T.-F. Yeh and H. Teng, *ACS Sustain. Chem.*, 2016, **4**, 5989-5997.
60. H. Wang, X. Zhang, J. Xie, J. Zhang, P. Ma, B. Pan and Y. Xie, *Nanoscale*, 2015, **7**, 5152-5156.
61. S. Kumar, S. Karthikeyan and A. Lee, *Catalysts*, 2018, **8**, 74.
62. Y. You, S. Wang, K. Xiao, T. Ma, Y. Zhang and H. Huang, *ACS Sustain. Chem.*, 2018, **6**, 16219-16227.
63. W. Shan, Y. Hu, Z. Bai, M. Zheng and C. Wei, *Appl. Catal. B Environ.*, 2016, **188**, 1-12.
64. Z. Wang, J. Lv, J. Zhang, K. Dai and C. Liang, *Appl. Surf. Sci.*, 2018, **430**, 595-602.
65. J. Chen, S. Shen, P. Guo, M. Wang, P. Wu, X. Wang and L. Guo, *Appl. Catal. B Environ.*, 2014, **152-153**, 335-341.
66. A. Paracchino, N. Mathews, T. Hisatomi, M. Stefik, S. D. Tilley and M. Grätzel, *Energy Environ. Sci.*, 2012, **5**, 8673-8681.
67. C. M. McShane, W. P. Siripala and K.-S. Choi, *J. Phys. Chem. Lett.*, 2010, **1**, 2666-2670.
68. S. K. Baek, K. R. Lee and H. K. Cho, *J Nanomater.*, 2013, **2013**, 7.
69. J. Cheng, Z. Hu, Q. Li, X. Li, S. Fang, X. Wu, M. Li, Y. Ding, B. Liu, C. Yang, L. Wen, Y. Liu and K. Lv, *Appl. Catal. B Environ.*, 2019, **245**, 197-206.
70. Y. Hong, E. Liu, J. Shi, X. Lin, L. Sheng, M. Zhang, L. Wang and J. Chen, *Int. J. Hydrog. Energy*, 2019, **44**, 7194-7204.
71. C. Bai, J. Bi, J. Wu, Y. Han and X. Zhang, *New J. Chem.*, 2018, **42**, 16005-16012.
72. J. Cheng, Z. Hu, K. Lv, X. Wu, Q. Li, Y. Li, X. Li and J. Sun, *Appl. Catal. B Environ.*, 2018, **232**, 330-339.
73. J. R. Holst and E. G. Gillan, *J. Am. Chem. Soc.*, 2008, **130**, 7373-7379.

74. J. Zhang, J. Sun, K. Maeda, K. Domen, P. Liu, M. Antonietti, X. Fu and X. Wang, *Energy Environ. Sci.*, 2011, **4**, 675-678.
75. Y. Cui, J. Huang, X. Fu and X. Wang, *Catal. Sci. Technol.*, 2012, **2**, 1396-1402.
76. S. Yang, Y. Gong, J. Zhang, L. Zhan, L. Ma, Z. Fang, R. Vajtai, X. Wang and P. M. Ajayan, *Adv. Mater.*, 2013, **25**, 2452-2456.
77. S. Wojtyła, K. Szmit and T. Baran, *J Inorg Organomet Polym*, 2018, **28**, 492-499.
78. D. Liu, W. Li, L. Li, H. Ling and T. You, *J. Colloid Interface Sci.*, 2018, **529**, 337-344.
79. Y. Sun, C. Liu, D. C. Grauer, J. Yano, J. R. Long, P. Yang and C. J. Chang, *J. Am. Chem. Soc.*, 2013, **135**, 17699-17702.
80. C. Han, Y. Wang, Y. Lei, B. Wang, N. Wu, Q. Shi and Q. Li, *Nano Res.*, 2015, **8**, 1199-1209.
81. S. Gopalakrishnan, G. M. Bhalerao and K. Jeganathan, *J. Power Sources*, 2019, **413**, 293-301.
82. F. Yang, V. Kuznietsov, M. Lublow, C. Merschjann, A. Steigert, J. Klaer, A. Thomas and T. Schedel-Niedrig, *J. Mater. Chem. A*, 2013, **1**, 6407-6415.
83. B. Liu, D. Yin, F. Zhao, K. K. Khaing, T. Chen, C. Wu, L. Deng, L. Li, K. Huang and Y. Zhang, *J. Phys. Chem. C*, 2019, **123**, 4193-4203.
84. H. Wang, T. Sun, L. Chang, P. Nie, X. Zhang, C. Zhao and X. Xue, *Electrochim. Acta*, 2019, **303**, 110-117.
85. S.-H. Hsu, C.-T. Li, H.-T. Chien, R. R. Salunkhe, N. Suzuki, Y. Yamauchi, K.-C. Ho and K. C. W. Wu, *Sci. Rep.*, 2014, **4**, 6983.
86. Y. Kong, H. Sun, W. Fan, L. Wang, H. Zhao, X. Zhao and S. Yuan, *RSC Adv.*, 2017, **7**, 15201-15210.
87. P. Iyengar, C. Das and K. R. Balasubramaniam, *J. Phys. D*, 2017, **50**, 10LT01.
88. I. Roger, R. Moca, H. N. Miras, K. G. Crawford, D. A. J. Moran, A. Y. Ganin and M. D. Symes, *J. Mater. Chem. A*, 2017, **5**, 1472-1480.

89. Y. Song, D. Cho, S. Venkateswarlu and M. Yoon, *RSC Adv.*, 2017, **7**, 10592-10600.
90. R. C. Pawar, S. Kang, S. H. Ahn and C. S. Lee, *RSC Adv.*, 2015, **5**, 24281-24292.
91. M. Q. Wen, T. Xiong, Z. G. Zang, W. Wei, X. S. Tang and F. Dong, *Opt. Express*, 2016, **24**, 10205-10212.
92. D. Wu, K. Cao, F. Wang, H. Wang, Z. Gao, F. Xu, Y. Guo and K. Jiang, *Chem. Eng. Sci.*, 2015, **280**, 441-447.
93. P. Wu, J. Wang, J. Zhao, L. Guo and F. E. Osterloh, *J. Mater. Chem. A*, 2014, **2**, 20338-20344.

Chapter 5

Passivation layers on a tandem silicon-copper oxide micropillar array photocathode made by pulsed laser deposition

The concept of photoelectrochemical (PEC) tandem device configurations that combine dual semiconducting photoabsorbers, carries great potential for robust, inexpensive and efficient unassisted solar water splitting. This work demonstrates the influence of high-quality protection layers on Si-Cu_2O micropillar arrays created by pulsed laser deposition (PLD), with the goal to overcome photodegradation and achieve long-term operation. Sequentially, we assessed planar and micropillar device designs with various parameters and their influence on PEC performance for the hydrogen formation reaction. The optimal Si pillar height was found to be 20 µm, while the most optimal pitch was 12 µm. An ITO-Au (∼85 nm) transparent conductive film was applied for coupling the top photoabsorber onto the engineered light-trapping micropillars. Furthermore, on planar substrates, a Cu_2O film thickness of 600 nm and a Cu_2O/CuO heterojunction layer with a 5:1 thickness ratio between Cu_2O to CuO were found to be optimal. As a result, the planar Si/Cu_2O/CuO heterostructure showed a higher PV performance (J_{sc} = 20 mA/cm^2) compared to the planar Si/Cu_2O device. In contrast, the heterostructure did not provide an improvement for the micropillared samples, and therefore these were furtheron covered with Cu_2O only. Multifunctional overlayers of ZnO (25 nm) and TiO_2 (100 nm) were employed on Si/Cu_2O planar and micropillar arrays to provide a hole-selective passivation layer that acts against photocorrosion. A micropillar Si/ITO-Au/Cu_2O/ZnO/TiO_2/Pt stack was compared with a planar device. Under optimized conditions, the Si/Cu_2O photocathode with Pt as a HER catalyst displayed a photocurrent of 7.5 mA cm^{-2} at 0 V vs RHE and an onset potential of 0.85 V vs RHE, with a stable operation for 75 h.

5.1 Introduction

Tandem devices are investigated to provide efficient solar-driven water splitting.[1-4] In such a solar-to-fuel (S2F) device, sunlight is absorbed by a pair of semiconductor photoelectrodes to split water into hydrogen and oxygen.[5, 6] Commonly, a bias voltage is needed from an external energy source for effective overall water splitting.[7] However, a practical S2F device should be a stand-alone cell with no need for an external voltage supply.[8] In order to gain sufficient photovoltage, many researchers have used a combination of two or more semiconductors in a tandem configuration.[9-11]

H. Doscher *et al*. and Cheng *et al*. have reported that the maximum achievable solar-to-fuel efficiencies for the production of H_2 are achieved using a pair of light absorbers with bandgaps of approximately 1.8 eV and 1.0 eV.[12, 13] Copper oxides (Cu_2O and CuO) are interesting top absorber photocathode materials,[14-17] with narrow bandgap energies 2.1 eV and 1.6 eV, which allow Cu_2O and CuO to absorb a wide range of the solar spectrum.[18, 19] The combination of Cu_2O with Si, that has a bandgap of 1.1 eV is therefore a logical choice for a tandem configuration. However, the mismatch between light absorption and carrier diffusion length in copper oxides and their very low photovoltage output restricts their use as effective photocathodes for unassisted water splitting.[14, 20]

To solve the photovoltage problem, an approach is to build a photovoltaic (PV)-photoelectrochemical (PEC) tandem configuration by combining a PEC device and series-connect it with a buried-junction PV cell.[21-24] Recent development in PV applications inspired the fabrication of 3D-structured Si micropillar arrays.[25-27] A micropillar-based Si/Cu_2O tandem device design offer many advantages including (i) the series addition of the photovoltage in both components of the tandem to split water without external bias,[28, 29] (ii) orthogonal absorption of visible light and photogenerated charge carrier separation and transport,[30, 31] (iii) increased surface area for catalytic reactions, (iv) decrease in photoactive material usage relative to planar

device designs, depending on pillar pitch and diameter,[32] and opportunities to decouple light absorption and catalytic activity spatially.[25]

To consider Si and Cu_2O as effective photocathode materials in the tandem device, however, surface passivation is needed to prevent photodegradation.[15, 33] Han *et al.* presented a simple method to prepare a Cu_2O/CuO heterostructure to protect the Cu_2O photocathode from photocorrosion in the PEC water splitting reaction.[34] The as-prepared Cu_2O/CuO composite showed improved stability for the hydrogen evolution reaction by increasing the coverage of CuO on the Cu_2O film. However, CuO has limited stability in aqueous electrolytes as suggested by the Pourbaix diagram.[35] Many studies have reported CuO as a photocathode for the PEC water reduction reaction, although it is uncertain how much of the photocurrent leads to H_2 evolution.[36-38] In other studies, attempts to address this issue and to achieve long stability were focused on modifying the semiconductor surface with various n-type oxides and cocatalyst layers like n-Ga_2O_3,[39] AZO,[14] CdS,[35] NiO,[40] TiO_2,[41] ITO,[42] Pt,[43] NiSi,[26] etc. Many researchers investigated the effect of various dopants (Mg, Al, Ga, Fe, Ni)[44-49] in the electron-selective oxide layer to increase the donor density to effectively prevent any resultant charge recombination, additionally improving the photovoltage. Numerous methods have been employed for passivating semiconductor photoabsorbers each with its own advantages and limitations.[50, 51] As a result of passivation, the semiconductor can be protected from the harsh acidic/basic electrolyte environment often needed for long-term operation.

Here, we demonstrate the use of pulsed laser deposition (PLD), by which ZnO and TiO_2 overlayers can be grown directly and homogeneously on Si/Cu_2O microstructures with an accurate film thickness and composition. We report the fabrication of tandem Si/Cu_2O micropillar array devices with passivation layers of ZnO and TiO_2 with a precise thickness deposited by PLD. This study exhibits that the PLD approach can be effective and scalable for designing efficient and stable silicon-based tandem photocathodes for solar water

splitting. In addition, we explore design aspects for these micropillar-based Si/Cu_2O PEC tandem devices. Specifically, we investigate the influence of geometrical variations to a micropillar array PEC device design on light absorption and onset potential (V_{OC}). An ITO-Au (85 nm) transparent conductive film is applied for coupling the top photoabsorber on the engineered light-trapping micropillars. In addition we fabricated a Cu_2O/CuO heterojunction on Si planar and micropillar arrays to investigate the effect of the Cu_2O/CuO composite in PV and PEC performances. A micropillar Si/ITO-Au/Cu_2O/ZnO/TiO_2/Pt stack is compared with a planar device. Furthermore, we evaluate the roles of the n-ZnO (25 nm) and TiO_2 (100 nm) thin films as hole-selective and passivation layers.

5.2 Results and discussion

5.2.1 Micropillar array design and fabrication

A schematic illustration of the fabrication procedure for the conductive Si micropillar substrate is shown in Figure 5.1. The substrates with vertically ordered micropillar arrays with radial *pn*-junctions (p-type base and n^+-type emitter) are first fabricated using deep-reactive ion etching (DRIE). The diameter and pitch of the silicon micropillar arrays can be adjusted by using a specific mask in the photolithography process, followed by adjusting the height by changing the etching time in the DRIE process. After deposition of an interlayer (here ITO/Au, see below), Cu_2O can be grown on these substrates by electrodeposition.

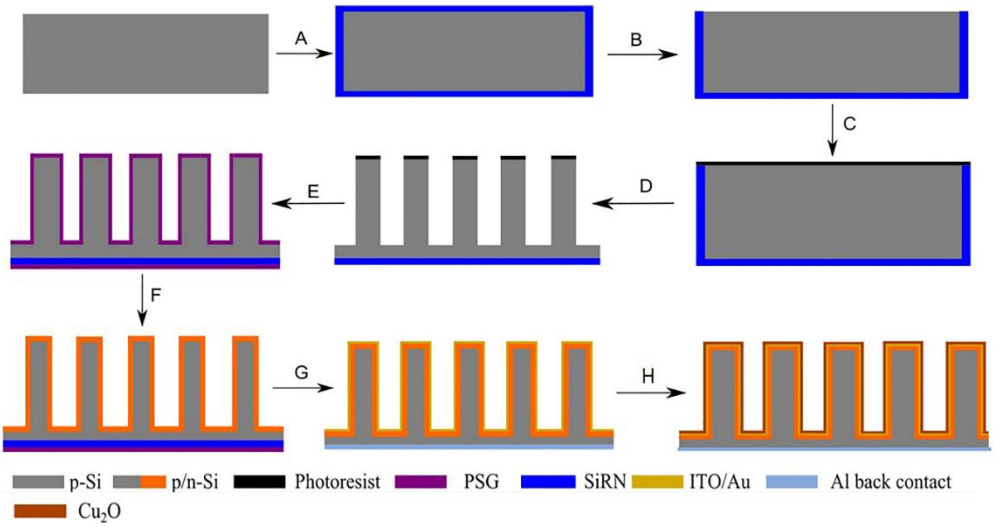

Figure 5.1 Schematic fabrication process of Si micropillar arrays with a radial junction . (A) p-type Si substrate is cleaned and covered with silicon-rich silicon nitride (SiRN), by LPCVD. (B) The SiRN on the front side is removed by reactive ion etching. (C) A photoresist polymer (Olin 906-12) is spin coated on the front side. (D) By means of standard photolithography and DRIE silicon micropillars are etched into the silicon wafer. (E) The deposition of a dopant oxide (*i.e.* phosphorus oxide) by LPCVD. (F) Formation of a radial *pn*-junction in the micropillars, by a drive-in step at 1050 °C for 15 min. (G) Deposition of a conductive seed layer for Cu_2O growth by sputtering of an ITO-Au film, followed by removal of the SiRN and deposition of Al back contacts by sputtering. (H) Cu_2O films were deposited from a lactate-stabilized copper sulfate bath kept at 50 °C in a two-electrode configuration cell at a constant potential of −0.8 V for 200-1300 s.

The light absorption ability in the micropillar structure is considerably improved not only by the increased surface area of the photoelectrode but also by the manifold light scattering within the micropillar structure (Figure 5.2).[27, 52] In a tandem device that is comprised of two photoabsorbers, the top cell is based on a large band gap (LBG) material that absorbs high energy

photons at short wavelength, and a bottom cell based on a small band gap (SBG) material that harvests low energy photons at long wavelength. It is therefore important to accurately control the top-cell bandgap and thickness, front-surface reflection, and parasitic absorption, in order to achieve high efficiency. Furthermore, the transparent conductive oxide (TCO) layer on the substrate can achieve an effective charge separation for a relatively thick film (Figure 5.2). In general, TCO–semiconductor Schottky contacts can lead to high recombination rates and therefore usually produce low V_{oc} values. However, when a PV junction is decorated with a TCO layer, high V_{oc} values can still be obtained.[53]

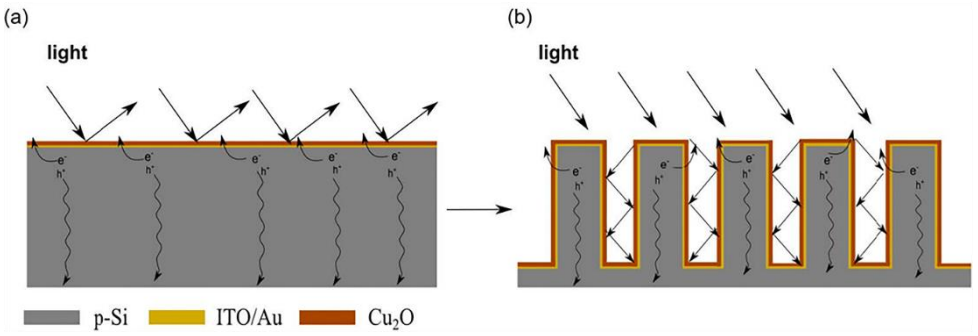

Figure 5.2 Schematic illustration of the light absorption mechanism and charge (electron-hole) separation of Cu_2O film on conductive (a) flat and (b) micropillar array substrates.

Upon following the fabrication process depicted in Figure 5.1 and after the DRIE process of the micropillars, a few samples were fractured and the side views were taken in a scanning electron microscope (Figure 5.3). The base and tip diameters of these micropillar arrays are approximately the same, indicating the highly anisotropic nature of the DRIE process. A slight tapering occurred at about ~20% from the top of the pillars. This effect was more pronounced for the 40 μm pillars (12 min etching), where the diameter decreased approximately 100-200 nm. In addition, the SEM images (Figure 5.3) show the entire side surface of the micropillars to be scalloped due to

the cyclic steps in the etching process, involving gas pulses of SF_6 (etching step) and C_4F_8 (passivation step), providing scallops with an overall height of ~340 nm, for each etching cycle.

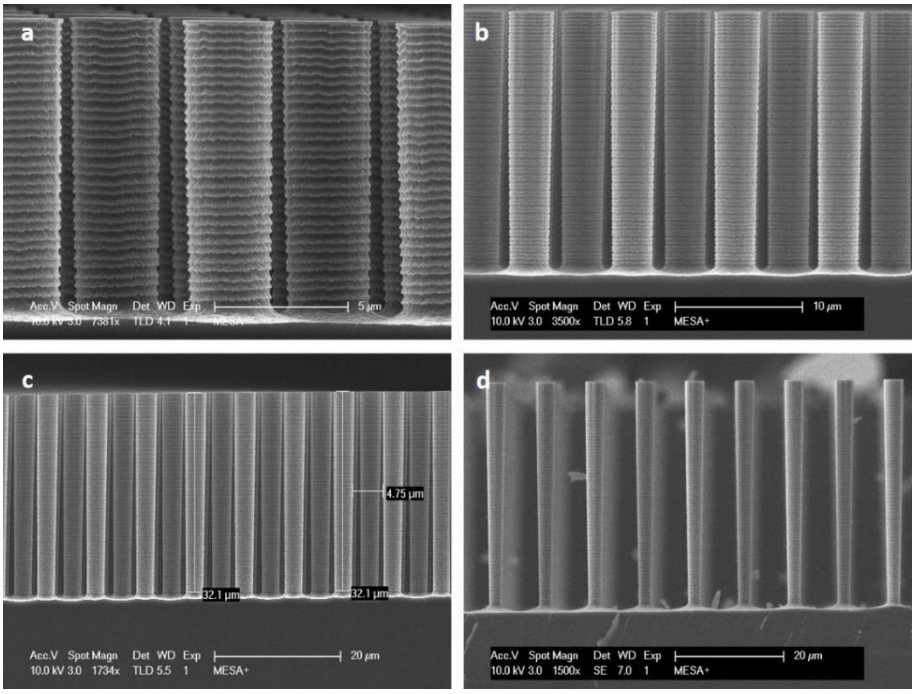

Figure 5.3 SEM images of bare Si micropillars after the DRIE process, with a different heights and pitches: (a) 10 µm, 8 µm; (b) 20 µm, 8 µm; (c) 30 µm, 8 µm; and (d) 40 µm, 10 µm, respectively.

5.2.2 Interlayer deposition

The first step to an efficient Si-Cu_2O tandem device is to find the ideal interlayer for the Cu_2O deposition on top of the Si micropillar array. Such a layer needs to be a transparent so that sunlight can pass through it and can reach the underlying Si photoabsorber. In addition, the interlayer must be conductive to provide an ohmic contact for the growth of Cu_2O film and allow charge carrier exchange between the Si and Cu_2O. Here, we

investigated different interlayers such as gold (Au), copper (Cu), molybdenum (Mo), platinum (Pt), indium tin oxide (ITO) and ITO/Au deposited using a magnetron sputtering system.

The growth of the Cu_2O film on different interlayers was characterized by scanning electron microscopy (SEM) as illustrated in Figure 5.4. By using Cu, Au and Pt interlayers, Cu_2O growth was compact and homogeneous on the Si substrate. But, due to the low conductivity of the Mo interlayer, Cu_2O grew into large cuboctahedral crystals without covering the Si surface in a conformal manner. However, none of these metallic interlayers is suited for the tandem device due to their low optical transparency. Thus, a thin layer of the conducting ITO (80 nm) with a thin layer of Au (nominally 5 nm) was deposited to enhance the conductivity without compromising in transparency. The short sputtering time, which leads to small Au nanoparticles instead of a dense homogeneous film, plays an important role in the electrodeposition of Cu_2O, leading to specifically oriented crystal growth on the substrate.[54] Furthermore, the combined ITO-Au nanoparticle film (*i.e.*, the ITO/Au layer) is sufficiently transparent and conductive to deposit Cu_2O effectively.[55, 56]

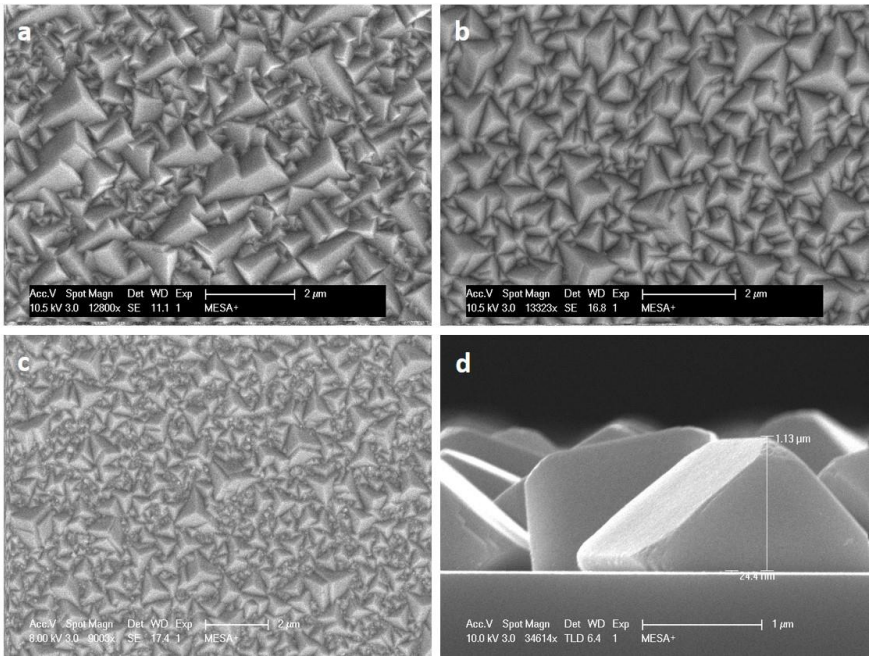

Figure 5.4 SEM images of a top view (a-c) and cross-section view (d) of the electrodeposited Cu_2O on a thin interlayer of (a) Cu, (b) Pt, (c) Au, and (d) Mo.

5.2.3 Optimization of Cu_2O film thickness

The second step is the deposition of Cu_2O on the conductive Si/ITO-Au planar and micropillar array substrates. The conformal, compact and semi-transparent Cu_2O films were prepared by chronoamperometric (CA) electrodeposition. To obtain a high-performance Cu_2O film, we deposited the material with different thicknesses (250-1300 nm) by changing the electrodeposition time (200-1300 s) at a constant cathodic potential (-0.8 V), and the temperature of the bath was maintained at 50 °C. It is important to notice that we did not elongate the deposition process for micropillar arrays with different lengths (10-40 µm) and for different pitches (8-14 µm) see Figure 5.5 to 5.7, due to the fact that the fastest growth kinetics is reached at the applied potential and temperature of the bath solution.[57-59]

Since the ITO-Au interlayer is conducting, and the system is mass transport-limited during the electrodeposition, a conformal layer of Cu_2O is deposited on the micropillars. It is observed that Cu_2O forms columnar crystals in a uniform manner on Si/ITO-Au planar substrates (Figure 5.6) and at the bottom side of the Si/ITO-Au micropillar array substrates (Figure 5.7) as well as in the sidewall scalloped area. This occurs despite the fact that the ITO/Au interlayer is thinner on the scalloped sides of the micropillars when compared to the bottom side of the Si substrate. This occurs due to the scallops causing a shadowing effect during the interlayer deposition by the directional magnetron sputtering process.

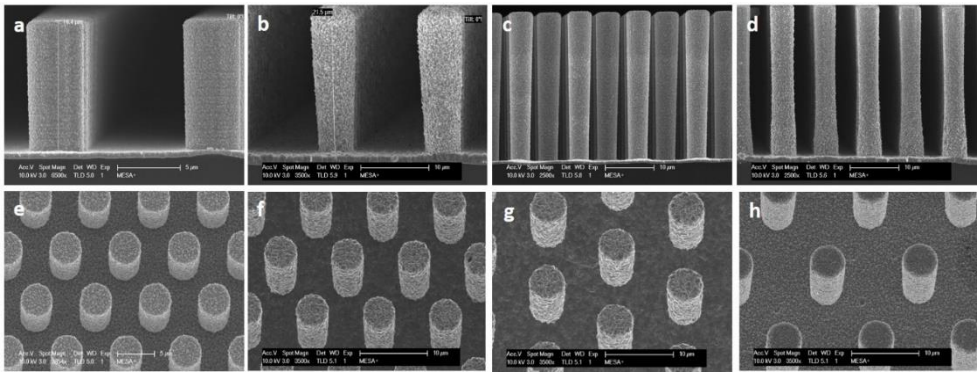

Figure 5.5 SEM images of *pn*-Si/ITO-Au/Cu_2O micropillar arrays with different heights and pitches: (a) 10 µm, 12 µm; (b) 20 µm, 14 µm; (c) 30 µm, 10 µm; (d) 40 µm, 12 µm; (e) 20 µm, 8 µm; (f) 20 µm, 10 µm; (g) 20 µm, 12 µm; and (h) 20 µm, 14 µm, respectively.

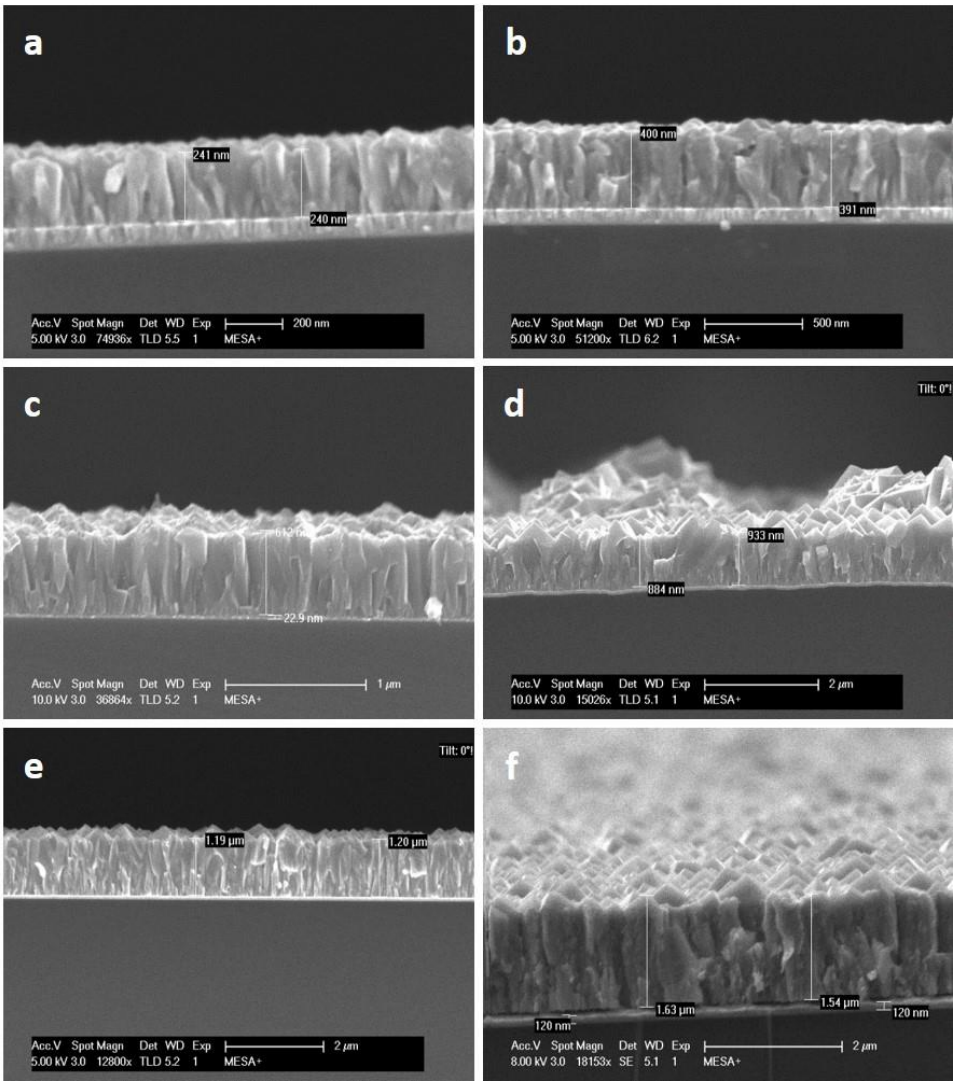

Figure 5.6 SEM images of *pn*-Si/ITO-Au/Cu_2O planar structures covered with Cu_2O films with different thicknesses: (a) 250 nm, (b) 400 nm, (c) 600 nm, (d) 900 nm, (e) 1100 nm, (f) 1500 nm, after deposition times of 200 s, 450 s, 700 s, 900 s, 1100 s, and 1300 s, respectively.

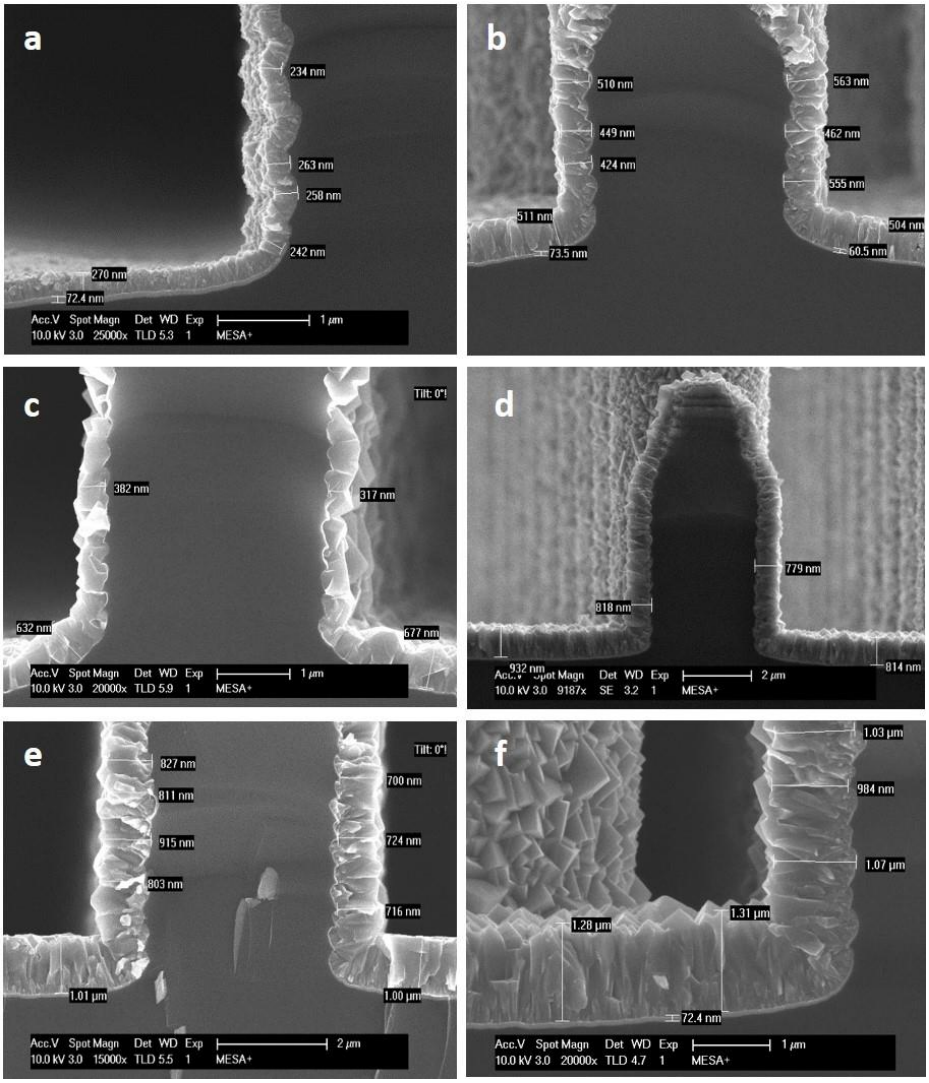

Figure 5.7 SEM images of *pn*-Si/ITO-Au/Cu_2O micropillar arrays (20 µm height and 12 µm pitch) covered with Cu_2O films of different thicknesses: (a) 250 nm, (b) 400 nm, (c) 600 nm, (d) 900 nm, (e) 1000 nm, (f) 1300 nm, after deposition times of 200 s, 450 s, 700s, 900 s, 1100 s, and 1300 s, respectively.

The SEM images (Figure 5.7) and X-ray diffraction (XRD) (Figure 5.8) characterization revealed that the prepared films have columnar triangular cubes or truncated cubic crystal growth with (111) orientation for shorter and longer deposition times, respectively. Paracchino *et al.* reported that the columnar film with cubes exposing the triangular (111) faces parallel to the substrate showed a higher photocurrent.[15] The crystal structure of the deposited layers was confirmed by X-ray diffraction (XRD). Figure 5.8 shows the XRD pattern of Cu_2O showing (110), (111) and (200) peaks at 30°, 36.9°, and 42.7° respectively on p-Si/ITO/Au micropillar array. For the ITO/Au interlayer, an ITO peak was found at 31° and for the Au (200) peak was found at 38.6°. For the silicon substrate, two peaks were observed, (200) and (400) at 33.3° and 61.3°, respectively. The intensity of the ITO peak diminished with increasing Cu_2O film thickness, as well as the Au peak, which was completely covered in a broad peak of the Cu_2O with higher intensity. Finally, a Cu_2O (220) peak was found in close proximity with the p-Si (400) peak at 61.3°, upon thicker Cu_2O deposition, which occurs from the difference in the surface energy of the cubic crystal facets.

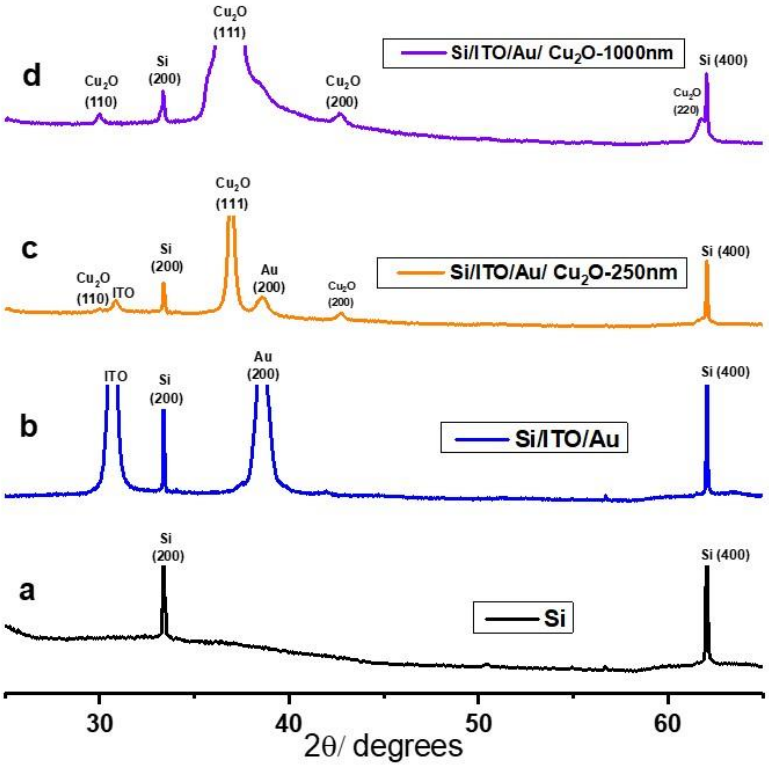

Figure 5.8 XRD patterns for (a) the Si Substrate, (b) Si/ITO-Au interlayer, (c) Si/ITO-Au/Cu_2O (250 nm thick film) and (d) Si/ITO-Au/Cu_2O (1000 nm thick film).

5.2.4 Preparation of Cu_2O/CuO heterojunction

After the electrodeposition, the Cu_2O film was subsequently converted into a Cu_2O/CuO heterojunction film by a thermal annealing process at 350 °C in air (see also Chapter 3). To optimize the film thickness ratio between Cu_2O and CuO, we followed two different strategies. Firstly, electrodeposited Cu_2O samples were prepared with different film thicknesses by variation of the deposition time on the Si/ITO-Au substrate, followed by annealing all samples at a constant annealing time of 1 h at 400 °C. Secondly, samples

were prepared with the same initial Cu_2O thickness, followed by annealing the samples at different annealing times (0.5 - 3 h) at 400 °C.

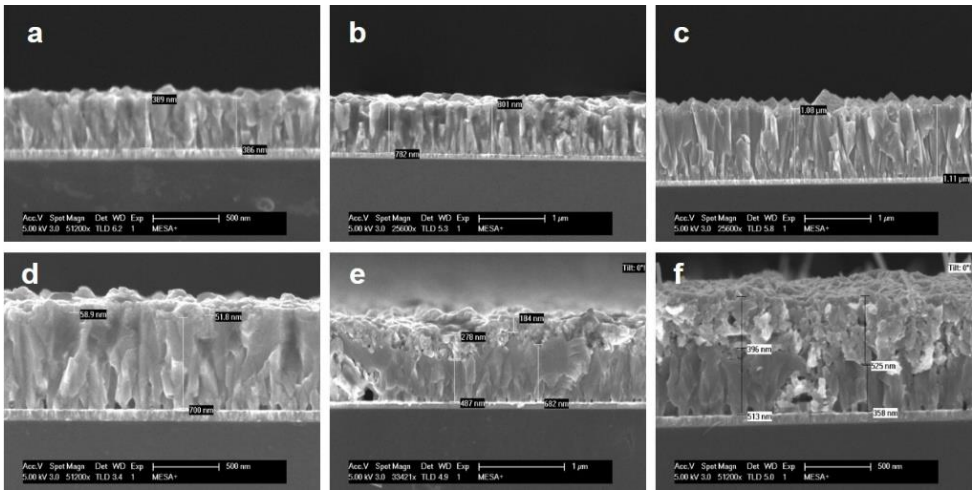

Figure 5.9 SEM images of Si/ITO-Au/Cu_2O/CuO films prepared by electrodeposition of Cu_2O at different deposition times of (a) 350 s (b) 700 s (c) 1000 s, followed by thermal oxidation for 1 h at 400 °C, or by electrodeposition of Cu_2O for 700 s, followed by thermal oxidation for (d) 0.5 h, (e) 1 h, and (f) 3 h at 400 °C.

SEM images were taken to provide the thicknesses of both copper oxides on the Si/ITO-Au substrates (Figure 5.9). The morphology of the sample changed after thermal oxidation in air, from a continuous film before thermal oxidation to a bilayer-structured film after thermal oxidation. This observation implies that the outer layer of the Cu_2O film was transformed into CuO, and a Cu_2O/CuO heterojunction was formed. When samples with a different initial thickness of Cu_2O were oxidized in air using the same annealing time (Figure 5.9a-c), the thickness of the newly formed CuO film on top of Cu_2O layer was the same. In the second case, when the thermal oxidation process time was increased from 0.5 h to 3 h (Figure 5.9d-f), the thickness of the outer CuO layer increased. As a consequence, by

consuming the Cu_2O layer underneath, the thickness of the inner Cu_2O layer was reduced. This trend is clearly indicated in Figure 5.10a. P. Diao *et al.* reported that, upon thermal oxidation in air at 400 °C for a prolonged time, the whole Cu_2O layer can be oxidized to CuO and the bilayered heterostructure will disappear, leading to a continuous porous film.[17] These results confirm that the Cu_2O to CuO thickness ratio can be controlled accurately by varying the deposition time of the initial Cu_2O film thickness and the subsequent thermal oxidation time.

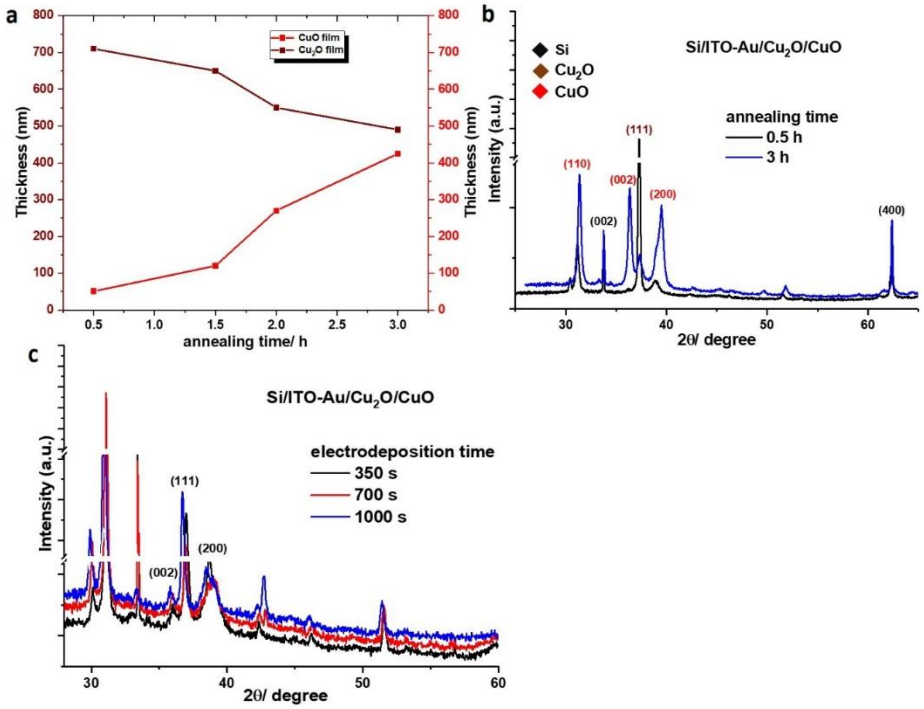

Figure 5.10 (a) Copper oxide (Cu_2O and CuO) film thicknesses as a function of annealing time. (b) XRD patterns of Si/ITO-Au/Cu_2O/CuO photocathodes after thermal oxidation at 400 °C for different annealing times. (c) XRD patterns of Si/ITO-Au/Cu_2O/CuO photocathodes at different electrodeposition times after annealing for 30 min at 400 °C.

The XRD patterns of the Cu_2O/CuO heterostructure film on Si/ITO-Au substrates in which the diffraction peaks of both cubic Cu_2O and monoclinic CuO appear (Figure 5.10b-c), provide direct evidence for the formation of the Cu_2O/CuO bilayer heterostructure. The emerging XRD diffraction peaks at 31.1°, 36.5° and 39.2° could be indexed to the (110), (002) and (200) planes of CuO, respectively. In addition, from the XRD plots at increasing annealing times (Figure 5.10b) the intensity of CuO [002] peaks increase, while the Cu_2O [111] peak intensities decrease. In contrast, when the initial Cu_2O film thickness is increased by the subsequent oxidation time is kept constant (Figure 5.10c), the spectrum hardly changes.

5.2.5 Photovoltaic (*JV*) measurements on Si micropillar arrays with a radial pn-junction

Micropillar array dimensions (height and pitch) have an influence on important functional parameters like surface area, light absorption and charge separation, which finally regulate the device efficiency. In addition, the relationships between the fabrication process and the characteristics of device performance are tough to predict. For instance, it is known that with increasing micropillar height, the total junction area in the solar cell increases and the reflectivity of sunlight probably decreases.[31, 52] The effect of micropillar dimensions (*i.e.* height and pitch) with integrating radial *pn*-junction was here investigated by examining the resulting photoelectrical performance.

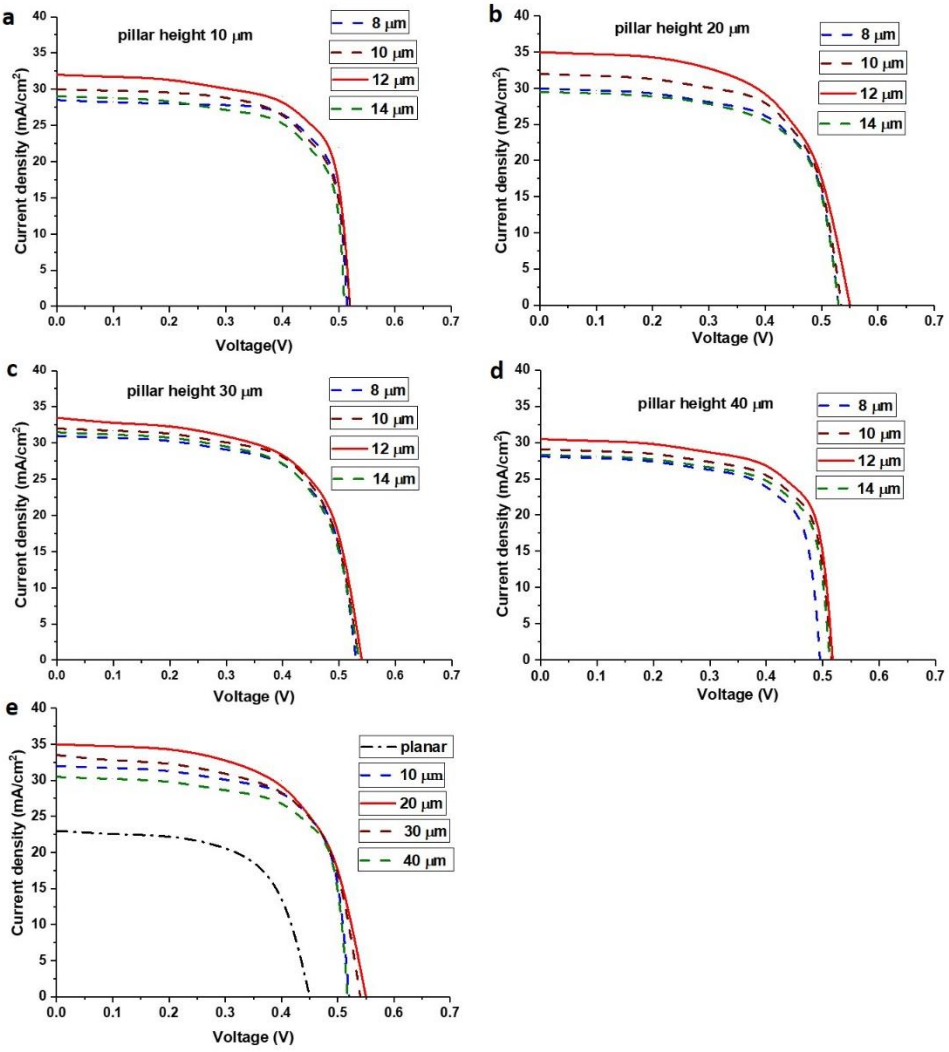

Figure 5.11 *JV* measurements of (a-d) pn-Si micropillar array substrates without Cu_2O, for varying pillar heights and pitches as indicated and (e) comparison between planar and micropillar arrays with varying pillar height and at a 12 μm pitch.

Figure 5.11 (a-d) shows the *JV* characteristics of samples with different pillar heights and pitch from 10 to 40 µm and 8 to 14 µm, respectively. Samples with pillars performed better in both current density (J_{SC}) and open circuit voltage (V_{OC}) compared to a flat sample, which indicates that the pillar structures significantly improve the properties like local surface area and light absorption properties in solar cells. The values of the fill factor (*FF*) and efficiency (η), along with their respective J_{SC} and V_{OC}, are shown in Table 5.1. A minor increase of V_{OC} is observed, from 450 mV for the flat sample to ≥ 550 mV for micropillars. The *FF* determines the maximum power point of a solar cell and can be calculated from J_{SC} and V_{OC} with equation 5.1. Using the fill factor (*FF*), short-circuit current density (J_{SC}) and open-circuit voltage (V_{OC}), the efficiency can be calculated using equation 5.2.

$$FF = \frac{J_{mp}V_{mp}}{J_{SC}V_{OC}} \qquad \text{Eq. 5.1}$$

$$\eta = \frac{V_{OC}J_{SC}}{P_{in}}FF \qquad \text{Eq. 5.2}$$

Where J_{mp} is the current density, V_{mp} is the voltage at the maximum power point and P_{in} is the input power, which is 100 mW/cm^2 (AM 1.5).

When viewing the dependence on pillar height (Figure 5.11e), J_{SC} values increase from the flat substrate up to 20 µm height, but drop again for ≥ 30 µm pillar heights. The latter decrease is due to charge carrier recombination by an increasing number of defect states with increasing micropillar height.[52, 60] Most likely, these defects have been introduced by the DRIE method used to make the pillars. The working principle of the applied Bosch process, which is an alternating process of etching (SF_6) and passivation (C_4F_8) steps, has led the scallop structures,[61] which further increases the number of defect states. We conclude that for these pillar arrays, optimal

performance is achieved with a 4 µm diameter, 12 µm pitch, and pillar height of 20 µm.

	J_{sc} (mA/cm^2)	V_{oc} (V)	FF (%)	η (%)
Planar				
	23	0.450	69	7.1
Pitch (µm)	**micropillar height 10 µm**			
8	28	0.515	72	10.4
10	30	0.512	69	10.6
12	32.4	0.520	73	12.3
14	27.8	0.508	70	9.9
micropillar height 20 µm				
8	30	0.528	71	11.2
10	32.4	0.525	68	11.5
12	35	0.550	72	13.8
14	29	0.523	71	10.7
micropillar height 30 µm				
8	31	0.521	69	11.1
10	32	0.520	68	11.3
12	33.5	0.540	71	12.8
14	31.5	0.523	70	11.5
micropillar height 40 µm				
8	28	0.498	67	9.3
10	29	0.518	70	10.5
12	31.5	0.520	69	11.3
14	28.2	0.516	68	9.9

Table 5.1. *JV* characteristics for the Si micropillar arrays with radial pn-junction, as determined from the *JV* graphs shown in Figure 5.11.

5.2.6 PV performance of copper oxide-covered micropillar arrays

In a tandem device, the overall photovoltage is generated by the absorption of two photons instead of one. Each of these photons creates a pair of charge carriers (e^- and h^+) in the total photoabsorber stack. Firstly, it is important to find the proper thickness of the top photoabsorber so that part of the sunlight can pass through it and illuminate the bottom photoabsorber to get the total photovoltage. Secondly, we fabricated Si micropillar substrates with varying heights, pitches and copper oxides thicknesses to find the maximum current density output resulting from these aspects. A Cu_2O film thickness of ~650 nm appears most favorable with respect to the resulting short circuit current density (J_{sc}), as shown in Figure 5.12a. It is well-known that a thicker layer limits the charge separation efficiency and a thinner layer does not absorb all incoming light. Si micropillars covered with optimized Cu_2O film thickness of ~650 nm were fabricated with varying pillar heights, from a planar substrate to 40 µm height, and the highest J_{sc} was produced at 20 µm height (Figure 5.12b). Finally, the micropillar pitches was varied between 8 and 14 µm, and 12 µm pitch gave the highest J_{sc}, see Figure 5.12c.

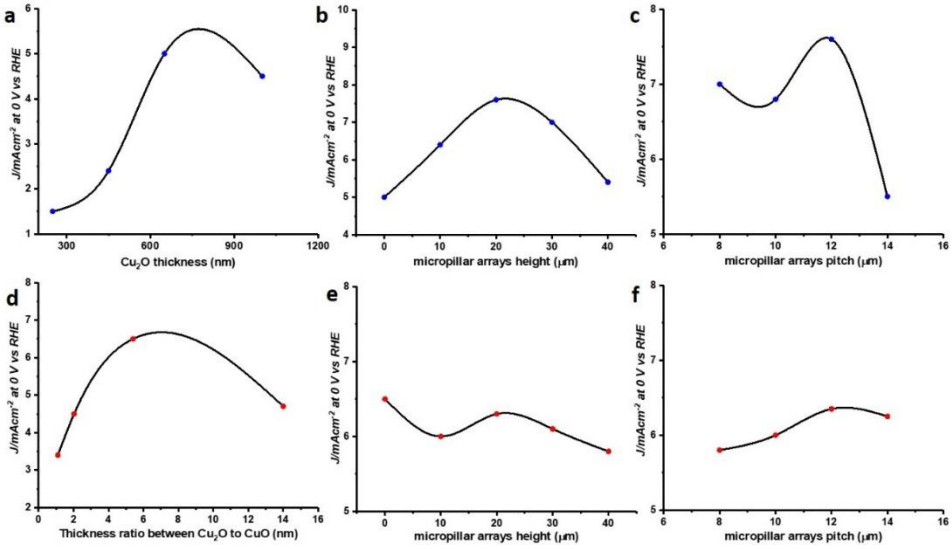

Figure 5.12 Plots of the current density as a function of different parameters of the Si/$Cu_{(x)}O$ PEC tandem samples with (a-c) Cu_2O film and (d-f) Cu_2O/CuO heterostructure film as top photoabsorbers: (a, d) varying the Cu_2O film and Cu_2O/CuO film thickness on planar substrates, (b, e) varying the micropillar height, for micropillar samples covered with a Cu_2O film (650 nm) or Cu_2O (630 nm)/CuO (120 nm) heterostructure film (with 5:1 thickness ratio between Cu_2O/CuO) at a pitch of 12 μm, and (c, f) varying the micropillar pitch, for micropillar samples covered with a Cu_2O film (650 nm) or Cu_2O (630 nm)/CuO (120 nm) heterostructure film (with 5:1 thickness ratio between Cu_2O/CuO) at a pillar height of 20 μm.

In case of Si/Cu_2O/CuO heterostructure fabrication, we deposited 650 nm thick Cu_2O on a planar substrate followed by thermal oxidation process at 400 °C while varying the annealing time as shown in Figure 5.10a. As a result, Cu_2O/CuO heterojunction layer with a different thickness ratio between Cu_2O and CuO film was formed on planar Si substrates. The highest J_{sc} output was observed for the Cu_2O (630 nm)/CuO (120 nm) heterostructure film with

thicknesses ratio 5:1 of on planar Si substrate respectively (Figure 5.12d). This is considered as an optimum Cu_2O/CuO heterostructure film for flat samples, and this was applied on Si micropillar substrates with varying micropillars height and pitch. When the optimized layer thickness of the Cu_2O/CuO heterostructure was placed on Si micropillars with varying heights and pitch, surprisingly no clear trends in the output current density were observed with respect to these parameters (Figure 5.12e/f). The observed behavior could possibly be due to parasitic resistances and optical losses, where the former occurs presumably between the copper oxides and between Cu_2O and silicon. In a comparison between the Cu_2O and Cu_2O/CuO heterojunction systems, the former all perform better at the optimized pillar parameters (Figure 5.12), while only at the low-performance sides of these parameters comparable performances are observed. Therefore, we conclude that Si micropillar arrays with a pitch of 12 µm, a height of 20 µm, and a (non-oxidized) Cu_2O layer thickness of 650 nm are optimal, and we fixed these for further study.

The *JV* curves of planar and micropillar Si substrates were measured without and with different overlayers on top (Figure 5.13). After depositing the ITO layer (~80 nm), the current density increased for both the planar and micropillar Si solar cells due to its anti-reflection property. After electrodepositing a Cu_2O film of ~650nm thickness over the Si/ITO-Au substrates, both the V_{oc} as well as the J_{sc} values dropped significantly, due to the parasitic light absorption by Cu_2O and the consequently reduced light intensity on the Si. For a planar solar cell, the J_{sc} decreased by 7 mA/cm^2 due to the Cu_2O layer, while for a Si micropillar solar cell the J_{sc} decreased with 22 mA/cm^2, making the output practically comparable. This indicates that the Cu_2O layer absorbs more sunlight when fabricated over the micropillar array.

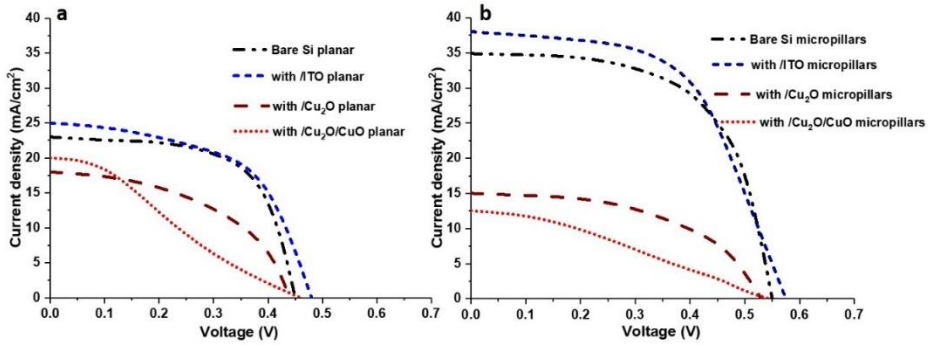

Figure 5.13 *JV* characteristics of (a) planar and (b) micropillar Si substrates covered with different overlayers; a bare substrate, with ITO, with Cu_2O and Cu_2O/CuO films over the ITO-Au layer.

Interestingly, when a Cu_2O (630 nm)/CuO(120 nm) heterojunction layer was deposited on the planar and micropillar substrates, the drop of the V_{oc} and J_{sc} values was nearly similar compared with the Cu_2O overlayer but the fill factor (*FF*) decreased considerably (Figure 5.13). The low slope close to V_{oc} in *JV* curves shows that the device behavior is dominated by a series resistance, which is attributed to a poor conductance between the top (Cu_2O/CuO) and bottom (Si) photoabsorber. Possibly, the thermal annealing process, which is carried out to prepare the Cu_2O/CuO heterojunction, leads to cracks at the Cu_2O-Si interface (see Figure 5.14).

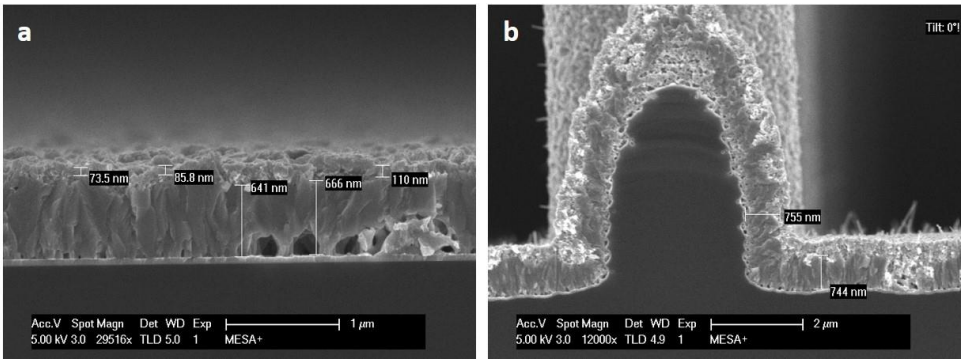

Figure 5.14 Cross-sectional SEM images of Si/ITO-Au/Cu_2O/CuO (a) planar and (b) micropillar array photocathodes.

5.2.7 Pulsed laser deposition of protection layers

For a high-performance Cu_2O-based PEC electrode, the quality of the buried p−n junction, the protection layer and the cocatalyst are the most important parameters. The p−n junction must be connecting and uniform, the protection layer must be conformal and pinhole-free, and the catalyst nanoparticle islands must be robust and adhered strongly on the electrode surface. A protection layer is needed to prevent direct contact of the Cu_2O film with the electrolyte to avoid photocorrosion, thus to maximize the performance of the device. Here, we explored the use of pulsed laser deposition (PLD) as a method to apply a conformal and high-quality protection overlayer on micropillar array structures.[62]

Previously, Luo *et al.* reported a high photocurrent density by fabricating a Cu_2O nanowire-structured photoelectrode.[63] Yet, the challenging part is to increase the photovoltage for unassisted water-splitting devices. The photovoltage is dependent on the difference between the quasi-Fermi level of the electrons in the n-type oxide layer and the holes in Cu_2O under illumination in a heterojunction device. Therefore, choosing a suitable n-type oxide layer is important for producing a high photovoltage.[39] We explored the use of zinc oxide (n-ZnO), an n-type material, combined with

titanium oxide (TiO_2) as a protective layer to improve the stability and performance of a Cu_2O-based photocathode.

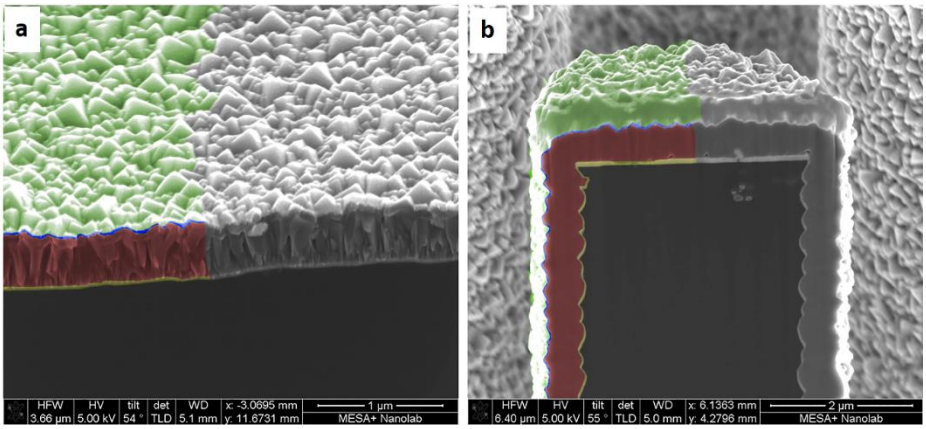

Figure 5.15 HR-SEM cross-section images of PLD-coated ZnO (20 nm) and TiO_2 (100 nm) on top of the Si/ITO-Au/Cu_2O (a) planar and (b) micropillar devices. False-colored on each figures indicates conformal layers (ITO/Au layer - yellow, Cu_2O film - light red, n-ZnO- blue, and TiO_2 - green).

HR-SEM images of the electrodes after protection layer deposition of 20 nm of ZnO and 100 nm of TiO_2 are shown in Figure 5.15a/b on both planar and micropillar samples. These images clearly show the homogeneous coating of the complete stack of layers won both substrates. The difference in contrast of each layer in images shows the quality and conformity of deposition achieved by the PLD technique. The band energy-level alignment diagrams of p-Cu_2O with n-ZnO and n-TiO_2 are shown in Figure 5.16. A conduction band offset between the Cu_2O and ZnO layer is about ~1 eV which improves the separation of the quasi-Fermi levels in the two oxides under illumination to 0.45 eV in agreement with the 0.45 V positive shift of the onset potential, and hence the build-up of an extra photovoltage for hydrogen generation.[64-66]

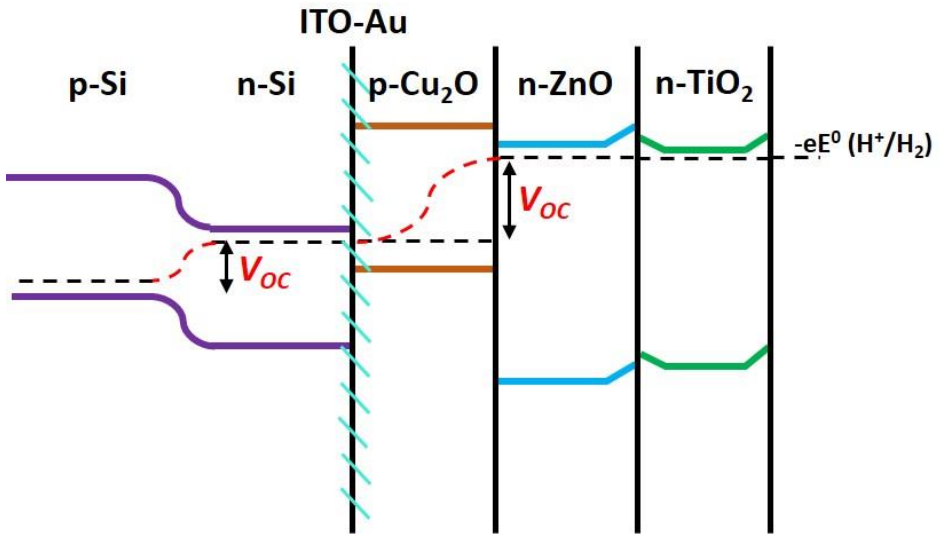

Figure 5.16 Schematic illustration of band diagrams for pn-Si/ITO-Au/Cu_2O/ZnO/TiO_2 photocathode under illumination.

5.2.8 Photoelectrochemical performance of the photocathodes

To assess the PEC performance of the devices, *JE* measurements of Cu_2O/ZnO/TiO_2/Pt on the Si/ITO-Au planar and micropillar array photocathodes were performed with the same Cu_2O film thickness of ~650 nm (see Figure 5.17). As a proof of concept, Pt was used as the HER catalyst, and it was deposited by electrochemically under dark condition using an aqueous solution of 1 mM H_2PtCl_6 for 15 min (for planar) and 19 min (for micropillars) with a thickness of nominally 3 nm using a procedure reported previously.[14] PEC measurements were performed under illumination in 0.5 M Na_2SO_4 with 0.1 M sodium phosphate buffer solution (pH 5) as electrolyte. The Cu_2O film on the planar substrate only delivered a photocurrent density of 5 mA cm^{-2} at 0 V vs RHE, which is lower than that on the micropillar substrate (7.5 mA cm^{-2}) (see Figure 5.17a). In addition, compared with the planar device, the electrode with the micropillar array showed a slightly higher anodic shift of the onset potential of +0.85 V versus RHE. It suggests

that a large proportion of photogenerated carriers effectively separate in the micropillar arrays. A stability test for planar and micropillar devices was performed for 75 h (Figure 5.17 b). The devices showed an excellent stability without degradation over time, indicating the PLD method is effective for conformal and pit-free layer deposition of ZnO and TiO_2.

To better understand the PEC performance of these photocathodes, we measured the incident-photon-to-current efficiency (IPCE) of both devices and used it to calculate the integrated photocurrent under AM 1.5 G (100 mW cm^{-2}) solar irradiation (Figure 5.17c). The overall current densities correspond well with the values of the photocurrent plotted in Figure 5.17a. The IPCE clearly shows a broad plateau response through a wider spectral range for the micropillar array compared to the planar device. The production of H_2 gas was confirmed by the formation of bubbles evolving, and measurements by gas chromatography for a micropillar photocathode biased at 0 V vs RHE displayed a faradaic efficiency close to 100 % (Figure 5.17d).

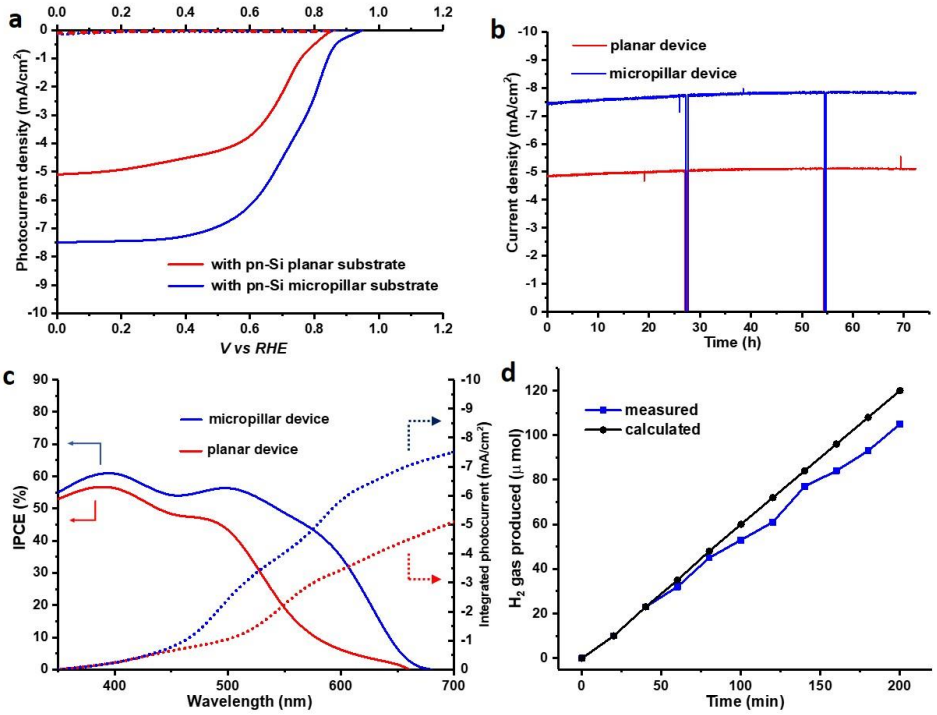

Figure 5.17 (a) PEC performance in the dark (dash lines) and under illumination (solid lines) from simulated 1 sun illumination for planar and micropillar $Cu_2O/ZnO/TiO_2/Pt$ photocathodes. (b) Current density−time behavior of pn-Si/ITO-Au/Cu_2O/ZnO/TiO_2/Pt photocathodes measured at 0 V vs RHE. Here, two "dark" periods were incorporated of each 30 min. (c) IPCE measurements of both photocathode devices at 0 V *vs.* RHE under monochromatic illumination (solid lines) and the integrated photocurrent over the solar spectrum (dotted lines). (d) Hydrogen gas produced and calculated vs time for the micropillar device.

5.3 Conclusions

In summary, we developed a highly photostable Si/Cu_2O tandem photocathode with passivating ZnO and TiO_2 overlayers directly on micropillar array devices by using the pulsed laser-deposition method. These conformal protection films grown with precise thickness formed on both planar and microstructure devices. The Cu_2O photocathode with a thickness of ~650 nm combined with Si micropillar arrays (20 µm height and 12 µm pitch) delivered a remarkable photocurrent 7.5 mA/cm^2 at 0 v vs RHE. A photovoltage of 0.85 V and stability beyond 75 h using an n-ZnO hole-selective layer, a TiO_2 protection layer, and a Pt HER catalyst. In case of Cu_2O/CuO heterostructure, an improved performance was gained for planar samples but not for a micropillared one. The high onset potential achieved in Si/Cu_2O micropillar sample is attributed to the radial buried pn-junction PV cell as the bottom photoabsorber. The ZnO layer forms a promising heterojunction with Cu_2O for a good separation of the photogenerated charge carriers in the film. As a result, high photostability is achieved by the protective layers that prevent photocorrosion of the PV-PEC tandem device. Our study presents a successful case for the use of PLD to achieve conformal coating of protective layers on high-aspect ratio micropillar arrays, which offers a new way for stable PEC water splitting devices as well as for high-efficiency solar cells.

5.4 Acknowledgements

Christos Zachariadis and Łukasz Witczak are acknowledged for assistance with fabrication and PEC measurements. Minh Nguyen (IMS) is acknowledged for PLD of ZnO and TiO_2 layers. Wouter Vijselaar is acknowledged for the discussions and his assistance with JV measurements. Henk van Wolferen is acknowledged for the FIB experiments.

5.5 Materials and methods

5.5.1 Fabrication of radial p/n-Si micropillar array

For the fabrication of radial pn-Si micropillar structure we followed a procedure as previously reported.[31] The wafers were subjected to a standard pre-furnace clean, in an RCA-2 (HCl : H_2O_2 : H_2O, 1:1:5 vol.%) solution. After a QDR cycle, the wafers were immersed (2 x 5 min) in 99% nitric acid (HNO_3), 10 min in fuming 69% nitric acid followed by a QDR cycle and 1 min immersion in hydrofluoric acid (HF) to remove any native oxide. After spin drying a 100 nm thick silicon-rich silicon nitride (SiRN) layer was deposited to prevent doping on the backside of the wafer. With reactive ion etching (RIE, Adixen AMS100DE octafluorocyclobutane (C_4F_8) and methane (CH_4)), the SiRN on the top side of the wafer was removed. Standard lithography was followed on the front side of the wafer, where a positive photoresist (OiR 906-12) was deposited by spin-coating (6000 rpm for 60 s). The exposure of the dots array pattern was done with an UV-lithography, where the wafers were aligned with the mask and exposed for 2.3 s at UV light in hard contact and vacuum mode. The mask that was used had an array of dots with a diameter of 4 μm and a pitch varying from 8-14 μm. After the development of the substrates, the micropillar array was formed by deep reactive ion etching (DRIE) (Bosch method; SPTS Pegasus), whereby the height of the pillars was defined by the number of cycles, alternated between sulfur hexafluoride (SF_6) gas for etching silicon and octafluorocyclobutane (C_4F_8) gas to create a passivation layer on the sidewalls. After DRIE, the removal of the photoresist layer and residual fluorocarbons was achieved by an oxygen plasma (TEPLA-360).

For the doping method, a phosphorus oxide layer (~ 420 nm) was grown with a PSG (TEOS) LPCVD method for 45 min, using phosphine (PH_3) as a dopant precursor, in a high-temperature oven (Tempress tube furnace). The dopant was transferred to the pillars with a thermal diffusion step by annealing in 1050 °C for 15 min. Then the wafers were immersed in a buffered aqueous hydrofluoric acid (BHF) solution to remove the silicon

oxide from the annealing step for 10 min, and then immersed for another 30 min in a 50% aqueous HF to strip the silicon nitride from the back side of the wafer. Finally, the wafers were subjected to magnetron sputtering to deposit the ITO/Au interlayer and the Al back contact.

5.5.2 Indium tin oxide-gold sputtering

Indium tin oxide (ITO) was deposited by means of an in-house built sputter device. The samples were placed on a rotating chuck (5 rpm), 44 mm from the ITO source, in a low-pressure reactor chamber (5.5×10^{-3} mbar) with a 40 sccm flow of argon. The ITO source had an angle of 45° with respect to the wafer surface. By means of a DC power of 50 W and a 20 sccm argon flow at the gun ITO was sputtered (2.6 nm/min deposition rate). Gold (Au) was deposited by means of the same in-house built sputter device. The samples were placed on a rotating chuck (5 rpm), 44 mm from the Au source, in a low-pressure reactor chamber (2×10^{-2} mbar) with a 100 sccm flow of argon. The Au source had an angle of 45° with respect to the wafer surface. By means of a DC power of 50 W and a 20 sccm argon flow at the gun Au was sputtered (15 nm/min deposition rate).

5.5.3 Electrodeposition of Cu_2O

The Cu_2O layer was electrodeposited on the prepared substrate at 50 °C from a lactate-stabilized copper sulfate solution.[15] The chemicals were used as received without further purification: $CuSO_4$ (Sigma-Aldrich, ≥99%), lactic acid (Fisher Scientific, 85%), K_2HPO_4 (Sigma-Aldrich, ≥99.5%), and KOH (Honeywell, extra pure). Briefly, an aqueous solution was prepared with an initial concentration of 0.2 M $CuSO_4$, 0.5 M K_2HPO_4, and 3 M lactic acid. The pH of the bath was adjusted to 12 by adding a 3 M potassium hydroxide solution (KOH). Cu_2O was deposited in time-based amperometric (i-t) mode using a Versastat 4 with a constant potential of −0.8 V. The thickness of the Cu_2O was also varied with the deposition time for 200-1300 s.

5.5.4 Preparation of Cu_2O/CuO heterojunction

The Cu_2O/CuO heterojunction was prepared by thermal oxidation of the Cu_2O film in air at 400 °C for different annealing times. The thickness ratio between Cu_2O and CuO layers can be controlled by varying the total deposition time for Cu_2O from 200 s to 1500 s and keeping annealing time constant (for 1 h, at 400 C) or, alternatively, by keeping the initial Cu_2O film thickness constant (650 nm) and changing the annealing time from 0.5 to 3 h in air at 400 °C.

5.5.5 Pulse laser deposition of ZnO and TiO_2 layers

Thin film stacks of zinc oxide (ZnO) and titanium dioxide (TiO_2) were grown on planar and micropillar array substrates using pulsed laser deposition (PLD) with a KrF excimer laser source (Lambda Physik, 248 nm wavelength). The deposition conditions for the n-ZnO film included a 4 Hz laser repetition frequency, deposition times of 12 min (micropillar) and 8 min (planar) at room temperature, a fluence of 2 J/cm^2, and 0.02 mbar O_2 pressure. The deposition conditions for n-TiO_2 film deposition on top of ZnO layer included a 8 Hz laser repetition frequency, deposition time for 18 min (micropillar) and 14 min (planar) at room temperature, a fluence of 2 J/cm^2, and 0.02 mbar O_2 pressure.

5.5.6 Pt HER catalyst deposition

As reported in earlier studies, platinum nanoparticles were potentiostatically electrodeposited in the dark from a solution of 1 mM H_2PtCl_6 in deionized water at −0.1 V versus Ag/AgCl for 15 min (for planar) and 19 min (for micropillar).[14]

5.5.7 Structural and optical characterization

The morphology of the substrate as well as the thickness of the deposited films on the Si micropillars was investigated by using a high-resolution scanning electron microscope (FEI Sirion HR-SEM) with a through-the-lens detector (TLD) operated at acceleration voltages of 10 kV. The samples were

imaged both by tilting the stage at 25° top view and by cutting the samples obtaining a cross-section. Cross sections for SEM of the micropillar samples were made by focused ion beam (FIB), using a Nova 600 Dual Beam – SEM/FIB setup. A Ga^+ liquid metal ion source was used to mill away approximately half of a single pillar, along the pillar length with respect to the footprint of an array, with a beam current of 0.92 nA and a 10 kV extraction voltage. X-ray diffraction patterns were acquired with a Bruker D2 Discover diffractometer in Bragg-Brentano mode, using a Cu tube with 1.54184 Å radiation. Spectra were acquired with a 2θ = 25-65° at a scan rate of 0.03°. The SiRN thickness, as well as the SiO_2, formed after the thermal diffusion step, was measured by Ellipsometry (Woollam M-2000UI) in the range of 245-1690 nm.

5.5.8 *JV* measurements

To measure the electrical characteristics of the coated Si microwires, samples were positioned perpendicular to a light source. *JV* measurements were recorded on a VersaSTAT 4 potentiostat using a linear voltage sweep from -0.7 to 0.7 V at a rate of 0.2 V/s. The light intensity was calibrated to AM 1.5G illumination at the position of the sample. The backside p-Si base was contacted through the aluminum contact on the back.

5.5.9 PEC measurements

The coated microwire photocathodes were photoelectrochemically tested using a potentiostat (VersaSTAT 4) in a three-electrode configuration, where the microwire photocathode with an exposed projected surface area of 0.5 cm^2 acted as the working electrode (WE), a platinum wire mesh as the counter electrode (CE) and an Ag/AgCl electrode as the reference electrode (RE). For The light intensity was calibrated to AM 1.5G illumination at the position of the sample.

5.5.10 Hydrogen production

The hydrogen evolution was measured using a Teflon-cell connected to a highly sensitive gas chromatograph (CompactGC Interscience). The GC was equipped with a Pulsed Discharge Detector to determine the amount H_2 in the argon carrier gas. Argon flowed with 5 ml/min through the 1 M Na_2SO_4 electrolyte consists of Ag/ AgCl in saturated KCl as a reference electrode, a Pt mesh as a counter electrode and the prepared copper oxide photocathode as a working electrode.

5.6 References

1. S. Chu, W. Li, Y. Yan, T. Hamann, I. Shih, D. Wang and Z. Mi, *Nano Futures*, 2017, **1**.
2. J. H. Kim, D. Hansora, P. Sharma, J.-W. Jang and J. S. Lee, *Chem. Soc. Rev.*, 2019, DOI: 10.1039/C8CS00699G.
3. Y. He, T. Hamann and D. Wang, *Chem. Soc. Rev.*, 2019, DOI: 10.1039/C8CS00868J.
4. B. Y. Alfaifi, H. Ullah, S. Alfaifi, A. A. Tahir and T. K. Mallick, *Veruscript Funct. Nanomater.*, 2018, **2**, BDJOC3.
5. B. Seger, I. E. Castelli, P. C. K. Vesborg, K. W. Jacobsen, O. Hansen and I. Chorkendorff, *Energy Environ. Sci.*, 2014, **7**, 2397-2413.
6. K. Zhang, M. Ma, P. Li, D. H. Wang and J. H. Park, *Adv. Energy Mater.*, 2016, **6**, 1600602.
7. M. S. Prévot and K. Sivula, *J. Phys. Chem. C*, 2013, **117**, 17879-17893.
8. J. Brillet, J.-H. Yum, M. Cornuz, T. Hisatomi, R. Solarska, J. Augustynski, M. Graetzel and K. Sivula, *Nature Photonics*, 2012, **6**, 824.
9. Y. Qiu, W. Liu, W. Chen, W. Chen, G. Zhou, P.-C. Hsu, R. Zhang, Z. Liang, S. Fan, Y. Zhang and Y. Cui, *Sci Adv.*, 2016, **2**, e1501764.
10. A. Vilanova, T. Lopes, C. Spenke, M. Wullenkord and A. Mendes, *Energy Storage Materials*, 2018, **13**, 175-188.

11. J. H. Kim, Y. Jo, J. H. Kim, J. W. Jang, H. J. Kang, Y. H. Lee, D. S. Kim, Y. Jun and J. S. Lee, *ACS Nano*, 2015, **9**, 11820-11829.
12. H. Döscher, J. F. Geisz, T. G. Deutsch and J. A. Turner, *Energy Environ. Sci.*, 2014, **7**, 2951-2956.
13. W.-H. Cheng, M. H. Richter, M. M. May, J. Ohlmann, D. Lackner, F. Dimroth, T. Hannappel, H. A. Atwater and H.-J. Lewerenz, *ACS Energy Lett.*, 2018, **3**, 1795-1800.
14. A. Paracchino, V. Laporte, K. Sivula, M. Grätzel and E. Thimsen, *Nat. Mat.*, 2011, **10**, 456.
15. A. Paracchino, J. C. Brauer, J.-E. Moser, E. Thimsen and M. Graetzel, *J. Phys. Chem. C*, 2012, **116**, 7341-7350.
16. Z. Zhang, R. Dua, L. Zhang, H. Zhu, H. Zhang and P. Wang, *ACS Nano*, 2013, **7**, 1709-1717.
17. Y. Yang, D. Xu, Q. Wu and P. Diao, *Sci. Rep.*, 2016, **6**, 35158.
18. Q. Huang, F. Kang, H. Liu, Q. Li and X. Xiao, *J. Mater. Chem. A*, 2013, **1**, 2418-2425.
19. X. Guo, P. Diao, D. Xu, S. Huang, Y. Yang, T. Jin, Q. Wu, M. Xiang and M. Zhang, *Int. J. Hydrog. Energy*, 2014, **39**, 7686-7696.
20. P. E. de Jongh, D. Vanmaekelbergh and J. J. Kelly, *Chem. Mater.*, 1999, **11**, 3512-3517.
21. C. R. Cox, J. Z. Lee, D. G. Nocera and T. Buonassisi, *Proc. Natl. Acad. Sci.*, 2014, **111**, 14057-14061.
22. Y. Xia, X. Pu, J. Liu, J. Liang, P. Liu, X. Li and X. Yu, *J. Mater. Chem. A*, 2014, **2**, 6796-6800.
23. F. Gao, X.-J. Liu, J.-S. Zhang, M.-Z. Song and N. Li, *J. Appl. Phys.*, 2012, **111**, 084507.
24. G. Ghadimkhani, N. R. de Tacconi, W. Chanmanee, C. Janaky and K. Rajeshwar, *ChemComm*, 2013, **49**, 1297-1299.
25. W. Vijselaar, P. Westerik, J. Veerbeek, R. M. Tiggelaar, E. Berenschot, N. R. Tas, H. Gardeniers and J. Huskens, *NAT ENERGY*, 2018, **3**, 185-192.

26. W. Vijselaar, R. M. Tiggelaar, H. Gardeniers and J. Huskens, *ACS Energy Lett.*, 2018, **3**, 1086-1092.
27. R. Elbersen, W. Vijselaar, R. M. Tiggelaar, H. Gardeniers and J. Huskens, *Adv. Mater.*, 2015, **27**, 6781-6796.
28. R. E. Rocheleau and E. L. Miller, *Int. J. Hydrog. Energy*, 1997, **22**, 771-782.
29. J. R. Bolton, S. J. Strickler and J. S. Connolly, *Nature*, 1985, **316**, 495-500.
30. N. C. Strandwitz, D. B. Turner-Evans, A. C. Tamboli, C. T. Chen, H. A. Atwater and N. S. Lewis, *Adv. Energy Mater.*, 2012, **2**, 1109-1116.
31. R. Elbersen, R. M. Tiggelaar, A. Milbrat, G. Mul, H. Gardeniers and J. Huskens, *Adv. Energy Mater.*, 2015, **5**, 1401745.
32. B. M. Kayes, H. A. Atwater and N. S. Lewis, *J. Appl. Phys.*, 2005, **97**, 114302.
33. S. Oh, J. B. Kim, J. T. Song, J. Oh and S.-H. Kim, *J. Mater. Chem. A*, 2017, **5**, 3304-3310.
34. J. Han, X. Zong, X. Zhou and C. Li, *RSC Adv.*, 2015, **5**, 10790-10794.
35. W. Septina, R. R. Prabhakar, R. Wick, T. Moehl and S. D. Tilley, *Chem. Mater.*, 2017, **29**, 1735-1743.
36. A. Cots, P. Bonete and R. Gómez, *ACS Appl. Mater. Interfaces*, 2018, **10**, 26348-26356.
37. U. Shaislamov, K. Krishnamoorthy, S. J. Kim, A. Abidov, B. Allabergenov, S. Kim, S. Choi, R. Suresh, W. M. Ahmed and H.-J. Lee, *Int. J. Hydrog. Energy*, 2016, **41**, 2253-2262.
38. S. Emin, F. F. Abdi, M. Fanetti, W. Peng, W. Smith, K. Sivula, B. Dam and M. Valant, *J. Electroanal. Chem.*, 2014, **717-718**, 243-249.
39. L. Pan, J. H. Kim, M. T. Mayer, M.-K. Son, A. Ummadisingu, J. S. Lee, A. Hagfeldt, J. Luo and M. Grätzel, *Nature Catalysis*, 2018, **1**, 412-420.
40. K. Sun, F. H. Saadi, M. F. Lichterman, W. G. Hale, H.-P. Wang, X. Zhou, N. T. Plymale, S. T. Omelchenko, J.-H. He, K. M. Papadantonakis, B. S. Brunschwig and N. S. Lewis, *Proc. Natl. Acad. Sci.*, 2015, **112**, 3612.

41. Z. Xing, F. Ren, H. Wu, L. Wu, X. Wang, J. Wang, D. Wan, G. Zhang and C. Jiang, *Sci. Rep.*, 2017, **7**, 43901.
42. S. Yamane, N. Kato, S. Kojima, A. Imanishi, S. Ogawa, N. Yoshida, S. Nonomura and Y. Nakato, *J. Phys. Chem. C*, 2009, **113**, 14575-14581.
43. C. U. Maier, M. Specht and G. Bilger, *Int. J. Hydrog. Energy*, 1996, **21**, 859-864.
44. M. N. H. Mia, M. F. Pervez, M. K. Hossain, M. Reefaz Rahman, M. J. Uddin, M. A. Al Mashud, H. K. Ghosh and M. Hoq, *Results in Physics*, 2017, **7**, 2683-2691.
45. X. Yan, S. Venkataraj and A. G. Aberle, *Energy procedia*, 2013, **33**, 157-165.
46. J. H. Lim, S. M. Lee, H.-S. Kim, H. Y. Kim, J. Park, S.-B. Jung, G. C. Park, J. Kim and J. Joo, *Sci. Rep.*, 2017, **7**, 41992.
47. S. Yang, C. Ge, Z. Liu, Y. Fang, Z. Li, D. Kuang and C. Su, *RSC Adv.*, 2011, **1**, 1691-1694.
48. T. Srinivasulu, K. Saritha and K. T. R. Reddy, *Modern Electronic Materials*, 2017, **3**, 76-85.
49. S. C. Das, R. J. Green, J. Podder, T. Z. Regier, G. S. Chang and A. Moewes, *J. Phys. Chem. C*, 2013, **117**, 12745-12753.
50. L. He, W. Zhou, D. Cai, S. S. Mao, K. Sun and S. Shen, *Catal. Sci. Technol.*, 2017, **7**, 2632-2638.
51. Y. Zhao and X. Sun, *ACS Energy Lett.*, 2018, **3**, 899-914.
52. R. Elbersen, W. Vijselaar, R. M. Tiggelaar, H. Gardeniers and J. Huskens, *Adv. Energy Mater.*, 2016, **6**, 1501728.
53. S. Hu, N. S. Lewis, J. W. Ager, J. Yang, J. R. McKone and N. C. Strandwitz, *J. Phys. Chem. C*, 2015, **119**, 24201-24228.
54. P. Malinský, P. Slepička, V. Hnatowicz and V. Švorčík, *Nanoscale Res. Lett.*, 2012, **7**, 241.
55. M. Layani, A. Kamyshny and S. Magdassi, *Nanoscale*, 2014, **6**, 5581-5591.
56. Y.-W. Lee, M. S. P. Reddy, B.-M. Kim and C. Park, *Opt. Mater.*, 2018, **81**, 109-114.

57. L. W. a. M. Taob, *Electrochem. Solid-State Lett*, 2000, **10**, 248-250.
58. M. J. Siegfried and K.-S. Choi, *Angew. Chem.*, 2005, **44**, 3218-3223.
59. K.-S. Choi, *Dalton Trans.*, 2008, DOI: 10.1039/B807848C, 5432-5438.
60. L.-B. Luo, X.-B. Yang, F.-X. Liang, H. Xu, Y. Zhao, X. Xie, W.-F. Zhang and S.-T. Lee, *J. Phys. Chem. C*, 2011, **115**, 18453-18458.
61. H. V. Jansen, M. J. de Boer, S. Unnikrishnan, M. C. Louwerse and M. C. Elwenspoek, *J. Micromech. Microeng*, 2009, **19**, 033001.
62. H.-U. Krebs, M. Weisheit, J. Faupel, E. Süske, T. Scharf, C. Fuhse, M. Störmer, K. Sturm, M. Seibt, H. Kijewski, D. Nelke, E. Panchenko and M. Buback, in *Advances in Solid State Physics*, ed. B. Kramer, Springer Berlin Heidelberg, Berlin, Heidelberg, 2003, vol. 43, pp. 505-518.
63. J. Luo, L. Steier, M.-K. Son, M. Schreier, M. T. Mayer and M. Grätzel, *Nano Lett.*, 2016, **16**, 1848-1857.
64. H. Lahmar, A. Azizi, G. Schmerber and A. Dinia, *RSC Adv.*, 2016, **6**, 68663-68674.
65. C. Wang, J. Xu, S. Shi, Y. Zhang, Y. Gao, Z. Liu, X. Zhang and L. Li, *J. Phys. Chem. Solids*, 2017, **103**, 218-223.
66. S. Kim, Y. Lee, A. Gu, C. You, K. Oh, S. Lee and Y. Im, *J. Phys. Chem. C*, 2014, **118**, 7377-7385.

Chapter 6

A synergistic effect between conformal cuprous oxide and silicon microwires for efficient hydrogen-producing photocathodes

Large research efforts have been devoted to solar-to-fuel (S2F) devices for water splitting over the past several decades, especially in optimizing the current density output of earth abundant photoabsorbers. However, a single photoabsorber is not able to produce a chemical fuel at a sufficient rate, requiring the development of materials combinations for efficient tandem devices. Here, we report a Cu_2O/Ga_2O_3 heterojunction microwire photocathode with an underlying buried radial Si *pn*-junction which achieves efficient light harvesting across the whole visible spectrum to over 600 nm, reaching an external quantum yield for hydrogen generation close to 80%. With a photocurrent onset over +1.35 V *vs.* RHE, a photocurrent density of $\sim$10 mA/cm^2 at 0 V *vs.* RHE, and an ideal regenerative efficiency of 5.5%, our electrode constitutes the best oxide-based photocathode for catalytic generation of hydrogen from sunlight known today. The optimal configuration had a microwire pitch of 4 µm, a height of 10 µm, a radius of 2 µm, and a Cu_2O layer thickness of $\sim$200 nm. We deconvoluted the different contributions to the regenerative efficiency of the Si *pn*-junction and the addition of the Si microwires, and finally of the Si microwires and the radial *pn*-junction combined, all with a conformal Cu_2O layer. Lastly, we show a stable operation exceeding 200 h at an average current density of 4.5 mA/cm^2.

6.1 Introduction

Solar-to-fuel (S2F) is the concept of turning solar energy into a storable fuel in an integrated process. To fabricate a fully integrated, efficient S2F device based on photo-electricity, a single or set of semiconductors must be combined with a proper electrocatalyst. Many single semiconductors are investigated as possible candidates for a photoanode (*e.g.,* Fe_2O_3,[1-3] $BiVO_4$,[4-6] WO_3,[7,8] TiO_2,[9-11] or ZnO[12,13]) or photocathode (e.g. III-V systems, CuO,[14,15] Cu_2O,[16] Si,[17,18], or SiC[19]). However, to date not a single semiconductor produces both a high photocurrent and enough photovoltage to drive a solar fuel reaction (*e.g.*, production of hydrogen (H_2) and oxygen (O_2)) at an acceptable efficiency.

Fountaine *et al.* showed that a combination of semiconductors with bandgaps of approximately 1.8 eV and 1.0 eV would give theoretically the highest overall efficiency.[20,21,22] In an ideal case, each material creates an equal current density (*i.e.*, current matching), and an enhanced photovoltage (V_{oc}) ia achieved when the stack is in series. A possible combination of materials could be cuprous oxide (Cu_2O) in series with silicon (Si), since they have bandgaps of 2.0 and 1.1 eV, respectively. Both materials are extensively investigated as materials in photovoltaic (PV) cells,[23-28] are earth abundant, non-toxic, and are relatively cost-effective to produce. However, a directly coupled tandem cell between Si and Cu_2O has never been investigated. Furthermore, both materials have their own drawbacks, which need to be addressed to improve the overall efficiency for a possible tandem cell.

A notable feature for all of the electrodeposited Cu_2O systems, whether used as a photocathode or in a solar cell, is the poor conversion of photons with wavelengths of 500–600 nm, due to the mismatch between the absorption depth of the photons and the diffusion length of the photo-generated electrons as a result of the relatively high acceptor concentration in electrodeposited films. Luo *et al.* surpassed this problem by the

fabrication of Cu_2O nanowires, which greatly enhanced the current density up to 9 mA cm^{-2} at 0 V vs RHE.[29] Pan *et al.* improved this and reported recently the best oxide photocathode known today with a Cu_2O/Ga_2O_3 heterojunction which achieves a photocurrent onset over 1 V *vs.* RHE and a photocurrent density of $\sim$10 mA cm^{-2} at 0 V versus RHE.[30-33] The smaller energy band offset and favorable band alignment (conduction band) between the Cu_2O and Ga_2O_3 layers diminishes interfacial recombination. As a result, the energy for the splitting of the quasi-Fermi levels between the two oxides is larger, hence leading to a higher photovoltage. However, Cu_2O nanowires are grown from a thick copper (Cu) film. A residual Cu film remains after fabrication and would block the incoming light for a possible underlying second low bandgap absorber (*e.g.*, Si) which could further increase the overall voltage and therefore overall efficiency of a S2F device. Furthermore, the photovoltage ($\sim$1 V) is not enough to produce hydrogen in a stand-alone configuration. Even with state-of-the-art materials (*e.g.*, Pt as reduction and IrO_x as oxidation catalyst), the overall required voltage to split water is theoretically 1.23 V, however practically >1.4 V.

Not only a heterojunction is important for increasing the photovoltage. Paracchino *et al.* showed that passivation and catalysis of this stack are as important.[34] They investigated different passivation layer thicknesses of titanium oxide (TiO_2), and found that they could extend the stability significantly. Such a passivation layer now well understood, and stability is even further increased.[33] Furthermore, to reduce the overpotential, a stable catalyst is required. Tilley *et al*. showed that one of the best performing and, above all, stable hydrogen evolution catalyst is ruthenium oxide (RuO_x).[35] Furthermore, in order not to obstruct the light absorption of the underlying layers, nano-particles are easily deposited by a combination of galvanostatic photodeposition.[36]

In order to increase the photovoltage, a second semiconductor can either be added behind or in front of the Cu_2O stack. Bornoz *et al.* already showed the latter is a viable option, however, the main reason for their low performance

was the lack of overall photovoltage.[37] The bandgap of Si is almost ideal, according to simulations as stated above. However, planar Si has an inherently high reflectivity (~30%) over a broad spectrum.[38] The reflectivity can be lowered substantially (< 1%) by introducing a Si microwire array with a radial *pn*-junction, and such arrays have proven to be very effective PV cells.[39,40] The microwires mostly improve the overall efficiency by improved charge collection, due to the lower reflectivity and thereby increase the current density. Furthermore, in a tandem cell (*e.g.*, in combination with Cu_2O), Si microwires with a junction can increase the photovoltage of the overall stack. However, direct coupling to Cu_2O has never been shown.

Here we show a geometry for a S2F device that is based on tapered Si microwire arrays, to overcome the aforementioned problems (*i.e.*, low light absorption and photovoltage of solely Cu_2O).[41-46] We present the realization and stability of a microwire Si/Cu_2O tandem cell, with a radial *pn*-junction in the Si microwires. We show that the addition of Si microwires enhances the overall absorption of the Cu_2O stack. Furthermore, the introduction of an underlying radial Si *pn*-junction increases the overall photovoltage. In order to show the addition of each aspect of the device, we compare the stacks with and without a microwire architecture and with and without a junction in the Si In this manner we can deconvolute the influence of every step. Additionally, we investigated the roles of ALD-grown n-Ga_2O_3, TiO_2 overlayers, and RuO_x as a cocatalyst in aiding protection from the electrolyte environment and PEC performance, respectively. Lastly, we optimized the Cu_2O layer thickness, and the pitch and height of the Si microwires, in order to obtain the highest overall photoconversion efficiency, photovoltage and current density.

6.2 Results and discussion

6.2.1 Fabrication and characterization of S2F device

We fabricated four different types of photocathodes, to investigate the effect of every change in the stack. Figure 6.1 is a schematic representation of the different stacks we are comparing throughout this manuscript. The sample depicted in Figure 6.1A is used as a baseline, which is fabricated as described in literature.[47] Hereafter a planar buried *pn*-junction in the Si is introduced, Figure 6.1B, to assess the impact of the junction on the produced photovoltage by the underlying Si. Therefore the solid Au layer in Figure 6.1A is replaced by a transparent ITO/Au-nanoparticle layer, as described by Dias *et al.*[47] Lastly, Si microwires are introduced in the stack of materials from Figure 6.1B, to obtain stacks without (Figure 6.1C) and with (Figure 6.1D) a radial *pn*-junction. Therefore, we can assess the contributions of the additions of the microwire and the junction separately.

Details of the fabrication processes are described in the experimental section. For Figure 6.1C/D we introduced Si microwires into the stack. Therefore, we etched straight Si microwires, with a width of 4 µm, by deep reactive ion etching (DRIE), and we tapered the microwires by a Si slow etchant (RSE-100). We and others have shown before that sputtering of materials on high aspect ratio microwires creates an inhomogeneous layer.[7,40] The latter is solved by tapering the Si microwires, thereby the microwire top does not form a shadow effect on the lower parts. Also, we taper the microwires to improve the light absorption properties by reducing the reflectivity. The height and pitch of microwires are known to have an effect on the light absorption capabilities.[39,48,49] Therefore, different bare Si microwire arrays with a pitch in the range of 4 to 24 µm have been fabricated, and with a height varying between 0 (planar, *i.e.*, no microwires) up to 15 µm. In order to use Si also a photo-absorber, we introduced a homogenous *pn*-junction into the Si, both in flat and in the microwire samples (Figure 6.1B/D). A layer of phosphorus oxide was created by

depositing a spin-on dopant (SOD). After a short low-temperature drying step, a thermal drive-in diffusion process was carried out to introduce the P dopant into the silicon at 900° C for 15 min under nitrogen flow. The junction depth was determined by the concentration of dopant and was measured to be around 900 nm.

Electrodeposition of Cu_2O on Si requires the presence of Au as a catalyst. On the reference stack, a layer of Au of 200 nm was sputtered (Figure 6.1A). Au is used to form an ohmic contact to the Cu_2O and to force the growth of Cu_2O in the <111> direction, which is known to have the highest electron conductivity as compared to other direction.[50] This was followed by electrodeposition of ~200 nm Cu_2O, whereby the thickness is controlled by the deposition time. A 20 nm heterogeneous emitter of gallium oxide (Ga_2O_3) and a 100 nm passivation/protection layer of titanium oxide (TiO_2) were both deposited by atomic layer deposition (ALD), and finally a ruthenium oxide (RuO_x) hydrogen evolution catalyst was deposited by galvanostatic photodeposition.[35]

For using the underlying Si substrate as a photo-absorber (Figure 6.1B/C/D), the Au layer needs to be transparent. Therefore, the Au layer in Figure 6.1A was replaced by sputtering 75 nm of indium-doped tin oxide (ITO) directly followed by sputtering ~5 nm of Au nanoparticles onto planar Si (Figure 6.1B), or microwired Si (Figure 6.1C/D). Since the Au is being sputtered, it does not form a continuous layer, but nanoparticulate islands are formed instead.[47] The transparent Au-nanoparticle-containing layer is referred to as ITO/Au throughout the rest of the paper. Hereafter we introduced the same $Cu_2O/Ga_2O_3/TiO_2/RuO_x$ layer stack as described above for the reference sample.

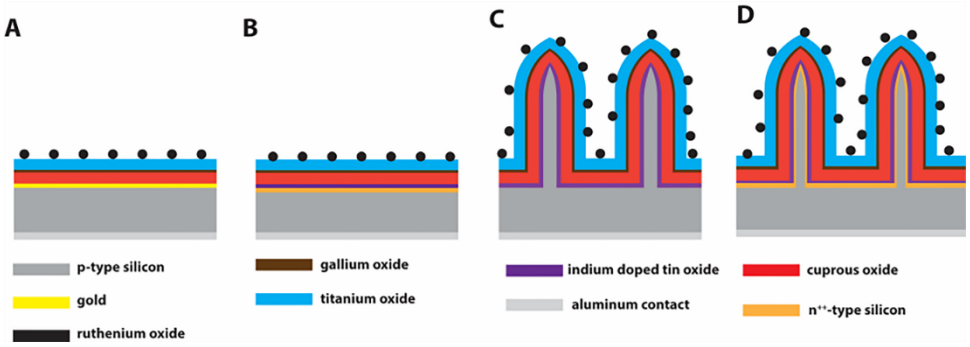

Figure 6.1 Schematic representation of the different device layer architectures (not to scale). (A) A Si substrate (*i.e.* not used as a photoabsorber) with a layer of gold (150 nm), electrodeposited Cu_2O (200 nm), an emitter of Ga_2O_3 (20 nm), a passivation layer of TiO_2 (100 nm), and a RuO_x catalyst (~2 nm). (B) A planar tandem stack of a Si substrate with a planar *pn*-junction, ITO (75 nm)/Au-particles (5 nm), electrodeposited Cu_2O (150 nm), an emitter of Ga_2O_3 (20 nm),a passivation layer of TiO_2 (100 nm), and a RuO_x catalyst (~2 nm).(C) A Si microwire array (15 µm in length), without a *pn*-junction, with ITO (75 nm)/Au-particles, electrodeposited Cu_2O (200 nm), an emitter of Ga_2O_3 (20 nm),a passivation layer of TiO_2 (100 nm), and a RuO_x catalyst (~2 nm). (D) A Si microwire array (15 µm in length), containing a radial *pn*-junction, with ITO (75 nm)/Au-particles, electrodeposited Cu_2O (200 nm), an emitter of Ga_2O_3 (20 nm),a passivation layer of TiO_2 (100 nm), and a RuO_x catalyst (~2 nm).

We used a mixed ITO/Au layer as tunnel junction, as described by Dias *et al.,* to stimulate conformal growth of the Cu_2O, while maintaining a transparent oxide conductor underneath the stack.[47] Dias *at al.* showed already the feasibility and electrical properties of a transparent FTO/Au layer in combination with Cu_2O and also compared the properties to a thick Au layer. Here we show the same is possible on ITO/Au. The growth was investigated by X-ray diffraction (XRD), see Figure 6.2. The addition of the Au particles acts clearly as a growth director in the <111> direction, promoting columnar growth of the Cu_2O layer.[47] The columnar morphology is also visualized by

HR-SEM (see Figure 6.2A-C), and the growth of the Cu_2O was found to be linear with time (~ 6 nm/min).

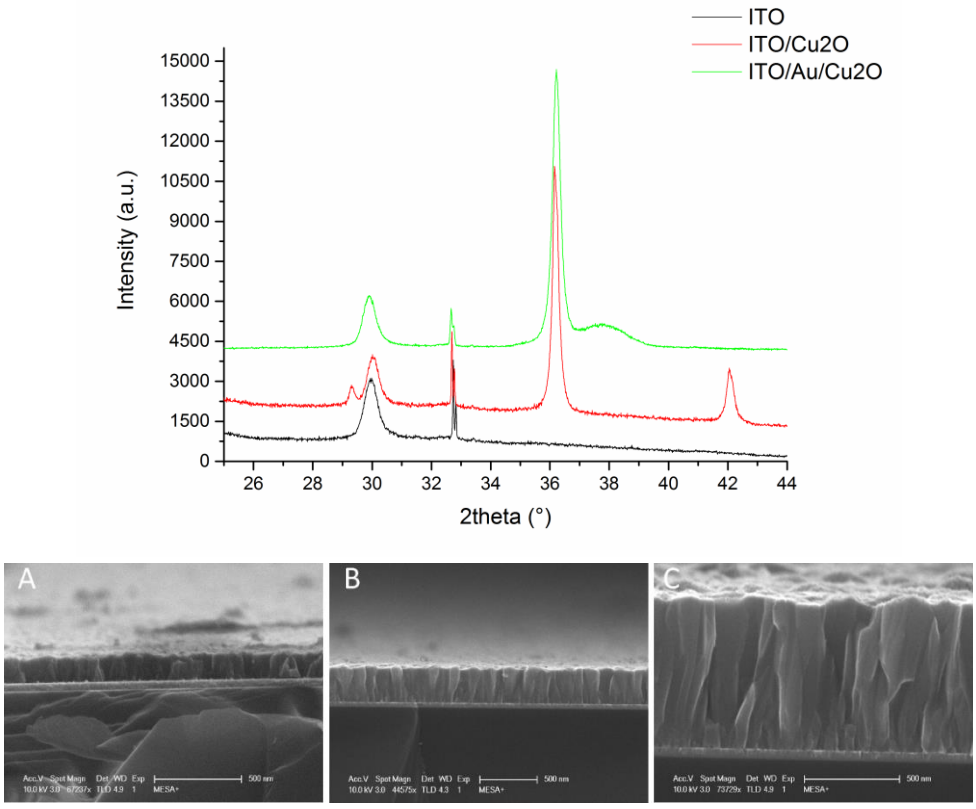

Figure 6.2 XRD patterns of the different Cu_2O on either pure ITO (red) or on the ITO-Au layer (green), with a ITO reference pattern (black) for comparison of the peaks. HR-SEM image of Cu_2O layers on top of ITO with Au particles, with different growth time. (A) 25 min, (B) 50 min, and (C) 105 min.

The layer thickness of the Cu_2O layer on the microwire samples was controlled by applying the same current density as for a planar sample, however increasing the deposition time according to the absolute increased geometric surface area. Table 6.1 shows the time factor for microwires with a length of 10 µm and for different pitches. The thickness of the deposited Cu_2O layer was investigated by HR-SEM by a cross section, as is shown in

Figure 6.3. Here two-time equivalents are shown of Figure 6.2A and B and the observed thicknesses correspond reasonably well with the thicknesses as expected for a planar surface.

Table 6.1 Calculation of the area enhancement due to the addition of microwires of 10 µm in height.

Pitch (µm)	**#Microwires/cm^2 (- - x 10^5)**	**Planar surface area (µm^2)**	**Microwire surface area (µm^2)**	**Time factor (- -)**
2	46.2	113.1	258.2	2.28
4	32.1	113.1	213.9	1.89
6	18.0	113.1	169.8	1.50
8	11.5	113.1	149.4	1.32
10	8.02	113.1	138.3	1.22
14	5.89	113.1	131.6	1.16
19	3.20	113.1	123.2	1.09
24	2.00	113.1	119.4	1.06

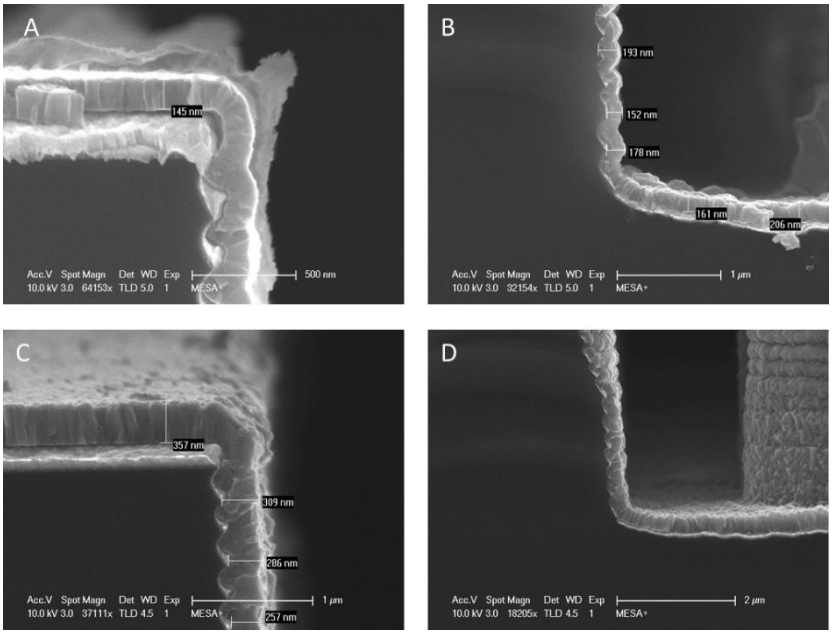

Figure 6.3 SEM images of Cu_2O layer over a sputtered ITO-Au layer for, (A) top side of a microwire (B) the bottoms side of a microwire with 37 min of growth time, and (C) the top side of a microwire and (D) the bottom of a microwire with a growth time of 75 min.

Figure 6.4 shows SEM images after each of the main process steps to fabricate the device in Figure 6.1D. After DRIE, the sample was immersed in a slow Si etching solution (RSE-100) for a short period time to taper the microwires (Figure 6.4A). Upon sputtering of ITO, the brightness of the SEM image increased (Figure 6.4B). Due to the tapering of the microwires, the ITO layer is more conformal over the microwires as compared to without tapering.[7,40] Additionally, Au was sputtered over the sample, which forms most likely islands on top of the ITO layer, but which are not visible in the HR-SEM images.[16,47] Since the ITO/Au layer is conducting, and the electrodeposition process is mass transport limited, a conformal layer of Cu_2O was deposited over the microwires (Figure 6.4C and 6.3). Furthermore, the conformality of the complete stack of materials was investigated by cutting a finished microwire along the z-direction by focused ion beam (FIB)

etching, see Figure 6.4D. The left-hand side is false-colored (as by the legend in Figure 6.4), to aid identification of each of the layers. The ITO layer is present completely over the Si microwire, however, within the crests of the Si microwire (caused by the Bosch etching process), less ITO is present due to the fact that it has been sputtered. Despite the inhomogeneity of the ITO layer all of the consecutive layers are conformal and not hindered by the scalloping of the Si microwires. Especially the thin Ga_2O_3 layer is conformal over the complete structure. The TiO_2 layer fills the remaining crests and smoothens the outside of the whole microwire.

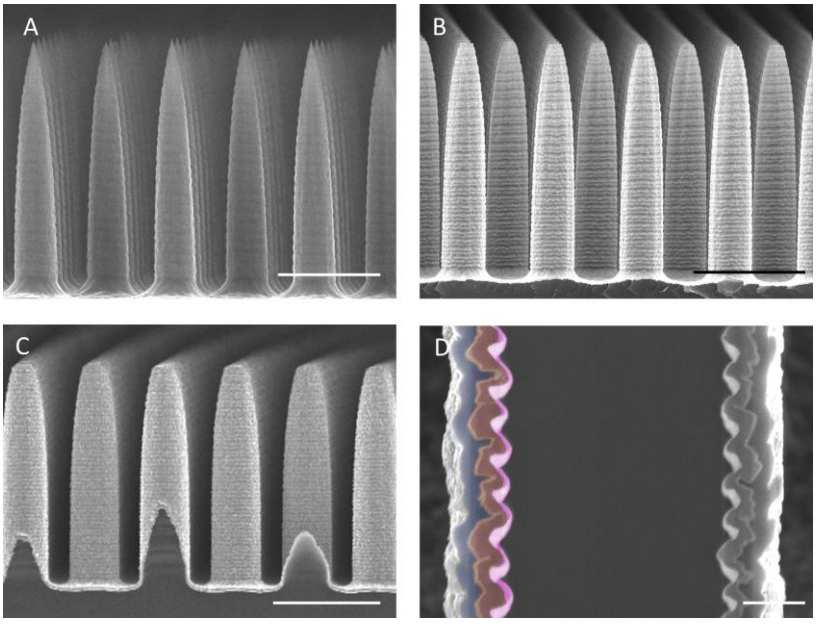

Figure 6.4 HR-SEM images of the microwire array samples after each of the main process steps steps of the fabrication process: (A) after the wet-etch step to taper the Si microwires; (B) after sputtering of the ITO/Au layer over the microwires; (C) after the electrodeposition of Cu_2O, and (D) after completing the whole fabrication process and cutting (by FIB) a microwire in the length direction. In D, the left-hand side is false-colored, ITO/Au (pink), Cu_2O (red), Ga_2O (orange), and TiO_2 (blue). Scale bar in A, B, and C is 5 µm; in D is 500 nm.

6.2.2 Si photovoltaic (PV) cell performance

The influence of the addition of Si microwires on the light absorption capabilities of solely the Cu_2O and ITO/Au layers can be indirectly assessed by investigating the loss in light absorption of the underlying Si PV cell. We tested the underlying Si PV cell after the addition of the ITO/Au layer, since it is known that ITO also acts as a passivation and anti-reflective layer for Si.[40] Therefore, to evaluate the absorption of light in the Cu_2O layer, we quantified the changes in light absorption due to the addition of the ITO/Au layer and after the subsequent addition of the Cu_2O layer, with and without Si microwires (geometry as shown in Figure 6.1B and D, but with Cu_2O as the outer layer), as depicted in Figure 6.5. The different measurement setups are illustrated in experimental section for both a planar and microwire setup, with or without the different overlayers and contacting points to the potentiostat. Figure 6.5A shows that, for a planar Si PV cell with ITO on top, both the J_{sc} and V_{oc} increase due to the addition of the ITO/Au layer. This increase is most likely due to the passivation and anti-reflection properties of the layer. After the addition of a Cu_2O layer on a planar PV cell, the V_{oc} and J_{sc} of the Si PV cell decreased again. The J_{sc} decreased with 4.5 mA/cm^2 due to the Cu_2O layer when compared with only an ITO layer. The decrease in V_{oc} of the planar Si PV cell is most likely due to the decrease in light intensity on the cell.

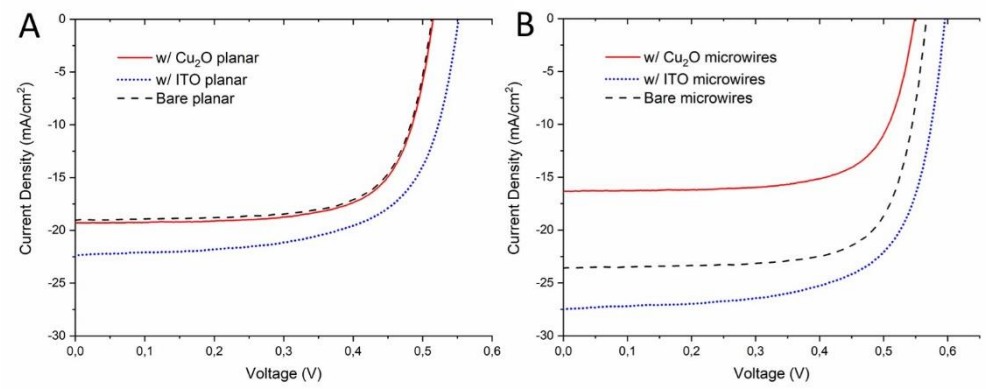

Figure 6.5 *JV* characteristics for dry Si PV cells: (A) planar and (B) microwires, with or without the different overlayers: bare (dashed), with ITO/Au (blue, dotted), and with an additional Cu_2O layer on top of the ITO/Au layer (red, solid).

The *JV* characteristics of bare Si microwires with a radial *pn*-junction were also measured (see Figure 6.5B). Both the V_{oc} and J_{sc} showed an increase with respect to a bare planar sample. This is due to the increase in light absorption capabilities of the Si microwires.[51] When applying an ITO layer over the Si microwires, the J_{sc} and V_{oc} increased even further, due to the anti-reflection and passivation properties. Upon addition of a Cu_2O layer, a substantial decrease in J_{sc} was observed. The J_{sc} for a Si microwire PV cell with Cu_2O decreased with ~11 mA/cm^2. This indicates that the Cu_2O layer absorbs even more sunlight when placed over the microwire sample as on the planar sample. Yet, the remaining current density (approx. 17 mA/cm^2) is sufficiently high for the Si substrate not to become the limiting layer in the overall current density of the device, since the maximum electron generation of the Cu_2O is limited to 14.5 mA/cm^2 [29]

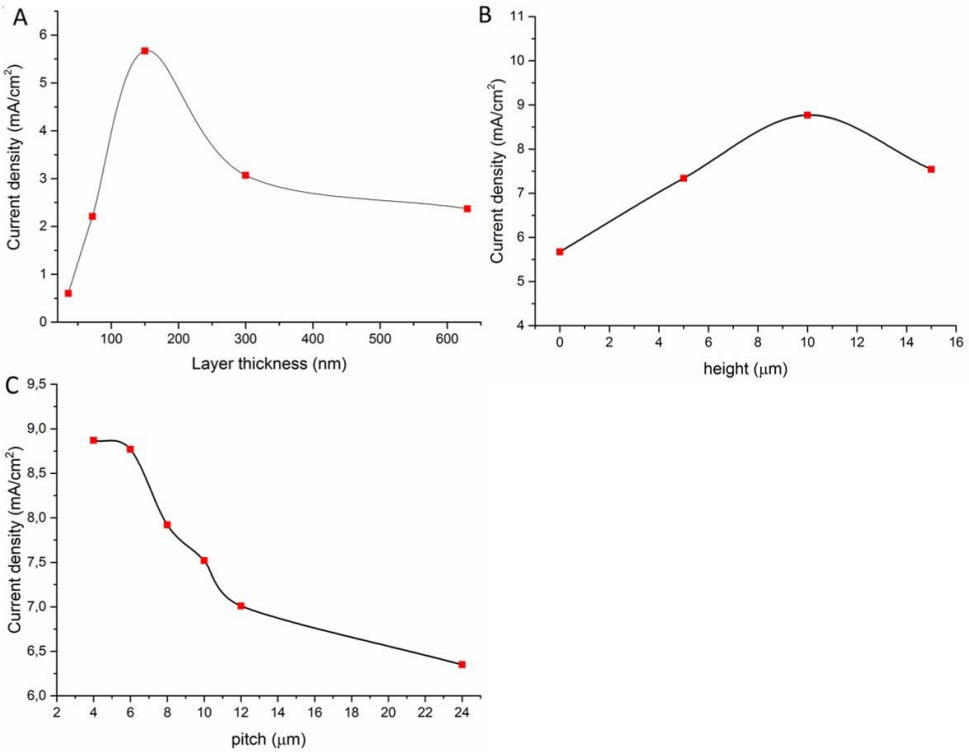

Figure 6.6 Plots of the current density vs. different geometric parameters of the Cu_2O-covered microwire arrays when assessing their *JV* characteristics: (A) planar Cu_2O layer thickness (pitch is 4 μm, height 10 μm), (B) Si microwire height (Cu_2O thickness ~ 200 nm, pitch is 4 μm), and (C) Si microwire pitch (height is 10 μm, Cu_2O thickness ~200 nm).

Secondly, we fabricated microwire samples with varying pitches, microwire heights and Cu_2O thicknesses (geometry as shown in Figure 6.1D, but with Cu_2O as the outer layer). We screened these parameters to find the optimum current density output (Figure 6.5). The Cu_2O layer thickness was optimized with respect to its short circuit current density (J_{sc}), see Figure 6.5A. It was found that a Cu_2O layer thickness of ~200 nm was optimal to achieve the highest J_{sc}. Most likely, a thinner layer does not absorb all the incoming sunlight, and therefore has a lower current density output. A thicker layer, however, will absorb more of the incoming light, but electrons generated deep within the Cu_2O layer will not reach the surface because of

recombination within the Cu_2O layer, due to the limited minority carrier diffusion length of maximally ~200 nm.[29,52,53] The J_{sc} was measured for the microwire arrays with different heights (from 0-15 µm), and microwires with a length of 10 µm gave the highest output (see Figure 6.5B). Lastly, the microwires pitch (core to core distance) was varied from 4-24 µm. Here it was found that a smaller pitch led to a higher J_{sc}, see Figure 6.5C. The highest tested pitch (24 µm) approached the performance of a planar surface, and the microwires were not providing any gain to the light absorption anymore. The pitch of the microwire arrays cannot be smaller than 4 µm, because the wire width (>2 µm) and combined layer thickness (of ITO, Cu_2O and TiO_2) would become higher than the pitch. Therefore, Si microwire arrays with a pitch of 4 µm, a height of 10 µm, and a Cu_2O layer thickness of ~200 nm were considered optimal.

6.2.3 Photoelectrochemical performance

Figure 6.7A shows the PEC performance of the four fabricated Si/Cu_2O photocathode samples (Figure 6.1A-D) measured in a three-electrode configuration using the Si/Cu_2O photocathodes as the working electrode, a platinum mesh as the counter electrode and Ag/AgCl as the reference electrode. All of the photocathodes were compared regarding the relevant values (*i.e.*, J_{ph}, or J_{sc}, V_{oc}, fill factor (*FF*), and efficiency (η)) which are tabulated in Table 6.2. The efficiency was calculated as an ideal regenerative cell (IRC) efficiency, which is described by an equation similar to that used to describe the efficiency of a PV device, see Equation 6.1:

$$\eta_{IRC} = \frac{V_{OC} J_{ph}\left(E_{H_2/H^+}\right) FF}{P_{in}} \qquad (6.1)$$

The values of *FF*, V_{oc} and, J_{ph} in Equation 6.1 were referenced to the equilibrium potential of the half-reaction being performed at the photocathode (the hydrogen evolution reaction), and P_{in} is the light power input (AM 1.5G, 100 mW/cm^2). Our optimized baseline sample, see Figure

6.1A, is depicted in green. From Figure 6.7A it becomes clear that the introduction of solely microwire structures underneath the Cu_2O (*i.e.*, Figure 6.1C), has no noticeable influence on the generated photovoltage. However, by introducing a planar *pn*-junction (*i.e.* Figure 6.1B) underneath the complete stack, the photovoltage is increased to ∼1.36 V, which is ∼500 mV higher than our baseline (Figure 6.1A). The latter is in agreement with the dry PV cell measurement as observed in Figure 6.5A. Furthermore, by introducing both Si microwires and a radial *pn*-junction (*i.e.*, Figure 6.1D), the photovoltage is again increased to ∼1.34 V (see Figure 6.7A).

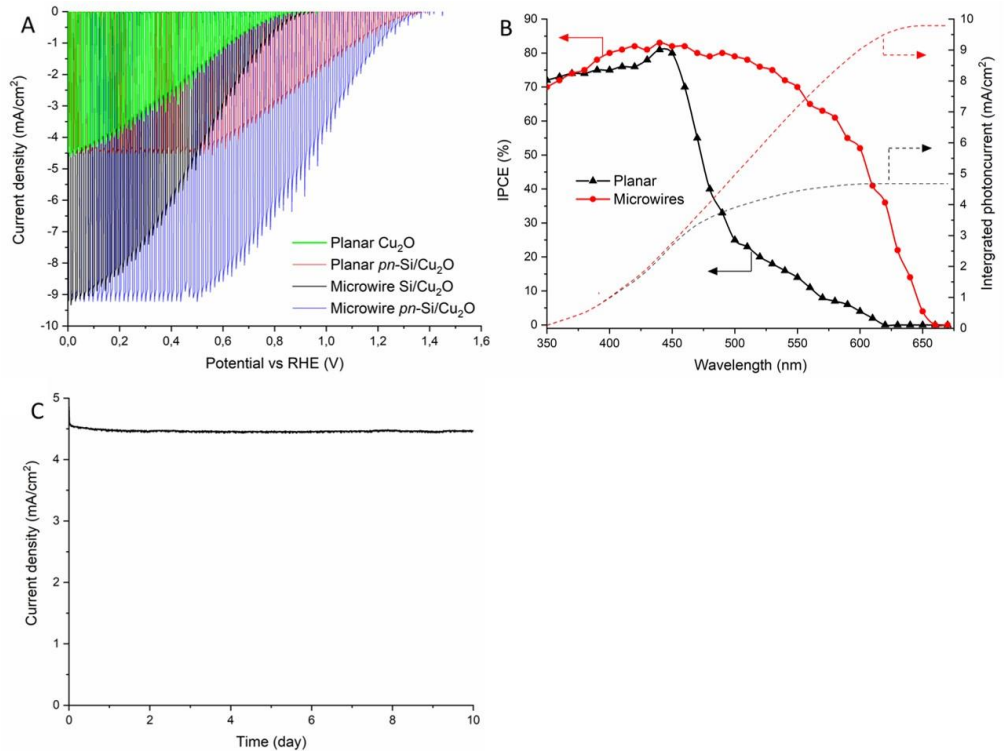

Figure 6.7 (A) PEC response under simulated AM 1.5 G chopped illumination for planar Si/Cu_2O (green), planar Cu_2O tandem with an underlying Si *pn*-junction (red), Cu_2O on microwire substrate (black), and Cu_2O tandem on microwires with an underlying *pn*-junction (blue) photocathodes (geometries as shown in Figure 6.1A-D, respectively; setup shown in experimental section. (B) Corresponding wavelength-dependent IPCE measurements for Si/Cu_2O planar and microwire samples with a buried radial *pn*-junction (as in Figure 6.1B and 1D) (C) PEC stability test of a Cu_2O tandem cell on microwires (Figure 6.1D) at a fixed bias of 1 V versus RHE under illumination, with continuous stirring and a platinum mesh used as a counter electrode. All measurements were performed at pH 5.0 using a combination of 0.5 M Na_2SO_4 and 0.1 M phosphate solution using a three-electrode configuration.

Table 6.2 Overview of the characteristics of the different Cu_2O photocathodes

	V_{oc} (V)	J_{sc} (mA/cm^2)	FF (%)	η_{irc} (%)
Planar Si/Cu_2O	0.88	-4.51	32.08	1.25
Planar *pn*-Si/Cu_2O	1.36	-4.43	44.31	2.70
Microwire Si/Cu_2O	0.92	-9.23	28.81	2.52
Microwire *pn*-Si/Cu_2O	1.34	-9.52	45.07	5.51

Incorporating a *pn*-junction into the Si does not alter the light absorption capabilities of the Cu_2O layer. This is clearly visible when comparing both planar samples (with geometries as shown in Figure 6.1A *vs.* Figure 6.1B), without (green) and with (red) a buried junction (see Figure 6.7A), which shows that the J_{sc} values are virtually the same. From Figure 6.5, it is clear that the Cu_2O layer is the photocurrent-limiting layer, since the underlying planar Si PV cell still generates 19 mA/cm^2, which is far more than the ~4.5 mA/cm^2 produced in the PEC cell. However, the short circuit density increased from 4.5 mA/cm^2 to 9.2 mA/cm^2 upon going from a flat to a microwired sample (Figure 6.1A *vs.* Figure 6.1C) . The increase in J_{sc} was expected by the observed decrease in J_{sc} of the underlying Si microwires PV cell, as discussed above for Figure 6.5.

The increase in current density is also well understood by measurements of the incident photon-to-current conversion efficiency (IPCE) of both a planar Cu_2O (Figure 6.1A) and a microwired *pn*-Si/Cu_2O (Figure 6.1C) photocathode with optimized parameters as discussed above, as presented in Figure 6.7B. Electrodeposited Cu_2O on a planar substrate absorbs light well up to 450 nm, beyond which the absorptivity drops rapidly to zero. The integrated photocurrent from the IPCE data combined with the AM 1.5 G solar

spectrum corresponds well to the value of the photocurrent presented in Figure 6.7A and to the current loss for a planar PV cell shown in Figure 6.5A. The IPCE for a microwire sample shows a broad plateau response across a wide spectral range. This broad response enhances the current density output tremendously, as is visible for both the integrated photocurrent and the output shown in Figure 6.7A, and this behavior is in accordance with the current decrease shown in Figure 6.5B. Our results are in agreement with to Niu *et al*.[54] who have shown that implementing a 3D nanostructure of Cu_2O yields a broad absorption from UV to 650 nm. We show here that the strategy of implementing the microwire 3D structure into electrodeposited Cu_2O can be utilized to harvest the red part of the incoming light.

The overall regenerative efficiency is a comprehensive manner to assess the overall effect of an increase of both the V_{oc} and J_{sc}. The η_{irc} of the planar tandem PEC cell (Figure 6.1B) doubles with respect our baseline planar photocathode (Figure 6.1A), from 1.25% to 2.70%, due to the increase in photovoltage. By incorporating the Cu_2O microwires (Figure 6.1C), the η_{irc} again doubles as compared to our baseline planar photocathode, from 1.25% to 2,52%, However, now by the substantial increase in J_{sc}. Combining these both systems, *i.e.* utilizing a radial Si *pn*-junction within Cu_2O microwires (Figure 6.1D). The Cu_2O microwires increase the overall J_{sc} and the underlying microwire Si PV cell boosts the maximum obtainable V_{oc}, all-in-all increasing the overall efficiency from 1.25% to a record 5.51%.

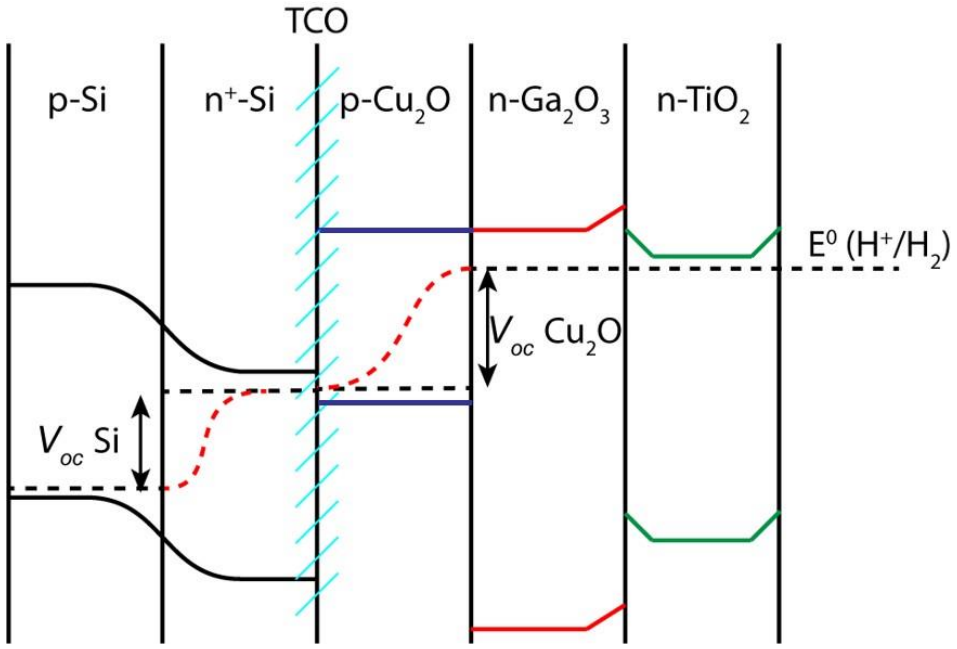

Figure 6.8 Illustration of the band diagram for *pn*-Si/Cu_2O photocathodes during PEC measurement under illumination.

Lastly, we have examined the TiO_2 protection layer deposited by ALD for suppressing photocorrosion. The ALD-deposited conformal TiO_2 layer protects the Cu_2O/Ga_2O_3 buried junction from direct contact with the electrolyte and transports the photogenerated electrons to the electrolyte where hydrogen evolution takes place (Figure 6.8). A PEC stability test under bias at 1 V *vs.* RHE showed hardly any degradation over time (Figure 6.7C). Only during the first day, a slight fall in current density was observed, which leveled off thereafter. Operation over a period of 10 days consecutively showed an excellent stability even under load. With more than 200 h this is the longest stability test reported for such Cu_2O photocathodes, to the best of our knowledge. The stable operation of the Si/Cu_2O photocathode protected by TiO_2 is attributed to three main factors: (i) the ALD-deposited TiO_2 film is highly stable in acidic/ basic solution; (ii) there

is no change in oxidation state of the titania film, and (iii) the HER catalyst (RuO_2) remains attached in a stable manner throughout the operation.

6.3 Conclusions

In summary, we have demonstrated a benchmark tandem Si/Cu_2O microwire photocathode featuring a current density of 9.5 mA/cm^2 at 0 V versus RHE, 4.5 mA/cm^2 at +1 V versus RHE, and a photovoltage of ~1.4 V utilizing a microstructured Cu_2O absorber, a Ga_2O_3 emitter layer, a TiO_2 protection layer, and a RuO_x HER catalyst. The IPCE curves showed a plateau between 300–600 nm for a microstructured Cu_2O layer, while dropping sharply in the blue region for a planar sample. The microstructuring doubled the overall current density. Making use of the transparent interlayer of ITO/Au-nanoparticles, a buried *pn*-junction in Si can be further employed. This extra junction pushed the obtainable open circuit potential from ~1 V to ~1.4 V. All-in-all, the better light absorption and the additional voltage from the underlying buried junction increased the efficiency of 1.25% for a planar Cu_2O photocathode to 5.51% for a microwired *pn*-Si/Cu_2O one. The stability test at 1 V vs RHE showed great promise to use the described geometry in a S2F device, since the stability did not change over the course of 10 days even under load (at 1 V vs RHE). In conclusion, our results provide rational design strategies for making efficient Cu_2O-based photocathodes and push the frontier of PEC water splitting.

6.4 Acknowledgements

Wouter Vijselaar is gratefully acknowledged for fruitful discussions and performed experiments. Thomas Moehl and David Tilley (Department of Chemistry, University of Zurich) are acknowledged for ALD of the Ga_2O_3 and TiO_2 layers. Henk van Wolferen is acknowledged for the FIB experiments and Mark Smithers is thanked for the HR-SEM images.

6.5 Materials and Methods section

6.5.1 Fabrication of radial n^+/p junctions in silicon microwire arrays

Silicon microwires with radial n^+/p junctions were fabricated as reported before, but without the use of silicon dioxide as a hard mask, see Figure 6.9.[39,40,55] In short, cleaned silicon substrates (Okmetic) were covered with a 100 nm thick silicon-rich silicon nitride layer (SiRN) using low-pressure chemical vapor deposition (LPCVD). The SiN_x layer was removed from the front side using reactive ion etching, leaving a protective SiN_x layer at the back side. After cleaning, a photoresist layer (OiR 906-12) on the front side was patterned by standard photolithography, resulting in 0.5 x 0.5 cm^2 hexagonal arrays of dots with a various pitch within each 2 x 2 cm^2 sample. This resist layer functioned as a mask during deep reactive ion etching of silicon using the Bosch process (Figure 6.9A). This process resulted in microwires with various lengths, depending on the etching time, and the samples were cleaned by an O_2/CF_4 plasma before further processing. Tapering of the microwires was performed by immersing the Si microwires in a slow etchant (RSE-100) for 10s (Figure 6.9B). Afterwards the samples were place in a quick dump rinse, to immediately stop the etching process. Hereafter, doping was performed on freshly cleaned substrates by depositing a dopant-containing oxide layer (SOD 509, Filmtronics), dried in two stages (100 °C for 5 min, and 200 °C for 30 min, Figure 6.9C) and followed by a thermal drive-in step to diffuse the dopant into the silicon. Thermal diffusion was performed at 900 °C for 15 min under nitrogen flow, starting at 800 °C with a ramp of 5°C/min and natural cool-down to 800 °C (Figure 6.9D).

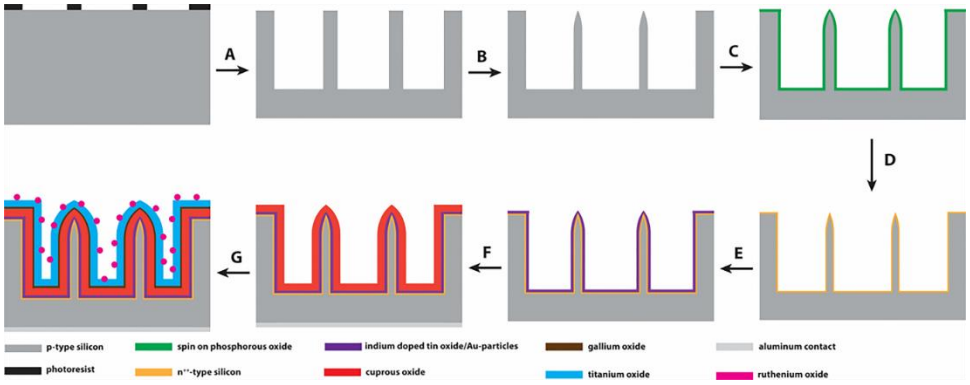

Figure 6.9 A schematic overview of the fabrication process of the radial *pn*-junctions in silicon microwire arrays with Cu_2O. (A) Deep reactive ion etching of the Si microwires. (B) Tapering of the Si microwires by a Si slow etchant. (C) spin coating a spin on dopant. (D) drive in of the phosphorous spin on dopant to create a radial *pn*-junction. (E) sputtering of ITO/Au layer. (F) Electrodeposition of the Cu_2O layer and back contacting by an aluminum layer. (G) Atomic layer deposition of Ga_2O_3 and TiO_2 followed by galvanostatic photodeposition of RuO_x.

6.5.2 Indium tin oxide and gold sputtering

Indium tin oxide (ITO) was deposited by means of an in-house built sputter device (Figure 6.9E). The samples were placed on a rotating chuck (5 rpm), 44 mm from the ITO source, in a low-pressure reactor chamber (5.5×10^{-3} mbar) with a 40 sccm flow of argon. The ITO source had an angle of 45° with respect to the wafer surface. By means of a DC power of 50 W and a 20 sccm argon flow at the gun ITO was sputtered (2.6 nm/min deposition rate).

Gold (Au) was deposited by means of the same in-house built sputter device (Figure 6.9E). The samples were placed on a rotating chuck (5 rpm), 44 mm from the Au source, in a low-pressure reactor chamber (2×10^{-2} mbar) with a 100 sccm flow of argon. The Au source had an angle of 45° with respect to the wafer surface. By means of a DC power of 50 W and a 20 sccm argon flow at the gun Au was sputtered (15 nm/min deposition rate).

6.5.3 Electrodeposition of Cu_2O on Au and ITO-Au

The Cu_2O layer was electrodeposited on the prepared substrate at 30 °C from a lactate-stabilized copper sulfate solution (Figure 6.9F). The chemicals were used as received without further purification: $CuSO_4$ (Sigma-Aldrich, ≥99%), K_2HPO_4 (Sigma-Aldrich, ≥99.5%), lactic acid (Fisher Scientific, 85%), and KOH (Honeywell, extra pure). Briefly, an aqueous solution was prepared with an initial concentration of 0.2 M $CuSO_4$, 0.5 M K_2HPO_4, and 3 M lactic acid. This solution was then diluted with a large volume of 2 M KOH until pH 12 was attained. Cu_2O was deposited in galvanostatic mode using a Versastat 4 with a current density of −0.1 mA/cm^2 with respect to the planar surface. Growth time as indicated in Table 6.1.

6.5.4 Atomic layer deposition of Ga_2O_3 and TiO_2 layers:[35]

The Ga_2O_3 and TiO_2 layers (Figure 6.9G) were deposited on the Cu_2O substrate using a thermal ALD system (PICOSUN, R-200). The Ga_2O_3 film was deposited at a reactor temperature of 160 °C using bis(μ-dimethylamino) tetrakis(dimethylamino)digallium (STREM, 98%) and H2O as the precursors of Ga and O. The TiO_2 film was deposited at a reactor temperature of 120 °C with tetrakis(dimethylamino)-titanium (Aldrich, 99.99%) and H_2O as the precursors of Ti and O. The temperature of the Ga, Ti, and O precursor cylinders were held at 150 °C, 85 °C, and room temperature, respectively. A “boost” sequence was implemented in the Picosun software for the Ga and Ti precursor cylinders. First, the ALD valve was opened, allowing the precursor to flow to the reaction chamber (referred to as precursor dosing). Then the line pressure was increased, forcing nitrogen back into the precursor cylinder. The ALD valve was then closed, trapping a higher pressure inside the precursor cylinder while the line pressure was reduced to the normal value. Upon the next ALD pulse, the larger pressure difference between the cylinder and the line ensures that more precursor was drawn into the reaction chamber during the dosing step, thus boosting the amount of precursor injected into the reaction chamber at a given precursor cylinder temperature. For Ga_2O_3, the Ga precursor ALD valve was opened for 2.5 s

(0.5 s dosing to the reactor, 2.1 s of increased line pressure), followed by a 7.0 s N_2 purge. Then a 0.1 s pulse of H2O was used, followed by a 4.0 s N_2 purge. For TiO_2, the Ti precursor ALD valve was opened for 1.6 s (0.5 s dosing to the reactor, 1.2 s of increased line pressure), followed by a 6.0 s N_2 purge. Then a 0.1 s pulse of H_2O was used, followed by a 6.0 s N_2 purge.

6.5.5 Electrodeposition of RuO_x as hydrogen evolution catalyst

Ruthenium oxide (RuO_x) was used as the hydrogen evolution reaction catalyst in the photocathode to get a stable water splitting performance. The RuOx was galvanostatically deposited under 1 sun illumination with a constant current density of 28.3 μA/cm^{-2} from a 1.3 mM potassium perruthenate ($KRuO_4$) solution, for 5 min (Figure 6.9G).[35]

6.5.6 Focused ion beam structuring

FIB structures were made with a Nova 600 Dual Beam – SEM/FIB setup. A Ga^+ liquid metal ion source was used to mill away approximately half of a single microwire, along the microwire length with respect to the footprint of an array, with a beam current of 0.92 nA and a 10 kV extraction voltage.

6.5.7 *JV* measurements

To measure the electrical characteristics of the coated Si microwires, samples were positioned perpendicular to a light source. *JV* measurements were recorded on a VersaSTAT 4 potentiostat using a linear voltage sweep from -0.7 to 0.7 V at a rate of 0.2 V/s. The light intensity was calibrated to AM 1.5G illumination at the position of the sample (see Figure 6.10).

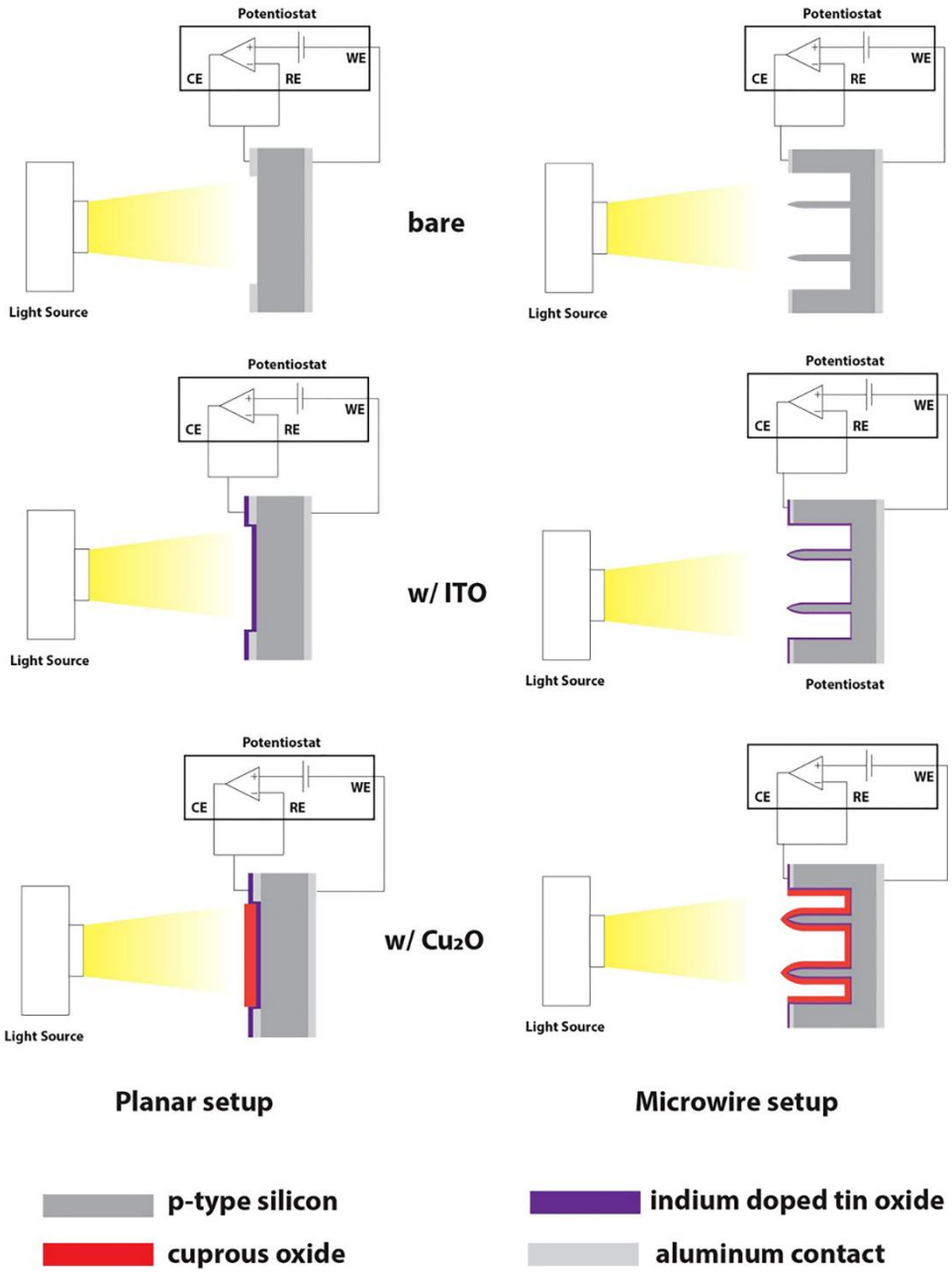

Figure 6.10 The used setups to investigate the impact of the ITO and Cu_2O overlayers on the underlying Si PV cell with respect to the J_{sc}, V_{OC} and *FF* (data shown in Figure 6.5)

6.5.8 PEC measurements

The coated microwire photocathodes were photoelectrochemically tested using a potentiostat (VersaSTAT 4) in a three-electrode configuration, where the microwire photocathode with an exposed projected surface area of 0.28 cm^2 acted as the working electrode (WE), a platinum wire mesh as the counter electrode (CE) and an Ag/AgCl electrode as the reference electrode (RE). For PEC measurements under illumination, the backside p-Si base was contacted through the aluminum contact on the back. Five full cyclic voltammetry measurements were done at a scan rate of 10 mV/s. The light intensity was calibrated to AM 1.5G illumination at the position of the sample (see Figure 6.11). The water layer on top of the sample was 15 mm thick. The absolute light absorption by the solution would lead to a decrease of 3 mA/cm^2 if it is assumed that every photon leads to an electron. The absorption was calculated by the Lambert-Beer relation and integrated over the solar spectrum in the range of 300 – 1200 nm.[56]

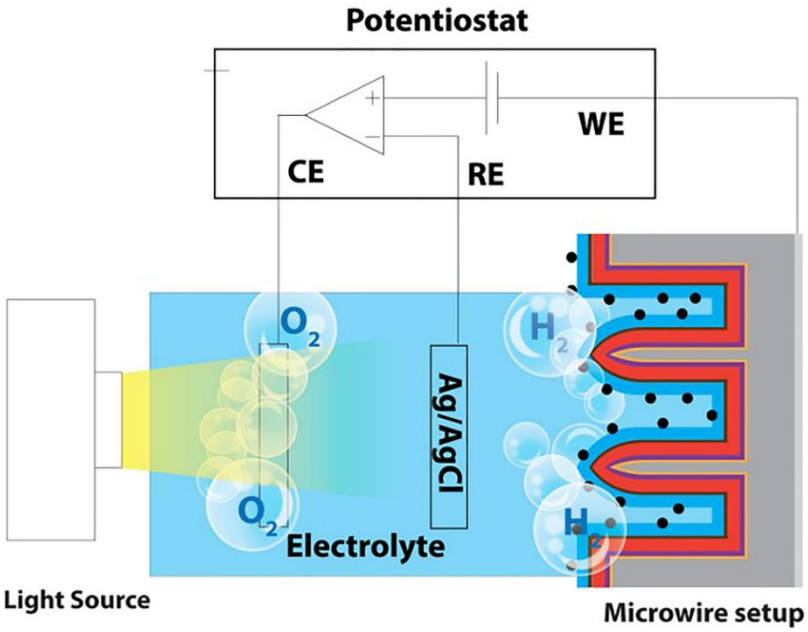

Figure 6.11 Schematic illustration of the photocathode setup. Working electrode (WE) is connected to the back side of the Si substrate, a reference electrode (RE) is connected to a Ag/AgCl reference electrode, and the counter electrode (CE) was connected to a Pt Mesh. The back side of PV cell was clamped in half an H-cell. The Pt mesh was outside the light path.

6.5.9 Light source and calibration

The light source that was used is a 300 W xenon arc light source, fitted with Air Mass filter (AM 1.5 G) from Newport, Oriel Instruments. Upon installation, the lamp was calibrated by Newport. Before every measurement the lamp was checked by a calibrated reference solar cell (91150V). The 91150V reference cell and meter consists of a readout device and a 2 x 2 cm calibrated solar cell made of monocrystalline silicon and a KG5 window. The cell is equipped with a thermocouple assembled in accordance with IEC 60904-2. The certification is accredited by NIST to the ISO-17025 standard. It reads solar simulator irradiance in sun units, whereby one sun is equal to 1000 W/m^2 at 25 °C and AM 1.5 Global Reference.

The solar simulator was checked for spectral mismatch by a spectrometer (AvaSpec-ULS2048XL-EVO) fitted with a CC-VIS/NIR, slit size of 10 µm, 1.4 nm resolution in the range of 300 - 1050 nm, an integration time of 8 ms, and averaged over 60 scans. The current density (assuming 100% IPCE) of the calibrated lamp and the ASTM spectrum match very well, 40.1 mA/cm^2 and 40.8 mA/cm^2 respectively, in the range of 300-1050 nm.

6.6 References

1 Zhong, D. K., Cornuz, M., Sivula, K., Grätzel, M. & Gamelin, D. R. *Energy Environ. Sci.* **4**, 1759-1764, (2011).

2 Zhong, D. K. & Gamelin, D. R. *J. Am. Chem. Soc.* **132**, 4202-4207 (2010).

3 Gurudayal *et al.* Perovskite–Hematite Tandem Cells for Efficient Overall Solar Driven Water Splitting. *Nano Lett.* **15**, 3833-3839, (2015).

4 Kim, T. W., Ping, Y., Galli, G. A. & Choi, K.-S. *Nat. Commun.* **6**, 8769, (2015).

5 Abdi, F. F., Firet, N. & van de Krol, R. *ChemCatChem* **5**, 490-496 (2013).

6 Kim, J. H. *et al*. *ACS Nano* **9**, 11820-11829, (2015).

7 Shaner, M. R. *et al*. *Energy Environ. Sci.* **7**, 779-790, (2014).

8 Miecznikowski, K., Ramirez-Caro, A., Fiechter, S. & Kulesza, P. J. *Meeting Abstracts* MA2015-01, 1752 (2015).

9 Bae, D., Seger, B., Vesborg, P. C. K., Hansen, O. & Chorkendorff, I. *Chem. Soc. Rev.* **46**, 1933-1954, (2017).

10 Verlage, E. *et al. Energy Environ. Sci.* **8**, 3166-3172, (2015).

11 Jiang, C., Moniz, S. J. A., Wang, A., Zhang, T. & Tang, J. *Chem. Soc. Rev.* **46**, 4645-4660, (2017).

12 Steinmiller, E. M. P. & Choi, K.-S. *Proc. Natl. Acad. Sci.* **106**, 20633-20636, (2009).

13 Abanades, S. & Chambon, M. *Energy & Fuels* **24**, 6667-6674, (2010).

14 Masudy-Panah, S., Siavash Moakhar, R., Chua, C. S., Kushwaha, A. & Dalapati, G. K. *ACS Appl. Mater. Interfaces* **9**, 27596-27606, (2017).
15 Septina, W., Prabhakar, R. R., Wick, R., Moehl, T. & Tilley, S. D. *Chem. Mater.* **29**, 1735-1743, (2017).
16 Son, M.-K. *et al. Energy Environ. Sci.* **10**, 912-918, (2017).
17 Oh, J., Deutsch, T. G., Yuan, H.-C. & Branz, H. M. *Energy Environ. Sci.* **4**, 1690-1694, (2011).
18 Warren, E. L., McKone, J. R., Atwater, H. A., Gray, H. B. & Lewis, N. S. *Energy Environ. Sci.* **5**, 9653-9661 (2012).
19 van Dorp, D. H., Hijnen, N., Di Vece, M. & Kelly, J. J. *Angew. Chem. Int. Ed.* **48**, 6085-6088, (2009).
20 Walter, M. G. *et al. Chem. Rev.* **110**, 6446-6473, (2010).
21 Doscher, H., Geisz, J. F., Deutsch, T. G. & Turner, J. A. *Energy Environ. Sci.* **7**, 2951-2956, (2014).
22 Bolton, J. R., Strickler, S. J. & Connolly, J. S. *Nature* **316**, 495-500, (1985).
23 Zhao, J., Wang, A., Altermatt, P. P., Wenham, S. R. & Green, M. A. *Sol. Energy Mater. Sol. Cells* **41-42**, 87-99, (1996).
24 Shah, A., Torres, P., Tscharner, R., Wyrsch, N. & Keppner, H. *Science* **285**, 692-698, (1999).
25 Saga, T. *NPG Asia Mater* **2**, 96-102 (2010).
26 Minami, T., Nishi, Y., Miyata, T. & Abe, S. *ECS Transactions* **50**, 59-68, (2013).
27 Lee, Y. S. *et al. Energy Environ. Sci.* **6**, 2112-2118, (2013).
28 Minami, T., Nishi, Y. & Miyata, T. *Thin Solid Films* **549**, 65-69, (2013).
29 Luo, J. *et al*. *Nano Lett.* **16**, 1848-1857, (2016).
30 Pan, L. *et al. Nature Catalysis* **1**, 412-420, (2018).
31 Lee, Y. S. *et al*. *Adv. Mater.* **26**, 4704-4710, (2014).
32 Wong, T. K. S., Zhuk, S., Masudy-Panah, S. & Dalapati, G. K. *Materials* **9**, (2016).
33 Li, C. *et al. Energy Environ. Sci.* **8**, 1493-1500, (2015).

34 Paracchino, A., Laporte, V., Sivula, K., Grätzel, M. & Thimsen, E. *Nat. Mater.* **10**, 456, (2011).

35 Tilley, S. D., Schreier, M., Azevedo, J., Stefik, M. & Graetzel, M. *Adv. Funct. Mater.* **24**, 303-311, (2014).

36 Niu, W. *et al. Adv. Energy Mater.* **8**, 1702323, (2018).

37 Bornoz, P. *et al. The Journal of Physical Chemistry C* **118**, 16959-16966, (2014).

38 Lee, K. *et al. Nanoscale* **8**, 14473-14479, (2016).

39 Elbersen, R., Vijselaar, W., Tiggelaar, R. M., Gardeniers, H. & Huskens, J. *Adv. Energy Mater.* **6**, 1501728, (2016).

40 Vijselaar, W., Elbersen, R., Tiggelaar, R. M., Gardeniers, H. & Huskens, J. *Adv. Energy Mater.* **7**, 1601497, (2017).

41 Dahl, S. & Chorkendorff, I. *Nat. Mater.* **11**, 100-101, (2012).

42 Hou, Y. *et al. Nat. Mater.* **10**, 434-438, (2011).

43 McFarlane, S. L., Day, B. A., McEleney, K., Freund, M. S. & Lewis, N. S. *Energy Environ. Sci.* **4**, 1700-1703, (2011).

44 Spurgeon, J. M., Walter, M. G., Zhou, J. F., Kohl, P. A. & Lewis, N. S. *Energy Environ. Sci.* **4**, 1772-1780, (2011).

45 Warren, E. L., McKone, J. R., Atwater, H. A., Gray, H. B. & Lewis, N. S. *Energy Environ. Sci.* **5**, 9653-9661, (2012).

46 Shaner, M. R., McKone, J. R., Gray, H. B. & Lewis, N. S. *Energy Environ. Sci.* **8**, 2977-2984, (2015).

47 Paula, D. *et al*. *Adv. Energy Mater.* **5**, 1501537, (2015).

48 Vijselaar, W. *et al. Nature Energy* **3**, 185-192, (2018).

49 Elbersen, R., Vijselaar, W., Tiggelaar, R. M., Gardeniers, H. & Huskens, J. *Adv. Mater.* **27**, 6781-6796, (2015).

50 Huang, M. H. *Small* **15**, 1804726, (2019).

51 Elbersen, R. *et al*. *Adv. Energy Mater.* **5**, 1401745, (2015).

52 Zhang, Z. *et al. ACS Nano* **7**, 1709-1717, (2013).

53 de Jongh, P. E., Vanmaekelbergh, D. & Kelly, J. J. *Chem. Mater.* **11**, 3512-3517, (1999).

54 Wenzhe, N. *et al. Adv. Energy Mater.* **8**, 1702323, (2018).

55 Elbersen, R. *et al. Adv. Energy Mater.* **5**, 1401745-1401753, (2015).

56 Hale, G. M. & Querry, M. R. *Appl. Opt.* **12**, 555-563, (1973).

Summary

At present, nearly 75% of the world's energy consumption is supplied from fossil fuels such as coal, petroleum, and natural gas. A major part of this is utilized by the transportation sector and the remainder is used for electricity generation in power stations that burn fossil fuels. The combustion of fossil fuels to harvest their stored carbon-based energy is a primary source of greenhouse gas emissions, mainly in the form of carbon dioxide (CO_2), and consequently is responsible for global warming. For these reasons, interest in and harvesting of solar energy as a crucial alternative clean energy source have developed quickly in current years. As a main source of energy, solar energy has the potential to deliver all energy desired by mankind.

Solar technology implementation has been broadly focused on electricity generation. Despite recent progress in solar electrical energy generation, important issues remain unsolved, such as the continued need for high-power energy demand for transport, central heating, and industrial processes, and the intermittency problem, such as caused by the alternation of summer and winter periods. One of the proposed solutions is to construct a solar-to-fuel (S2F) device, which describes the concept of turning solar energy into storable fuel. To fabricate a fully integrated, efficient S2F device based on photo-electricity, a single or set of semiconductors must be combined with a proper electrocatalyst. In this thesis, we show various geometries and materials combinations for a S2F device, primarily based on copper-based photocatalysts with structured silicon as a base material, employing device structuring and modification.

The main body of this thesis can be divided into three parts. The first part is introductive and comprises the first two chapters. **Chapter 1** gives a general overview of the energy and environmental problem and underlines the importance and urgency of switching to a green and sustainable economy. The great potential of solar water splitting for hydrogen production is

pointed out. **Chapter 2** is a review article that describes the fundamental aspects of protection strategies for achieving stable and practical photoelectrochemical (PEC) solar water splitting and the working principles of a PEC cell. It lists the main requirements that a photo-electrode should fulfill to ensure good performance: efficiency and stability. Moreover, it introduces briefly the selected materials and explains the reasons for the choices.

The second part of the thesis includes **Chapters 3** and **4** and presents the work done on Cu_2O-based photoelectrodes protected with carbon-based materials (carbon and graphitic-C_3N_4).

Chapter 3 deals with a carbon thin layer-protected Cu_2O photocathode. The deposition of the solution-based carbon precursor and subsequent carbonization strategy provided a thin protective carbon layer on unstable semiconductor nanostructures, which constitutes a solution to the commonly occurring photocorrosion problem of many semiconductors. A proof-of-concept has been provided by using glucose as the carbon precursor to form a protective carbon coating onto cuprous oxide (Cu_2O) films which were synthesized by electrodeposition. The carbon layer-protected Cu_2O film exhibited remarkably improved photostability as well as considerably enhanced photocurrent density. The optimized electrodes showed photocurrents up to 6.5 mA/cm^2 and 7.5 mA/cm^2 at potentials of 0 V and -0.1 V vs RHE at pH 5.5, respectively. The stabilities of the Cu_2O/C and Cu_2O/CuO/C photocathodes, at a low bias of 0.3 V vs RHE, were retained after 50 h.

Chapter 4 is focused on the fabrication and characterization of a novel Cu_2O/g-C_3N_4/CoS triple-layered photocathode designed for the PEC hydrogen evolution reaction. In this photocathode, the Cu_2O film was covered by graphitic carbon nitride, g-C_3N_4, as the protective layer, due to its good chemical stability. The g-C_3N_4 could also form a *p-n* junction with Cu_2O to increase the light-to-electricity conversion efficiency. Further modification with CoS as a HER catalyst exhibited an increased photoactivity.

Of particular importance are interfacial engineering, coating techniques, and nanostructure control to facilitate charge separation and migration. In this work, the Cu_2O photocathode was protected by a thin film of g-C_3N_4 nanosheets or nanowires by spin-coating or electrospinning methods, respectively. Under optimized conditions, the Cu_2O/5wt% g-C_3N_4 NWs/CoS photocathode showed the best performance: ca. 6.6 mA/cm^2 was achieved at 0 V_{RHE} and the processed photocathode exhibited 5 h solar to chemical conversion under AM 1.5 illumination in Na_2SO_4 electrolyte solution without a sacrificial agent.

The third part of the thesis presents the work done by integrating a semitransparent copper oxide top photoabsorber layer in tandem with a radial p/n junction Si microwire array for unassisted solar water splitting, as is described in **Chapters 5** and **6.**

In **Chapter 5**, we developed a tandem PEC device with p-Cu_2O as a top photoabsorber and pn-Si as a bottom photoabsorber. The p-Cu_2O nanofilm was grown by electrodeposition on the pn-Si substrate. We compared the performance of Si micropillar arrays with p-Cu_2O (Si/ITO-Au/Cu_2O/ZnO/TiO_2/Pt stack) and compared this stack with a planar device. Introducing a radial p/n junction in the Si microwires enabled maximum photovoltage of the Si substrate. Electrodeposition of Cu_2O ensured a conformal layer over these high aspect ratio structures. We optimized each of the layer thicknesses over different geometries, to minimize the overall reflectivity and optimize the absorption. Pulsed-laser deposition (PLD) is one of the most promising techniques for the conformal coating of complex structures. Protection layers (n-ZnO and TiO_2) aided in the charge separation and maximized the photovoltage of the underlying p-Cu_2O photon absorber. Additionally, we analyzed the role of the transparent conductive interlayer between the two photoabsorbers to enhance light absorption and charge transport, and protection layers enabled better band alignment that reduced photocorrosion.

In **Chapter 6**, further optimization of the tandem Si/Cu_2O photocathode for S2F devices is presented by fabricating a tapered Si microwire architecture. Introducing a radial *pn*-junction in the Si microwires enables maximum photovoltage of the Si substrate. We show the simulation of the reflectivity of the different layers in the stacks and the optimized thickness of the different interlayers. We optimized the Cu_2O layer thickness and the microwire dimensions (height and pitch), in order to obtain the highest overall photoconversion efficiency. Conformal protection layers, deposited by atomic layer deposition (ALD), effectively shield the underlying Cu_2O film which enables a high photocurrent density and stable PEC operation for over 10 days.

In summary, the findings presented in this thesis focus primarily on copper oxides (Cu_2O & CuO) in photocathodes. Because of its band gap of 2.0 eV, Cu_2O could theoretically provide a solar to hydrogen conversion efficiency of 18% for a single junction Cu_2O photocathode under established working conditions for water splitting. The results present in previous studies have come close to the material limit. However, the major limiting factors are the material stability and the positioning of the Cu_2O redox potentials in between its band gap, which promotes self-corrosion under light irradiation. Furthermore, the mismatch between the optimal thickness for light absorption and the charge carrier diffusion length limits the PEC performance. As shown in this thesis, micro/nanostructuring is favorable for enhancing the efficiency, and can provide devices that deliver higher performance compared to planar architectures.

To improve the performance of photoelectrochemical photocathodes based on Cu_2O, composite materials have been used, heterojunctions have been developed, and the surface has been passivated with stable oxide materials with improved optical absorption and charge extraction properties. The tandem PEC configuration is shown to be superior, concerning aspects of high efficiency, stability, and the use of earth abundant materials. These improvements may lead to design strategies for fabricating efficient

photocathodes and push the boundary of solar water splitting, possibly beyond the target of 10% solar-to-hydrogen efficiency.

Samenvatting

Tegenwoordig wordt bijna 75% van de wereldwijd verbruikte energie opgewekt door middel van fossiele brandstoffen zoals steenkool, olie en gas. Een groot deel hiervan wordt door de transportsector gebruikt en de rest wordt gebruikt voor het opwekken van energie in energiecentrales die fossiele brandstoffen verbranden. Door deze verbranding komt de in koolstof opgeslagen energie vrij, maar dit is tevens een primaire bron van de uitstoot van broeikasgassen, met name in de vorm van koolstofdioxide (CO_2), hetgeen bijdraagt aan de opwarming van de aarde. Hierdoor is de ontwikkeling van zonne-energie als zeer belangrijke, alternatieve en schone brandstof over de afgelopen jaren snel toegenomen. Zonne-energie heeft de potentie om alle energie te genereren die de mens nodig heeft.

De implementatie van zonne-energie is grotendeels gefocust op het opwekken van elektriciteit. Ondanks recente vooruitgang in de opbrengst van elektriciteit uit zonne-energie blijven er nog belangrijke problemen onopgelost, zoals de continue behoefte aan elektriciteit voor transport, centrale verwarming en industriële processen, en het niet op elkaar afgestemd zijn van vraag naar en aanbod van energie (bijvoorbeeld het verschil in energieverbruik in de zomer en de winter). Een van de voorgestelde oplossingen is het maken van een zonlicht-naar-brandstof (‘solar-to-fuel’, S2F) apparaat. Dit is een concept waarin zonne-energie omgezet wordt in een brandstof die opgeslagen kan worden. Om een volledig geïntegreerd en efficiënt S2F-apparaat te maken dat gebaseerd is op foto-elektriciteit, moeten halfgeleiders gecombineerd worden met een elektrokatalysator. In dit proefschrift worden verschillende combinaties van geometrieën en materialen voor een S2F-apparaat gepresenteerd, die alle primair gebaseerd zijn op koper-gebaseerde fotokatalyse met gestructureerd silicium als basismateriaal, waarin we het apparaat structureren en modificeren.

De bevindingen die in dit proefschrift gepresenteerd worden richten zich met name op het gebruik van koperoxides (Cu_2O en CuO) in fotokathodes. Vanwege de energetische bandafstand ('band gap') van 2.0 eV kan Cu_2O in theorie een efficiëntie van de conversie van zonne-energie naar waterstof van 18% behalen voor een Cu_2O-fotokathode onder de condities voor het splitsen van water. De resultaten van eerdere onderzoeken kwam dichtbij de materiaal-bepaalde limiet. Desondanks blijven de materiaalstabiliteit en de positionering van de Cu_2O-redoxpotentiaal in de band gap, dat zelf-corrosie door lichtabsorptie stimuleert, belangrijke limiterende factoren. Bovendien beperkt de mismatch tussen de optimale dikte voor de absorptie van licht en de diffusielengte van de ladingsdrager de fotoëlectrochemische prestatie. Zoals te lezen is in dit proefschrift, is micro/nanostructurering voordelig voor het verhogen van de efficiëntie en kan het zorgen voor apparaten die betere prestaties leveren in vergelijking met een vlakke architectuur.

Om de prestaties van de op Cu_2O-gebaseerde fotoelektrochemische (PEC) fotokathodes te verbeteren, zijn samengestelde materialen gebruikt, heterojuncties ontwikkeld en is het oppervlak gepassiveerd met stabiele oxides met verbeterde optische absorptie en ladingsextractie-eigenschappen. De in serie geschakelde PEC-configuratie was het best met betrekking tot hoge efficiëntie, stabiliteit en het gebruik van veelvoorkomende materialen. Deze aspecten kunnen leiden tot betere ontwerpstrategieën voor het maken van fotokathodes en ze verleggen de grens van watersplitsing met zonne-energie, mogelijk zelfs voorbij het doel van 10% efficiëntie in de conversie van zonne-energie naar waterstof.

Meer informatie is verstrekt in de Engelstalige samenvatting van dit proefschrift.

Acknowledgments

Firstly, I would like to express my sincere gratitude to my advisor Jurriaan Huskens for the continuous support of my Ph.D study and related research, for his patience, motivation, and immense knowledge. His guidance helped me in all the time of research and writing of this thesis. I could not have imagined having a better advisor and mentor for my Ph.D study.

This work would not have been possible without the financial support from the Karnataka Government under D.Devaraja Urs Videshi Vyasanga Vethana scholarship scheme.

I appreciate very much that Wouter, Alexander, Pieter and Janneke for all the discussion and helps of lab experiments and cleanroom fabrication techniques. I have learned many things from you all which I should have spent weeks to understand. My PhD research considerably depended on the microfabrication work in the cleanroom of the MESA+ Institute for Nanotechnology. Hence, I would like to thank all cleanroom staff members for instructions me how to use the equipment and maintaining the normal operation.

Thanks to all collaborators Prof. David Tilley, Thomas Moehl (University of Zurich, Switzerland) for ALD technique. Dr. Nguyen Minh (IMS), Karin and Cavit (MCS) for fruitful discussions and performed PLD, electrospinning experiments.

I really appreciate MnF/BNT secretaries Nicole and Izabel for their help in organization and taking care of all the paperwork. Big thanks also to the technicians Marcel, Regine, Richard, and Bianca for their help in offering me the resources in running the program. I would also like to extend my thanks to academic staffs Jeroen, Pascal, Nathalie, Jos, Tibor, Mul, Hans, David and Bastian for the suggestions and discussions during colloquia presentations and TBSC solar meetings.

It is a great pleasure to be a part of MnF/BNT group for the past 3.5 years. Thank you all group members Salmeen, Almu, Jenny, Cande, Nicole, Yao, Qin, Fangyuan, Min, Manee, Deepak, Gaurav, Aref, Sara, Maike, Gülistan, Nico, Erik, Gigi, Naomi for creating such a pleasant environment, thereby bringing me a wonderful PhD

time decorated with those enjoyable workweeks, CHAINS, summer BBQs, Saturday lunch at Fusion wok, spontaneous dinners, card games and coffee+ cake-moments.

I'm very grateful to my wonderful paranymphs Luca, Daniele and Jacopo for all your help and support, not only during the preparation of this thesis and the defense, but also during our time together as a PhD.

Robin, special thanks for your help with the translating the summary and I really enjoyed all our talks.

During the time in Enschede I did not only meet people from the University, but also many people from outside. Thanks to a group of friends, the Flying Nerds (Super fun Volleyball), when I arrived in Enschede. A special thanks to Isa, for the precious time warm feeling of home here in Enschede. Omid, Liwia, Bakr, Aliki, Sandro, Philip, Desi, Igors, Kirill, Zarko, Andrea, Effie, Matteo, Lucia, Jozef, Bojan, and all others from all over the world, thank you for being there, playing volleyball, ice-skating, BBQs, and evening out in the city centre.

I also want to acknowledge VAS Arashi group, the martial arts association, especially my beloved master Rene, Rohit, Ron, Aarya for Pukulan training.

In addition, I would like to thank my parents for their wise counsel and sympathetic ear. You are always there for me. Finally, there are my friends, who were of great support in deliberating over our problems and findings, as well as providing a happy distraction to rest my mind outside of my research.

Pramod

Enschede, July 2019

About the author

Pramod Patil Kunturu was born in Huvina Hadagali, India on August 6, 1989. He studied basic science at the JSS Science College, Karnataka University, India, where he gained his Bachelor's degree (B.Sc.) in January 2010. Apart from his study, he was also selected as a Summer Research Fellow in the DESE group of Prof. Manoj Neergat at the Indian Institute of Bombay, India, between May 2012 and July 2012, which programme is jointly sponsored by IASc (Bangalore), INSA (New Delhi) and NASI (Allahabad).

In March 2013 he got the Master's degree (M.Sc.) in organic chemistry at the Kuvempu University, India, with a thesis entitled "Shape-controlled synthesis of Pd and its electrochemical study in acidic electrolyte for low-temperature fuel cell". The work was carried out in the group of Prof. Dr. V. P. Vaidya and Prof. Manoj Neergat. From January 2014 to October 2014, he worked as an R&D assistant in the group of Prof. Ujjal K. Gautam at the New Chemistry Unit, JNCASR, Bengaluru. During this period, he and co-workers studied and synthesized Pt-Pd alloys, Pt nanosheets, Pt-nanotetrahedra particles for efficient electrocatalytic applications for fuel cells.

Since January 2016, he has been working as a Ph.D. candidate at the Molecular Nanofabrication group, University of Twente under the supervision of Prof. dr. ir. Jurriaan Huskens. The results of this research are described in this thesis.

List of Publications

1. “Demonstrator devices for artificial photosynthesis: general discussion”, Faraday Discuss., **2019.**
2. “Pathways to electrochemical solar-hydrogen technologies”, *Energy Environ. Sci.***, 2018**.
3. “A tandem Cu_2O/Si microwire hydrogen evolving photocathode with photovoltage exceeding 1.3 V”, **submitted**.
4. “Pd-Pt alloy nanowires as support-less electrocatalyst with high synergistic enhancement in efficiency for methanol oxidation in acidic medium”, *J. Colloid Interface Sci.*, **2016**.
5. “Mechanochemical synthesis of free-standing Pt nanosheets and their electrocatalytic properties”, *Adv. Mater.*, **2015**.
6. “High-yield synthesis of sub-10 nm Pt nanotetrahedra with bare ⟨111⟩ facets for efficient electrocatalytic applications”, *ACS Appl. Mater. Interfaces.*, **2015**.

In preparation:

7. “Boosting solar water splitting performance of photoelectrodes by surface protection strategies”.
8. “Efficient solar water splitting photocathodes comprising a copper oxide heterostructure protected by a thin carbon layer”.
9. “Improving charge separation in Cu_2O/g-C_3N_4/CoS photocathodes by a Z-scheme heterojunction to achieve enhanced performance and photostability”.
10. “Passivation layers on a tandem silicon-copper oxide micropillar array photocathode made by pulsed laser deposition”.